Quantum Optics with Rydberg Atoms and Ions

DISSERTATION

zur Erlangung des akademischen Grades

“Doctor of Philosophy”

an der

Fakultät für Mathematik, Informatik und Physik

der

Leopold-Franzens-Universität Innsbruck

vorgelegt von

Mag. rer. nat. Alexander W. Glätzle

September 2014

(updated Oct. 13th 2014)

Doktorvater/Thesis Advisor:

Prof. Peter Zoller, Innsbruck

Für meine Eltern Rosmarie und Wolfgang

ZUSAMMENFASSUNG

Rydberg-Atome eignen sich in idealer Weise stark korrelierte Quantensysteme zu untersuchen und sind eine vielversprechende Plattform für die Quanteninformationsverarbeitung. Insbesondere Rydberg-Atome in optischen Gittern haben ein großes Potenzial um Quanten-Vielteilchensysteme zu simulieren. Sie bieten neue, aussichtsreiche Eigenschaften wie flexible, isotrope oder anisotrope, langreichweitige Wechselwirkungspotentiale; die Möglichkeit effektive Wechselwirkungspotentiale mit Laserparametern zu gestalten; schnelle und präzise Steuerung des simulierten Hamiltonoperators und einstellbare und kontrollierbare dissipative Effekte.

Der erste Teil der Dissertation untersucht Mischungen von Rydberg Atomen und polaren Molekülen als offene Quantensysteme. Insbesondere präsentieren wir eine Möglichkeit, dreidimensionale Wechselwirkungspotentiale zwischen Rydberg Atomen und polaren Molekülen zu konstruieren, mit dem Ziel, generische polare Moleküle direkt zu kühlen. Die Atome dienen als (Niedertemperatur-) Reservoir sowohl für elastische wie auch für inelastische Stöße mit bemerkenswerten und potenziell nützlichen Eigenschaften: stark abstoßende langreichweitige Potentiale schützen vor ungewollten inelastische Kollisionen auf kurze Entfernung, und sehr große elastische Streuquerschnitte führen zu schneller Thermalisierung. Darüber hinaus konzipieren wir eine kontrollierte dissipative (inelastisch) Kollision, bei der ein spontan emittiertes Photon die (kinetische) Energie der Kollisionspartner – ähnlich wie bei einem ‘Sisyphus-Effekt’ – abtransportiert, wodurch eine erhebliche Menge an Energie in einer einzigen Kollision entfernt werden kann. Zusätzlich untersuchen wir die Langzeitstabilität eines Rydberg Gases, wenn Dekohärenzprozesse, wie spontane Emission und Schwarzkörperstrahlung nicht vernachlässigt werden können und zu starken mechanischen Effekten führen. Im Speziellen untersuchen wir das Zusammenspiel von Laser-Kühlung und Heizdynamik durch Dekohärenz mit Hilfe von Molekulardynamik-Simulationen.

Ein zweites Thema dieser Arbeit bezieht sich auf die Implementierung von Quantensimulatoren für verschiedene Quanten-Spin-Modelle mit Rydberg-Atomen und Ionen im speziellen frustrierter Magnetismus. Wir präsentieren einen Vorschlag zur Implementierung von Quanten-Spin-Eis – ein paradigmatisches Beispiel ist, wie die Physik der frustrierten Magnete mit Eichtheorien zusammenhängt. Das Ziel ist es, mit kalten Rydbergatomen Wechselwirkungen zu entwerfen, die ein vereinfachtes Modell von Quanten-Spin-Eis auf einem zweidimensionalen Schachbrettgitter realisieren. Wir entwickeln dafür eine Atomphysik Toolbox, die auf den neuesten experimentellen Fortschritten aufbaut, und die starke Winkelabhängigkeit der van-der-Waals-Wechselwirkungen zwischen hohen Drehimpuls Rydberg-Zuständen mit der Möglichkeit stufenartigen Potenziale zu konstruieren kombiniert. Dies erlaubt es uns, abelsche Eichtheorien basierend auf verschiedenen Geometrien zu konstruieren, die mit den momentanen Experimenten realisiert werden können.

ABSTRACT

Rydberg atoms are a promising platform for quantum information processing with the prospect to explore the quantum dynamics of strongly-correlated systems. In particular, Rydberg atoms in optical lattices have a great potential for simulating quantum many-body physics. They offer genuinely new capabilities including tunable, isotropic or anisotropic long-range interactions, the possibility to shape the effective interaction potentials using laser parameters, fast and precise control of the simulated Hamiltonian and the engineering of controlled dissipative effects.

The first part of this thesis is concerned with mixtures of Rydberg atoms and polar molecules as open quantum systems. In particular, we propose a scheme to engineer three dimensional interaction potentials between laser-dressed Rydberg atoms and ground state polar molecules in order to achieve direct cooling of generic polar molecules. The atoms act as a designed (low-temperature) reservoir for both elastic and inelastic collisions with remarkable and potentially useful properties: strong repulsive shields protect from inelastic collisions at short range and exceedingly large elastic scattering cross sections lead to rapid thermalization. Moreover, we discuss a dissipative (inelastic) collision where a spontaneously emitted photon carries away (kinetic) energy of the collisional partners similar to a 'collisional Sisyphus' effect, thus providing a significant energy loss in a single collision. Additionally, the long-time stability of a Rydberg dressed gas is studied, where decoherence processes such as spontaneous emission and black-body radiation can lead to strong mechanical effects. We investigate the interplay between laser-cooling and heating dynamics due to decoherence by performing molecular dynamics simulations.

The second topic of this thesis concerns the implementation of quantum simulators for various quantum-spin models characterizing frustrated magnets using Rydberg atoms and ions. In particular, we present a discussion of quantum spin ice, which represents a paradigmatic example on how the physics of frustrated magnets is related to gauge theories. The goal is to assemble a system of cold Rydberg atoms and to design interactions that realize a toy model of quantum spin ice on a two-dimensional checkerboard lattice. We develop an atomic toolbox, building on the recent experimental advances and combine the strong angular dependence of van der Waals interactions between high angular momentum Rydberg states with the possibility of designing step-like potentials using ground state atoms weakly dressed by Rydberg states. This allows us to implement Abelian gauge theories in a series of geometries, which could be demonstrated within state of the art experiments.

CONTENTS

CHAPTER 1

GENERAL INTRODUCTION

1.1 The world of quantum optics and ultra cold atoms

The immense experimental progress during the last decades allows the possibility to now trap and control a single atom or photon in a definite region of space and prepare and manipulate it in a well-defined quantum state. This is so spectacular, that even the founding fathers of quantum physics were initially skeptical:

> "*We never experiment with just one electron or atom or (small) molecule. In thought-experiments we sometimes assume that we do; this invariably entails ridiculous consequences.*" (W. Schrödinger, 1952) [1]

This incredible journey started in the mid 80s, when the physics Nobel price laureates of 2012, S. Haroche and D. Wineland, and others developed ground-breaking experimental methods to control individual photons and atoms. This was a breakthrough, which opened a new door to explore the fascinating and exotic world of quantum physics and laid the foundation for a new generation of physicists to take the first steps towards building quantum computers and atomic clocks with unimaginable speed and precision. Today, quantum physicists around the world are actually able to perform what used to be 'Gedanken-experiments' and reveal deeper lying aspects of the quantum world which decades ago were considered to be pure abstraction.

Both S. Haroche and D. Wineland work in the field of *quantum optics*, which studies the non-relativistic interaction of atoms with quantized light and is in the front line exploring the exotic quantum world [2, 3]. A field, where theory and experiments profit from each other in a remarkable synergy. The formulation of a quantized theory of light started in the mid 1920s right after the birth of quantum mechanics when P. Dirac and others published seminal papers on the quantum theory of radiation. During the next decades lot of effort was put into the calculation of optical spectra and the explanation the natural line width of spectral lines due to the quantized vacuum. Undoubted, the development of the maser and the laser by C. H. Townes, A. L. Schawlow and others and its theoretical description, in particular by Haken, Lamb, Lax and Scully, was a revolution, both on the experimental but also on the theoretical side. On the experimental side it opened a new era where light with a well defined frequency can be produced at a very high power, while on the theoretical side it triggered the investigation of open quantum systems, where a system interacts with a noisy environment. Glauber, Wolf, Sudarshan, Mandel, Klauder and many others were the first to look for unambiguous quantum effects in light and described states with non-classical statistical properties. In the 1970s, H. J. Carmichel and D. F. Walls predicted that these non-classical states can be generated in resonance fluorescence experiment from a two-level atom. Experiments at the single particle level, which triggered the 'Golden Age' of experimental quantum optics, have become possible in the 1980s with the development of ion trap techniques by H. G. Dehmelt and W. Paul. The first observation of non-classical light by J. Kimble et al. [4], the violation of Bell's inequalities by A. Aspect et al. [5] and the group of A. Zeilinger [6] and the first teleportation of atoms by the group of R. Blatt [7] are only a few experimental highlights of the last decades which showed that there is indeed a crucial difference between the classical and the quantum world. Quantum optics first entered the field of quantum information science with the seminal proposal of Cirac and Zoller in 1995 to use trapped ion to preform quantum gates [8]. As shown by recent experiments, in particular in the labs of D. Wineland in Boulder and R. Blatt in Innsbruck, ion traps currently provide one of the most promising approaches to quantum information processing [9].

Another major breakthrough was the development of cooling and trapping techniques of neutral atoms using laser light by the groups of S. Chu, C. Cohen-Tannoudji and W. D Phillips in the beginning of the 90s together with pioneering theoretical work from G. Ashkin, S. Stenholm, C. Cohen-Tannoudji and many others [10, 11]. The key idea was to use the photon recoil together with Doppler shifts to decelerate an atomic beam down to temperatures of micro-Kelvin. This, together with evaporative cooling methods, culminated in the first experimental observation of Bose-Einstein condensates by the groups of E. A. Cornell, C. E. Wieman and W. Ketterle in 1995 – a new quantum state of matter predicted already in 1924 by S. Bose and A. Einstein [12].

The possibility of manipulating and controlling quantum many-body states of matter has paved the way towards the investigation of strongly correlated phases and phenomena, which are ubiquitous in various fields of physics ranging from high-energy physics to condensed matter physics. The regime of strongly correlated systems with ultra cold atoms was first accessed in 2002 by I .Bloch, T. Hänsch and coworkers [13]. In a groundbreaking experiment they observed a quantum phase transition from a superfluid to a Mott-insulator state in an optical lattice realizing a seminal proposal of P. Zoller and coworkers [14]. The key idea is to use the dipole forces of two counter-propagating laser beams, forming a spatially periodic intensity pattern, acting on neutral atoms in order to realize a periodic potential. Such optical lattices play the very same role as ions in solid-state crystals, providing an underlying potential which affects the motion of the atoms as the ions do with the electrons. Optical lattices provide a highly tunable quantum system where all parameters can be externally controlled, e.g. the height of the potential can be tuned by varying the laser intensity leading to a competition between quantum tunneling and interactions. Today, optical lattices have become a widely used tool in many labs around the world to study strongly correlated many-body physics [15]. Moreover, cold atoms in optical lattices provide a unique platform to realize interacting quantum spins systems in various lattice geometries with tunable interactions, and thus the basic ingredients of competing magnetic orders and frustrated magnetism. We will make use of these recent experimental advances in III in order to implement various types of spin models using Rydberg atoms in optical lattices.

1.2 Laser excited Rydberg atoms

Rydberg states are highly excited electronic states of atoms and molecules [16]. The existence of these highly excited states was first demonstrated by Johann Balmer in 1885 who studied the wavelength of light emitted by hydrogen atoms. Three years later Johannes Rydberg, who soon became the eponym of these states, found a more generalized version of Balmer's formula which nowadays is known as the Rydberg formula. It predicts an infinite series of energy levels which converges to an ionization limit.

Rydberg atoms have been studied for almost a century, mainly in the context of high precision light-matter interactions, spectroscopy and plasma physics [16–19]. Due to their exaggerate properties they have become an ideal testing platform for modern quantum physics, e.g. to study the quantized vacuum in resonant cavities in the group of S. Haroche [20] or the development of the atom maser by D. Meschede et al.[21]. Rydberg atoms first entered the stage of quantum optics in 2000 as an ideal candidate for quantum information processing by a seminal proposal from P. Zoller, M. Lukin and coworkers [22, 23]. Since then quantum optics with Rydberg atoms became an extremely flourishing and successful field which connects atomic physics and quantum optics with quantum information science, condensed-matter and many-body physics in an interdisciplinary way [24].

What makes these highly excited atoms so special?

The properties of Rydberg atoms are compelling in many aspects: The electronic level structure of Rydberg states in alkali atoms resembles the one of hydrogen atoms (up to corrections due to quantum defects [25]) which is mainly determined by the principal quantum number n [16–19]. They can be excited from atomic or molecular ground-states by laser light via absorption of one or more photons, with Rabi frequencies scaling as $\sim n^{-3/2}$. This requires lasers with both, large intensities and a narrow frequency width, in order to achieve a coherent evolution within the natural lifetime. Rydberg atoms can have an orbital radius $r \sim a_0 n^2$ as large as μm, with a_0 Bohr's radius, and is only loosely bound to the atomic core. This leads to a very large polarizability $\alpha \sim n^7$ and therefore to a very high sensitivity to external electric or electromagnetic fields. These highly excited electronic states are long-lived, with life-times τ scaling as $\tau \sim n^3$ ($\tau \sim n^5$) for low (high) angular momentum states, and can easily exceed hundreds of μs.

In contrast to neutral ground state atoms or ions, Rydberg atoms possess both strong and tunable interactions over distances of several micrometers. These interactions can be more than ten orders of magnitudes larger than van der Waals (vdW) interactions between neutral ground state atoms at comparable distances and have the advantage, e.g. compared to ions, that they are tunable in strength and shape using external fields. In the absence of external fields and for distances larger than the Rydberg orbit, the dominant interaction is of the van der Waals type, $V_{\mathrm{VdW}} \sim (ea_0)^4 n^{11}/R^6$, with e the electron charge. The interactions can be either attractive or repulsive (in contrast to the vdW interactions of two ground state atoms) and can be isotropic for Rydberg s states or anisotropic for higher angular momentum states [26, 27]. In the presence of external static electric or electromagnetic fields, or close to a Förster resonance, the Rydberg-Rydberg interaction becomes dipolar, $V_{\mathrm{dd}} \sim (ea_0 n^2)^2/R^3$, which is both long-range and anisotropic. Additional tunability can be achieved using external AC or DC electric and magnetic fields. Recent experiments with cold and ultracold alkali atoms have demonstrated vdW and dipole-dipole interactions for two Rydberg atoms as well as many-body interactions [28–41].

Most applications of these strong interactions rely on the so-called *Rydberg-blockade mechanism*, which was first discovered in the context of quantum information processing with cold atoms [22, 23]. In the blockade regime the presence of a single atom laser excited to a Rydberg state shifts the energy levels of the surrounding atoms within a characteristic radius r_b ($\sim \mu$m), such that the laser excitation probability to the Rydberg state for any other atom within a volume $\sim r_b^3$ is strongly suppressed. In this case the excitation becomes coherently delocalized among all particles within r_b, which are now collectively coupled to the laser with an enhanced Rabi frequency $\sqrt{N_b}\Omega$, where N_b is the atom number within r_b and Ω is the single-particle Rabi frequency. This is often referred to a as *superatom* and has been observed in remarkable experiments in the groups of M. Saffman in Wisconsin [42] and P. Grangier and A. Browaey in Paris [43], with two atoms trapped in a deep optical potential as a key ingredient to realize two-qubit gates [44, 45]. Usually, quantum information is stored in long-lived hyperfine states, only one of which is coupled by laser light to the Rydberg state. Rydberg-blockade effects can be then utilized for acquiring collisional phase shifts conditional on the atomic ground state population.

Similar ideas have been recently extended to encode and process quantum information in ensembles of multilevel atoms [46], to generate many-particle entanglement [47], single-atom or single-photon sources [48], or electromagnetically induced transparency in dense ensembles of Rydberg atoms [49]. A fundamental new twist has been introduced by combining Rydberg-excited atoms with optical lattices [36, 37] in order to study strongly correlated states. Part III of this thesis builds on that experimental progress and extends previous work by combining Rydberg atoms in optical lattices with anisotropic interactions present in higher angular momentum Rydberg states.

The strong, tunable and long-range interactions of Rydberg atoms, together with their long lifetime, make them an ideal candidate to study novel many-body effects. Recently, Rydberg interactions and blockade effects have been observed both in cold gases ($<$ mK) as well as in ultracold ($\lesssim 100$ nK) Bose-Einstein condensates in the so-called *frozen gas* regime [50]. In the latter, the average kinetic energies and spontaneous emission rates ($\sim$ kHz) are much smaller than interactions ($\sim$ GHz), and thus the motion of the atoms can be neglected during the experimental timescales. This justifies neglecting the atomic kinetic energy term in the Hamiltonian and treating the interacting gas as ‘frozen’ in a given configuration. In this limit the interacting gas of Rydberg atoms can be modeled as an ensemble of two-level systems, where the ground and Rydberg states correspond to spin down- and up-states, respectively, implying a fully coherent spin-model. This triggered a variety of theoretical studies, which predict interesting ground states of these spin systems and analyzed the formation of correlated Rydberg excitations [51–54]. In the superatom regime the spatial distribution of excitations can become correlated giving rise to crystal-like patterns, while the atoms themselves act as a featureless background medium. This has been recently demonstrated in notable experiments in Munich [37].

Most interesting phenomena in condensed matter, however, seem to occur when the atomic kinetic energy becomes comparable to, or even larger than, the average interaction energy. The competition between these two energy scales can in turn determine phase transitions between various classical and quantum many-body phases. For Rydberg atoms, this requires going beyond the frozen-gas regime, where the external atomic motion has to be taken into account.

Early work in Ref. [55] has proposed to explore this regime either (i) by weakly admixing the Rydberg state to the electronic groundstate using an off-resonant continuous-wave laser or (ii) via a stroboscopic excitation of the Rydberg state using pulsed lasers. In both schemes the average interaction strength between atoms can be made orders of magnitude smaller than the corresponding interaction between Rydberg states, and thus comparable with the mean kinetic energies. In addition, the average decay rate from the Rydberg state is considerably suppressed in both schemes, leading to an increased lifetime of the effective laser-dressed two-level system [56]. Compared to polar molecules [57] laser-driven Rydberg atoms have not only the advantage of a large and tunable dipole moment, which can be of the order of several tens of Debye, but also to create ‘step-like’ potentials due to the blockade effect [58]. This allows one to explore strongly correlated many-body physics with controllable long-range interactions for which a variety of novel classical and quantum many-body phases have been predicted [59–62]. For example, recent theoretical work based on the scheme (i) above has demonstrated that the groundstate of Rydberg-dressed atoms in the weakly interacting regime can be a supersolid [63–66]. For strong interactions, correlated quantum and classical phases can be realized, including a self-assembled crystal [67] with individual atoms arranged in a periodic structure. As we discuss in Chapter 3, however, stronger interactions usually come at the expense of a comparatively shorter lifetime, and this can lead to strong mechanical effects, which can crucially alter the dynamics of such interacting gases.

1.3 Quantum Simulations

The groundbreaking experimental achievements with ultra cold atoms, molecules and ions mentioned in the previous section paved the way towards the investigation of strongly correlated many-body systems. From the computational viewpoint, simulating a strongly correlated, many-particle problem often challenges or even surmounts the capabilities of a classical computer already at the few particle level, especially when fermions or frustrated interactions are involved. Consider for example 100 spins – the number of possible configurations is 2^{100}, which already exceeds the number of particles in the entire (known) universe. Storing the Hamiltonian on a classical computer is thus a hopeless task. This was already pointed out by R. Feynamn in 1982 who proposed to use a controllable and clean quantum system in order to simulate another quantum system under investigation

> “*Let the computer itself be built of quantum mechanical elements which obey quantum mechanical laws.*” [68]

In recent years, the field of quantum simulation – quantum devices which simulate a particular kind of quantum system – grew rapidly in an interdisciplinary way bringing together the fields of ultra cold atomic, molecular and optical physics (AMO) with quantum information, condensed matter physics and recently high-energy physics [69, 70].

In a *digital* version of a quantum simulator [71] the quantum system is encoded in a register of qubits and the time evolution is then split up into elementary quantum gates. A small set of so called ‘universal single and two-qubit gate operations’ is sufficient to approximate the time evolution of any (finite) quantum system with quasi-local interactions. Many platforms are currently being developed including ions, atoms, molecules, photons, superconductors and solid-state systems. One of the most advanced approaches to general quantum information processing uses strings of cold ions [72]. The drawback of the ‘digital’ approach is that high accuracy comes at the cost of very small time steps and therefore a very large number of quantum gates. On the other hand this approach provides the universality and flexibility to simulate higher-order interactions, like three- or four-body interactions, and error-bounds are very well understood, which can even be corrected using more involved error correction protocols [73].

An alternative approach is the ‘analog’ quantum simulator, where the time-evolution of the quantum system under investigation is mapped one-to-one onto another well-controlled quantum system. Several platforms are currently being developed, ranging from trapped, cold samples of atoms and molecules, to trapped ions and circuit QED systems. In particular, ultra cold atoms in optical lattices have been proven to be a very promising candidate, where bosonic or fermionic atoms are well isolated from the environment and can be controlled with very high precision. Additionally, single-site resolution allows one to individually manipulate and read-out atoms [74]. Recently, strongly correlated systems in the presence of static gauge potentials such as spin-orbit couplings and artificial magnetic fields [75–77], which in part build on proposals from Innsbruck [78], have been realized. This illustrates an additional advantage of quantum simulators: they can reach parameter regimes that are not accessible in condensed matter systems, e.g. artificial magnetic fields larger than a few thousand Tesla. Further extensions of this experimental toolbox will pave the way to quantum simulation of more complex lattice gauge theories with dynamical gauge fields, which appear in both condensed matter and high-energy physics [79, 80].

Gauge theories are the typical playground where quantum simulation can provide notable insights. In high-energy physics, the standard model of particle physics is described in terms of gauge theories. In particular, the theory of strong interactions, QCD, still presents notable challenges, due to the limitation of classical algorithms to access the so-called finite density regimes, which are relevant for both understanding colliding experiments and the interior of complex astrophysical objects such as neutron stars.

There is currently a strong ongoing effort to develop theoretical proposals of quantum simulators for such lattice gauge theories with cold atoms (in optical lattices) [81–86]. In this respect, Rydberg atoms in optical lattices are a very promising add-on, offering genuinely new capabilities for simulating many-body spin systems [87]. These include tunable long-range interactions, the possibility to shape the effective interaction potentials using laser parameters, fast and precise control of the simulated Hamiltonian and the engineering of controlled dissipative effects. This allows to realize a broad class of models including non-equilibrium systems, spin glasses, and both isotropic and anisotropic spin models. In part III of this thesis, we develop a quantum simulator based on Rydberg atoms in optical lattices in order to implement toy models of quantum spin ice, a condensed matter version of quantum electrodynamics.

1.4 Overview of the thesis

The results of the present thesis have been grouped into three parts that mainly contain reprints of already published peer-reviewed articles and of manuscripts that have been submitted and are available online as preprints. The reprints may differ slightly from the referenced originals for editorial reasons, and at the beginning of each reprint a footnote indicates the contributions that the author of the present thesis has made to the respective work. Some parts contain additional material which is the basis of preprints currently being written.

Part I of this thesis studies mixtures of Rydberg atoms and polar molecules as open quantum systems. In particular, this part of the thesis (i) presents a new scheme to cool generic polar molecules from the milli-Kelvin to the micro-Kelvin regime and (ii) investigates strongly interacting laser-cooled Rydberg atoms in a two-dimensional layer configuration.

The production of quantum degenerate gases of polar molecules is a key goal of cold gas physics. In fact, cooling molecules to temperatures of the order of μK or below would enable a variety of breakthroughs in physics and chemistry [57], ranging from controlled ultra cold chemistry to better precision spectroscopy and probes of fundamental symmetries and constants, in addition to the realization of quantum phases of dipolar matter [60]. Several breakthroughs have been recently realized in the groups of J. Ye and D. Jin, who for the first time produced a high-density gas of ultracold KRb polar molecules in their absolute rovibrational ground state and achieved "evaporative cooling" of hydroxyl molecules [88]. A very promising approach to reach degeneracy specific to bialkali molecules is to start from already ultracold atomic mixtures and then use a Feshbach resonance to create heteronuclear molecules in a highly excited vibrational state [89]. These molecules must then be brought to the vibrational ground state, e.g. by STIRAP processes, as demonstrated at JILA with fermionic KRb molecules and in the group of H.-C. Nägerl in Innsbruck with bosonic RbCs [90].

The goal of Chapter 2 is to identify a coupling and cooling mechanism for *generic* molecules which exploits efficient energy-transfer with a properly-designed environment, based on long-range ($>$ 100 nm scale) interactions. This would make the cooling mechanism largely independent of the internal molecular structure (usually important below <10 nm) and thus an ideal generic mechanism to cool comparatively complex molecules beyond bialkali ones to μK temperatures. The main innovation of our work is that we have identified cold Rydberg atoms as ideal candidates to act as an efficient coolant for molecules in atom-molecule mixtures, where large collisional cross-sections based on, e.g., dipole-dipole or van der Waals repulsive interactions can ensure efficient energy transfer even at long distances. In particular, propose a scheme to engineer three dimensional interaction potentials between laser-dressed Rydberg atoms and ground state polar molecules, in order to achieve direct cooling of generic polar molecules. The atoms act as a tailored (low-temperature) reservoir for both elastic and inelastic collisions with remarkable and potentially useful properties: strong repulsive shields protect from inelastic collisions at short interparticle distances and exceedingly large elastic scattering cross sections lead to rapid thermalization. Moreover, we discuss a dissipative (inelastic) collision where a spontaneously emitted photon carries away (kinetic) energy of the collisional partners similar to a 'collisional Sisyphus' effect, thus providing a significant energy loss in a single collision. This work has been inspired by recent experiments in the group of G. Rempe in Munich, where they opto-electrically cooled CH_3F molecules using a similar Sisyphus effect [91] and by U. Vogel and M. Weitz who demonstrate laser cooling of an atomic gas based on collisional redistribution of radiation, using rubidium atoms in argon buffer gas [92]. The main results are presented in Chapter 2 as a reprint of the publication

- *Atomic Rydberg Reservoirs for Polar Molecules*
  B. Zhao*, A. Glätzle*, G. Pupillo, P. Zoller (* both authors contributed equally to this work)
  Phys. Rev. Lett. **108** 193007 (2012-05-11).

Due to the finite lifetime of Rydberg states, the stability of a Rydberg gas is an obvious concern for applications requiring long experimental time scales, e.g. cooling polar molecules or dynamically preparing many-body phases of dressed atoms. In particular, decoherence effects such as spontaneous emission and blackbody radiation of the Rydberg states are important to consider, taking place on a timescale of microseconds. We studied this problem and found that indeed such dissipative dynamics are crucial and can alter the stability of the self assembled atomic crystals. The spontaneous emission from a Rydberg state is followed by cascaded processes through intermediate states. Atoms occupying one of those intermediate states can possess a huge dipole moment when external fields such as an electric DC field is present. These large dipoles induce strong mechanical forces and lead to heating or melting of the crystals. We investigate the interplay between interactions, spontaneous emission and laser cooling for Rubidium atoms taking into account more than 3000 internal electronic levels and simulated the (classical) motion and the cascaded decay using semi-classical molecular dynamics simulations. It becomes apparent that the mechanical heating effects can be substantially mitigated by performing active laser cooling, which is discussed in Chapter 3 as a reprint of the publication

- *Driven-dissipative dynamics of a strongly interacting Rydberg gas*
  A. Glätzle, R. Nath, B. Zhao, G. Pupillo, P. Zoller
  Phys. Rev. A **86** 043403 (2012-10-02).

As an alternative way to cool polar molecules with Rydberg atoms we aim to understand strong, long-range dipolar interactions between hot polar molecules and a cold gas of Rydberg atoms trapped in two separate two-dimensional layers in order to ensure collisional stability. We show that the molecular kinetic energy can be efficiently transferred from the gas of hot molecules to the cold atoms via the long-range interactions. Moreover, the spatial crystalline structure of the atoms can be used to dynamically tailor the spatial structure of the molecules, which can form atom-molecule bound states over both layer as the steady state of the cooling dynamics. We present these results as additional material in Chapter 4 which is the basis of a preprint currently being written.

Part II of this thesis proposes setups and schemes for quantum information processing and quantum simulation using Rydberg *ions*. As part of the CHIST-ERA Rydberg ion consortium, our studies focus on proposing quantum computation and simulation, making use of the properties of Rydberg excitations in an ionic crystals [93].

Motivated by and building on new experimental possibilities realizing two-dimensional arrays of ions we investigated a mechanism that permits the parallel execution of multiple quantum gate operations within a single long linear ion chain. The approach is based on large coherent forces that occur when ions are electronically excited to long-lived Rydberg states. The presence of Rydberg ions drastically affects the vibrational mode structure of the ion crystal, giving rise to modes that are spatially localized on isolated sub-crystals, which can be individually and independently manipulated. We theoretically discuss this Rydberg mode shaping in an experimentally realistic setup and illustrate its power by analyzing the fidelity of two conditional phase flip gates executed in parallel. This is discussed in Chapter 5 as a reprint of the publication

- *Parallel execution of quantum gates in a long linear ion chain via Rydberg mode shaping*
  W. Li, A. Glätzle, R. Nath, I. Lesanovsky
  Phys. Rev. A **87** 052304 (2013-05-06)

The ability to dynamically shape vibrational modes on the single-ion level might find applications in future quantum simulators and quantum computation architectures.

Part III of this thesis is concerned with anisotropic Rydberg interactions present in states such as Rydberg p-states. Our main focus is on implementing quantum simulators for various quantum-spin models characterizing frustrated magnets, a challenging field for both experimentalists and theoreticians. The frustration can arise either due to the geometry (e.g. triangular or pyrochlore lattices) or due to the non-trivial interaction pattern (which we try to engineer with Rydberg p-states).

In the first project we showed how to implement a toy model of quantum spin ice on a 2D checkerboard lattice, which represents a textbook example on how the physics of frustrated magnets is related to gauge theories. The core part of the paper consists of developing an atomic toolbox building on recent experimental advances and opportunities in engineering many-body interactions with laser excited Rydberg states. The goals is to design a set of constrained interactions between cold Rydberg atoms giving rise to a six-fold degenerate ground state manifold obeying the “ice-rules”. This demands the exploitation of the strong angular dependence of van der Waals interactions between Rydberg p-states. Together with the possibility of designing step-like potentials using ground state atoms weakly dressed by Rydberg states, we can implement Abelian gauge theories in a series of geometries, which could be demonstrated within state of the art experiments. Our motivation is not only to realize the 2D spin ice per se, but to develop the atomic physics tools for this much broader class of lattice gauge models including the quantum dimer and other vertex models. We emphasize in particular the connection to quantum link models, as developed originally in a high energy physics context (see references in the paper), which for the U(1) case can be understood as a quantum spin ice on a square lattice. In addition, also the conventional isotropic s-state Rydberg-Rydberg interactions can be utilized together with quite intricate lattice geometries, e.g. a 4-8 lattice, to simulate frustrated magnetism. Our results are presented in Chapter 6 as a reprint of the publication

- *Quantum Spin Ice and dimer models with Rydberg atoms*
  A. Glätzle, M. Dalmonte, R. Nath, I. Rousochatzakis, R. Mössner, P. Zoller
  Phys. Rev. X **4** 041037 (2014-11-25).

In a further project regarding many-body physics with anisotropic interactions between Rydberg atoms excited to p-states we study the adiabatic laser-excitation of Rubidium atoms in an optical lattice. This can be seen as an extension of a recent experiment done in the group of I. Bloch and C. Gross in Munich [37] where they used isotropic s-states. In Chapter 7, which is a reprint of the publication

- *Dynamical preparation of laser-excited anisotropic Rydberg crystals in 2D optical lattices*
  B. Vermersch, M. Punk, A. Glätzle, C. Gross, P. Zoller
  arXiv:1408.0662 (2014-08-04),

we developed a time-dependent variational mean field ansatz to model large but finite two-dimensional systems in experimentally accessible parameter regimes. Additionally, we present numerical simulations to illustrate the dynamical formation of both isotropic and anisotropic Rydberg crystals.

In the last chapter of this part we show how to implement Quantum Kagome Ice [94] with ‘non-particle number conserving’ spin-flip terms of the form $S_+S_+ + S_-S_-$ using Rydberg dressed atoms excited to p-states. While in the previous work of Chapter 6 spin-flip terms were engineered by using tunneling in an optical lattice after mapping the spin degrees of freedom onto hard-core bosons, here, we take an alternative route: The central idea is to represent the quantum spin degree of freedom using two hyperfine ground states of Alkali atoms and weakly admix them with high-lying Rydberg states of a given fine structure component using laser light. In such a set-up single atoms are prepared in a Mott state and kept frozen at each lattice site. This leads to much more favorable exchange energy scales by considering laser excited Rydberg atoms in large spacing optical lattices and allows a complete toolbox of general spin-spin interactions with variable range, i.e. nearest neighbor, or next nearest neighbor couplings etc. in the lattice, as well as the realization of anisotropic spin couplings. Additionally, lattice spacings of a few micrometers allow single-site addressing with laser light and thus individual manipulation and readout of atomic spins. These results are presented as a reprint of the publication

- *Frustrated Quantum Magnetism with Laser-Dressed Rydberg Atoms*
  A. W. Glaetzle, M. Dalmonte, R. Nath, Christian Gross, Immanuel Bloch, and P. Zoller
  arXiv:1410.3388 (2014-10-05).

Bibliography

[1] E. Schroedinger, The Britisch Journal for the Philosophy of Science **3**, 109 (1952).

[2] C. Gardiner and P. Zoller, *Quantum Noise: A Handbook of Markovian and Non-Markovian Quantum Stochastic Methods with Applications to Quantum Optics*, Springer Series in Synergetics (Springer, 2004).

[3] D. F. Walls and G. J. Milburn, *Quantum Optics*, SpringerLink: Springer e-Books (Springer, 2008).

[4] H. Kimble, M. Dagenais, and L. Mandel, Physical Review Letters **39**, 691 (1977).

[5] A. Aspect, P. Grangier, and G. Roger, Physical Review Letters **49**, 91 (1982).

[6] T. Jennewein, C. Simon, G. Weihs, H. Weinfurter, and A. Zeilinger, Physical Review Letters **84**, 4729 (2000).

[7] M. Riebe, H. Häffner, C. F. Roos, W. Hänsel, J. Benhelm, G. P. T. Lancaster, T. W. Körber, C. Becher, F. Schmidt-Kaler, D. F. V. James, and R. Blatt, Nature **429**, 734 (2004).

[8] J. Cirac and P. Zoller, Physical Review Letters **74**, 4091 (1995).

[9] R. Blatt and D. J. Wineland, Nature **453**, 1008 (2008).

[10] H. Metcalf and P. van der Straten, Physics Reports **244**, 203 (1994).

[11] V. G. Minogin and V. S. Letokhov, *Laser Light Pressure on Atoms* (Taylor and Francis, 1987).

[12] C. J. Pethick and H. Smith, *Bose–Einstein Condensation in Dilute Gases* (Cambridge University Press, 2008).

[13] M. Greiner, O. Mandel, T. Esslinger, T. W. Hänsch, and I. Bloch, Nature **415**, 39 (2002).

[14] D. Jaksch, C. Bruder, J. Cirac, C. Gardiner, and P. Zoller, Physical Review Letters **81**, 3108 (1998).

[15] I. Bloch, J. Dalibard, and W. Zwerger, Reviews of Modern Physics **80**, 885 (2008).

[16] T. F. Gallagher, *Rydberg Atoms*, Cambridge Monographs on Atomic, Molecular and Chemical Physics (Cambridge University Press, 2005).

[17] M. Saffman, T. G. Walker, and K. Mølmer, Reviews of Modern Physics **82**, 2313 (2010).

[18] D. Comparat and P. Pillet, Journal of the Optical Society of America B **27**, A208 (2010).

[19] R. Löw, H. Weimer, J. Nipper, J. B. Balewski, B. Butscher, H. P. Büchler, and T. Pfau, Journal of Physics B: Atomic, Molecular and Optical Physics **45**, 113001 (2012).

[20] M. Brune, J. Raimond, P. Goy, L. Davidovich, and S. Haroche, Physical Review Letters **59**, 1899 (1987).

[21] D. Meschede, H. Walther, and G. Müller, Physical Review Letters **54**, 551 (1985).

[22] D. Jaksch, J. I. Cirac, P. Zoller, R. Côté, and M. D. Lukin, Physical Review Letters **85**, 2208 (2000).

[23] M. D. Lukin, M. Fleischhauer, R. Côté, L. M. Duan, D. Jaksch, J. I. Cirac, and P. Zoller, Physical Review Letters **87**, 037901 (2001).

[24] C. S. Hofmann, G. Günter, H. Schempp, N. L. M. Müller, A. Faber, H. Busche, M. Robert-de Saint-Vincent, S. Whitlock, and M. Weidemüller, Frontiers of Physics , 1 (2013).

[25] A. Burgess and M. J. Seaton, Reviews of Modern Physics **120**, 121 (1960).

[26] A. Reinhard, T. Liebisch, B. Knuffman, and G. Raithel, Physical Review A **75**, 032712 (2007).

[27] T. G. Walker and M. Saffman, Physical Review A **77**, 032723 (2008).

[28] R. Heidemann, U. Raitzsch, V. Bendkowsky, B. Butscher, R. Löw, and T. Pfau, Physical Review Letters **100**, 033601 (2008).

[29] W. Anderson, J. Veale, and T. Gallagher, Physical Review Letters **80**, 249 (1998).

[30] D. Maxwell, D. J. Szwer, D. Paredes-Barato, H. Busche, J. D. Pritchard, A. Gauguet, K. J. Weatherill, M. P. A. Jones, and C. S. Adams, Physical Review Letters **110**, 103001 (2013).

[31] A. Schwarzkopf, D. A. Anderson, N. Thaicharoen, and G. Raithel, Physical Review A **88**, 061406 (2013).

[32] H. Schempp, G. Günter, M. Robert-de Saint-Vincent, C. S. Hofmann, D. Breyel, A. Komnik, D. W. Schönleber, M. Gärttner, J. Evers, and S. Whitlock, Physical Review Letters **112**, 013002 (2014).

[33] A. Tauschinsky, R. M. T. Thijssen, S. Whitlock, H. B. van Linden van den Heuvell, and R. J. C. Spreeuw, Physical Review A **81**, 063411 (2010).

[34] J. D. Carter and J. Martin, Physical Review A **88**, 043429 (2013).

[35] H. Kübler, J. P. Shaffer, T. Baluktsian, R. Löw, and T. Pfau, Nature Photonics **4**, 112 (2010).

[36] Y. O. Dudin and A. Kuzmich, Science (New York, N.Y.) **336**, 887 (2012).

[37] P. Schauß, M. Cheneau, M. Endres, T. Fukuhara, S. Hild, A. Omran, T. Pohl, C. Gross, S. Kuhr, and I. Bloch, Nature **491**, 87 (2012).

[38] L. Li, Y. O. Dudin, and A. Kuzmich, Nature **498**, 466 (2013).

[39] M. Ebert, A. Gill, M. Gibbons, X. Zhang, M. Saffman, and T. G. Walker, Physical Review Letters **112**, 043602 (2014).

[40] M. M. Valado, N. Malossi, S. Scotto, D. Ciampini, E. Arimondo, and O. Morsch, Physical Review A **88**, 045401 (2013).

[41] D. Barredo, S. Ravets, H. Labuhn, L. Béguin, A. Vernier, F. Nogrette, T. Lahaye, and A. Browaeys, arXiv.org (2014), 1402.4077v1 .

[42] E. Urban, T. A. Johnson, T. Henage, L. Isenhower, D. D. Yavuz, T. G. Walker, and M. Saffman, Nature Physics **5**, 110 (2009).

[43] A. Gaëtan, Y. Miroshnychenko, T. Wilk, A. Chotia, M. Viteau, D. Comparat, P. Pillet, A. Browaeys, and P. Grangier, Nature Physics **5**, 115 (2009).

[44] L. Isenhower, E. Urban, X. L. Zhang, A. T. Gill, T. Henage, T. A. Johnson, T. G. Walker, and M. Saffman, Physical Review Letters **104**, 010503 (2010).

[45] T. Wilk, A. Gaëtan, C. Evellin, J. Wolters, Y. Miroshnychenko, P. Grangier, and A. Browaeys, Physical Review Letters **104**, 010502 (2010).

[46] E. Brion, K. Mølmer, and M. Saffman, Physical Review Letters **99**, 260501 (2007).

[47] R. Unanyan and M. Fleischhauer, Physical Review A **66**, 032109 (2002).

[48] M. Saffman and T. G. Walker, Physical Review A **66**, 065403 (2002).

[49] M. Fleischhauer and M. Lukin, Physical Review Letters **84**, 5094 (2000).

[50] I. Mourachko, D. Comparat, F. de Tomasi, A. Fioretti, P. Nosbaum, V. Akulin, and P. Pillet, Physical Review Letters **80**, 253 (1998).

[51] H. Weimer, R. Löw, T. Pfau, and H. P. Büchler, Physical Review Letters **101**, 250601 (2008).

[52] T. Pohl, E. Demler, and M. D. Lukin, Physical Review Letters **104**, 043002 (2010).

[53] J. Schachenmayer, I. Lesanovsky, A. Micheli, and A. J. Daley, New Journal of Physics **12**, 103044 (2010).

[54] I. Lesanovsky, Physical Review Letters **106**, 025301 (2011).

[55] L. Santos, G. V. Shlyapnikov, P. Zoller, and M. Lewenstein, Physical Review Letters **85**, 1791 (2000).

[56] J. B. Balewski, A. T. Krupp, A. Gaj, S. Hofferberth, R. Löw, and T. Pfau, New Journal of Physics **16**, 063012 (2014).

[57] L. D. Carr, D. DeMille, R. V. Krems, and J. Ye, Journal of Physics B: Atomic and Molecular Physics **11**, 055049 (2009).

[58] T. Macrì and T. Pohl, Physical Review A **89**, 011402 (2014).

[59] M. A. Baranov, Physics Reports **464**, 71 (2008).

[60] T. Lahaye, C. Menotti, L. Santos, M. Lewenstein, and T. Pfau, Journal of Physics B: Atomic and Molecular Physics **72**, 126401 (2009).

[61] M. Boninsegni and N. V. Prokof'ev, Reviews of Modern Physics **84**, 759 (2012).

[62] M. A. Baranov, M. Dalmonte, G. Pupillo, and P. Zoller, Chemical Reviews **112**, 5012 (2012).

[63] F. Cinti, P. Jain, M. Boninsegni, A. Micheli, P. Zoller, and G. Pupillo, Physical Review Letters **105**, 135301 (2010).

[64] N. Henkel, F. Cinti, P. Jain, G. Pupillo, and T. Pohl, Physical Review Letters **108**, 265301 (2012).

[65] F. Cinti, T. Macrì, W. Lechner, G. Pupillo, and T. Pohl, Nature Communications **5** (2014).

[66] N. Henkel, R. Nath, and T. Pohl, Physical Review Letters **104**, 195302 (2010).

[67] G. Pupillo, A. Micheli, M. Boninsegni, I. Lesanovsky, and P. Zoller, Physical Review Letters **104**, 223002 (2010).

[68] R. P. Feynman, International Journal of Theoretical Physics **21**, 467 (1982).

[69] I. M. Georgescu, S. Ashhab, and F. Nori, Reviews of Modern Physics **86** (2014).

[70] T. H. Johnson, S. R. Clark, and D. Jaksch, EPJ Quantum Technology **1**, 10 (2014).

[71] S. Lloyd, Science (New York, N.Y.) **273**, 1073 (1996).

[72] H. Häffner, C. F. Roos, and R. Blatt, Physics Reports **469**, 155 (2008).

[73] D. Nigg, M. Müller, E. A. Martinez, P. Schindler, M. Hennrich, T. Monz, M. A. Martin-Delgado, and R. Blatt, Science (New York, N.Y.) **345**, 302 (2014).

[74] W. S. Bakr, J. I. Gillen, A. Peng, S. Fölling, and M. Greiner, Nature **462**, 74 (2009).

[75] Y. J. Lin, K. Jiménez-García, and I. B. Spielman, Nature **471**, 83 (2011).

[76] M. Aidelsburger, M. Atala, S. Nascimbène, S. Trotzky, Y. A. Chen, and I. Bloch, Physical Review Letters **107**, 255301 (2011).

[77] J. Dalibard, F. Gerbier, G. Juzeliūnas, and P. Öhberg, Reviews of Modern Physics **83**, 1523 (2011).

[78] D. Jaksch and P. Zoller, New Journal of Physics **5**, 56 (2003).

[79] X. G. Wen, *Quantum Field Theory of Many-Body Systems:From the Origin of Sound to an Origin of Light and Electrons: From the Origin of Sound to an Origin of Light and Electrons*, Oxford Graduate Texts (OUP Oxford, 2004).

[80] H. J. Rothe, *Lattice Gauge Theories: An Introduction*, World Scientific lecture notes in physics (World Scientific, 2012).

[81] C. Castelnovo, R. Moessner, and S. L. Sondhi, Annual Review of Condensed Matter Physics **3**, 35 (2012).

[82] E. Fradkin, *Field Theories of Condensed Matter Systems*, Advanced Books Classics Series (Perseus Books, 1997).

[83] S. Tewari, V. W. Scarola, T. Senthil, and S. Das Sarma, Physical Review Letters **97**, 200401 (2006).

[84] D. Banerjee, M. Bögli, M. Dalmonte, E. Rico, P. Stebler, U. J. Wiese, and P. Zoller, Physical Review Letters **110**, 125303 (2013).

[85] L. Tagliacozzo, A. Celi, A. Zamora, and M. Lewenstein, Annals of Physics **330**, 160 (2013).

[86] E. Zohar, J. I. Cirac, and B. Reznik, Physical Review Letters **110**, 125304 (2013).

[87] H. Weimer, M. Müller, I. Lesanovsky, P. Zoller, and H. P. Büchler, Nature Physics **6**, 382 (2010).

[88] B. K. Stuhl, M. T. Hummon, M. Yeo, G. Quéméner, J. L. Bohn, and J. Ye, Nature **492**, 396 (2012).

[89] H.-C. Nägerl, M. J. Mark, E. Haller, M. Gustavsson, R. Hart, and J. G. Danzl, **264**, 012015 (2011).

[90] T. Takekoshi, L. Reichsöllner, A. Schindewolf, J. M. Hutson, C. R. Le Sueur, O. Dulieu, F. Ferlaino, R. Grimm, and H.-C. Nägerl, ArXiv e-prints (2014), arXiv:1405.6037 [cond-mat.quant-gas] .

[91] M. Zeppenfeld, B. G. U. Englert, R. Glöckner, A. Prehn, M. Mielenz, C. Sommer, L. D. van Buuren, M. Motsch, and G. Rempe, Nature **491**, 570 (2012).

[92] U. Vogl and M. Weitz, Nature **461**, 70 (2009).

[93] F. Schmidt-Kaler, T. Feldker, D. Kolbe, J. Walz, M. Müller, P. Zoller, W. Li, and I. Lesanovsky, New Journal of Physics **13**, 075014 (2011).

[94] J. Carrasquilla, Z. Hao, and R. G. Melko, ArXiv e-prints (2014), arXiv:1407.0037 [cond-mat.str-el] .

Part I

Rydberg atoms and polar molecules as open quantum systems

CHAPTER 2

PUBLICATION

Atomic Rydberg Reservoirs for Polar Molecules[†]

Phys. Rev. Lett. **108**, 193007, (2012)

A. W. Glaetzle[1,*], B. Zhao[1,*], G. Pupillo[1,2], M. Baranov[1], and P. Zoller[1]

[1] *Institute for Theoretical Physics, University of Innsbruck,*
and Institute for Quantum Optics and Quantum Information,
Austrian Academy of Sciences, Technikerstrasse 25, A-6020 Innsbruck, Austria
[2] *ISIS (UMR 7006) and IPCMS (UMR 7504), Université de Strasbourg and CNRS, Strasbourg, France*

We discuss laser dressed dipolar and Van der Waals interactions between atoms and polar molecules, so that a cold atomic gas with laser admixed Rydberg levels acts as a designed reservoir for both elastic and inelastic collisional processes. The elastic scattering channel is characterized by large elastic scattering cross sections and repulsive shields to protect from close encounter collisions. In addition, we discuss a *dissipative* (inelastic) collision where a spontaneously emitted photon carries away (kinetic) energy of the collision partners, thus providing a significant energy loss in a single collision. This leads to the scenario of rapid thermalization and cooling of a molecule in the mK down to the μK regime by cold atoms.

2.1 Introduction

There is at present significant interest in preparing and manipulating cold samples of molecules [1–3]. A promising avenue towards this goal seems to employ the ubiquitous ultracold atomic gases as cold reservoirs, and to study mixtures of atomic and molecular gases, where molecules and atoms interact via collisional processes [4]. Given the well developed tools in manipulating atoms with external

---

[†] The author of the present thesis was strongly involved in doing the calculation presented in this work and in writing the manuscript. In particular, he developed the Sisyphus cooling scheme, derived the coupled Liouville-equations and did the molecular dynamics simulations of the collisional process.

[*] These authors contributed equally to this work.

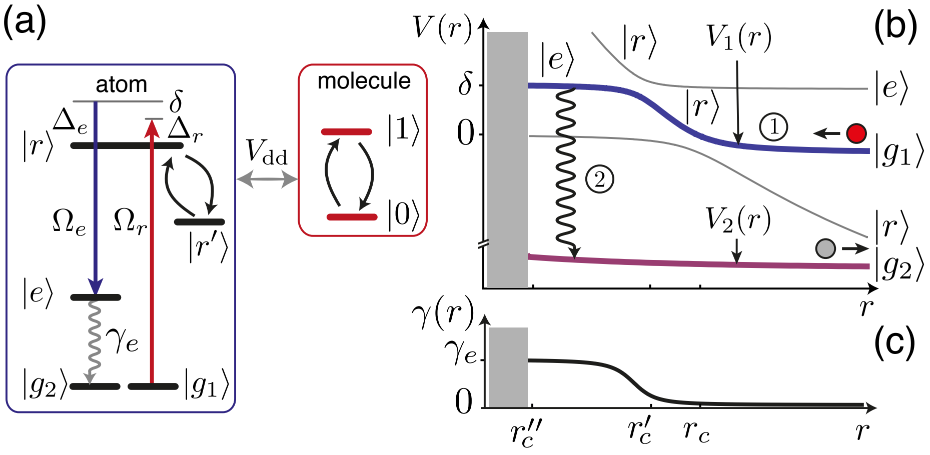

Figure 2.1. *(a) Energy levels of a laser excited atom and a rotational spectrum of a polar molecule. The Rydberg state $|r\rangle$ interacts with the molecule via a dipole-dipole interaction V_{dd} (see text). (b) Born-Oppenheimer (BO) potentials for the laser dressed atom + molecule complex. We consider a dissipative collision, where (1) the particles collide on the potential curve $V_1(r)$ with the atom in $|g_1\rangle$, climb the "blue shield" step at r_c, and (2) are quenched to the potential $V_2(r)$ with atom in g_2. The dominant atomic state is indicated with the molecule in its ground state. (c) Decay rate $\gamma_1(r)$ of the BO potential (see text).*

electromagnetic fields [5], it is natural to ask whether we can "design" these atom-molecule interactions, thus effectively engineering an atomic reservoir with desired (collisional) properties. Below we will describe a specific scenario of engineered elastic and inelastic collisions involving laser-dressed atoms and ground state molecules with remarkable, and potentially useful properties. This includes (i) strong repulsive shields to protect from inelastic collisions and chemical reactions and (ii) exceedingly large scattering cross sections for elastic scattering between the atom and the molecule. The relevant energy (temperature) range includes several mK down to μK. Equally important, we will show that (iii) we can design a "dissipative collision" where a spontaneously emitted photon carries away (kinetic) energy of the collision partners, thus providing a significant energy loss in a single collision what could be called "collisional Sisyphus" effect [6], in analogy to Sisyphus laser cooling of single atoms in external trapping potentials [7]. This suggests rapid thermalization and cooling of a molecule by the cold atom reservoir.

The atomic and molecular level scheme, and the collisional process we have in mind are illustrated in Figs. 8.1(a) and (b), respectively. The basic ingredient is the long range dipolar interaction between molecules in the rovibrational ground state and laser excited Rydberg atoms. The Rydberg state $|r\rangle$ is chosen so that its electric dipole transitions to neighboring states approximately matches the rotational excitation spectrum of the polar molecule with frequencies in the microwave regime (cf. Fig. 8.1a), implying a near resonant exchange of molecular and atomic excitations. We focus below on the conceptually simplest configuration, where this interaction reduces to a large repulsive and isotropic Van der Waals interaction, $V_{\mathrm{vdW}}(r) = C_6/r^6$, a situation analogous to the large Rydberg-Rydberg interactions underlying the dipole blockade mechanism and the formation of superatoms [8–11]. This interaction is admixed to the atomic ground state $|g_1\rangle$ with a blue detuned laser $\Delta_r > 0$, thus providing an effective interaction between the ground state atoms and molecules. The relevant Born-

Oppenheimer (BO) potential for the laser dressed complex is sketched in Fig. 8.1(b) as $V_1(r)$ (see below), and defines a collision channel for a molecule and atom initially in $|g_1\rangle$. In this collision the particles moving adiabatically on $V_1(r)$ will encounter a steep "blue shield" potential [12] at a distance $V_{\rm vdW}(r_c) = \Delta_r$, where typically $r_c \gtrsim 100$ nm. By adding a second laser which couples the long-lived Rydberg state $|r\rangle$ down to a low-lying short lived excited state $|e\rangle$ with a detuning $\Delta_e = \delta + \Delta_r > 0$ (see Fig. 8.1a), we can add a plateau for $r < r_c'$ to the adiabatic potential $V_1(r)$, so that atoms are efficiently quenched to the ground state $|g_2\rangle$ with potential $V_2(r)$ according to the rate $\gamma_1(r)$ in Fig. 8.1(c).

This leads to the following overall picture of collisions illustrated in Fig. 8.1(b): (i) for a kinetic energy of relative motion less than the potential step in $V_1(r)$, i.e. $E_{\rm kin} < \delta$, we have an elastic collision from an effective hard core potential with (large) radius r_c; (ii) in a collision with $E_{\rm kin} > \delta$ the particles will climb the potential step entering the flat dissipative region, which acts as a "trap door" so that in a single collision the kinetic energy $\sim \delta$ is carried away by the spontaneous photon with the atom being left in $|g_2\rangle$. Below we will work out a quantitative description of these collisional processes, and argue that they can occur with high fidelity. An essential argument is that during the collision the particles never enter the small distance regime [shaded region in Fig. 8.1(b)], and thus the collisional dynamics does not couple significantly to other channels. The above collision cycle can be repeated by pumping atoms from $|g_2\rangle$ back to $|g_1\rangle$ so that a significant amount of energy can be lost in a few collisions. Besides, due to the large collision cross sections for elastic processes there is efficient thermalization of the molecules and atoms (sympathetic cooling).

2.2 Master equation

The dynamics of the atom and molecule for a dissipative collision is described by a master equation, $\dot\rho = -i[H,\rho] + \mathcal{L}\rho$, with the RHS as sum of a Hamiltonian and dissipative part, and ρ the reduced system density operator after tracing over the vacuum modes of the radiation field. Such an equation is readily written down as an extension of the familiar master equations of laser cooling for atoms by including the molecular dynamics and the atom-molecule interactions. We neglect, however, recoil kicks from laser absorption and spontaneous emission, and Doppler shifts, as they provide only small corrections to our collisional dynamics.

The Hamiltonian has the form $H = \hat T + \hat H_I(\mathbf{r})$, where $\hat T = \mathbf{P}^2/2M + \mathbf{p}^2/2\mu$ is the kinetic energy with $\mathbf{P}$ ($\mathbf{p}$) the center of mass (relative) momentum and M (μ) the total (reduced) mass, and $\hat H_I(\mathbf{r}) = H_{0M} + H_{0A} + V_{dd}(\mathbf{r})$ is the Hamiltonian for the internal degrees of freedom as sum of a molecular and atomic Hamiltonian, and the dipole-dipole interaction. For the molecule we assume a rigid rotor Hamiltonian $H_{0M} = B\mathbf{N}^2$ with B the rotational constant, and $\mathbf{N}$ the angular momentum. For the atomic Hamiltonian we write in the rotating wave approximation

$$H_{0A} = \delta\hat\sigma_{ee} - \sum_{s=r,r'} \Delta_s \hat\sigma_{ss} + \left[\frac{1}{2}\Omega_r\hat\sigma_{rg_1} + \frac{1}{2}\Omega_e\hat\sigma_{re} + \text{h.c.}\right]$$

with notation $\hat\sigma_{ij} = |i\rangle\langle j|$ for the atomic transition operators, and atomic states according to Fig. 1(a). Here we consider the conceptually simplest situation where $|r\rangle = |n,s\rangle$ and $|r'\rangle = |n-1,p\rangle$, with n the principal quantum number and s and p the orbital angular momentum quantum number [13]. By Δ_r (δ) and Ω_r (Ω_e) we denote the detuning and Rabi frequency of the exciting (quenching) lasers, respectively, and by $-\Delta_{r'}$ the energy of the $|r'\rangle$ state. For an energy mismatch $E_0 = E_a - E_m \ll$

$\min\{E_a, E_m\}$ between the atomic Rydberg states, $E_a = E_r - E_{r\prime}$, and the rotational splitting of the molecule, $E_m = 2B$, the interaction is dominated by the dipole-dipole interactions between the two channels $|r\rangle|0\rangle$ and $|r'\rangle|1\rangle$. The interaction Hamiltonian between a Rydberg atom and the molecule separated by a distance $\mathbf{r} = r\hat{\mathbf{r}}$ is $V_{dd} = [\mathbf{d}_r \cdot \mathbf{d}_m - 3(\mathbf{d}_r \cdot \hat{\mathbf{r}})(\mathbf{d}_m \cdot \hat{\mathbf{r}})]/r^3(|r\rangle\langle r'| \otimes |0\rangle\langle 1| + \text{h.c.})$ for distances larger than the size of the Rydberg atom, $r > r_s \sim n^2 a_0$, where a_0 is Bohr's radius. Here, $\mathbf{d}_r = \langle r|\hat{\mathbf{d}}|r'\rangle$ and $\mathbf{d}_m = \langle 0|\hat{\mathbf{d}}|1\rangle$ are the atomic and molecular transition dipole moments, respectively, with $\hat{\mathbf{d}}$ the dipole operator. For distances $r > r_{c_0} = (d_r d_m/E_0)^{1/3}$, we can adiabatically eliminate $|r'\rangle|1\rangle$ and obtain the effective interaction between $|r\rangle$ and $|0\rangle$, which is a repulsive and isotropic van-der-Waals interaction C_6/r^6 *in three-dimensions* with strength $C_6 = 2d_r^2 d_m^2/3E_0$. Finally, the Liouvillian $\mathcal{L}$ in the master equation describes dissipative processes due to spontaneous emission. We write $\mathcal{L} = \mathcal{L}_e + \mathcal{L}_p + \mathcal{L}_b$, where $\mathcal{L}_e = \gamma_e \mathcal{D}[\hat{\sigma}_{eg_2}]$ and $\mathcal{L}_p = \gamma_2 \mathcal{D}[\hat{\sigma}_{g_2 g_1}]$ account for spontaneous decay from $|e\rangle$ to $|g_2\rangle$ and re-pumping from $|g_2\rangle$ to $|g_1\rangle$, respectively, with Lindblad term $\mathcal{D}[\hat{\sigma}]\rho = \hat{\sigma}\rho\hat{\sigma}^\dagger - \hat{\sigma}^\dagger\hat{\sigma}\rho/2 - \rho\hat{\sigma}^\dagger\hat{\sigma}/2$. The third term $\mathcal{L}_b \rho$ describes undesired decays, including in particular spontaneous emission from the Rydberg state, as discussed below.

2.3 Born-Oppenheimer approximation

We proceed by identifying the BO potentials of the dressed atom-molecule complex as eigenvalues of the internal Hamiltonian $\hat{H}_I(r)|i(r)\rangle = V_i(r)|i(r)\rangle$ depending parametrically on r [compare Fig. 8.1(b)], which, in an adiabatic approximation, provide effective interaction potentials for atoms and molecules. In particular, the dressed groundstate potential $V_1(r)$ corresponds to the BO energy surface that asymptotically connects to the ground state of the atom at large distances, i.e., $|1(r \to \infty)\rangle \sim |g_1, 0\rangle$. There, atom and molecule are essentially non-interacting. As explained above, the step-like character is obtained in combination with laser dressing on two internal atomic transitions: (i) by coupling $|g_1\rangle$ with $|r\rangle$ in the weak-dressing regime $\Omega_r/\Delta_r < 1$ and for blue detuning $\Delta_r > 0$, $V_1(r)$ becomes approximately $V_1(r) \simeq C_6/r^6$ for distances $r < r_c$, with $r \sim r_c = (C_6/\Delta_r)^{1/6}$ a resonant Condon point with typical values in the hundreds of nm. This design of interactions is similar to blue-shielding techniques with cold atoms and molecules, however it exploits repulsive vdW-interactions and thus works in three-dimensions. The dominant contribution to the $|1(r)\rangle$ is now $|r, 0\rangle$, with $\tau_r \sim n^3$ the lifetime of $|r\rangle$, e.g., in the hundreds of μs regime for $n \sim 80$ [10]. (ii) A second Condon point can be engineered at distances $r_c' \equiv (C_6/\Delta_e)^{1/6} < r_c$ by weakly admixing $|r\rangle$ with the low-energy excited state $|e\rangle$, using laser light with $\Omega_e/\Delta_e < 1$ and $\Delta_e > \Delta_r$. Here we assume that $|e\rangle$ interacts only weakly with the molecule and thus $V_1(r)$ becomes essentially flat for $r \lesssim r_c'$. Population in $|e\rangle$ quickly decays to a second groundstate $|g_2\rangle$ at a rate $\gamma_e \sim$ MHz. This makes the decay rate from $|1(r)\rangle$ strongly position-dependent as $\gamma_1(r) = \gamma_e |\langle 1(r)|e, 0\rangle|^2$, see sketch in Fig. 8.1(c). The BO potential $V_2(r)$ with $|2(r)\rangle \sim |g_2, 0\rangle$ is essentially flat, Fig. 8.1(b).

Different BO potentials are coupled via residual non-adiabatic transitions at r_c and r_c'. In particular, population transfer at r_c from $|1(r)\rangle$ to the BO eigenstate that connects to $|r, 0\rangle$ for $r \gg r_c$ could induce significant heating and losses. An estimate of the non-adiabatic transition probability can be computed for $b \ll r_c$ within a 1D Landau Zener model as $P_{LZ} = \exp(-2\pi\Omega_r^2/(\alpha v))$, with α is the difference of the gradient of the bare potentials at r_c. This shows that for any given velocity v (in relative coordinates) non-adiabatic transitions can be always suppressed by increasing Ω_r. Full 3D computations of the non-adiabatic transition probabilities in the semiclassical limit confirm these predictions, see Supplementary. Since $|e\rangle$ decays to $|g_2\rangle$, diabatic transitions at r_c' from $|1(r)\rangle$ to the

BO eigenstate which adiabatically connects to $|e, 0\rangle$ for $r \gg r_c'$ are allowed in our scheme.

Additional diabatic crossings with potential surfaces involving different Rydberg states as well as attractive resonant dipole-dipole interactions lead to collisional two-body losses for distances $r \lesssim r_{c_0}$. Moreover, interactions between the Rydberg-electron and the molecule play a significant role for $r \lesssim r_s$ [14]. These effects are suppressed by a "blue-shield" at $r_c'' > \max\{r_s, r_{c_0}\}$ confining particles' motion to $r > r_c''$ [15].

2.4 Reservoir engineering and molecular cooling

In our scheme, we consider hot molecules undergoing a few scattering processes with cold, interacting, Rydberg-dressed atoms, with lifetime $\tau_d \simeq \tau_r(\Omega_r/2\Delta_r)^{-2}$. Cooling of the molecules comes as a combination of sympathetic cooling with atoms with large elastic cross sections $\sigma \sim \pi r_c^2$ as well as photon-assisted controlled inelastic interactions in a timescale $\tau_c \lesssim \tau_d$ to avoid spontaneous emission from $|r\rangle$ and collisional losses with Rydberg-excited atoms [16].

The basic scheme of photon-assisted inelastic collisions can be understood for just an atom and a molecule initially interacting via the BO potential $V_1(r)$. It comprises two steps: Firstly, spontaneous emission from $|e\rangle$ couples $|1(r)\rangle$ and $|2(r)\rangle$, according to the spatially-dependent rate $\gamma_1(r)$, removing an amount of energy $\lesssim \delta$; secondly, a weak re-pumping laser can transfer population back from $|2(r)\rangle$ to $|1(r)\rangle$, thus closing the cooling cycle. By focussing on $V_1(r)$ and $V_2(r)$ only and neglecting for a moment unwanted effects described by $\mathcal{L}_b\rho$, within the secular approximation the dissipative collisional dynamics in the relative-coordinate frame can be described semiclassically by two coupled Liouville-equations

$$\left(\frac{\partial}{\partial t} + \frac{\mathbf{p}}{\mu}\frac{\partial}{\partial \mathbf{r}}\right) f_i = \left[\frac{\partial V_i}{\partial \mathbf{r}}\frac{\partial}{\partial \mathbf{p}} - \gamma_i(r)\right] f_i + \gamma_j(r) f_j. \tag{2.1}$$

Here $f_i(\mathbf{r}, \mathbf{p}, t)$ is the Liouville density accounting for the phase-space distribution of the atom-molecule system in state $|i(r)\rangle$ $(i, j \in \{1, 2\}, i \neq j)$. The first term in the RHS is the interaction force, proportional to the gradient of the BO potentials discussed above. The second and third terms are the spatially dependent decay rate $\gamma_1(r)$ and the re-pumping rate γ_2, coupling the two equations. The step-like shape of $\gamma_1(r)$ sketched in Fig. 8.1(c) reflects the one of $V_1(r)$, such that $\gamma_1(r) \simeq \gamma_e$ for $r_c'' < r < r_c'$ and $\gamma_1(r) \simeq 0$ otherwise. As a result, for incoming relative kinetic energies $E_{\mathrm{kin}} < \delta$, particles are reflected elastically at $r \approx r_c$, while particles with $E_{\mathrm{kin}} > \delta$ can reach the region $r < r_c'$ with a velocity $v' = \sqrt{2(E_{\mathrm{kin}} - \delta)/\mu}$ and undergo photon-assisted inelastic collisions. For any given v', spontaneous emission from $|e\rangle$ to $|g_2\rangle$ [and thus population transfer from $|1(r)\rangle$ to $|2(r)\rangle$] can be made to occur *deterministically* in a region of length $d = r_c' - r_c''$, by choosing d such that $\gamma_e d/v' > 1$. This removes an energy of order $E_{\mathrm{loss}} \simeq \delta$ in *every* single collision, with δ as large as mK, as shown below. We ensure that the inverse re-pumping from $|2(r)\rangle$ to $|1(r)\rangle$ takes place for distances $r > r_c$ by requiring $\gamma_2 d/v' \ll 1$. In addition, we choose $\gamma_e[\Omega_r\Omega_e/(4\Delta_r\delta)]^2 < \gamma_2$ to ensure that the effective Raman transfer rate of population from $|g_1\rangle$ to $|g_2\rangle$ via $|r\rangle$ is small, and thus the atomic population is in $|g_1\rangle$ at $r \gg r_c$. These requirements can be satisfied for realistic atom/molecule configurations, as shown below.

We investigate numerically this dissipative scheme by performing molecular dynamics simulations of the collision of an atom and a molecule, based on Eq. (2.1). The extension to the case of several atoms and molecules is straightforward. In a semiclassical approximation, the mean energy

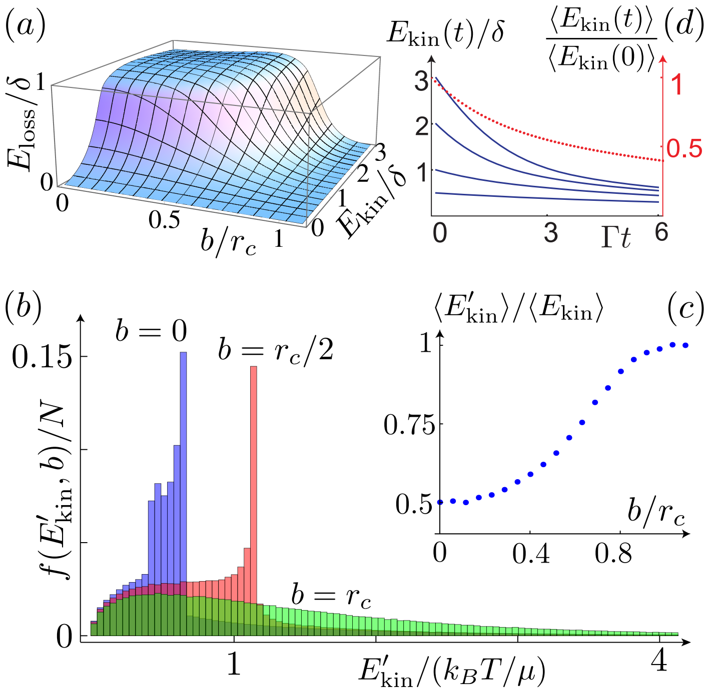

Figure 2.2. *Dissipative collisions: (a) Energy loss $E_{\rm loss}$ per collision vs impact parameter b and initial relative kinetic energy $E_{\rm kin}$. (b) Distribution f of final relative kinetic energies $E'_{\rm kin}$ after a single collision for different b, for an initial Boltzmann distribution with $k_BT/\delta \approx 0.5$. (c) Average final kinetic energy $\langle E'_{\rm kin}\rangle$ of the corresponding distribution after a single collision. (d) $E_{\rm kin}$ (solid lines, left axis) and the average relative kinetic energy $\langle E_{\rm kin}\rangle$ (dotted line, right axis) vs time with $\Gamma = \rho\sigma v_\mu \approx 2\pi \times 2.3$ kHz the collision rate (see text). Parameters: $d_m = 7$ Debye, $d_r = 4400$ Debye, $E_0 = 2\pi \times 2.5$ GHz, $\Delta_r = 2\pi \times 60$ MHz, $\Omega_r/\Delta_r = 0.42$, $\delta/\Delta_r = 0.33$, $\Omega_e/\Delta_r = 0.25$, $r_c \approx 218$ nm, $r'_c/r_c \approx 0.95$, and $r''_c/r_c \approx 0.81$.*

loss $E_{\rm loss}$ in a collision in 3D is computed as $E_{\rm loss} = \int[V_1(\mathbf{r})-V_2(\mathbf{r})]\gamma_1(\mathbf{r}_{\rm cl})p(\mathbf{r}_{\rm cl})dt$, where $\mathbf{r}_{\rm cl}$ denotes the classical trajectory of the atom/molecule collision, and $p(\mathbf{r}_{\rm cl})$ is the probability that the atom decays at a given position $\mathbf{r}_{\rm cl}$, with $\dot{p}(t) = -\gamma_1(\mathbf{r}_{\rm cl})p(t)$. As an example, in the calculations we consider a NaH molecule ($d_m \approx 7$ Debye) and a Cs atom with Rydberg states $|r\rangle = |46s\rangle$ and $|r'\rangle = |45, p\rangle$, respectively, with $d_r \approx 4400$ Debye and $E_0 = 2\pi \times 2.5$ GHz. The laser parameters are $\Delta_r = 2\pi \times 60$ MHz, $\Omega_r/\Delta_r = 0.42$, $\delta/\Delta_r = 0.33$, $\Omega_e/\Delta_r = 0.25$, so that $r_c \approx 218$ nm, $r'_c \approx 208$ nm, and $r''_c \approx 177$ nm [17]. Figure 8.2(a) shows the computed $E_{\rm loss}$ as a function of the initial relative kinetic energy $E_{\rm kin}$ and the impact parameter b. For $b > r_c$ the collision is essentially elastic, as expected. However, for $b \lesssim r_c$ and energies $E_{\rm kin} > \delta$ the molecule is able to climb the potential step δ of V_1 at $r \sim r_c$, thus undergoing deterministic decay to $|2(r)\rangle$.

The effects of this dissipative collisional cooling on a molecular gas with an initial thermal distribution with average temperature $T = 0.5$ mK where $\delta \approx 2k_BT$ with k_B Boltzmann's constant is shown in panel (b). For each fixed value of b we perform $N \simeq 10^5$ computations of the collision dynamics, by randomly generating a sample of initial kinetic energies $E_{\rm kin}$, according to a Boltzmann distribution. The figure shows the final population distribution f as a function of the final energy $E'_{\rm kin} = E_{\rm kin} - E_{\rm loss}$, for fixed values of b, with laser parameters as in Fig. 8.2(a). We find that for impact parameters $b > r_c$ the distribution f in relative coordinates is largely unaffected by the collision (case $b = r_c$ in the figure). For $b < r_c$, however, *all population* with initial energy $E_{\rm kin} > \delta$ is shifted by an amount $\sim \delta$ towards lower energies. The corresponding average final $E'_{\rm kin}$ is shown in Fig. 8.2(c) as a function of b. For heads-on collisions with $b = 0$ approximately 50 % of the initial kinetic energy is removed after a single collision.

For given δ, $E_{\rm kin}$ and atoms at rest, the energy loss rate is estimated as

$$-dE_{\rm kin}/dt = \rho(2E_{\rm kin}/\mu)^{1/2}\mathcal{F}(E_{\rm kin}),$$

with $\mathcal{F}(E_{\rm kin}) = \int_0^{r_c} E_{\rm loss}(b, E_{\rm kin})2\pi b db$ and ρ the atomic gas density. The latter is limited by atom-atom interactions of the form $V_{\rm aa} \simeq (\Omega_r/(2\Delta_r))^4 V_{rr}$ for atomic distances $r > \rho_{\rm max}^{-1/3}$, with $V_{rr} = \tilde{C}_6/r^6$ the vdW interaction between Rydberg states and $\rho_{\rm max}^{-1/3} = [\tilde{C}_6/(2\Delta_r)]^{1/6}$ a resonant Condon radius ($\rho_{\rm max}^{-1/3} \simeq 1.7$ μm for the parameters above). Figure 8.2(d) shows the presence of two cooling timescales (solid lines): For $E_{\rm kin} > \delta$, cooling of an energy $\sim \delta$ is achieved on a fast timescale of a few Γt, with $\Gamma = \rho\sigma v_\mu \approx 2\pi \times 2.3$ kHz the collision rate, for $\rho = (2\,\mu\text{m})^{-3}$, $r_c \approx 218$ nm, $T = 0.5$ mK, $v_\mu = \sqrt{3k_BT/\mu} \approx 0.78$ m/s. For $E_{\rm kin} < \delta$ cooling proceeds slowly, in accordance with the small $\gamma_1(r)$, for $r > r_c$. The same qualitative behavior is found in the average kinetic energy (dots). The lifetime of the dressed state is here $\tau_d \approx 1$ ms ($\tau_r \approx 45$ μs), and thus for the parameters above more than 10 collisions are allowed while cooling. We note that δ can be dynamically reduced in experiments.

In the lab frame, a molecule loses its energy due to a combination of both collisional dissipative cooling and sympathetic cooling. The dominant effect depends on the mass ratio m_A/m_M. For an atom initially at rest, an analytic estimate for the atomic and molecular velocities v'_A and v'_M after the collision can be obtained from a simplified model where the total energy is reduced by δ whenever $\mu v_M^2/2 > \delta$, with v_M the initial molecular velocity, and is conserved otherwise, as

$$\begin{aligned} v'_M &= V(1 - m_A/m_M\sqrt{1 - 2\delta/(\mu v_M^2)}) \\ v'_A &= V(1 + \sqrt{1 - 2\delta/(\mu v_M^2)}). \end{aligned} \tag{2.2}$$

Here, $V = m_M v_M/M$ is the center of mass velocity. Figure 8.3 shows the result of molecular dynamics simulations where we study the energy loss of the molecule $E_{\rm loss}^{(\rm M)} = E_{\rm kin}^{(\rm M)} - (1/2)m_M v_M'^2$ for different mass ratios and laser parameters as in Fig. 8.2. In the figure, the dashed and continuous lines correspond to pure sympathetic cooling and the predictions of Eqs. (2.2), respectively, while squares and dots are numerical results for different values of $E_{\rm kin}^{(\rm M)}$, averaged over 200 simulations. For $m_A < m_M$ the dominant energy loss mechanism is sympathetic cooling. However, for $m_A > m_M$ the energy loss of the molecule is mainly caused by dissipative collisional cooling, and is of the order of δ, as expected. The *effective* atomic mass may be tuned using external confining potentials, e.g., optical lattices. For example, atoms can be confined in an optical trap with depth $V_{\rm tr} \gtrsim 2m_A V^2$, which for NaH with $v_M = \sqrt{3k_BT/m_M}$ and $T = 0.5$ mK and Cs atoms with $m_A/m_M \approx 5.5$ implies $V_{\rm tr} > 0.78 k_BT \approx 0.4$ mK.

2.5 Conclusion

In conclusion, we have discussed a scenario where a molecule scatters successively from cold (stationary) atoms in designed elastic and inelastic processes. In this situation reminiscent of a "microscopic

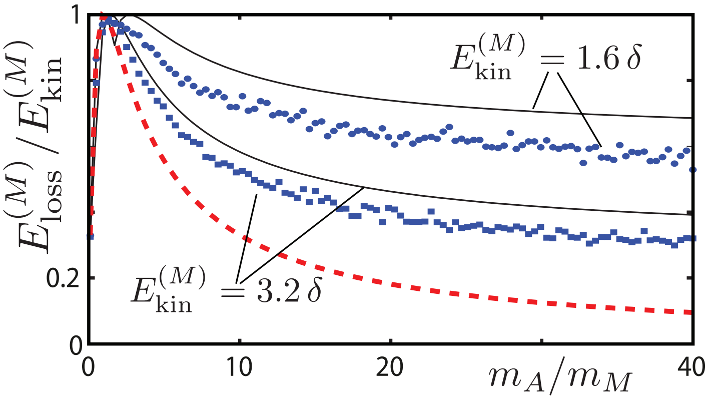

Figure 2.3. *Energy loss vs mass ratio m_A/m_M. The dashed red and solid black lines are analytic results for a model of sympathetic cooling only ($\delta = 0$) and finite δ, respectively, see Eqs. (2.2) and text. Blue dots and squares are averages over 200 runs of molecular dynamics simulations for finite δ, for laser parameters as in Fig. 8.2.*

version of a pinball machine", inelastic scattering events are associated with the emission of a photon implying a "collisional Sisyphus" cooling. While we focused on the simplest possible setup based on Van der Waals interactions, variants based on, e.g. dipole-dipole interactions and low dimensional trapping geometries seem possible. We will investigate the role of many-atom interactions in the dynamics of the gas in future work.

Note

In the final stages of work we became aware of S.D. Huber and H.P. Büchler's proposal for Doppler cooling of polar molecules, where atomic Rydberg excitations serve as a bath for rotational molecular excitations [18].

Acknowledgments

We thank F. Herrera for discussions, and S.D. Huber and H.P. Büchler for sharing with us their work before publication. Work supported by the Austrian Science Fund, EU grants AQUTE, COHERENCE and NAME-QUAM, and by MURI, AFOSR, and EOARD.

2.A Non-adiabatic transition

We calculate the classical trajectory by $\mu\ddot{\mathbf{r}}_{\rm cl} = -\nabla V_1(\mathbf{r}_{\rm cl})$. Plugging the trajectory into the Schrödinger equations governing the dynamics of internal states and calculating the transition probabilities after the molecule has reached the falt region. The results are shown in the Fig.-S2.4, with laser parameters as in Fig. 2. p_1 is the computed transition probability from $|1(r)\rangle$ to the BO eigenstate that connect to $|r, 0\rangle$ for $r \gg r_c$, which is on the order of 10^{-2} for large kinetic energies $E_{\rm kin} \leq 3\delta$. p_2 is the transition

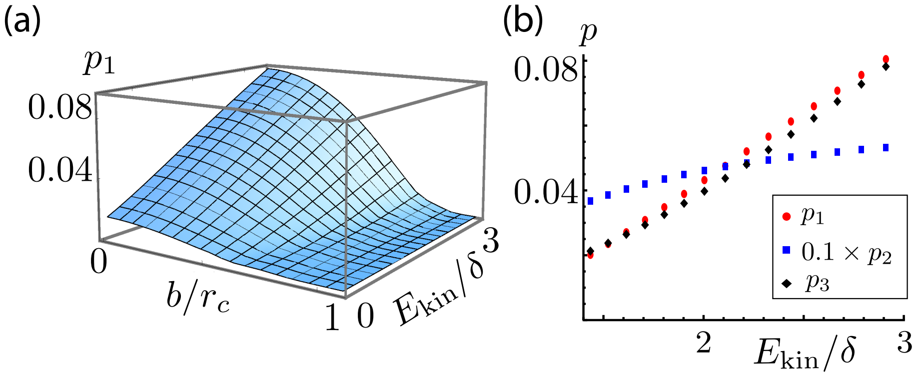

Figure 2.4. *Diabatic transitions between different BO eigenstates. (a)* p_1 *versus impact parameter* b *and initial kinetic energy. (b) Transition probabilities for* $b = 0$.

probability from $|1(r)\rangle$ to the BO eigenstate that connect to $|e, 0\rangle$ for $r \gg r_c'$, which is tolerant as discussed in the Letter. p_3 is the non-adiabatic transition probability in $|2(r)\rangle$ at r_c'', which is calculated in a similar way. Note that non-adiabatic transition probability in $|1(r)\rangle$ at r_c'' is not important, since spontaneous decay almost takes place deterministically. All the non-adiabatic transitions can be further suppressed by increasing the Rabi frequency.

Bibliography

[1] K. Ni *et al.*, Science **322**, 231 (2008); J.G. Danzl *et al.*, Science **321**, 1062 (2008).

[2] W.C. Campbell *et al.*, Phys. Rev. Lett. **98**, 213001 (2007); B. Sawyer *et al., ibid.* **98**, 253002 (2007); S.D. Hogan, C. Seiler, and F. Merkt, *ibid.* **103**, 123001 (2009); E. S. Shuman, J. F. Barry, and D. DeMille, Nature **467**, 820 (2010); P. C. Zieger *et al.*, Phys. Rev. Lett. **105**, 173001 (2010); B. G. U. Englert *et al.*, arXiv:1107.2821 (2011).

[3] R.V. Krems, Int. Rev. Phys. Chem. **24**, 99 (2005); L.D. Carr *et al.,* New J. Phys. **11**, 055049 (2009); M.A. Baranov *et al.*, submitted to Chem. Rev.

[4] P. Staanum *et al.*, Phys. Rev. Lett. **96**, 023201 (2006); N. Zahzam *et al., ibid.* **96**, 023202 (2006); A.O.G. Wallis and J.M. Hutson, *ibid.* **103**, 183201 (2009); M.T. Hummon *et al., ibid.* **106**, 053201 (2011).

[5] H. J. Metcalf and P. van der Straten, Laser Cooling and Trapping (Springer) (1999).

[6] U. Vogl and M. Weitz, Nature **461**, 70 (2009).

[7] J. Dalibard and C. Cohen-Tannoudji, J. Opt. B, **6**, 2023 (1989); C. Cohen Tannoudji and W.D. Phillips, Phys. Today **43**, 33 (1990).

[8] T.F. Gallagher, Rydberg Atoms, Cambridge University Press (1994).

[9] D. Jaksch *et al.*, Phys. Rev. Lett. **85**, 2208 (2000); M.D. Lukin *et al., ibid.* **87**, 037901 (2001); D. Tong *et al., ibid.* **93**, 063001 (2004); R. Heidemann *et al., ibid.* **99**, 163601 (2007); E. Urban *et al.,* Nature Physics **5**, 110 (2009); A. Gätan *et al., ibid.* **5**, 115 (2009).

[10] M. Saffman, T.G. Walker, and K. Mølmer, Rev. Mod. Phys. **82**, 2313 (2010).

[11] H. Weimer *et al.,* Phys. Rev. Lett. **101**, 250601 (2008); N. Henkel *et al., ibid.* **104**, 195302 (2010); D. Petrosyan *et al., ibid.* **107**, 213601 (2011).

[12] J. Weiner *et al.,* Rev. Mod. Phys., **71**, 1 (1999); A. Micheli *et al.,* Phys. Rev. A **76** 043604 (2007); G. Pupillo *et al.,* Phys. Rev. Lett. **104**, 223002 (2010).

[13] For simplicity we do not explicitly reveal the degeneracy of the p-Rydberg-states in $|r'\rangle$.

[14] C.H. Greene, A.S. Dickinson, and H.R. Sadeghpour, Phys. Rev. Lett. **85**, 2458 (2000); S.T. Rittenhouse and H.R. Sadeghpour, *ibid.* **104**, 243002 (2010); E. Kuznetsova, *et al.*, arXiv:1105.2010 (2011).

[15] Blue shielding at r_c'' can be achieved by coupling $|e\rangle$ or $|g_2\rangle$ to Rydberg states that have strong repulsive interaction with the molecule.

[16] A. Glätzle *et al.*, unpublished.

[17] We may couple $|e\rangle$ ($|g_2\rangle$) to Rydberg states $|45s\rangle$ ($|44s\rangle$) with a blue detuning $0.92\Delta_r$ ($0.67\Delta_r$) and Rabi frequency $0.33\Delta_r$ ($0.37\Delta_r$) to engineer the blue shielding at $r_c'' \approx 177$ nm.

[18] S.D. Huber and H.P. Büchler, arXiv:1112.0554 (2011).

CHAPTER 3

PUBLICATION

Driven-dissipative dynamics of a strongly interacting Rydberg gas[†]

Phys. Rev. A **86**, 043403, (2012)

A. W. Glaetzle[1,3,4], R. Nath[1], B. Zhao[1], G. Pupillo[1,2], and P. Zoller[1,3,4]

[1]*Institute for Theoretical Physics, University of Innsbruck,*
and Institute for Quantum Optics and Quantum Information,
Austrian Academy of Sciences, Technikerstrasse 25, A-6020 Innsbruck, Austria
[2]*ISIS (UMR 7006) and IPCMS (UMR 7504), Université de Strasbourg and CNRS, Strasbourg, France*
[3]*ITAMP, Harvard-Smithsonian Center for Astrophysics, Cambridge, Massachusetts 02138, USA*
[4]*Joint Quantum Institute, National Institute of Standards and Technology, and University of Maryland, Gaithersburg, Maryland 20899, USA*

We study the nonequilibrium many-body dynamics of a cold gas of ground-state alkali-metal atoms weakly admixed by Rydberg states with laser light. On a timescale shorter than the lifetime of the dressed states, effective dipole-dipole or van der Waals interactions between atoms can lead to the formation of strongly correlated phases, such as atomic crystals. Using a semiclassical approach, we study the long-time dynamics where decoherence and dissipative processes due to spontaneous emission and blackbody radiation dominate, leading to heating and melting of atomic crystals as well as particle losses. These effects can be substantially mitigated by performing active laser cooling in the presence of atomic dressing.

3.1 Introduction

Rydberg states are highly excited electronic states of atoms and molecules with large principle quantum numbers n [1–5]. The remarkable properties of Rydberg states include their size $r \sim a_0 n^2$ with

---

[†] The author of the present thesis was strongly involved in doing the calculation presented in this work and in writing the manuscript. In particular, he derived the effective interaction potentials, derived the Fokker-Planck equation for laser cooling of dressed atoms and did the molecular dynamics simulations.

a_0 the Bohr radius, implying huge polarizabilities $\alpha \sim n^7$ and large electric dipole moments between Rydberg states, and thus strong coupling to external electric dc and microwave ac fields. Rydberg states can be excited from atomic or molecular ground-states by laser light via absorption of one or more photons, with Rabi frequencies scaling as $\sim n^{-3/2}$. On the other hand, Rydberg states are long-lived, with lifetimes τ scaling as $\tau \sim n^3$ ($\tau \sim n^5$) for low (high) angular momentum states. For typical present experiments with $n \sim 50$ these can be as large as tens of μs. Furthermore, atoms prepared in Rydberg states interact strongly, and these interactions can be controlled and enhanced by external fields. In particular, the van der Waals (vdW) interaction between ns-states scales as $V_{\text{VdW}} \sim (ea_0)^4 n^{11}/r^6$, with e the electron charge, and can be made both attractive and repulsive. In the presence of external dc or ac electric fields the Rydberg-Rydberg interaction is a dipolar interaction, $V_{\text{dd}} \sim (ea_0 n^2)^2/r^3$. The latter is both *long-range* and *anisotropic*. Additional tunability can be achieved using, for example, Förster resonances. These phenomena have been explored in recent experiments [6–20].

The remarkable properties of Rydberg states and the tunability and strength of interactions between Rydberg atoms are reflected in novel many-particle physics of Rydberg gases [21–31] and provide the basis for applications in quantum information processing, for example in implementing (fast) quantum gates [32–37]. An underlying principle is the *Rydberg-blockade mechanism*, as first proposed in Refs. [32] and [33]. In the blockade regime the presence of a single atom excited to a Rydberg state shifts the energy levels of the surrounding atoms within a characteristic radius r_b ($\sim \mu$m), such that the laser excitation probability to the Rydberg state for any other atom within a volume $\sim r_b^3$ is strongly suppressed. This excitation will be delocalized among all particles within r_b, forming a "superatom," with a collectively enhanced Rabi frequency $\sqrt{N_b}\Omega$. Here, N_b is the number of atoms within r_b^3 constituting a superatom and Ω is the single-particle Rabi frequency. Various phenomena in the fields of many-body physics, quantum information applications, and quantum optics related to the dipole-blockade mechanism have been discussed recently in Refs. [38–48].

Present experiments on Rydberg gases as a many-body system created by laser excitation from BECs [49, 50], MOTs [6–18, 20, 51], atomic vapor cells [52], or optical lattices [19] have mainly explored the *frozen gas regime*. This corresponds to a *short-time dynamics*, where the atomic motion can be ignored and (resonant) laser excitation of the Rydberg levels leads to large Rydberg-Rydberg interactions. In this limit atomic dissipation, for example spontaneous emission from Rydberg states, is negligible [53] and the dynamics maps to effective spin models, described by *Hamiltonian* dynamics [21, 23, 30, 54].

An alternative regime is the *Rydberg-admixed gas regime* [25–28, 55]: There the idea is to admix the strong Rydberg-Rydberg interactions by off-resonant laser light weakly to the atomic ground-states, thus providing an effectively much smaller, but still tunable vdW or dipolar ground-state dynamics. That is, instead of kilodebye dipole moments of Rydberg states one obtains effective ground-state dipoles in the range of tens of debyes [56]. Thus, kinetic energies and effective interactions can become comparable, while at the same time spontaneous emission from the Rydberg state due to off-resonant laser tuning is strongly reduced. This effectively extends the lifetime of the gas, making it reminiscent of the dynamics of dipolar gases of polar molecules, as reviewed in [57–61].

An interesting question emerging from the above discussion is, whether it is possible to form interesting condensed-matter phases with these engineered *atomic* dipolar gases; an example is provided by the formation of (stable) *dipolar crystals of cold atomic gases* in analogy to dipolar crystals

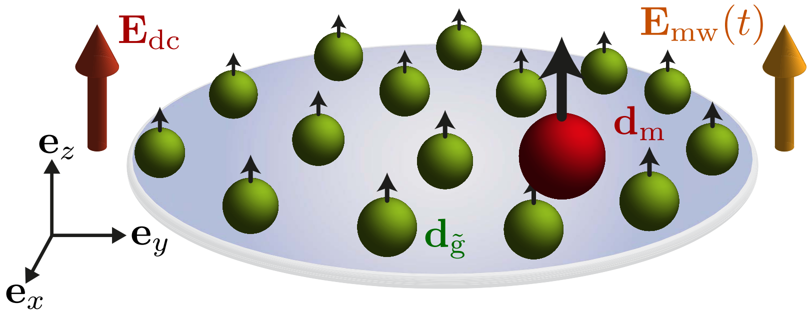

Figure 3.1. *(Color online) Sketch of the proposed setup: Rydberg-dressed ground-state atoms confined in the x-y plane, for example by an optical lattice (not shown), are polarized perpendicular to the plane by a dc electric field,* $\mathbf{E}_{\rm dc}$*, or an ac microwave field,* $\mathbf{E}_{\rm mw}(t)$*. Atoms can be in either the dressed ground-state* $|\tilde{g}\rangle$ *(small particles) with a dipole moment* $\mathbf{d}_{\tilde{g}}$ *or one of the intermediate Rydberg states* $|m\rangle$ *(large particle) with a dipole moment* $\mathbf{d}_m$ *(see text), resulting in strong dipole-dipole interactions.*

discussed for polar molecules [62]. In contrast to polar molecules [1] for Rydberg-admixed gases, dissipation and decoherence due to spontaneous emission is non-negligible for long times, and this raises the question of describing the long-time nonequilibrium dynamics of heating in such gases.

Understanding the long-term dynamics of Rydberg dressed atoms can also have important applications beyond many-body dynamics *per se*. For example, recent proposals have investigated the possibility to efficiently couple cold atomic Rydberg gases to comparatively hot molecular ensembles via long-range dipolar or vdW interactions in order to achieve Doppler [63] and collisional Sisyphus-like [64] cooling schemes for molecules.

The paper is organized as follows: In Sec. 3.2 we give an overview of various atomic configurations studied, identify the main questions, and summarize the main results of the paper. Technical details of our calculations can be found in the remainder of the paper. In Sec. 7.2 we introduce the model and the notation which we will use throughout the paper. In Sec. 3.4.1 we discuss the Hamiltonian for a single Rydberg-dressed atom in the presence of external static and electromagnetic fields. The interaction Hamiltonian of two Rydberg-dressed atoms in the presence of external fields is considered in Sec. 3.4.2, where Born-Oppenheimer potentials are derived for both dc electric and ac microwave fields. In Sec. 3.4.3 we study the validity of the 2D treatment. In Sec. 3.5 we derive Fokker-Planck equations for laser-cooled ground-state atoms in the presence of Rydberg dressing. We find an additional two-body diffusion term due to the interaction between two Rydberg-dressed atoms. The dynamics of decay from the Rydberg state can be modeled by coupled Fokker-Planck equations for atoms effectively in the dressed and laser-cooled ground-state and atoms in one of the intermediate excited states. In Sec. 3.6.1 we study numerically spontaneous emission and blackbody radiation of a single Rydberg dressed atom. Population of intermediate excited states after decay from the Rydberg state will lead to a fluctuating dipole moment and heating of the motion due to photon recoil. The case of an interacting *ensemble* of Rydberg dressed atoms is numerically studied in Sec. 3.6.3. We find that the fluctuations of the dipole moment lead to strong mechanical effects and

---

[1] On relevant experimental time scales decoherence due to spontaneous emission between rotational states of polar molecules is negligible. However, in a high temperature environment, $T \sim 1$ K, blackbody radiation accounts for the dominant heating mechanism.

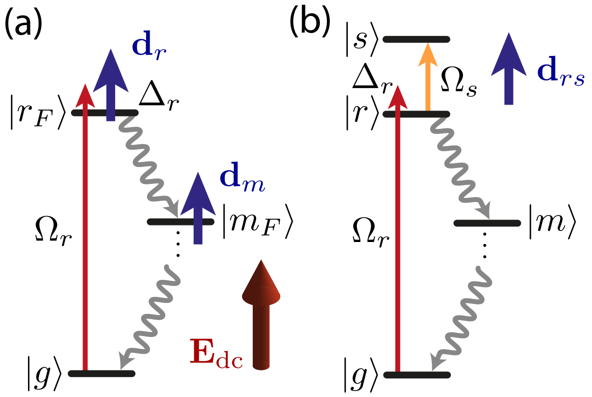

Figure 3.2. *(Color online) Qualitative sketch of the energy levels (black lines), lasers (thin solid arrows) and decay paths (wiggly arrows) for (a) the dc electric field dressing scheme and (b) the ac microwave dressing scheme. In both schemes the ground-state $|g\rangle$ is weakly dressed with a Rydberg-state $|r_F\rangle$ ($|r\rangle$) using a far detuned laser with Rabi frequency Ω_r and detuning $\Delta_r \gg \Omega_r$. In the long-time limit cascaded decay from the Rydberg states $|r\rangle$, $|s\rangle$, or $|r_F\rangle$ (wiggly arrows) will populate intermediate Rydberg states $|m_{(F)}\rangle$ due to spontaneous emission and blackbody radiation. In panel (a) a static electric field, $\mathbf{E}_{\mathrm{dc}} = F\mathbf{e}_z$, polarizes the atoms leading to new Stark-split eigenstates, indicated with an index F. Both, the Rydberg state $|r_F\rangle$ and intermediate states $|m_F\rangle$ will obtain an intrinsic dipole moment $\mathbf{d}_r$ and $\mathbf{d}_m$, respectively (thick arrows). In panel (b) a near resonant ac microwave field, $\mathbf{E}_{\mathrm{mw}}(t)$, with Rabi frequency Ω_s couples two Rydberg states $|r\rangle$ and $|s\rangle$ and induces an oscillating dipole moment proportional to $\mathbf{d}_{rs}$. The intermediate Rydberg states $|m\rangle$ have no dipole moment.*

heating of the external motion, which strongly depends on the atomic density and the dressing scheme used. We study numerically the effect of laser cooling and melting in the presence of an optical lattice with the aim to extend the lifetime of the gas.

3.2 Overview of results

Before presenting a detailed discussion of the dynamics of strongly interacting Rydberg dressed atoms, we find it worthwhile to summarize the main features of Rydberg dressing in a gas of (realistic) atoms, and the resulting many-particle dynamics. The processes we summarize here are derived in detail in Secs. 7.2 - 3.6.

Motivated by proposals for many-body physics with dipolar gases [62, 65], here we focus on the dynamics of a Rydberg-dressed dipolar gas. We assume that the system is initially prepared in a crystalline state, for example by preparing a Mott insulator state of atoms in an optical lattice, and turning on adiabatically the Rydberg admixture while switching off the optical lattice, so that a dipolar crystal is formed. Similar to the setups of self-assembled crystals for polar molecules studied in Refs. [62, 65], we assume a two-dimensional (2D) configuration, that is, atoms are confined to the $(x - y)$ plane by an external optical field, for example, an optical lattice, in the z direction (see Fig. 3.1), such that in-plane dipole-dipole interactions are purely repulsive. As explained below, this will minimize collisional losses linked to the attractive part of dipole interactions. This analysis is readily extended to, and actually simplified in the case of isotropic repulsive vdW interactions in three dimensions [66].

The main question we want to address is how heating and dissipation affect the many-body dynamics due to decay from the Rydberg state in the long-time limit. In fact, for times long enough, spontaneous emission and blackbody radiation will inevitably redistribute the population from the Rydberg state to various different excited states, which invalidates the simple two-level approximation for the internal dynamics of a single atom, mostly discussed so far [21–31]. Given the fact that atoms in these other excited states can interact very differently from those prepared in the dressed ground-state, for example they can have different dipole moments, decay from the Rydberg state can lead to strong mechanical effects and collisional losses in an ensemble of interacting Rydberg dressed atoms. In the following we investigate this complex many-body dynamics. In particular, we explore how to mitigate and control these effects using laser cooling or in-plane optical lattices for a realistic scenario where each atom comprises a large number of internal states.

3.2.1 Atomic configuration

The atomic configurations we have in mind are summarized in Fig. 3.2. (i) In panel (a) a dc electric field with strength F polarizes each atom by splitting its energy levels into the Stark structure; the new Stark-split Rydberg state $|r_F\rangle$ obtains an intrinsic dipole moment d_r which can be either *parallel* or *antiparallel* with respect to the external field. (ii) in panel (b) an ac (microwave) field of Rabi frequency Ω_s is used to strongly couple two Rydberg states $|r\rangle$ and $|s\rangle$, which induces an oscillating dipole proportional to the transition dipole moment d_{rs}.

In both configurations of Fig. 3.2 we weakly admix the ground-state $|g\rangle$ of each atom with the Rydberg state $|r_F\rangle$ or $|r\rangle$, respectively, using an off-resonant continuous wave laser with Rabi frequency Ω_r and detuning $\Delta_r \gg \Omega_r$. This immediately results in an effective dipole moment $d_{\tilde{g}} \sim (\Omega_r/2\Delta_r)^2 d_0$ into the dressed ground-state $|\tilde{g}\rangle \sim |g\rangle + (\Omega_r/2\Delta_r)|r\rangle$, which can be tuned using the laser parameters (see Sec. 3.4). Here, $d_0 = d_r$ or $d_0 = d_{rs}$ for dc electric fields or ac microwave fields, respectively (see Sec. 3.4.2). This dressed ground-state $|\tilde{g}\rangle$ has now a finite, albeit comparatively long, lifetime $\sim 1/\Gamma_{\tilde{g}}$, where $\Gamma_{\tilde{g}} \sim (\Omega_r/2\Delta_r)^2\Gamma_r$ with Γ_r the decay rate of the Rydberg state.

For time scales which are comparable to, or even larger than, $1/\Gamma_{\tilde{g}}$ population in each of the Rydberg states $|r_F\rangle$ or $|r\rangle$ and $|s\rangle$ will be redistributed due to spontaneous emission and blackbody radiation among several excited states $|m\rangle$. In the long-time limit, after, for example, a spontaneous emission event from the Rydberg states, the atomic state will in general not return to the ground-state directly, but via a cascade process where several $|m\rangle$-states are populated. Since each $|m\rangle$ state has a finite lifetime, the cascade will not happen instantaneously. Population of these intermediate states can induce strong mechanical effects on the gas dynamics, leading to heating and losses, as explained below in Sec. 3.6. It turns out that these effects depend crucially on how the dipole moment d_0 in the Rydberg states is created [see Figs. 3.2(a) and 3.2(b)].

We analyze these effects in detail by performing semiclassical molecular dynamics simulations for an ensemble of interacting Rydberg-dressed atoms confined to a 2D geometry including a large number of internal states. In Figs. 3.3(a) and 3.3(b), we provide representative examples for the cases (i) and (ii) above, respectively, for a system comprising $N = 67$ atoms in a box with hard walls. The external dynamics is treated classically, while quantum jumps from the Rydberg state account for spontaneous emission and blackbody radiation, leading to a time-dependent dipole moment of the atoms. In the simulation we use model-atoms with several thousands of internal electronic states

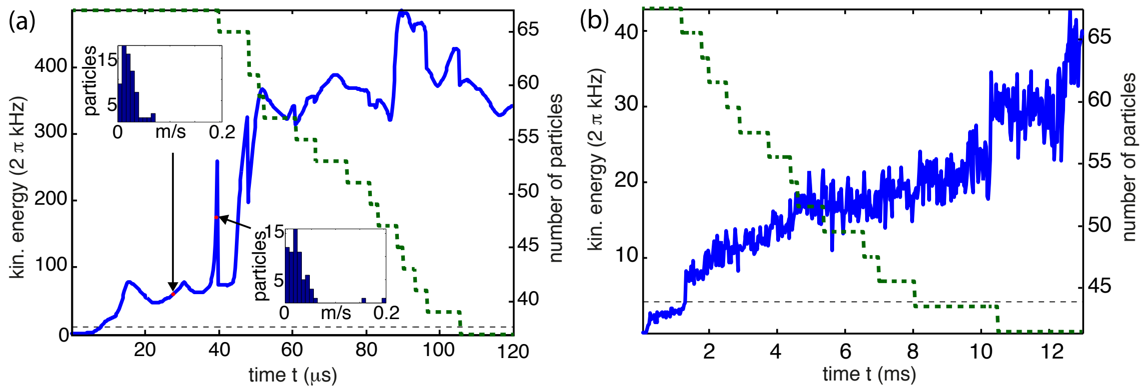

Figure 3.3. *(Color online) Single trajectory of a semiclassical molecular dynamics simulation studying the nonequilibrium and melting dynamics of a 2D Rydberg-dressed crystal as a function of time t. Heating due to decay from the Rydberg states and population of intermediate states $|m_{(F)}\rangle$ leads to a rapid increase of the mean kinetic energy, $E_{\mathrm{kin}}(t)$ (solid line, left axis) and a reduction of the particle number due to losses (dotted line, right axis). In panel (a) the dipole moment in the Rydberg state is created using the dc electric field dressing scheme of Sec. 3.2.2 and the same atomic parameters as given there. Initially we choose a density $n_{2D} = 1\,\mu m^{-2}$. Two insets show histograms of the momentum distribution at $t = 27\ \mu s$ and $t = 40\ \mu s$. In panel (b) the dipole moment in the Rydberg state is created using the ac microwave dressing scheme of Sec. 3.2.3 with the same atomic parameters as given in the text. The initial density is $n_{2D} = 0.2\,\mu m^{-2}$. In both panels the simulation time corresponds to the effective lifetime of the dressed ground-state atoms, $\tau_{\tilde{g}} = 125\,\mu s$ or $\tau_{\tilde{g}} = 12.8$ ms, respectively. The thin dashed line is the initial melting temperature, T_M, of the crystal.*

with the level structure and mass M of ^{85}Rb. At time $t = 0$ the atoms are prepared in a triangular crystal structure with a given density n_{2D} (see figure caption) at zero temperature $T = 0$. In Fig. 3.3, the thin dashed lines are the initial melting temperatures $T_M = 0.089\ d_{\tilde{g}}^2 n_{2D}^{3/2}/k_B$ as determined in Ref. [67], with k_B Boltzmann's constant. The solid (blue) and dotted (green) lines correspond to the mean atomic kinetic energy $E_{\mathrm{kin}}(t)$ and the total atom number $N(t)$, respectively, plotted as a function of time t. In each plot, the simulation time corresponds to $1/\Gamma_{\tilde{g}}$, for the given choice of parameters.

3.2.2 Rydberg dressing with a dc electric field

Figure 3.3(a) shows an example where we choose a very strong dc field with strength $F = 3$ kV/cm in order to polarize ^{85}Rb atoms. Such a high electric field is motivated by studying mixtures of polar molecules and Rydberg atoms where both species are polarized by the same field [68]. In order to avoid, for example, field-ionization with threshold scaling as $F_{\mathrm{ion}} \sim n^{-4}$, the choice of Rydberg states is thus limited to those with a low principal quantum number, for example $n \sim 16$. Here, we use $|r\rangle = |16d, m = 0\rangle$, with lifetime $\tau_r \sim 5.5\,\mu$s and field-induced dipole moment $d_r \sim 680$ D. We choose a dressing laser with $\Omega_r/\Delta_r = 0.42$, resulting in $d_{\tilde{g}} \sim 30$ D and a lifetime $\tau_{\tilde{g}} \sim 125\ \mu$s. Note that in the long run blackbody radiation can lead to population of Rydberg states with $n > 18$, which will eventually be field-ionized with ionization rates ~ 1 kHz calculated in Ref. [69]. Since we are only interested in the dynamics happening in a duration of one effective lifetime of the Rydberg dressed atom, which is smaller compared to the blackbody-induced ionization time, we neglect any ionization effects.

Figure 3.3(a) shows that $E_{\text{kin}}(t)$ (blue thick solid line) rapidly increases and exceeds T_M after about 10 μs. This is due to spontaneous emission events, and the ensuing population of various $|m\rangle$ states, which have different dipole moments [see also scheme in Fig. 3.2(a)]. The population of these intermediate states leads to a picture of fluctuating dipoles, where the energy of local crystal distortions due to dipole-dipole interactions is rapidly redistributed among all particles as heat. The corresponding momentum distribution of the atoms is shown in the first inset. The heating effect from the fluctuating dipole moments is dominant over single-particle recoil effects (with a characteristic rate of a few hundreds of kHz/ms, as discussed in Sec.3.6.1 below).

In addition, the solid (blue) line in panel (a) of Fig. 3.3 shows rapid large variations, or "spikes," of E_{kin}, for example at $t \sim 40\,\mu$s, which correspond to rare events, where one of the atoms populates a $|m\rangle$ state with either a large dipole moment parallel to the dc electric field and long lifetime resulting in a strong repulsive interaction, or an anti-parallel dipole moment resulting in strong in-plane dipolar attraction. This out-of-equilibrium situation is reflected in a temporary change in the distribution of momenta of the atoms, as shown in the second inset by the appearance of small peaks at high momenta. Such rare events result in collisional losses of the most energetic particles, similar to a filtering process, as well as small local "explosions," where a large number of particles can be lost.

The heating and loss processes described above are interaction-dependent (since the interaction strength scales as $\sim n_{2D}^{3/2}$) and thus decrease considerably for a smaller atomic density. In Sec. 3.6.3 below we show how active laser cooling and an additional in-plane optical lattice can affect these processes.

3.2.3 Rydberg dressing with a ac microwave field

In Fig. 3.3(b) we choose a resonant ac microwave field to couple the Rydberg states $|r\rangle = |50s\rangle$ and $|s\rangle = |49p\rangle$ [see level scheme of Fig. 3.2(b)], which have a transition dipole moment of $d_{rs} \sim 5.9$ kD. A dressing laser with $\Omega_r/\Delta_r = 0.14$ yields dressed ground-states atoms with $d_{\tilde{g}} \sim 30$ D and $\tau_{\tilde{g}} \sim 12.8$ ms. The comparatively long lifetime is due to the choice of a state with a larger principal quantum number $n \sim 50$. The microwave dressing can enhance photoionization effects by mixing the s states with the p state. In the following we do not include this in our studies as it can be suppressed by cooling to temperatures in the tens of μK-regime or also by choosing a higher-lying Rydberg state [70]. Since $F = 0$ intermediate Rydberg states $|m\rangle$ have essentially no dipole moment and we consider them as non-interacting.

Figure 3.3(b) shows that $E_{\text{kin}}(t)$ increases with t. This is again due to fluctuations of the atomic dipole moment between the value $d_{\tilde{g}}$ and zero, corresponding to the atom being in the dressed ground-state $|\tilde{g}\rangle$ or in one of the intermediate states $|m\rangle$, respectively, together with photon recoil after a decay event. As discussed before, heating comes from the redistribution of the energy associated to local crystal distortions due to dipole fluctuations among all particles. For $t \lesssim 1.5$ ms the Rydberg dressed atoms are in a crystal-like phase, with $E_{\text{kin}}(t) < k_B T_M$.

In comparison with the dc electric field case of Fig. 3.3(a) the heating rate $E_{\text{kin}}(\tau_{\tilde{g}})\gamma_{\tilde{g}}$ of the ac microwave-dressing scheme is approximately one order of magnitude smaller while the particle loss rate $N(\tau_{\tilde{g}})\gamma_{\tilde{g}}$ is approximately equal. This is because the initial density is smaller and the intermediate states have negligible dipole moments for ac microwave scheme.

In the remainder of this work we derive a microscopic model for the long-time heating dynamics of Rydberg dressed atoms and discuss quantitatively the dependence of the heating and particle loss rates on the system parameters, for example, the atomic density. We state under what conditions standard laser cooling can be performed in the presence of Rydberg dressing, and numerically investigate how it counters heating effects.

3.3 The model

The purpose of this section is to introduce the physical model and the notation that we use throughout the paper. The system is illustrated in Fig. 3.1: N identical (alkali-metal) atoms with momenta $\mathbf{p}_i$ at positions $\mathbf{r}_i$ ($1 \leq i \leq N$) are confined to a quasi-2D geometry in the (x-y) plane by a strong confinement along the z axis.

The Hamiltonian dynamics of the system is governed by

$$H = \sum_{i=1}^{N} H^{(i)} + \sum_{i<j}^{N} H_{\text{int}}^{(ij)}, \tag{3.1}$$

which consists of a sum over single-particle terms $H^{(i)}$ (see Sec. 3.4) and two-particle interaction terms,

$$H_{\text{int}}^{(ij)} = \frac{\hat{\mathbf{d}}_i \cdot \hat{\mathbf{d}}_j - 3(\hat{\mathbf{d}}_i \cdot \hat{\mathbf{r}})(\hat{\mathbf{d}}_j \cdot \hat{\mathbf{r}})}{4\pi\epsilon_0 r^3}, \tag{3.2}$$

which account for the dipole-dipole interaction between two atoms. Here, $\mathbf{r} = \mathbf{r}_i - \mathbf{r}_j = \hat{\mathbf{r}}\, r$ is the relative distance between the atoms, $\hat{\mathbf{d}}_i$ is the dipole operator of the ith atom, and ϵ_0 is the vacuum permittivity.

3.3.1 Internal level structure and setup

We denote $|\alpha\rangle = |n_\alpha, \ell_\alpha, j_\alpha, m_\alpha\rangle$ and $\hbar\omega_\alpha = E_{n_\alpha \ell_\alpha j_\alpha}$ as the unperturbed eigenfunctions and eigenenergies, respectively, of the atomic Hamiltonian H_{at}. Here, n_α is the principal quantum number, ℓ_α is the orbital angular momentum, j_α is the total angular momentum and m_α is projection of the total angular momentum along a specified axis.

In this manifold of states we focus on three specific states (see Fig. 3.4): (i) the energetic ground-state of the atom denoted by $|g\rangle$ (All internal energies will be measured relative to the energy of this state, for example $\hbar\omega_g = 0$.), (ii) a highly excited Rydberg states $|r\rangle$ with energy $\hbar\omega_r$ and (iii) a lower-lying excited state $|e\rangle$ with energy $\hbar\omega_e \ll \hbar\omega_r$, which will be utilized for laser cooling. All other states $|\alpha\rangle$ can be occupied via spontaneous emission or blackbody radiation from the high-lying Rydberg states. As we have already mentioned in Sec. 3.2, the ground-state of each atom is off-resonantly coupled to a high-lying Rydberg state $|r\rangle$ using a continuous-wave laser with a Rabi frequency Ω_r and detuning $\Delta_r (\gg \Omega_r)$ (see Fig. 3.4). Typically, in alkali-metal-atom experiments, the atoms are excited to the Rydberg state via two-photon transitions in which Δ_r and Ω_r are the effective detuning and Rabi frequency. In addition, we use a laser field with Rabi frequency Ω_e and detuning Δ_e to couple $|g\rangle$ to a nearby excited state $|e\rangle$ ($\hbar\omega_e \ll \hbar\omega_r$), forming a closed cycle for laser cooling.

Besides the general setup described above, we consider two different scenarios to create a strong dipole moment in the Rydberg state. (i) An homogeneous electric dc field of strength F polarizes the atoms perpendicular to the 2D plane by splitting the energy levels into the Stark structure [see Fig. 3.4(a)]. The new Stark-split eigenstates $|\alpha_F\rangle$ obtain a large intrinsic dipole moment, for example $\mathbf{d}_0 = \langle r_F|\hat{\mathbf{d}}|r_F\rangle$. (ii) a resonant microwave field with Rabi frequency Ω_s couples $|r\rangle$ to a nearby Rydberg state $|s\rangle$. Thereby, the atom acquires a large oscillating dipole moment proportional to the transition dipole moment $\mathbf{d}_0 = \langle r|\hat{\mathbf{d}}|s\rangle$. In both scenarios, the dipole moments can be as large as kilodebyes. The corresponding dipole-dipole interaction between two atoms in the Rydberg states is governed by H_{int} of Eq. (3.2).

3.3.2 Master equation dynamics

The dynamics of the driven-dissipative many-body system made of interacting Rydberg-dressed atoms is described by the master equation

$$\dot{\rho} = -i\,[H,\rho] + \mathcal{L}\rho, \tag{3.3}$$

where the system density operator ρ acts on the Hilbert space of both internal $|\alpha_1,\alpha_2,\dots\alpha_N\rangle$ and external $\{(\mathbf{r}_1,\ \mathbf{p}_1),\dots(\mathbf{r}_N,\ \mathbf{p}_N)\}$ degrees of freedom. This equation is readily written as an extension of the familiar master equations of laser cooling for multi-level atoms including interaction between atoms [71, 72]. We denote $\mathcal{L}$ as the Lindblad operator, accounting for the decoherence due to spontaneous emission and blackbody radiation

$$\mathcal{L}\rho = \sum_{i=1}^{N}\sum_{\alpha,\beta}\Gamma_{\alpha\beta}\mathcal{D}^{(i)}_{\alpha\beta}\rho, \tag{3.4}$$

which results from the coupling between the atomic system and the vacuum modes of the electromagnetic field, which have been adiabatically eliminated. The decay rate from state $|\alpha\rangle$ to $|\beta\rangle$,

$$\Gamma_{\alpha\beta} = \Gamma^{\text{(SE)}}_{\alpha\beta} + \Gamma^{\text{(BBR)}}_{\alpha\beta}, \tag{3.5}$$

is obtained as the sum of respective contributions from spontaneous emission (SE) and blackbody radiation (BBR) [73], with

$$\Gamma^{\text{(BBR)}}_{\alpha\beta} = \bar{n}_{\alpha\beta}(T)A_{\alpha\beta}, \tag{3.6a}$$

$$\Gamma^{\text{(SE)}}_{\alpha\beta} = \begin{cases} A_{\alpha\beta}, & \omega_\alpha > \omega_\beta; \\ 0, & \omega_\alpha \leqslant \omega_\beta. \end{cases} \tag{3.6b}$$

Here, $A_{\alpha\beta}$ is the Einstein A coefficient and $\bar{n}_{\alpha\beta}$ is the photon distribution, with

$$A_{\alpha\beta} = \frac{|\omega_\alpha - \omega_\beta|^3}{3c^3\pi\hbar\epsilon_0}|\,\langle\alpha|\hat{\mathbf{d}}|\beta\rangle\,|^2, \tag{3.7a}$$

$$\bar{n}_{\alpha\beta}(T) = \frac{1}{e^{\hbar|\omega_\alpha-\omega_\beta|/k_BT}-1}, \tag{3.7b}$$

respectively. We use the notation

$$\begin{aligned}\mathcal{D}^{(i)}_{\alpha\beta}\rho = &\int d^2\hat{\mathbf{k}}N_{\alpha\beta}(\hat{\mathbf{k}})e^{-ik_{\alpha\beta}\hat{\mathbf{k}}\cdot\mathbf{r}_i}\sigma^{(i)}_{\beta\alpha}\rho\sigma^{(i)}_{\alpha\beta}e^{ik_{\alpha\beta}\hat{\mathbf{k}}\cdot\mathbf{r}_i}\\ &-\frac{1}{2}\sigma^{(i)}_{\alpha\alpha}\rho - \frac{1}{2}\rho\sigma^{(i)}_{\alpha\alpha}\end{aligned} \tag{3.8}$$

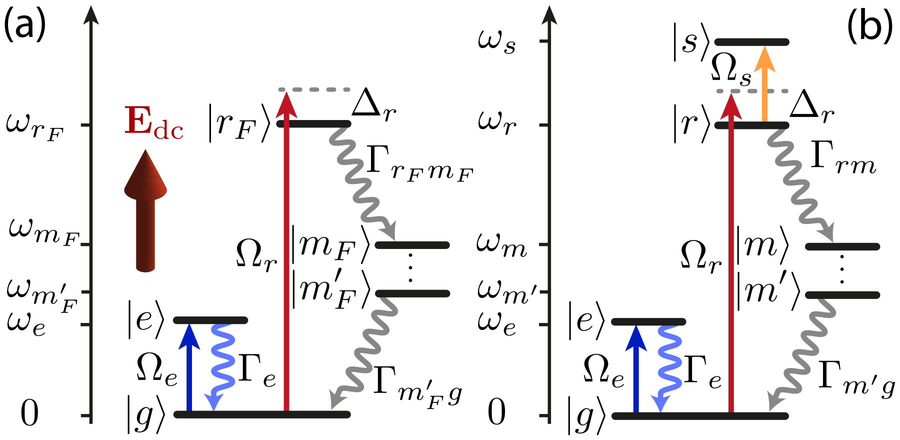

Figure 3.4. *(Color online) Energies ω_α, states $|\alpha\rangle$ (solid black lines), lasers (solid arrows) and decay paths (wiggly arrows) for (a) the dc electric field and (b) the ac microwave dressing scheme. Additionally to Fig. 3.2 a lower-lying excited state $|e\rangle$ is coupled in both schemes to the ground-state $|g\rangle$ using a near-resonant laser with Rabi frequency Ω_e. State $|e\rangle$ decays directly to the ground-state with a rate Γ_e yielding a closed cycle for laser cooling. Cascaded decay from the Rydberg states $|r\rangle$, $|r_F\rangle$ and $|s\rangle$ (not shown) will populate intermediate Rydberg states $|m_{(F)}\rangle$ and $|m'_{(F)}\rangle$ according to the decay rates $\Gamma_{\alpha\beta}$ (see text).*

to denote a general Lindblad term accounting for population redistribution from level $|\alpha_i\rangle$ to $|\beta_i\rangle$ of the i-th atom ($1 \leqslant i \leqslant N$) with $\sigma^{(i)}_{\alpha\beta} = |\alpha_i\rangle\langle\beta_i|$. With $N_{\alpha\beta}(\hat{\mathbf{k}})$ we denote the angular distribution of SE from level α to β, which we assume to be a normalized and even function. The terms $e^{\pm i k_{\alpha\beta}\hat{\mathbf{k}}\cdot\mathbf{r}_i}$ describe the recoil of the atom due to a spontaneously emitted photon, where $k_{\alpha\beta} = (\omega_\alpha - \omega_\beta)/c$ is the wave number of the corresponding transition, with c the speed of light and $\hat{\mathbf{k}}$ a unit vector in the direction of SE.

3.4 Hamiltonian dynamics

We now turn to analyze the single-particle and two-particle-interaction Hamiltonians of Eq. (3.1). In particular, we derive the effective Born-Oppeheimer (BO) potential surfaces for two interacting Rydberg-dressed atoms in the presence of either a dc electric-field (Sec. 3.4.2) or an ac microwave-field (Sec. 3.4.2).

3.4.1 Single-particle Hamiltonian

The single-particle Hamiltonian $H^{(i)}$ of Eq. (3.1) consists of five terms

$$H^{(i)}(t) = \frac{\hat{\mathbf{p}}_i^2}{2M} + H^{(i)}_{\mathrm{at}} + H^{(i)}_{\mathrm{dc}} + H^{(i)}_{\mathrm{laser}}(t) + H^{(i)}_{\mathrm{trap}}. \tag{3.9}$$

The first term in Eq. (3.9) accounts for the kinetic energy of the i-th atom with mass M. The second term

$$H_{\mathrm{at}}^{(i)} = \sum_{\alpha} \hbar\omega_{\alpha}\sigma_{\alpha\alpha}^{(i)}, \tag{3.10}$$

accounts for the internal atomic energy levels, in the absence of external fields. The third term in Eq. (3.9) reads

$$H_{\mathrm{dc}}^{(i)} = -\hat{\mathbf{d}}^{(i)} \cdot \mathbf{E}_{dc} = -\hat{d}_z^{(i)} F, \tag{3.11}$$

and describes the interaction of an atom with a static electric field, where $\hat{\mathbf{d}}^{(i)}$ is the atomic dipole operator of the i-th atom. The effect of a static electric field $\mathbf{E}_{dc} = F\mathbf{e}_z$ is to polarize the atoms along the field direction $\mathbf{e}_z$, by splitting the energies into the Stark structure [74], with F the strength of the field. The new Stark-split eigenstates $|\alpha_F\rangle$ have an intrinsic dipole moment, which in the linear Stark regime is approximately given by $d_\alpha = (3/2)ea_0n_\alpha(n_1 - n_2)$ with a_0 Bohr's radius and n_1 and n_2 the parabolic quantum numbers of state $|\alpha_F\rangle$. In this regime the energy levels are shifted proportional to the field strength, for example $\Delta E_\alpha = d_\alpha F$. Coupling between adjacent n-manifolds can be neglected for field strength $F < F_{\mathrm{IT}}$, where $F_{\mathrm{IT}} \sim n^{-5}$ is the Inglis-Teller-limit [1].

The term $H_{\mathrm{laser}}^{(i)}$ in Eq. (3.9) describes the interaction of an atom with (for example, microwave or optical) laser fields and consists of three terms

$$H_{\mathrm{laser}}^{(i)}(t) = H_{\mathrm{eg-laser}}^{(i)}(t) + H_{\mathrm{rg-laser}}^{(i)}(t) + H_{\mathrm{sr-laser}}^{(i)}(t), \tag{3.12}$$

where each term has the form

$$H_{\alpha\beta-\mathrm{laser}}^{(i)}(t) = \frac{\hbar\Omega_\alpha}{2}\sigma_{\beta\alpha}^{(i)} e^{-i(\mathbf{k}_{L\alpha}\mathbf{r}_i - \omega_{L\alpha}t)} + \mathrm{H.c.}. \tag{3.13}$$

Here $k_{L\alpha} = \omega_{L\alpha}/c$ is the wave-number of the laser with $\omega_{L\alpha}$ the frequency of the laser, H.c. denotes the Hermitian conjugate, and Ω_α is the Rabi frequency. The first term $H_{\mathrm{eg-laser}}^{(i)}$ in Eq. (3.12) describes the coupling of the atom to the cooling laser on the ($|g_{(F)}\rangle$-$|e_{(F)}\rangle$) transition, with Rabi frequency Ω_e and frequency ω_{Le} detuned by Δ_e. The term $H_{\mathrm{rg-laser}}^{(i)}$ describes the coupling of the atom to the Rydberg-dressing laser on the ($|g_{(F)}\rangle$-$|r_{(F)}\rangle$) transition, with Rabi frequency Ω_r and a frequency ω_{Lr} detuned by Δ_r. In the following we are interested in the regime of large detuning $\Delta_r \gg \Omega_r$ in order to weakly admix the Rydberg state to the ground-state. Finally, $H_{\mathrm{sr-laser}}^{(i)}$ describes the coupling to a microwave field strongly mixing the Rydberg-states $|r\rangle$ and $|s\rangle$, with Rabi frequency Ω_s and laser frequency ω_{Ls} detuned by Δ_s.

In addition $H_{\mathrm{trap}}^{(i)}$ of Eq. (3.9) accounts for external trapping potentials.

3.4.2 Two-particle Hamiltonian: Born-Oppenheimer potentials

In this section we study the interaction between *two* Rydberg dressed atoms in the presence of an external static electric field (Sec. 3.4.2) or a microwave field (Sec. 3.4.2). For relative distances between the atoms larger than the size of the Rydberg atom $r \sim a_0n_r^2$ and in the presence of external fields the atoms interact via dipole-dipole interaction governed by the Hamiltonian of Eq. (3.2). In particular, we derive the BO potential surfaces which, in the adiabatic approximation, play the role of effective interaction potentials [62] [Eqs. (3.18) and (3.28)]. They form the basis for the analysis of the time-dependent dynamics of Rydberg-dressed atoms which we discuss below in Secs. 3.6 and 3.5.

dc electric field

We consider two atoms in the presence of a static dc field of strength F, driven by the Rydberg-dressing laser, in the configuration of Fig. 3.4(b). The microwave and the cooling laser are absent, that is, $\Omega_e = \Omega_s = 0$. The new Stark-split eigenstates $|g_F\rangle \sim |g\rangle$ and $|r_F\rangle$ are obtained by diagonalizing $H_{\rm at} + H_{\rm dc}$ and the detuning of the dressing laser Δ_r is defined relative to the shifted energy levels. To obtain the BO potentials we first neglect dissipation and treat the position operators $\hat{\mathbf{r}}_i$ as parameters $\mathbf{r}_i$. Within this limit each atom can be described by a two-state model consisting of $|g\rangle$ and $|r_F\rangle$, coupled by a dressing laser. This is valid for distances larger than $r_n \sim (D/\Delta E_n)^{1/3}$, where diabatic crossings between BO surfaces of neighboring n manifolds can be neglected. Here, $D = d_0^2/(4\pi\epsilon_0)$ is the dipolar coupling strength and $\Delta E_n \gg \hbar\Delta_r$ is the energy separation between neighboring states. In a rotating frame the single-particle Hamiltonian describing this model system reduces to

$$H^{(i)} = -\hbar\Delta_r\sigma_{rr}^{(i)} + \frac{\hbar\Omega_r}{2}(\sigma_{rg}^{(i)} + \sigma_{gr}^{(i)}), \tag{3.14}$$

where the operator $\sigma_{\alpha\beta}^{(i)} = |\alpha_F\rangle\langle\beta_F|$ acts on the new Stark-split eigenstates, $i \in \{1, 2\}$, and $\Delta_r = \omega_{Lr} - \omega_r$ is the detuning from the ($|r_F\rangle - |g\rangle$) resonance. Position-dependent phases of Eq. (3.13) are included in Sec. 3.5, where they lead to recoil kicks from laser absorption, SE, BBR, and Doppler shifts.

Since the dc electric field aligns the dipoles of the atoms along the direction of the field and the dominant dipole moment is $\mathbf{d}_0 = \langle r_F|\hat{\mathbf{d}}|r_F\rangle$, the interaction term in Eq. (3.2) is

$$H_{\rm int}^{(ij)} = \frac{D(1 - 3\cos^2\vartheta)}{|\mathbf{r}_i - \mathbf{r}_j|^3}\left[\sigma_{rr}^{(i)} \otimes \sigma_{rr}^{(j)}\right], \tag{3.15}$$

where ϑ is the angle between the dipole axis and the radial vector between two atoms. When the atoms are confined in a 2D plane, for example by a strong optical field, the angle is fixed to $\vartheta = \pi/2$, resulting in a purely repulsive interaction. Within this model, the total Hamiltonian [Eq. (3.1)] for two atoms in the basis $\{|g, g\rangle, |r_F, g\rangle, |g, r_F\rangle, |r_F, r_F\rangle\}$ reads as

$$H = \hbar\begin{pmatrix} 0 & \frac{1}{2}\Omega_r & \frac{1}{2}\Omega_r & 0 \\ \frac{1}{2}\Omega_r & -\Delta_r & 0 & \frac{1}{2}\Omega_r \\ \frac{1}{2}\Omega_r & 0 & -\Delta_r & \frac{1}{2}\Omega_r \\ 0 & \frac{1}{2}\Omega_r & \frac{1}{2}\Omega_r & V(r) - 2\Delta_r \end{pmatrix}, \tag{3.16}$$

with

$$\hbar V(r) = \langle r_F, r_F|H_{\rm int}^{(12)}|r_F, r_F\rangle = \frac{D}{r^3}. \tag{3.17}$$

The BO potentials for the scattering of two Rydberg-dressed atoms are obtained by diagonalizing the Hamiltonian of Eq. (3.16) for fixed relative position and zero kinetic energy (see Fig. 3.5). We assume that the linewidths of the corresponding states are smaller than the energy separation between them, and that the relevant kinetic energies are small enough, such that Landau-Zener transitions between different BO surfaces can be neglected (secular approximation). In this case the resulting position-dependent eigenvalues act as potentials in each state manifold [62, 75]. Asymptotically (for example, at large distances where the dipole interaction is negligible), the new dressed eigenstates are

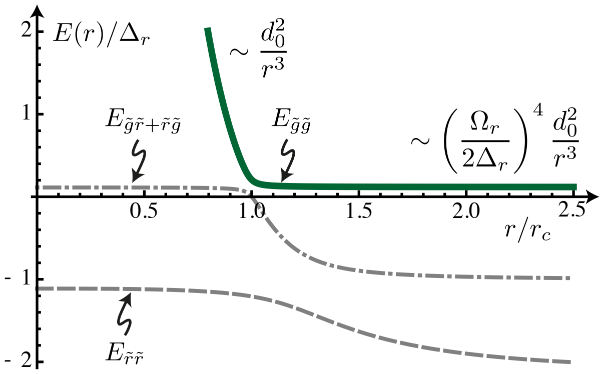

Figure 3.5. *(Color online) Energy eigenvalues* $E(\mathbf{r})$ *(dressed BO potential surfaces) of Rydberg-dressed atoms confined in a 2D geometry obtained by diagonalizing the Hamiltonian of Eq.* (3.16)*. Here,* $\mathbf{r} = r(\cos\varphi, \sin\varphi, 0)$ *is the 2D coordinate in the plane with* $z = 0$*. Atoms are polarized by the dc electric field dressing scheme of Sec.* 3.4.2 *and* $\Delta_r = 2\Omega_r$*. Energy surfaces are labeled using arrows:* $E_{\tilde{g}\tilde{g}}$ *(solid line),* $E_{\tilde{g}\tilde{r}+\tilde{r}\tilde{g}}$ *(dash-dotted line) and* $E_{\tilde{r}\tilde{r}}$ *(dashed line). At the Condon point* $r = r_c$ *an avoided crossing leads to a rapid change of the ground-state interaction potential* $E_{\tilde{g}\tilde{g}}$*: For* $r > r_c$ *atoms prepared in the dressed ground-state* $|\tilde{g}\rangle$ *are weakly interacting,* $E_{\tilde{g}\tilde{g}} \sim (\Omega_r/2\Delta_r)^4 d_0^2/r^3$*, while for* $r < r_c$ *the potential inherits the character of the Rydberg-Rydberg interaction,* $E_{\tilde{g}\tilde{g}} \sim d_0^2/r^3$*.*

$|\tilde{g}\rangle = |g\rangle + (\Omega_r/2\Delta_r)\,|r_F\rangle$ and $|\tilde{r}_F\rangle = |r_F\rangle - (\Omega_r/2\Delta_r)\,|g\rangle$. We note that the dynamics governed by the Hamiltonian of Eq. (3.16) for atoms initially in the ground-state is restricted to the symmetric subspace made of the three states which asymptotically connect to the states $|\tilde{g}, \tilde{g}\rangle$, $(|\tilde{r}_F, \tilde{g}\rangle + |\tilde{g}, \tilde{r}_F\rangle)/\sqrt{2}$, and $|\tilde{r}_F, \tilde{r}_F\rangle$, with energies slightly perturbed by the (Rydberg-dressing) laser field; the antisymmetric state $(|\tilde{r}_F, \tilde{g}\rangle - |\tilde{g}, \tilde{r}_F\rangle)/\sqrt{2}$ is decoupled and does not contribute to the dynamics.

In the following, we focus on blue detuning, for example $\Delta_r > 0$. Figure 3.5 shows the BO potentials as a function of the interparticle distance r for a specific choice of parameters. Because of the choice of blue-detuning, the figure shows that the ground-state BO potential $E_{\tilde{g}\tilde{g}}$ (solid line) corresponding to the energy of the two-particle asymptotically in the state $|\tilde{g}, \tilde{g}\rangle$ has the highest energy. The energy of this BO potential can be calculated perturbatively up to fourth order in the small parameter $\Omega_r \ll |V(r) - 2\Delta_r|$ as

$$E_{\tilde{g}\tilde{g}}(r) = \frac{\Omega_r^2}{2\Delta_r} - \frac{\Omega_r^4}{4\Delta_r^3} - \frac{\Omega_r^4}{4\Delta_r^2\,(V - 2\Delta_r)} \tag{3.18a}$$

$$\approx \frac{\Omega_r^2}{2\Delta_r} - \frac{\Omega_r^4}{8\Delta_r^3} + \left(\frac{\Omega_r}{2\Delta_r}\right)^4 V(r). \tag{3.18b}$$

where the second line is valid in the limit $V(r) \ll \Delta_r$, that is, $r \gg r_c$ (see below). While the first two terms on the right-hand side of Eq. (3.18) are simple light shifts, the equation shows that at large distances the effective ground-state BO potential has an effective spatial dependence $V_{\tilde{g}\tilde{g}}(r) = (\Omega_r/\Delta_r)^4 d_r^2/r^3$. As explained in Refs. [25–28, 55], this means that by dressing the particles with the laser field we have achieved a dipole-dipole interaction for atoms prepared in their (dressed) ground-state, and the strength of the interaction is tunable by varying the ratio Ω_r/Δ_r.

Figure 3.5 shows that the energy of the dressed two-particle ground-state state $E_{\tilde{g}\tilde{g}}$ (solid line) is strongly affected by the dipole-dipole interactions, and for $V(r) \sim 2\Delta$ avoided crossings occur among the BO potentials of all symmetric states. Note that the energy of the antisymmetric state $(|\tilde{r}_F \tilde{g}_F\rangle - |\tilde{g}_F \tilde{r}_F\rangle)/\sqrt{2}$ is uncoupled and not shown. In particular, there is a resonant Condon point at

$$r_c = \left(\frac{d_0^2}{8\pi\epsilon_0 \hbar \Delta_r} \right)^{1/3} \tag{3.19}$$

between the ground-state BO potential and other energy surfaces. As a consequence, there is a sudden change in the slope of the energy surface for $r \sim r_c$, where the ground-state BO potential inherits the character of the one that asymptotically connects to the energy of the state $|\tilde{r}_F, \tilde{r}_F\rangle$, and becomes strongly repulsive. This effect has been discussed in Refs. [62, 66, 75] in the context of so-called blue-shielding techniques, where the strong repulsion for $r < r_c$ does not allow for particles to come close to each other in a scattering event, thus preventing collisional losses due to, for example, collision-induced ionization at short distance. In the reminder of this work, we will be mostly interested in confining the dynamics to distances $r > r_c$.

ac microwave-field

In this section we consider the Hamiltonian dynamics of two atoms in the presence of a linearly polarized, *near-resonant* microwave field with Rabi frequency Ω_s coupling the Rydberg states $|r\rangle$ and $|s\rangle$ [see Fig. 3.4(b)]. The ground-state is again weakly dressed with the state $|r\rangle$ using an off-resonant laser with Rabi frequency Ω_r and a large detuning $\Delta_r \gg \Omega_r$. The dc electric field and the cooling laser are absent, that is, $\Omega_e = 0$ and $F = 0$. The explicit choice of a *near-resonant* microwave field is to obtain large dipoles for atoms in the dressed ground-state, which scale as $\sim (\Omega_r/\Delta_r)^2$, similar to the dc electric field case of Sec. 3.4.2. Again neglecting dissipation and the external degrees of freedom for a moment we are left with a three-level system consisting of the ground-state $|g\rangle$ and the two Rydberg states $|r\rangle$ and $|s\rangle$. Since the electric dc field is absent, these states are the bare eigenstates of H_{at}. Below we show that, by a judicious choice of systems parameters, it is possible to obtain an interaction strength and Condon radius of similar magnitude as in the previous scheme of Sec. 3.4.2 above.

In a frame rotating with the laser frequencies the single-particle Hamiltonian of Eq. (3.1) for this model system reduces to

$$\begin{aligned} H^{(i)} =& -\hbar\Delta_r \sigma_{rr}^{(i)} - \hbar(\Delta_r + \Delta_s)\sigma_{ss}^{(i)} \\ &+ \frac{\hbar\Omega_r}{2}(\sigma_{rg}^{(i)} + \sigma_{gr}^{(i)}) + \frac{\hbar\Omega_s}{2}(\sigma_{sr}^{(i)} + \sigma_{rs}^{(i)}), \end{aligned} \tag{3.20}$$

where the operator $\sigma_{\alpha\beta}^{(i)} = |\alpha\rangle\langle\beta|$ acts on the bare eigenstates, $i \in \{1, 2\}$, and $\Delta_s = \omega_{Ls} - \omega_s$ is the detuning of the microwave laser from the $(|r\rangle - |s\rangle)$ resonance. The corresponding dipole-dipole interaction Hamiltonian of Eq. (3.2) reduces to

$$H_{\text{int}}^{(ij)} = \frac{d_0^2}{4\pi\epsilon_0} \frac{1 - 3\cos^2\vartheta}{|\mathbf{r}_i - \mathbf{r}_j|^3} \left[\sigma_{sr}^{(i)}\sigma_{rs}^{(j)} + \sigma_{rs}^{(i)}\sigma_{sr}^{(j)} \right], \tag{3.21}$$

with ϑ defined as before.

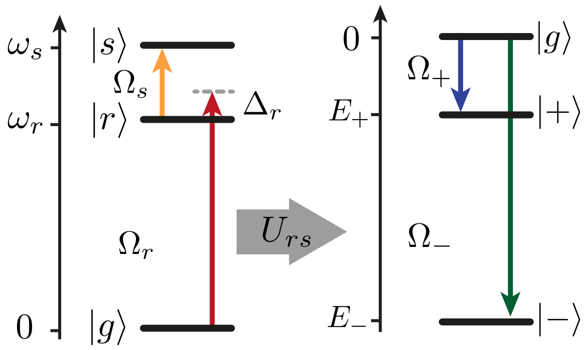

Figure 3.6. *(Color online) Illustration of the ac microwave dressing scheme. (Left) Energies ω_α, states $|\alpha\rangle$ (solid lines), and lasers (solid arrows) of the system described by the Hamiltonian of Eq. (4.7). The unitary transformation U_{rs} of Eq. (3.22) diagonalizes the Rydberg subspace $\{|r\rangle, |s\rangle\}$. (Right) In a rotating frame the new states $|+\rangle$ and $|-\rangle$ with energies $E_\pm$ are separated by an energy difference $\sqrt{\Omega_s^2 + \Delta_s^2}$ and individually coupled to the ground-state with Rabi frequencies $\Omega_\pm$ according to the Hamiltonian of Eq. (3.25) .*

In the case of a *near-resonant* microwave field, where $\Delta_s \ll \Omega_s$, it is convenient to perform a unitary transformation [76]

$$U_{rs}^{(i)} = \exp\left\{\frac{1}{2}\tan^{-1}\left(\frac{\Omega_s}{\Delta_s}\right)\left(\sigma_{rs}^{(i)} - \sigma_{sr}^{(i)}\right)\right\}, \tag{3.22}$$

which diagonalizes the Hamiltonian in the subspace $\{|r\rangle_i, |s\rangle_i\}$. The corresponding new eigenstates are $|\pm\rangle_i = a_\mp |s\rangle_i \pm a_\pm |r\rangle_i$, with

$$a_\pm = \frac{1}{\sqrt{2}}\left(1 \pm \frac{\Delta_s}{\sqrt{\Delta_s^2 + \Omega_s^2}}\right)^{1/2}, \tag{3.23}$$

with the corresponding eigenenergies,

$$E_\pm = -\Delta_r - \frac{1}{2}\left(\Delta_s \mp \sqrt{\Delta_s^2 + \Omega_s^2}\right). \tag{3.24}$$

After the transformation, the single-particle Hamiltonian of Eq. (4.7) in the basis $\{|g\rangle, |+\rangle, |-\rangle\}$ is

$$U_{rs}^{(i)} H^{(i)} U_{rs}^{(i)\dagger} = \hbar \begin{pmatrix} 0 & \frac{1}{2}\Omega_+ & -\frac{1}{2}\Omega_- \\ \frac{1}{2}\Omega_+ & E_+ & 0 \\ -\frac{1}{2}\Omega_- & 0 & E_- \end{pmatrix}, \tag{3.25}$$

with the effective Rabi frequencies $\Omega_\pm = a_\pm \Omega_r$. In this transformed picture the new eigenstates $|\pm\rangle$ are coupled to the ground-state by lasers with Rabi frequencies $\Omega_\pm$ and have a dipole moment $\mathbf{d}_\pm = \langle\pm|\hat{\mathbf{d}}|\pm\rangle = \pm\langle r|\hat{\mathbf{d}}|s\rangle = \pm\mathbf{d}_0$, (see Fig. 3.6).

Again, the dynamics of the symmetric and antisymmetric states are decoupled. For two particles the dynamics of the symmetric subspace is governed by the Hamiltonian $H = H^{(1)} + H^{(2)} + H_{\text{int}}^{(12)}$, which, represented in the basis $\{|g,g\rangle, \frac{1}{\sqrt{2}}(|g,+\rangle + |+,g\rangle), \frac{1}{\sqrt{2}}(|g,-\rangle + |-,g\rangle), \frac{1}{\sqrt{2}}(|-,-\rangle + |+,+\rangle), \frac{1}{\sqrt{2}}(|+,-\rangle +$

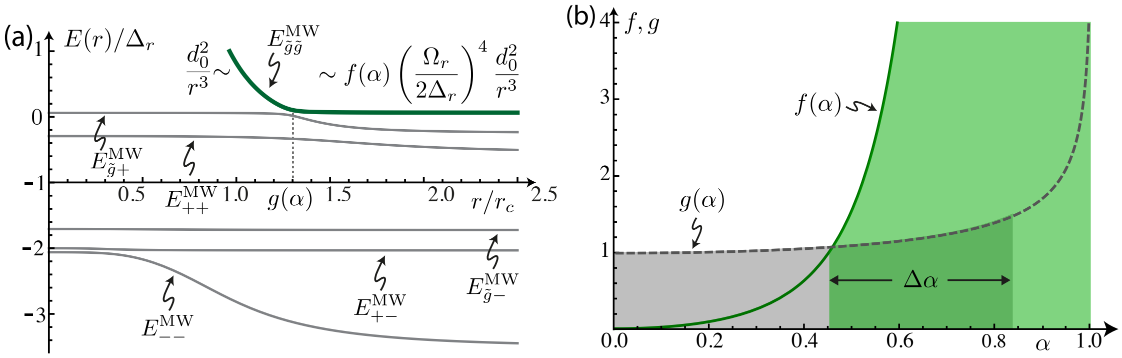

Figure 3.7. *(Color online) (a) Energy eigenvalues $E(\mathbf{r})$ (dressed BO potential surfaces) of Rydberg-dressed atoms confined in a 2D geometry obtained by diagonalizing the Hamiltonian of Eq. (3.26). Here, $\mathbf{r} = r(\cos\varphi, \sin\varphi, 0)$ is the 2D coordinate in the plane with $z = 0$. Atoms are polarized by the ac microwave dressing scheme of Sec. 3.4.2 and $\Delta_r = 4\Omega_r$, $\Omega_s = 1.5\Delta_r$ and $\Delta_s = 0$. Energy surfaces are labeled using arrows. The energies $E_{++}^{\mathrm{MW}}(r)$ and $E_{--}^{\mathrm{MW}}(r)$ are strongly affected by the dipole interaction and at the Condon point $r_c^{\mathrm{MW}} = g(\alpha)r_c$ an avoided crossing leads to a rapid change of the ground-state interaction potential $E_{\tilde{g}\tilde{g}}^{\mathrm{MW}}(r)$ (thick line): For $r > r_c$ atoms prepared in the dressed ground-state $|\tilde{g}\rangle$ are weakly interacting, $E_{\tilde{g}\tilde{g}}^{\mathrm{MW}} \sim f(\alpha)(\Omega_r/2\Delta_r)^4 d_0^2/r^3$, while for $r < r_c$ the potential inherits the character of the Rydberg-Rydberg interaction, $E_{\tilde{g}\tilde{g}}^{\mathrm{MW}} \sim d_0^2/r^3$. The figure shows that the Condon radius is slightly shifted to larger values compared to the dc dressing scheme of Fig. 3.5. Panel (b) shows the dependence of the interaction strength, $f(\alpha)$ (solid line), and the Condon radius, $g(\alpha)$ (dashed line), defined in Eq. (3.28) on α. There exists a region $\Delta\alpha$ where $f(\alpha) > 1$ and $g(\alpha) < 1.5$.*

$|-,+\rangle)$, $\frac{1}{\sqrt{2}}(|-,-\rangle - |+,+\rangle)\}$, reads

$$H_{\mathrm{sym}} = \hbar\begin{pmatrix} 0 & \frac{\Omega_r}{2} & -\frac{\Omega_r}{2} & 0 & 0 & 0 \\ \frac{\Omega_r}{2} & -\Delta_r + \frac{\Omega_s}{2} & 0 & \frac{\Omega_r}{2\sqrt{2}} & -\frac{\Omega_r}{2\sqrt{2}} & -\frac{\Omega_r}{2\sqrt{2}} \\ -\frac{\Omega_r}{2} & 0 & -\Delta_r - \frac{\Omega_s}{2} & -\frac{\Omega_r}{2\sqrt{2}} & \frac{\Omega_r}{2\sqrt{2}} & -\frac{\Omega_r}{2\sqrt{2}} \\ 0 & \frac{\Omega_r}{2\sqrt{2}} & -\frac{\Omega_r}{2\sqrt{2}} & -2\Delta_r & 0 & -\Omega_s \\ 0 & -\frac{\Omega_r}{2\sqrt{2}} & \frac{\Omega_r}{2\sqrt{2}} & 0 & -2\Delta_r & 0 \\ 0 & -\frac{\Omega_r}{2\sqrt{2}} & -\frac{\Omega_r}{2\sqrt{2}} & -\Omega_s & 0 & V - 2\Delta_r \end{pmatrix}, \tag{3.26}$$

where we assumed exact resonance of the microwave field, that is, $\Delta_s = 0$.

The BO potentials are obtained by diagonalizing the Hamiltonian H_{sym}, leading to the new dressed eigenstates which parametrically depend on r. An analytic expression for the BO potential of two atoms in the dressed ground-state can be obtained perturbatively in the limit $\Omega_r \ll \{\Delta_r, \Omega_s\}$

$$E_{gg}^{\mathrm{MW}} = \frac{2\Delta_r\Omega_r^2}{4\Delta_r^2 - \Omega_s^2}\left[1 - \frac{\Omega_r^2(4\Delta_r^2 + 3\Omega_s^2)}{\left(4\Delta_r^2 - \Omega_s^2\right)^2} - \frac{\Omega_r^2[\Omega_s^4 - 16\Delta_r^4 - (4\Delta_r^2 + 3\Omega_s^2)(\Omega_s^2 - 4\Delta_r^2)]}{\left(4\Delta_r^2 - \Omega_s^2\right)^2(2V\Delta_r - 4\Delta_r^2 + \Omega_s^2)}\right]. \tag{3.27}$$

Note, that there are two resonances at $\Delta_r = \Omega_s/2$ and $2V(r_c^{\mathrm{MW}})\Delta_r - 4\Delta_r^2 + \Omega_s^2 = 0$. The first one corresponds to the level crossing between the states $|g-\rangle$ and $|--\rangle$ (red detuning) or $|g+\rangle$ and $|++\rangle$

(blue detuning) with the two-particle ground-state $|gg\rangle$. The second one corresponds to a Condon point r_c^{MW}, similar to the one we have discussed before for the dc electric field case.

We now focus on the case $\Omega_s/2 \lesssim \Delta_r$ in which the single-particle $|+\rangle$-state with energy $E_+ \simeq -\Delta_r + \frac{1}{2}\Omega_s \approx -\epsilon$ $(0 < \epsilon \ll \Delta_r)$ gets almost degenerates with the ground-state $|g\rangle$, while the state $|-\rangle$ with energy $E_- \simeq -\Delta_r - \frac{1}{2}\Omega_s \approx -2\Delta_r$ is separated by a large energy gap of $2\Delta_r$. In order to investigate the behavior of Eq. (4.9) near this resonance we set $\Omega_s = \alpha 2\Delta_r$ with $\alpha < 1 - \Omega_r/\Delta_r$. The latter inequality comes from the fact that we assume Ω_r is the smallest frequency scale for the non-degenerate perturbation theory to be valid. Therefore, these two states must not be exactly degenerate. With this assumption we find for the ground-state energy and the Condon radius

$$\begin{aligned} E_{gg}^{\mathrm{MW}} &= E_{\mathrm{const.}} + f(\alpha)\left(\frac{\Omega_r}{2\Delta_r}\right)^4 V(r), \\ r_c^{\mathrm{MW}} &= g(\alpha)\sqrt[3]{\frac{d_0^2}{8\pi\epsilon_0\hbar\Delta_r}}, \end{aligned} \tag{3.28}$$

with $E_{\mathrm{const.}} = \Omega_r^2/[2\Delta_r(1-\alpha^2)] - \Omega_r^4(1+\alpha^2)/[8\Delta_r^3(1-\alpha^2)^3]$, $f(\alpha) = 2\alpha^2/(1-\alpha^2)^4$ and $g(\alpha) = 1/(1-\alpha^2)^{1/3}$. In the limit $\alpha \to 0$ the state $|s\rangle$ is not coupled to $|r\rangle$ and we obtain the same light shifts as in Eq. (3.18). Note that in this limit the interaction strength vanishes, $f(\alpha) \to 0$. This is due to the fact that in the absence of a dc electric field the bare state $|r\rangle$ has no intrinsic dipole moment.

Figure 3.7(a) shows the BO potentials for the symmetric states as a function of the interparticle distance r for a specific set of parameters near resonance, as discussed above. The energy of the dressed two-particle states $|--\rangle$ and $|++\rangle$ is strongly shifted by the dipole-dipole interaction, and avoided crossings occur among the BO potentials of all symmetric states. This leads to a sudden change in the slope of the energy surface of, for example E_{gg}, at the Condon radius r_c^{MW}.

The functions $f(\alpha)$ and $g(\alpha)$ versus α are shown in Fig. 3.7(b). Increasing α towards 1 will on one hand increase the effective ground-state interaction potential according to $f(\alpha)$. On the other hand it will increase the Condon radius r_c^{MW} according to $g(\alpha)$. Figure 3.7(b) shows that there is a region, $\Delta\alpha$, for which $f(\alpha) > 1$ but $1 < g(\alpha) < 1.5$ between $0.45 < \alpha < 0.84$. Operating in this region leads to formal similar interaction strength and Condon radii as for the dc electric field dressing scheme, for example, Eqs. (3.18) and (6.15).

3.4.3 Validity of the 2D treatment

In this section we examine in detail under what criteria we can treat the system of interacting Rydberg dressed atoms as purely 2D in nature. As mentioned before, the atoms are trapped in the $(x-y)$ plane by a strong harmonic confinement along the z direction. The resulting 3D potential in relative coordinates reads

$$V_{3D}(\mathbf{r}) = \frac{1}{4}M\omega_\perp^2 z^2 + \hbar E_{gg}(\mathbf{r}), \tag{3.29}$$

where the first term is the harmonic confinement with trapping frequency $\omega_\perp$. The second term, $E_{gg}(\mathbf{r})$, is the BO potential of two interacting dressed ground-state atoms, obtained by numerically diagonalizing the Hamiltonian of (3.16), taking into account the full 3D characteristic of the dipole-dipole interactions.

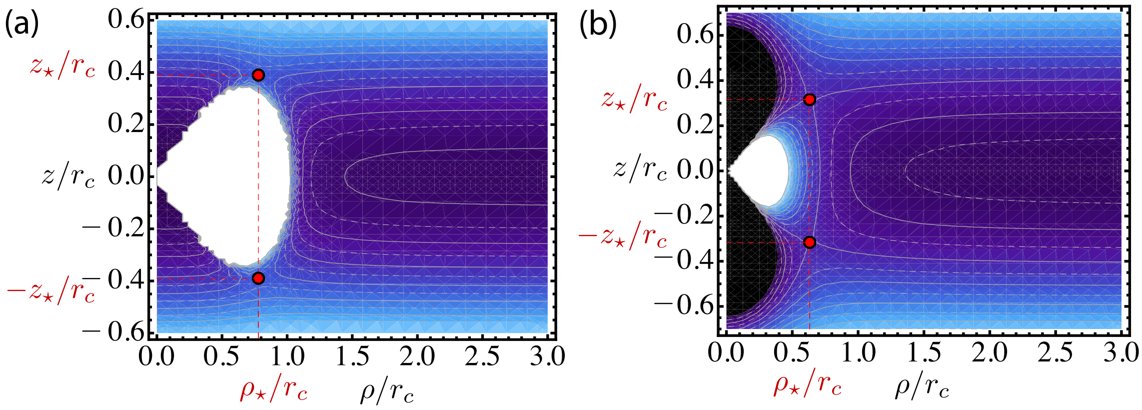

Figure 3.8. *(Color online) Contour plots of the 3D-potentials $V_{3D}(\mathbf{r})$ and $V_{3D}^{\text{mol}}(\mathbf{r})$ of Eq. (3.29) and (3.30) are shown in panels (a) and (b), respectively, in units of $V_0 = 2\Delta_r\,(\Omega_r/2\Delta_r)^4$. Here, $\mathbf{r} = (\rho\cos\varphi, \rho\sin\varphi, z)$ is the relative distance between two atoms, with ρ the in-plane radial coordinate and z the transversal coordinate. Brighter regions represent stronger repulsive interactions. Two saddle points (circles) located at $(\rho_\star, \pm z_\star)$ separate the repulsive from the attractive short-range region.*

Figure 3.8(a) shows a contour plot of the 3D potential $V_{3D}(\mathbf{r})$ of Eq. (3.29) in the (ρ-z) plane where $\rho = \sqrt{x^2+y^2}$. We consider ^{85}Rb atoms with $\Delta_r = 2\pi \times 250$ MHz, $\Omega_r = 2\pi \times 100$ MHz, $r_c = 520$ nm and $\omega_\perp = 2\pi \times 200$ kHz. In the figure, darker color corresponds to deeper potentials. The potential exhibits two saddle points, at $(\rho_\star, z_\star) = (0.78, \pm 0.39)\,r_c$, with a height $V_{3D}(\rho_\star, z_\star) = 220\ \mu\text{K}\cdot k_B$, which serve as an energy barrier separating the repulsive long-range dipole-dipole interaction regime from an attractive short-distance regime [62, 65]. For relative kinetic energies smaller than the height of the potential barrier, the interaction is purely repulsive and the system can be stabilized against collapse due to the attractive part of the interaction. For blue detuning of the dressing laser there is a resonant Condon point at $\rho = r_c$ for $z = 0$, where we observe a rapid increase of the interaction potential, which is discussed in Sec. 3.4.2. Along the axial direction z (for $\rho = 0$) there is no resonant point and the potential approaches smoothly zero where inelastic or reactive collisions will occur.

For relative distances larger than the Condon radius, r_c [Eq. (6.15)], the interaction can be approximated by dipole-dipole interaction. In this case, the 3D potential can be rewritten as

$$V_{3D}^{\text{mol}}(\mathbf{r}) = V_0\left[\kappa\tilde{z}^2 + \frac{\tilde{\rho}^2 - 2\tilde{z}^2}{(\tilde{\rho}^2+\tilde{z}^2)^{5/2}}\right], \tag{3.30}$$

which is reminiscent of polar molecules [62, 65]. Here, $\tilde{z} = z/r_c$ and $\tilde{\rho} = (x^2+y^2)^{1/2}/r_c$. The corresponding contour plot is shown in Fig. 3.8(b). The dimensionless parameter κ characterizes the strength of the confinement relative to the interaction

$$\kappa = \left(\frac{2\Delta_r}{\Omega_r}\right)^4 \frac{M\omega_\perp^2 r_c^2}{8\hbar\Delta_r} = 2\left(\frac{\Delta_r}{\Omega_r}\right)^3 \frac{\omega_\perp}{\Omega_r}\left(\frac{r_c}{a_{\text{ho}}}\right)^2, \tag{3.31}$$

where $a_{\text{ho}} = \sqrt{\hbar/M\omega_\perp}$ is the harmonic oscillator length in transversal direction. For $\kappa \gg 1$ the confinement in the z direction dominates over the dipole-dipole interaction. Analytic analysis of Eq. (3.30) yields the saddle points

$$\rho_\star = \pm 2z_\star \qquad \text{and} \qquad z_\star = \frac{3^{1/5}}{\sqrt{5}\kappa^{1/5}}. \tag{3.32}$$

The height of the potential at the saddle point, corresponding to the height of the energy barrier separating the repulsive region from the attractive region, is

$$V_{3D}^{\text{mol}}(z_\star, \rho_\star) = V_0 \left(\frac{\kappa}{3}\right)^{3/5}, \tag{3.33}$$

which is independent of Δ_r for a fixed ratio of Ω_r/Δ_r. For the same parameters used above we obtain $\kappa = 30$ which yields a potential barrier at the saddle point corresponding to $T_\star = 150\,\mu$K. Comparing Figs. 3.8(a) and 3.8(b) one can see the rapid change of the interaction strength at the Condon radius for Eq. (3.29) [panel (a)] leads to a repulsive shield which leads to a slightly higher potential barrier corresponding to $T_\star = 220\,\mu$K compared to the case of a pure inverse-cubic interaction potential [panel (b)] with $T_\star = 150\,\mu$K. Additionally, we find that the saddle point in panel (a) is shifted to larger ρ values than in panel (b).

In a 3D scenario two particles undergo collapse when they have large-enough collisional energy to overcome the energy barrier at the saddle points. In the numerical simulations of Sec. 3.6 we treat the system as purely 2D with a $1/r^3$ potential [see Eq. (3.42)], assuming particles are being lost if they collapse in 3D. For a specific set of parameters we use the latter analysis to calculate the height of the potential at the saddle point, $V_{3D}(\rho_\star, z_\star)$, in a 3D scenario. The height of the saddle point will then be translated into a critical 2D distance, ρ_{loss}, at which $E_{\tilde{g}\tilde{g}}(\rho_{\text{loss}}) = V_{3D}(\rho_\star, z_\star)$, with $E_{\tilde{g}\tilde{g}}$ defined in Eq. (3.18b).

3.5 Laser cooling of dressed Rydberg atoms

In this section we examine in detail the dissipative processes in Eq. (3.3) and study laser cooling of interacting atoms in the presence of Rydberg dressing. As an example we consider Doppler cooling but the model can be extended to sub-Doppler cooling schemes. For simplicity of the *analytic* treatment in Sec. 3.5.1, we first consider model atoms where we neglect decay from the Rydberg state in order to derive semiclassical Fokker-Planck equations which describe the cooling dynamics in the presence of Rydberg-dressing and interactions. In Sec. 3.5.2 we include decay from the Rydberg state which couples the dressed ground-state via rate equations to one of the intermediate states. Again for simplicity of the analytic treatment in this section, we first consider model atoms with a single intermediate state $|m\rangle$. In Sec. 3.6 we numerically investigate the interplay of laser cooling and heating due to population of intermediate states of an ensemble of dressed Rydberg atoms taking into account a large number of internal states. We show that laser cooling can alleviate the heating dynamics for interacting Rydberg atoms described above, extending the lifetime of strongly interacting phases in these systems, as for self-assembled crystals.

3.5.1 Fokker-Planck equation

In the following we derive equations of motion for the external dynamics (position and momentum) of model atoms consisting of a ground-state $|g\rangle$ which is coupled with a far detuned laser to a Rydberg state $|r\rangle$ with Rabi frequency Ω_r and detuning $\Delta_r \gg \Omega_r$. Additionally, the ground-state $|g\rangle$ is coupled to a lower-lying excited state $|e\rangle$ using a counter-propagating laser with Rabi frequency Ω_e and detuning Δ_e. The state $|e\rangle$ decays directly to the ground-state $|g\rangle$ with a fast decay rate Γ_e, realizing a closed cycle transition. Atoms which are both in the Rydberg state interact via dipole-dipole interaction described by the Hamiltonian Eq. (3.15).

The derivation of equations of motion for the external degrees of freedom is done in four steps [72, 77]: (i) first we use the Wigner function formalism to map the density operator ρ onto a quasi-probability distribution in phase space

$$\begin{aligned} &W^{(N)}(\mathbf{r}_1,\dots,\mathbf{r}_N;\mathbf{p}_1,\dots,\mathbf{p}_N;t) = \\ &\int \frac{d\mathbf{u}_1}{h^3},\dots,\frac{d\mathbf{u}_N}{h^3}\langle \mathbf{r}_1+\tfrac{\mathbf{u}_1}{2},\dots,\mathbf{r}_N+\tfrac{\mathbf{u}_N}{2}|\rho|\mathbf{r}_1-\tfrac{\mathbf{u}_1}{2},\dots,\mathbf{r}_N-\tfrac{\mathbf{u}_N}{2}\rangle\, e^{-i\mathbf{u}_1\cdot\mathbf{p}_1/\hbar},\dots,e^{-i\mathbf{u}_N\cdot\mathbf{p}_N/\hbar}. \end{aligned} \tag{3.34}$$

(ii) We derive the equation of motion for W using the master equation Eq. (3.3) and expand the resulting equation of motion up to second order in terms of the photon momentum in order to obtain a positive probability function in the semiclassical limit. (iii) We adiabatically eliminate the Rydberg state $|r\rangle$ in the limit of a large detuning Δ_r. The resulting two-level systems - consisting of a dressed ground-state $|\tilde{g}\rangle = |g\rangle + (\Omega_r/2\Delta_r)|r\rangle$ with dipole moment $d_{\tilde{g}}$ and an excited state $|e\rangle$ - interact only when the atoms are in the dressed ground-state. (iv) Finally, we adiabatically eliminate the fast internal degrees of freedom of this effective two-level system in favor of the (much slower) external dynamics. Due to the Rabi oscillations between the dressed ground-state $|\tilde{g}\rangle$ (with dipole moment $d_{\tilde{g}}$) and the lower-lying excited state $|e\rangle$ (with negligible dipole moment) the dipole of the atom is fluctuating in time. This leads to an additional diffusion term in the equation of motion in addition to the standard Doppler-cooling diffusion terms. After a lengthy calculation one obtains for two atoms in their dressed ground-state, $W^{(2)}_{\tilde{g}\tilde{g}} = \langle\tilde{g}\tilde{g}|W|\tilde{g}\tilde{g}\rangle$, the equation of motion

$$\left(\frac{\partial}{\partial t}+\sum_{i=1}^{2}\frac{\mathbf{p}_i}{M}\frac{\partial}{\partial\mathbf{r}_i}\right)W^{(2)}_{\tilde{g}\tilde{g}} = \sum_{i=1}^{2}\left[\frac{\partial}{\partial\mathbf{p}_i}\mathbf{f}_c+\mathcal{D}^{(i)}_1\right]W^{(2)}_{\tilde{g}\tilde{g}} - \mathbf{f}_{12}\cdot\left(\frac{\partial}{\partial\mathbf{p}_1}-\frac{\partial}{\partial\mathbf{p}_2}\right)W^{(2)}_{\tilde{g}\tilde{g}} + \mathcal{D}_{12}W^{(2)}_{\tilde{g}\tilde{g}}, \tag{3.35}$$

which is valid when $\Delta_r \gg \Omega_r, \Omega_e, \Gamma_e \gg \hbar k_{eg}^2/m$, where k_{eg} is the wave number of the ($|e\rangle$-$|g\rangle$) transition. Additional to the free motion term on the left-hand side, the first term on the right-hand side describes single-particle Doppler cooling with the cooling force $\mathbf{f}_c = \beta\hat{\mathbf{k}}_{Le}\ \mathbf{k}_{Le}\cdot\mathbf{p}$ and the standard diffusion operator $\mathcal{D}_1 = \sum_k D_k\partial^2_{p_k}$ accounting for SE and diffusion due to the cooling laser in various spatial directions $k \in \{x, y, z\}$ [77]. Here we assumed two counter-propagating laser beams and expanded the resulting radiation pressure forces up to second order in $\mathbf{k}_{Le}$. The third term of Eq. (3.35) proportional to

$$\mathbf{f}_{12} = \frac{\Omega_r^4}{4\Delta_r^2(V-2\Delta_r)^2}\frac{\partial V}{\partial\mathbf{r}_1} = -\frac{\partial E_{\tilde{g}\tilde{g}}}{\partial\mathbf{r}_1} \tag{3.36}$$

accounts for the interaction between the two atoms. We note that this term can be rewritten, using the potential of the dressed ground-state [Eq. (3.18)] obtained in Sec. 3.4.2. Besides those standard laser cooling terms, [72, 77], the term

$$\mathcal{D}_{12} = \frac{4\Omega_e^2\Gamma_e}{(\Gamma_e^2+4\Delta_e^2)^2}\left[\mathbf{f}_{12}\cdot\left(\frac{\partial}{\partial\mathbf{p}_1}-\frac{\partial}{\partial\mathbf{p}_2}\right)\right]^2 \tag{3.37}$$

is a two-body diffusion term which accounts for the fluctuations of the force (which is present only in the dressed ground-state), due to Rabi-oscillations between $|e\rangle$ and $|\tilde{g}\rangle$. For near-resonant laser light it is proportional to the population and lifetime of the excited state. In the limit $\mathbf{f}_{12} \ll \hbar\Gamma_e\mathbf{k}_{Le}$ this diffusion term is small compared to the single-particle diffusion terms and one can approximate the system with two interacting atom, which are independently laser-cooled.

3.5.2 Quantum jumps and rate equations

A quantum jump occurs when the atom in the Rydberg state $|r\rangle$ decays to an intermediate state $|m\rangle$ due to SE or BBR. In the following, we allow for the possibility that the intermediate state $|m\rangle$ is long-lived, with a lifetime $\sim 1/\Gamma_{mg}$ comparable with the external dynamics and thus cannot be adiabatically eliminated. This will lead to two coupled equations of motion: (i) an equation for laser-cooled atoms in the dressed ground-state, with dipole moment $d_{\tilde{g}} = (\Omega_r/2\Delta_r)^2 d_r$, and (ii) an equation of motion for atoms in the $|m\rangle$ state (and possibly with a dipole moment d_m), which do not experience a cooling force.

To simplify the notation for the analytic treatment, we consider only a single atom in the presence of the cooling and dressing lasers. The generalization to two atoms is straightforward. After preforming steps (i)-(iv) of the latter section we find the following coupled FPEs for the dynamics of the dressed ground-state $|\tilde{g}\rangle$ and the intermediate state $|m\rangle$:

$$\left(\frac{\partial}{\partial t} + \frac{\mathbf{p}}{M} \cdot \frac{\partial}{\partial \mathbf{r}}\right) W_{\tilde{g}}^{(1)} = -\Gamma_{\tilde{g}} W_{\tilde{g}}^{(1)} + (\Gamma_m + \mathcal{D}_{mg}) W_m^{(1)} + \left[\frac{\partial}{\partial \mathbf{p}} \cdot \mathbf{f}_c + \mathcal{D}_1\right] W_{\tilde{g}}^{(1)}, \tag{3.38a}$$

$$\left(\frac{\partial}{\partial t} + \frac{\mathbf{p}}{M} \cdot \frac{\partial}{\partial \mathbf{r}}\right) W_m^{(1)} = -\Gamma_m W_m^{(1)} + \left[\Gamma_{\tilde{g}} + \left(\frac{\Omega_r}{2\Delta_r}\right)^2 \mathcal{D}_{rm}\right] W_{\tilde{g}}^{(1)}, \tag{3.38b}$$

where $W_\alpha^{(1)} = \langle\alpha|W^{(1)}|\alpha\rangle$ is the single-particle Wigner function for the atom in state $|\alpha\rangle$ ($\alpha \in \{\tilde{g}, m\}$). The equations are coupled by the effective ground-state decay rate

$$\Gamma_{\tilde{g}} = \left(\frac{\Omega_r}{2\Delta_r}\right)^2 \Gamma_{rm} \tag{3.39}$$

due to optical pumping via the Rydberg state $|r\rangle$. The terms $\mathcal{D}_{\alpha\beta}$ are standard diffusion operators [77] accounting for SE from state $|\alpha\rangle$ to $|\beta\rangle$.

3.6 Dissipative dynamics of dressed Rydberg atoms

We now analyze numerically the dissipative processes of Eq. (3.3), which are associated with the finite lifetime of excited Rydberg states. In Sec. 3.6.1 below, we consider the case of a *single* atom, in which we investigate the population of intermediate states due to SE or BBR. As a consequence, the atom acquires a time-dependent dipole moment. In addition, SE and BBR act as small heating sources due to the photon recoil. In Sec. 3.6.2 we summarize our previous discussion of the driven-dissipative dynamics of laser-cooled and interacting Rydberg-dressed atoms as a prescription for a molecular dynamics simulation. The effect of population in intermediate states will be more substantial in the case of an *ensemble* of Rydberg-dressed atoms, as we discuss in Sec. 3.6.3. In particular, we find that the dominant heating effect originates from the time-dependent dipole moment which induces strong mechanical effects in the many-body system. A crucial point is that the time dependence of the dipole moment exhibits characteristically different behavior in the dc electric field case compared to the ac microwave one. For example, in the case of a static electric field ($F > 0$) the states $|\alpha_F\rangle$ can have large *parallel* or *antiparallel* dipoles, $\mathbf{d}_\alpha = \langle\alpha_F|\hat{\mathbf{d}}|\alpha_F\rangle$, on the order of kilodebye, causing strong dipole-dipole interactions with other Rydberg-dressed atoms, whereas in the case of a ac microwave field (and no dc electric field) the intermediate states do not have any dipole moment.

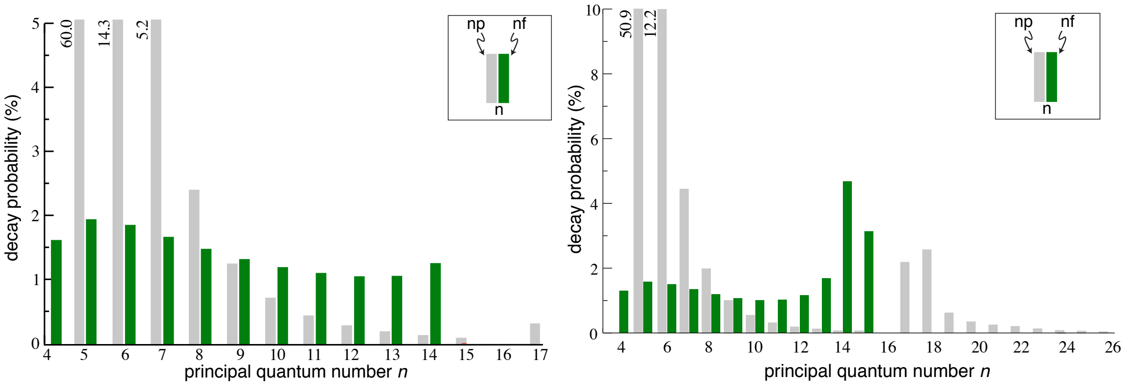

Figure 3.9. *(Color online) Relative decay rates $\Gamma_{r,n\ell}/\Gamma_r$ of the $|r\rangle = |16\,d_{5/2}, m_j = -5/2\rangle$ state of ^{85}Rb. Green (dark gray) and gray (light gray) bars indicate decay rates to $|np\rangle$- and $|nf\rangle$-states, respectively. In both cases we summed over j and m_j. The top and bottom panels show the relative decay rates for $T = 0$ K and $T = 300$ K, respectively. The total decay rate of $\Gamma_{16d} = 2\pi\times$ 51 kHz (43 kHz) for $T = 300$ K ($T = 0$) agrees well with calculations carried out in [73]. Note that in the top and bottom panels the y axes are cut at 5 % and 10 %, respectively. For states with a higher decay rate percentage numbers on the left side of the bars indicate their value.*

3.6.1 Decoherence of a single atom

The dressed ground-state $|\tilde{g}\rangle$ has a finite lifetime $\tau_{\tilde{g}} = \Gamma_{\tilde{g}}^{-1}$, where $\Gamma_{\tilde{g}} = (\Omega_r/2\Delta_r)^2\Gamma_r$, and $1/\Gamma_r$ is the lifetime of the Rydberg state. The latter is, in general, given by BBR and SE, which redistribute population from the $|r\rangle$ ($|r_F\rangle$) state to all possible intermediate states $|m\rangle$. Such a decay event from the Rydberg state is followed by a cascade process where several intermediate states $|m\rangle$ can be populated. It is crucial to note that the cascade process in general does not happen instantaneously, due to the finite lifetime of the intermediate states. As we discuss below, this has far-reaching consequences in the long-time dynamics of Rydberg-dressed crystals.

We calculated the decay constants $\Gamma_{\alpha\beta}$ given in Eqs. (3.6a) and (3.6b) numerically using both quantum defect theory [78–80] and a model potential method [81]. With the first method we calculated the decay matrix including all angular momentum states up to $n = 18$, while with the second method we obtained the decay matrix up to $n = 110$ including s, p, d, f, and g angular momentum states. With $\Gamma_\alpha = \sum_\beta \Gamma_{\alpha\beta}$ we denote the total decay rate of the state $|\alpha\rangle$ and $\Gamma_0 \equiv \Gamma_{\tilde{g}} = (\Omega_r/2\Delta_r)^2\Gamma_r = (\Omega_r/2\Delta_r)^2 \sum_\beta \Gamma_{r\beta}$ is the effective decay rate of the dressed ground-state. Figure 3.9 shows the branching ratio of decay in the absence of external fields from the $|16d\rangle$ state to $|np\rangle$ and $|nf\rangle$ states, where we summed over j and m_j levels. For $T = 0$ K (top panel) the only contribution to the decay rate comes from SE, which favors decay to low-lying states. About 60 % of the population in the $|16d\rangle$ state decays to the $|5p\rangle$ state. The bottom panel of Fig. 3.9 shows the branching ratio for $T = 300$ K. In this case the decay rate is determined not only by SE but also by BBR, which in addition leads to substantial decay to neighboring states. Hence, only 51 % of the population in the $|16d\rangle$ states decays directly to the $|5p\rangle$ state. From this it is clear that in current cold-atom experiments performed in room-temperature environments the role of high-lying intermediate states cannot be neglected in the long-time limit.

The internal dynamics corresponding to a cascade process of the electron towards the ground-state

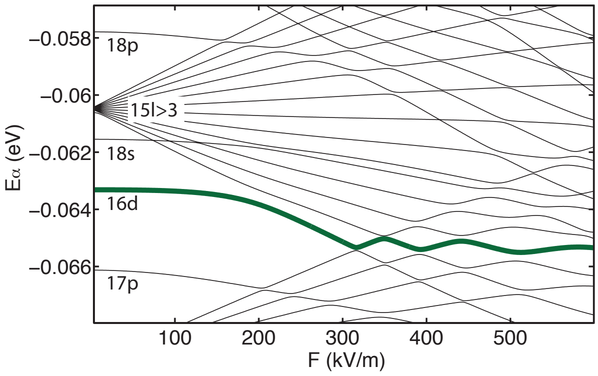

Figure 3.10. *(Color online) Stark map: Atomic energy levels $E_\alpha(F)$ of ^{85}Rb as a function of the field strength F around the state $|16d, m = 0\rangle$. Note that we plot only states with magnetic quantum number $m = 0$. States with an angular quantum number $\ell > 3$ have a negligible quantum defect and show a linear Stark effect, while s, p and d states show a quadratic. The energy of the state which for $F \to 0$ connects to $|16d, m = 0\rangle$ (thick line) is well separated in energy from neighboring states up to a field strength of $F \approx 300$ kV/m.*

following a decay event vim the Rydberg states is given by

$$\frac{d}{dt}\begin{pmatrix} p_0 \\ p_1 \\ p_2 \\ \vdots \end{pmatrix} = \begin{pmatrix} -\Gamma_0 & \Gamma_{10} & \Gamma_{20} & \\ \Gamma_{01} & -\Gamma_1 & \Gamma_{21} & \dots \\ \Gamma_{02} & \Gamma_{12} & -\Gamma_2 & \\ & \vdots & & \end{pmatrix}\begin{pmatrix} p_0 \\ p_1 \\ p_2 \\ \vdots \end{pmatrix}, \tag{3.40}$$

where p_α is the probability of being in the state $|\alpha_{(F)}\rangle$ in the absence (presence) of a static electric field, $F = 0$ ($F > 0$). Note that in the case of a dc electric field ($F > 0$) the decay rates $\Gamma_{\alpha_F\beta_F}$ are a sum of several decay rates between bare states, $\Gamma_{\alpha\beta}$, according to the contributions of various different angular momentum states to the Stark split states $|\alpha_F\rangle$ and $|\beta_F\rangle$.

dc electric field: The Stark structure of atomic states (including only $m = 0$ states) is shown in Fig. 3.10 for a electric field along $\mathbf{e}_z$. States with an angular momentum $\ell > 3$ are almost degenerate and exhibit a linear Stark effect, while lower angular momentum states, which have a larger quantum defect which breaks the degeneracy, exhibit a quadratic Stark shift. Figure 3.10 shows that the $|16d\rangle$ state (thick line) is well separated from the neighboring states by an energy gap of ~ 200 GHz up to a field strength of $F \sim 3$ kV/cm and experiences a strong energy shift, corresponding to a large dipole moment. For an electric field $\mathbf{E}_{\mathrm{dc}} = F\,\mathbf{e}_z$ only $m = 0$ states are coupled and the resulting dipole moments are polarized along the direction of the external field. Figure 3.11 shows the z component of the dipole moment, $\mathbf{d}_\alpha$, for different states $|\alpha_F\rangle$ and a field strength of $F = 3$ kV/cm. The figure shows that states $|\alpha_F\rangle$ gain a large dipole moment of hundreds of debyes which can be *positive* and *negative*. The dipole moment of the state which for $F \to 0$ connects to $|16d, m = 0\rangle$ is about 680 D.

The time evolution of Eq. (3.40) is readily simulated. We prepare the atom in the dressed ground-state $|\tilde{g}\rangle$, that is $p_{\tilde{g}} = p_0 = 1$. After a time step Δt much smaller than the time scales associated with the decay rates a random number determines if and to which internal state $|\alpha_{(F)}\rangle$ the atom makes a transition (quantum jump) according to the rates of Eq. (3.40). During each time step the dipole moment $d(t)$ of the atom is equal to the dipole moment of the current state, $d_{\alpha_{(F)}}$. This new configuration then again propagated another time step Δt.

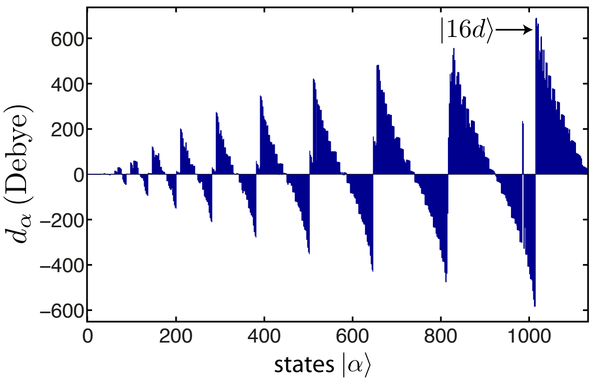

Figure 3.11. *(Color online) Electric dipole moment $d_\alpha = \langle\alpha_F|\hat{d}_z|\alpha_F\rangle$ of the Stark split states $|\alpha_F\rangle$ of a ^{85}Rb atom in an electric dc field with strength $F = 3$ kV/cm. States are numbered with increasing energy, for example the state $|16d, m = 0\rangle$ corresponds to $\alpha = 1017$. The figure shows that depending on the state the dipole moment d_α can be positive (parallel) or negative (antiparallel) leading to a repulsive or attractive interaction.*

Figure 3.12(a) shows an example result for the time evolution of the atomic dipole moment $d(t)$ of a ^{85}Rb atoms polarized by a dc electric field with strength $F = 3$ kV/cm. The ground-state is coupled to the Rydberg state $|r_F\rangle$, which in the absence of a dc electric field ($F = 0$) connects to the $|r\rangle = |16d, m = 0\rangle$ state using a Rydberg-laser with $(\Omega_r/2\Delta_r) = 0.21$. We initially prepare the atom in the dressed ground-state $|\tilde{g}_F\rangle$, and compute the time evolution using Eq. (3.40). The trajectory in Fig. 3.12(a) shows a typical result for the deviation of the atomic dipole from the dipole moment of the dressed ground-state $d_{\tilde{g}} = 30$ Debye as a function of time t, in units of the ground-state lifetime $\tau_{\tilde{g}} = 125$ μs. The figure shows large positive and negative spikes for the values of d, followed by long times where the system is in the dressed ground-state, with dipole moment $d_{\tilde{g}}$. The large "spikes" correspond to the population of intermediate states $|\alpha_F\rangle$, during the cascade process towards the ground-state, following a SE event. These large positive and negative fluctuations of $d(t)$ will cause strong dipole-dipole interactions and hence large mechanical effects when a gas of interacting Rydberg atoms is considered.

Microwave dressing and F=0: In this case we couple the ground-state $|5s\rangle$ of Rubidium to the state $|17s\rangle$ using a laser with $(\Omega_r/2\Delta_r)^2 = 0.05$. An additional microwave field couples the states $|17s\rangle$ and $|17p\rangle$ such that the dressed ground-state obtains a dipole moment of $d_{\tilde{g}} = 30$ Debye. The solid (blue) trajectory in Fig. 3.12(b) shows a typical trajectory for the time evolution of the dipole moment as a function of time in units of $\tau_{\tilde{g}} = 90$ μs. For this dressing scheme the intermediate states $|m\rangle$ do not possess a dipole, and thus the dipole fluctuates between long periods when it has the value $d_{\tilde{g}}$, corresponding to the atom in the dressed ground-state, to periods where the atom has no dipole, corresponding to the cascade processes following SE, like a "blinking dipole".

In comparison, in the dc electric field case [solid trajectory in panel (a)] the dipole fluctuations are much larger and can take both positive and negative values, whereas in the microwave case [red trajectory in panel (b)] the dipoles fluctuate between zero and $d_{\tilde{g}}$.

In the following we examine the *external dynamics* of a *single* atom. It is dominated by small momentum fluctuations associated with the photon recoil following a series of cascade decay events.

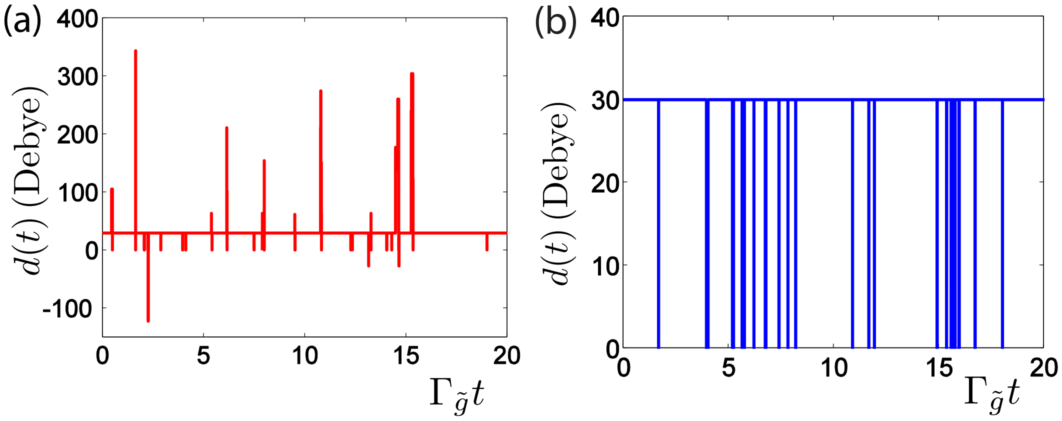

Figure 3.12. *(Color online) Time evolution of the atomic dipole moment $d(t)$ according to population of various internal states governed by Eq. (3.40) for a ^{85}Rb atom. In panel (a) the atom is polarized using the dc electric field dressing scheme while in panel (b) it is polarized with the ac microwave dressing scheme using the same parameters as given in Sec. 3.6.1. In both cases the dipole moment of the dressed ground-state is $d_{\tilde{g}} = 30$ D. In the case of the dc electric field dressing scheme [panel (a)] the dipole moment fluctuates between large positive and negative values due to population of intermediate states, while in the case of the ac microwave dressing scheme [panel (b)] the dipole moment jumps between $d(t) = 0$ and $d(t) = 30$ D.*

As an example, we simulate heating due to decay from the $|r\rangle = |16d\rangle$ state using the same parameters as before. The result of a molecular dynamics simulation is shown in Fig. 3.13, where we plot single kinetic energy trajectories as a function of time (thin black lines). We propagate the internal dynamics according to Eq. (3.40). Each decay event is associated with a momentum kick in a random direction corresponding to the transition (see next section). It is shown in the figure that as time progresses the kinetic energy increases due to photon recoils. We perform a statistical average over 50 runs of simulations (thick line) which yields an average heating rate of $2\pi \times 106.3$ kHz/ms. It will be shown below that for high enough densities this single-particle heating rate is much smaller than the heating rate due to interactions associated with fluctuations of the dipole moment in the many-body case, as discussed in the next section.

3.6.2 Molecular dynamics simulation

In our semiclassical description the state of each atom at time t is specified by $\{\mathbf{r}_i(t), \mathbf{p}_i(t), \alpha_i\}$, where $\mathbf{r}_i(t)$ and $\mathbf{p}_i(t)$ are the center-of-mass coordinate and momentum of the i-th atom, respectively, and $\alpha \in \{\tilde{g}, m, m', \ldots\}$ denotes the internal electronic state with $i = 1, \ldots, N$. The internal state is either the ground-state $|\tilde{g}\rangle$, dressed by the admixure of the Rydberg state, and the excited state $|e\rangle$ from the laser cooling (see Fig. 3.4), or one of the many intermediate states $|m\rangle$ populated during a decay cascade back to the ground-state. The dynamics of the gas is described by a set of coupled equations, as written for the case of one or two atoms in Eqs. (3.38) and (3.35), respectively. These results can be generalized immediately to N atoms. Mathematically, they are a set of coupled Fokker-Planck equations for the external motion and rate equations for the internal electronic states, describing a combined diffusive and jump Markov process for the probability density $W^{(N)}(\mathbf{r}_1, \mathbf{p}_1, \alpha_1; \ldots, \mathbf{r}_N, \mathbf{p}_N, \alpha_N; t)$. This

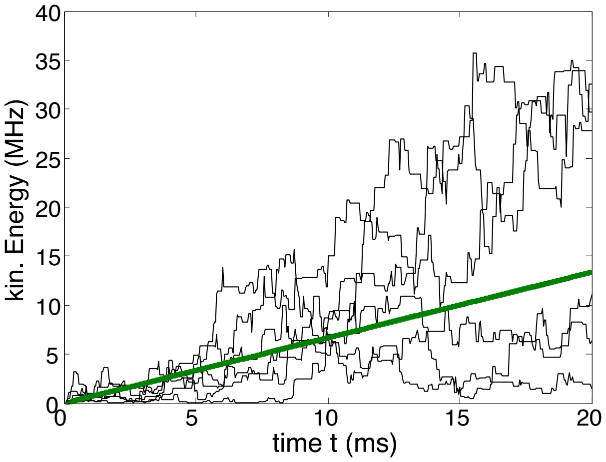

Figure 3.13. *(Color online) Single kinetic energy trajectories, E_{kin}, as a function of time t for a single Rydberg-dressed ^{85}Rb atom (thin black lines). We observe an increase in kinetic energy due to photon recoil due to decay events from the Rydberg state. The thick line is a linear fit of 50 single trajectories which gives a mean heating rate of* $2\pi \times 106.3$ *kHz/ms.*

stochastic process is readily simulated.

Consider atom i, which we assume to be in the dressed ground-state $|\tilde{g}\rangle$. Its center-of-mass motion obeys the Langevin equations

$$\dot{\mathbf{r}}_i = \frac{\mathbf{p}_i}{M}, \tag{3.41a}$$

$$\dot{\mathbf{p}}_i = \sum_{j\neq i} \mathbf{f}_{\mathrm{int}}^{(ji)} - \beta \mathbf{p}_i + \mathbf{f}_{\mathrm{ex}}^{(i)} + \mathbf{F}^{(i)}, \tag{3.41b}$$

where on the right-hand side of Eq. (3.41b) we sum over the forces from all the other ground-state atoms, as well as the forces from atoms in one of the intermediate states $|m\rangle$, with

$$\mathbf{f}_{\mathrm{int}}^{(ji)}(t) = -\frac{d_{\alpha_i} d_{\alpha_j}}{4\pi\epsilon_0} \frac{\partial}{\partial \mathbf{r}_i} \frac{1}{|\mathbf{r}_i - \mathbf{r}_j|^3}. \tag{3.42}$$

Here, $d_{\alpha_i} = d_{\tilde{g}}$ is the effective dipole moment of the dressed ground-state [see Eqs. (3.18) and (3.28) for the dc and ac field cases, respectively] and d_{α_j} can either be equal to $d_{\tilde{g}}$ if the j-th atom is in the dressed ground-state $|\tilde{g}_j\rangle$ or equal to d_m if the j-th atom is in the state $|m\rangle$. In the dc electric field case $d_m = \langle m_F|\mathbf{d}|m_F\rangle$, while in the ac microwave field case $d_m = 0$ (see Sec. 3.6.1). In addition, we have added in Eq. (3.41b) the familiar terms describing possible laser cooling [77], and an external trapping force $\mathbf{f}_{\mathrm{ex}}^{(i)}$. The last term in Eq. (3.41b) is a stochastic force [82] from quantum fluctuations due to the recoil of SE events from both the Rydberg state repopulating the ground-state, but also from laser cooling, obeying

$$\langle F_k^{(i)}(t) F_l^{(j)}(t')\rangle = D_k \delta_{kl} \delta_{ij} \delta(t - t'), \tag{3.43}$$

with $k, l \in \{x, y, z\}$ and $i, j \in 1, \ldots, N$ and D_k the diffusion coefficients of Eq. (3.35). We make the simplifying assumption that the cross-noise term of Eq. (3.37) arising from the fluctuating ground-state dipole due to laser cooling discussed in Sec. 3.5 is negligible.

Similarly, atom i in one of the intermediate states $|m\rangle$ obeys the equation of motion

$$\dot{\mathbf{r}}_i = \frac{\mathbf{p}_i}{M}, \qquad \dot{\mathbf{p}}_i = \sum_{j \neq i} \mathbf{f}_{\text{int}}^{(ji)}, \tag{3.44}$$

where again $\mathbf{f}_{\text{int}}^{(ji)}$ are the forces of Eq. (3.42) and $d_{\alpha_i} = d_m$. Note that atoms in one of the (intermediate) Rydberg states $|m\rangle$ are assumed to be neither trapped, $\mathbf{f}_{\text{ex}}^{(i)} = 0$, nor laser-cooled, $\beta = 0$.

Optical pumping from $|\tilde{g}\rangle$ to one of the intermediate states $|m\rangle$ and the following cascaded decay, $|\tilde{g}\rangle \to |m\rangle \to \ldots \to |m'\rangle \to |\tilde{g}\rangle$, back to the dressed ground-state will redistribute the atomic populations according to the rate equations (3.40). We can simulate this many-body dynamics by starting with a given atomic configuration, and propagating Eqs. (3.41) and (3.44) for a time step Δt, much smaller than the time scales corresponding to the above mentioned rates. We then determine the probabilities for atom i in state α_i to make a transition (jump) to another internal state according to the rate equations (3.40) for optical pumping and decay, and pick a new configuration according to these probabilities. Each cascade of quantum jump is associated with momentum kicks $\hbar\mathbf{k}_{rm}$, ..., $\hbar\mathbf{k}_{m'g}$ in random spatial directions according to the distribution $N_{\alpha\beta}$ of Eq. (3.8) and with $\mathbf{k}_{\alpha\beta}$ the wavevector of the corresponding transition. This new configuration is then again propagated for another time step according to Eqs. (3.41) and (3.44).

Due to the population of intermediate states in the long-time limit and the resulting time-dependent dipole moments we expect a rapid heating caused by fluctuations of the interaction force described above. In addition, we also expect atomic losses. For example, when a ground-state atom collides with an atom in an intermediate $|\alpha\rangle$ state with a large dipole moment the kinetic energy released in the collision can (i) be of the order of the height of the saddle point (see Sec. 3.4.3). In this case the atoms will overcome the potential barrier and experience an attractive interaction. Alternatively, (ii) the energy released can be of the order of the depth of external confinement in the transversal direction. A third loss mechanism is be Penning ionization at distances smaller than $4n^2a_0$ [83–85]. Each of these processes leads to two-body or one-body losses. In the simulations, we utilize a model including two-particle losses, where two particles are lost whenever their relative distance r becomes smaller than a certain critical radius r_{loss} (see Sec. 3.4.3).

3.6.3 Effects of decoherence on the dynamics of many interacting Rydberg atoms

In this section we numerically investigate the effects of SE and BBR on the long-time dynamics of an *ensemble* of interacting Rydberg atoms by performing semiclassical molecular dynamics simulations. As discussed above, the population of intermediate states $|m\rangle$ with different interaction properties, for example, different dipole moments, will lead to strong fluctuations of the interparticle forces in the many-body case.

Using semiclassical molecular dynamics simulations we study the resulting nonequilibrium dynamics of an ensemble constitution of $N = 67$ Rydberg-dressed ^{85}Rb atoms. Initially they are prepared in a perfect triangular crystal in a box with hard walls at $T = 0$. For both dressing schemes we choose system parameters such that the ground-state dipole moment is $d_{\tilde{g}} = 30$ D, corresponding to a melting temperature of $T_M = 0.6\ \mu$K ($2\pi\times$ 12 kHz) for $n_{2D} = 1\ \mu\text{m}^{-2}$. Additionally, the effect of laser cooling and a triangular in-plane optical lattice is analyzed in order to stabilize the atomic crystal. Note that we assume that only dressed ground-state atoms experience both the cooling laser and the lattice with a depth of 50 E_R, with $E_R = 2\pi \times 3.8$ kHz, while atoms in one of the intermediate states $|m\rangle$ do not [see Eqs. (3.41) and (3.44)].

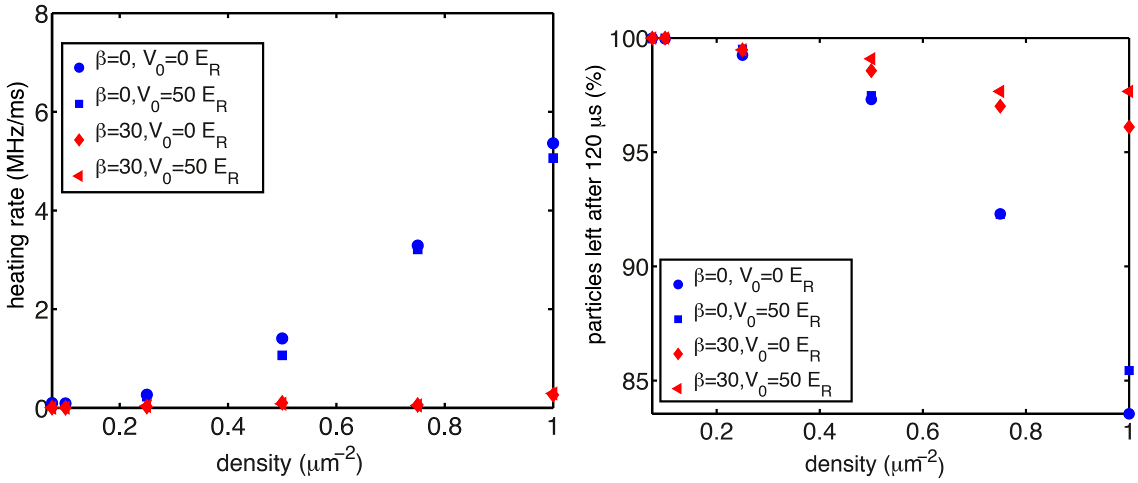

Figure 3.14. *(Color online) dc electric field case: We numerically investigate the heating rate (top panel) and the remaining particle number after a time* $\tau_{\tilde{g}} = 125\ \mu s$ *(bottom panel) as a function of the density* n_{2D} *for different laser cooling parameters* β *and lattice depths* V_0*. Parameters see text.*

dc electric field dressing

Figure 3.14 analyzes heating in a gas of Rydberg dressed atoms using the dc electric field scheme of Fig. 3.4(b) with the same parameters as in Sec. 3.2.2. For $\Delta_r = 2\pi \times 250$ MHz the Condon point is at $r_c \sim 520$ nm. For a transversal trapping frequency of $\omega_\perp = 2\pi \times 200$ kHz the height of the potential barrier at the saddle point is $\sim 150\ \mu$K. Each marker in Fig. 3.14 is an average over 50 runs of the simulation, where we simulated the dynamics for a time $\tau_{\tilde{g}}$.

Figure 3.14(a) shows the heating rate, $\gamma_{\tilde{g}} E_{\mathrm{kin}}(t = \tau_{\tilde{g}})$ as a function of the atomic density for different cooling and lattice parameters, with $E_{\mathrm{kin}}(t)$ the mean kinetic energy of all N atoms. In the case of no laser cooling, $\beta = 0$, there is a strong dependence of the heating rate on the density, while for a cooling rate of $\beta = 2\pi \times 30$ kHz the heating rate is almost zero and a steady state is realized on a timescale $\beta^{-1} \ll \tau_{\tilde{g}}$. This steady state is due to the interplay of laser cooling and heating together with loss of high energy particles from the 2D confinement. This is shown in Fig. 3.14(b), where the number of remaining particles after a time $\tau_{\tilde{g}}$ is shown as a function of the atomic density. Again, there is a strong dependence on the density and also on the laser cooling rate β. For densities $n_{2D} \lesssim 0.04\ \mu\mathrm{m}^{-2}$ the effect of the fluctuating dipoles can be neglected on surrounding atoms, while for densities $n_{2D} \sim 1\ \mu\mathrm{m}^{-2}$ the particle number has been decreased by 3% (with cooling) or 15 % (no cooling) after a time $\tau_{\tilde{g}} = 120\ \mu$s. Similar to Fig. 3.3, we observe an accelerated loss of particles, resulting in a dramatic decrease of the particle number for times $t > \tau_{\tilde{g}}$. The effect of an in-plane optical lattice is small and hardly changes the heating rate or particle number shown in Fig. 3.14.

ac microwave field dressing

Figure 3.15 shows heating dynamics in a gas of Rydberg dressed atoms using the *microwave dressing scheme* of Fig. 3.4(c) with the same parameters as in Sec. 3.2.3. For $\Delta_r = 2\pi \times 1.0$ GHz and $\alpha = 0.5$

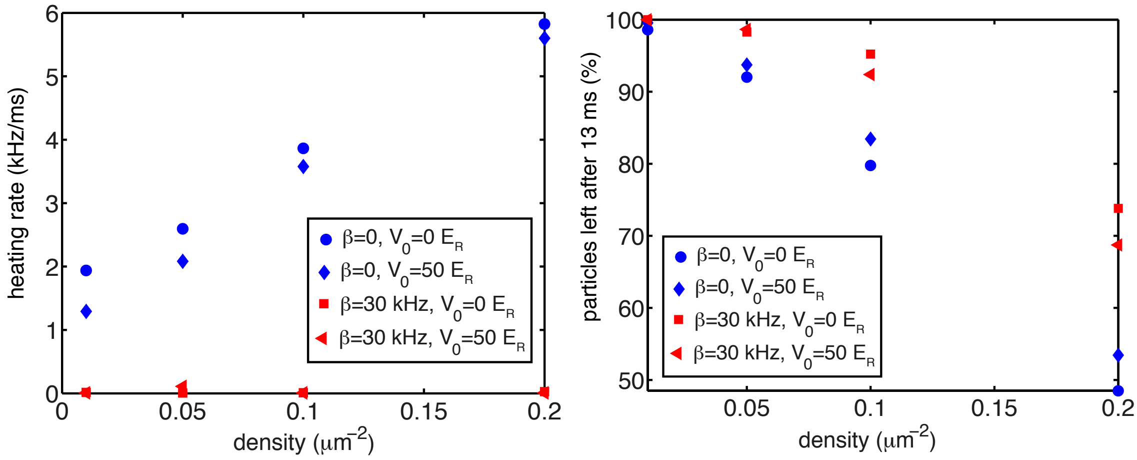

Figure 3.15. *(Color online) ac microwave field case: We numerically investigate the heating rate (upper panel) and the remaining particle number after a time $\tau_{\tilde{g}} = 12.8$ ms (lower panel) as a function of the density n_{2D} for different laser cooling parameters β and lattice depths V_0. Parameters see text.*

we find $r_c \sim 1.38\ \mu$m. With $\omega_\perp = 2\pi \times 100$ kHz the hight of the barrier at the saddle points is $\sim 70\ \mu$K.

In our treatment, the basic heating process of a crystal comes from its spatial rearrangement, once one of the atoms decays to an intermediate state $|m\rangle$ with zero dipole moment. We explain this as follows: Due to the lack of dipole moment, particles in the intermediate state $|m\rangle$ can travel a distance v_R/Γ_m without interacting with neighboring atoms, where v_R is the recoil velocity and Γ_m the mean lifetime of an intermediate state. (i) if v_R/Γ_m is of the order of the mean particle distance in the crystal $n_{2D}^{-1/2}$ two particles will most probably come closer than the critical radius $r_{\rm loss}$ and get lost. We find that this latter process can result in an unusual *collisional* evaporative cooling effect. (ii) If v_R/Γ_m is smaller than the mean particle distance in the crystal the atom may return to the ground-state with a finite dipole moment, resulting in large time-dependent fluctuations of the dipole-dipole interaction between neighboring atoms. The net heating rate of the crystal is a competition between processes (i) and (ii).

We note that accidental vdW interactions may occur between atoms in one of the intermediate states $|m\rangle$, which may lead to additional heating. However, these processes are not considered here.

Figure 3.15(a) shows the mean heating rate, $\gamma_{\tilde{g}} E_{\rm kin}(t = \tau_{\tilde{g}})$ as a function of the atomic density for different cooling and lattice parameter, with $E_{\rm kin}(t)$ the mean kinetic energy of all N atoms. Again, each marker in Fig. 3.15 is an average over 50 runs of the simulation, where we simulated the dynamics for a time $\tau_{\tilde{g}} = 12.8$ ms. Similar as in the dc electric field case of Fig. 3.14, there is a strong dependence of the heating rate on the density and on the laser cooling rate β, while the effect of an in-plane optical lattice is weak. Additional laser cooling of the atoms with a rate $\beta = 30$ kHz again leads to a steady state of the mean kinetic energy [see panel (a)] and diminishes the particle loss rate, which is shown in Fig. 3.14(b). The number of remaining particles after a time $\tau_{\tilde{g}}$ is shown as a function of the atomic density. Remarkably, more than 70% (50%) of the particles are left with (without) laser cooling and densities of $n_{2D} = 0.2/\mu\text{m}^2$ after $t = \tau_{\tilde{g}}$.

3.7 Conclusions and Outlook

In this work we have investigated the long-time nonequilibrium dynamics of an ensemble of cold ground-state atoms, weakly admixed with a Rydberg state using laser light. For times comparable to or larger than the effective lifetime of the ground-state, the population of intermediate Rydberg states following SE significantly affects the atomic motion in a strongly interacting gas, by providing a dominant heating and loss mechanism. We analyzed in detail two scenarios in which the atoms have been polarized either by an additional dc electric field or by an additional ac microwave field.

Numerical simulations indicate that, due to the absence of dipole moments in the intermediate Rydberg states, ensembles of atoms polarized by ac microwave fields exhibit a significantly different long-time dynamics, compared to atoms dressed by dc electric fields: In the dc field case the nonequilibrium dynamics is followed by local explosions or implosions resulting in a large atom number loss due to the fluctuating dipoles present in the intermediate states. In both cases, we find that the heating and loss rates decrease quickly with a decreasing atomic density. In addition, these effects can be substantially mitigated by performing active laser cooling in the presence of atomic dressing.

Understanding this long-time dynamics is relevant for the experimental demonstration of laser-dressing techniques [86], as well as the creation of long-lived strongly correlated atomic phases such as self-assembled atomic crystals. Related to recent work on mixtures of polar molecules and Rydberg atoms [63, 64], we speculate that long-lived cold crystals may be used as cold reservoirs for achieving, for example, sympathetic cooling of polar molecules [68].

Acknowledgment

The authors thank E. Arimondo, M. Baranov, I. Lesanovsky, M. D. Lukin and H. R. Sadeghpour for stimulating discussions. PZ and AG thank ITAMP, the Harvard Physics Department and the Joint Quantum Institute, University of Maryland, for their hospitality where part of this work was done. Work was supported in parts by COHERENCE, EOARD and EPSRC through CHIST-ERA R-ION, and the Austrian Science Fund. GP was funded by the ERC Starting Grant (307688).

Bibliography

[1] T. F. Gallagher, *Rydberg Atoms* (Cambridge University Press, 2005).

[2] M. Saffman, T. G. Walker, and K. Mølmer, Rev. Mod. Phys. **82**, 2313 (2010).

[3] D. Comparat and P. Pillet, J. Phys. B **27**, 208 (2010).

[4] M. J. Seaton, Rep. Prog. Phys. **46**, 167 (1983).

[5] R. Löw, H. Weimer, J. Nipper, J. B. Balewski, B. Butscher, H. P. Büchler, and T. Pfau, J. Phys. B **45**, 113001 (2012).

[6] W. R. Anderson, J. R. Veale, and T. F. Gallagher, Phys. Rev. Lett. **80**, 249 (1998).

[7] K. Singer, M. Reetz-Lamour, T. Amthor, L. G. Marcassa, and M. Weidemüller, Phys. Rev. Lett. **93**, 163001 (2004).

[8] D. Tong, S. M. Farooqi, J. Stanojevic, S. Krishnan, Y. P. Zhang, R. Côté, E. E. Eyler, and P. L. Gould, Phys. Rev. Lett. **93**, 063001 (2004).

[9] T. C. Liebisch, A. Reinhard, P. R. Berman, and G. Raithel, Phys. Rev. Lett. **95**, 253002 (2005).

[10] K. Afrousheh, P. Bohlouli-Zanjani, J. Carter, A. Mugford, and J. Martin, Phys. Rev. A **73**, 063403 (2006).

[11] T. Carroll, S. Sunder, and M. Noel, Phys. Rev. A **73**, 032725 (2006).

[12] R. Heidemann, U. Raitzsch, V. Bendkowsky, B. Butscher, R. Löw, L. Santos, and T. Pfau, Phys. Rev. Lett. **99**, 163601 (2007).

[13] T. Vogt, M. Viteau, A. Chotia, J. Zhao, D. Comparat, and P. Pillet, Phys. Rev. Lett. **99**, 073002 (2007).

[14] T. Amthor, M. Reetz-Lamour, S. Westermann, J. Denskat, and M. Weidemüller, Phys. Rev. Lett. **98**, 023004 (2007).

[15] C. S. E. van Ditzhuijzen, A. F. Koenderink, J. Hernández, F. Robicheaux, L. Noordam, and H. B. van den Linden van den Heuvell, Phys. Rev. Lett. **100**, 243201 (2008).

[16] T. Johnson, E. Urban, T. Henage, L. Isenhower, D. Yavuz, T. Walker, and M. Saffman, Phys. Rev. Lett. **100**, 113003 (2008).

[17] J. Pritchard, D. Maxwell, A. Gauguet, K. Weatherill, M. Jones, and C. Adams, Phys. Rev. Lett. **105**, 193603 (2010).

[18] S. Sevinçli, C. Ates, T. Pohl, H. Schempp, C. S. Hofmann, G. Günter, T. Amthor, M. Weidemüller, J. D. Pritchard, D. Maxwell, et al., J. Phys. B **44**, 184018 (2011).

[19] Y. O. Dudin and A. Kuzmich, Science **336**, 887 (2012).

[20] J. Nipper, J. B. Balewski, A. T. Krupp, B. Butscher, R. Löw, and T. Pfau, Phys. Rev. Lett. **108**, 113001 (2012).

[21] H. Weimer, R. Löw, T. Pfau, and H. P. Büchler, Phys. Rev. Lett. **101**, 250601 (2008).

[22] R. Löw, H. Weimer, U. Krohn, R. Heidemann, V. Bendkowsky, B. Butscher, H. Büchler, and T. Pfau, Phys. Rev. A **80**, 033422 (2009).

[23] T. Pohl, E. Demler, and M. D. Lukin, Phys. Rev. Lett. **104**, 043002 (2010).

[24] H. Weimer and H. P. Büchler, Phys. Rev. Lett. **105**, 230403 (2010).

[25] J. Honer, H. Weimer, T. Pfau, and H. P. Büchler, Phys. Rev. Lett. **105**, 160404 (2010).

[26] G. Pupillo, A. Micheli, M. Boninsegni, I. Lesanovsky, and P. Zoller, Phys. Rev. Lett. **104**, 223002 (2010).

[27] N. Henkel, R. Nath, and T. Pohl, Phys. Rev. Lett. **104**, 195302 (2010).

[28] F. Maucher, N. Henkel, M. Saffman, W. Królikowski, S. Skupin, and T. Pohl, Phys. Rev. Lett. **106**, 170401 (2011).

[29] E. Sela, M. Punk, and M. Garst, Phys. Rev. B **84**, 085434 (2011).

[30] J. Schachenmayer, I. Lesanovsky, A. Micheli, and A. J. Daley, New J. Phys. **12**, 103044 (2010).

[31] H. Weimer, N. Y. Yao, C. R. Laumann, and M. D. Lukin, Phys. Rev. Lett. **108**, 100501 (2012).

[32] D. Jaksch, J. Cirac, P. Zoller, S. Rolston, R. Cote, and M. Lukin, Phys. Rev. Lett. **85**, 2208 (2000).

[33] M. D. Lukin, M. Fleischhauer, R. Cote, L. Duan, D. Jaksch, J. Cirac, and P. Zoller, Phys. Rev. Lett. **87**, 037901 (2001).

[34] E. Urban, T. A. Johnson, T. Henage, L. Isenhower, D. D. Yavuz, T. G. Walker, and M. Saffman, Nature Phys. **5**, 110 (2009).

[35] A. Gaëtan, Y. Miroshnychenko, T. Wilk, A. Chotia, M. Viteau, D. Comparat, P. Pillet, A. Browaeys, and P. Grangier, Nature Phys. **5**, 115 (2009).

[36] L. Isenhower, E. Urban, X. L. Zhang, A. T. Gill, T. Henage, T. A. Johnson, T. G. Walker, and M. Saffman, Phys. Rev. Lett. **104**, 010503 (2010).

[37] T. Wilk, A. Gaëtan, C. Evellin, J. Wolters, Y. Miroshnychenko, P. Grangier, and A. Browaeys, Phys. Rev. Lett. **104**, 010502 (2010).

[38] E. Brion, K. Mølmer, and M. Saffman, Phys. Rev. Lett. **99**, 260501 (2007).

[39] M. Saffman and K. Mølmer, Phys. Rev. A **78**, 012336 (2008).

[40] D. Møller, L. Madsen, and K. Mølmer, Phys. Rev. Lett. **100**, 170504 (2008).

[41] M. Müller, I. Lesanovsky, H. Weimer, H. P. Büchler, and P. Zoller, Phys. Rev. Lett. **102**, 170502 (2009).

[42] B. Olmos, R. González-Férez, and I. Lesanovsky, Phys. Rev. Lett. **103**, 185302 (2009).

[43] H. Weimer, M. Müller, I. Lesanovsky, P. Zoller, and H. Büchler, Nature Phys. **6**, 382 (2010).

[44] Y. Han, B. He, K. Heshami, C.-Z. Li, and C. Simon, Phys. Rev. A **81**, 052311 (2010).

[45] B. Zhao, M. Müller, K. Hammerer, and P. Zoller, Phys. Rev. A **81**, 052329 (2010).

[46] E. Kuznetsova, S. T. Rittenhouse, H. R. Sadeghpour, and S. F. Yelin, Phys. Chem. Chem. Phys. **13**, 17115 (2011).

[47] A. V. Gorshkov, J. Otterbach, M. Fleischhauer, T. Pohl, and M. D. Lukin, Phys. Rev. Lett. **107**, 133602 (2011).

[48] T. E. Lee, H. Häffner, and M. C. Cross, Phys. Rev. Lett. **108**, 023602 (2012).

[49] R. Heidemann, U. Raitzsch, V. Bendkowsky, B. Butscher, R. Löw, and T. Pfau, Phys. Rev. Lett. **100**, 033601 (2008).

[50] M. Viteau, M. Bason, J. Radogostowicz, N. Malossi, D. Ciampini, O. Morsch, and E. Arimondo, Phys. Rev. Lett. **107**, 060402 (2011).

[51] T. Amthor, C. Giese, C. S. Hofmann, and M. Weidemüller, Phys. Rev. Lett. **104**, 013001 (2010).

[52] H. Kübler, J. P. Shaffer, T. Baluktsian, R. Löw, and T. Pfau, Nature Photon. **4**, 112 (2010).

[53] I. Mourachko, D. Comparat, F. de Tomasi, A. Fioretti, P. Nosbaum, V. M. Akulin, and P. Pillet, Phys. Rev. Lett. **80**, 253 (1998).

[54] I. Lesanovsky, Phys. Rev. Lett. **106**, 025301 (2011).

[55] W. Li, L. Hamadeh, and I. Lesanovsky, Phys. Rev. A **85**, 053615 (2012).

[56] L. Santos, G. Shlyapnikov, P. Zoller, and M. Lewenstein, Phys. Rev. Lett. **85**, 1791 (2000).

[57] M. Baranov, Phys. Rep. **464**, 71 (2008).

[58] L. Carr, D. DeMille, R. Krems, and J. Ye, New J. Phys. **11**, 055049 (2009).

[59] T. Lahaye, C. Menotti, L. Santos, M. Lewenstein, and T. Pfau, Rep. Prog. Phys. **72**, 126401 (2009).

[60] M. Boninsegni and N. Prokofev, Rev. Mod. Phys. **84**, 759 (2012).

[61] M. A. Baranov, M. Dalmonte, G. Pupillo, and P. Zoller, arXiv:1207.1914 (2012).

[62] H. P. Büchler, E. Demler, M. Lukin, A. Micheli, N. Prokofev, G. Pupillo, and P. Zoller, Phys. Rev. Lett. **98**, 060404 (2007).

[63] S. D. Huber and H. P. Büchler, Phys. Rev. Lett. **108**, 193006 (2012).

[64] B. Zhao, A. W. Glaetzle, G. Pupillo, and P. Zoller, Phys. Rev. Lett. **108**, 193007 (2012).

[65] A. Micheli, G. Pupillo, H. P. Büchler, and P. Zoller, Phys. Rev. A **76**, 043604 (2007).

[66] A. V. Gorshkov, P. Rabl, G. Pupillo, A. Micheli, P. Zoller, M. D. Lukin, and H. P. Büchler, Phys. Rev. Lett. **101**, 073201 (2008).

[67] R. Kalia and P. Vashishta, J. Phys. C **14**, 643 (1981).

[68] A. W. Glaetzle et. al., in preperation.

[69] I. I. Beterov, D. B. Tretyakov, I. I. Ryabtsev, A. Ekers, and N. N. Bezuglov, Phys. Rev. A **75**, 052720 (2007).

[70] M. Saffman and T. G. Walker, Phys. Rev. A **72**, 022347 (2005).

[71] J. Cirac, R. Blatt, P. Zoller, and W. Phillips, Phys. Rev. A **46**, 2668 (1992).

[72] J. Dalibard and C. Cohen-Tannoudji, J. Phys. B **18**, 1661 (1985).

[73] I. Beterov, I. Ryabtsev, D. Tretyakov, and V. Entin, Phys. Rev. A **79**, 052504 (2009).

[74] M. Zimmerman, M. Littman, M. Kash, and D. Kleppner, Phys. Rev. A **20**, 2251 (1979).

[75] J. Weiner, V. S. Bagnato, S. Zilio, and P. S. Julienne, Rev. Mod. Phys. **71**, 1 (1999).

[76] A. B. Klimov, L. L. Sanchez-Soto, A. Navarro, and E. C. Yustas, J. Mod. Opt. **49**, 2211 (2002).

[77] V. G. Minogin and V. S. Letokhov, *Laser Light Pressure on Atoms* (Harwood Academic, 1987).

[78] D. Bates and A. Damgaard, Phil. Trans. R. Soc. Lond. A **242**, 101 (1949).

[79] F. Gounand, J. Phys. France **40**, 457 (1979).

[80] D. Branden, T. Juhasz, T. Mahlokozera, C. Vesa, R. Wilson, M. Zheng, A. Kortyna, and D. Tate, J. Phys. B **43**, 015002 (2010).

[81] M. Marinescu, H. R. Sadeghpour, and A. Dalgarno, Phys. Rev. A **49**, 982 (1994).

[82] C. Gardiner, *Handbook of Stochastic Methods: for Physics, Chemistry and the Natural Sciences* (Springer, 2004), 3rd ed.

[83] R. E. Olson, Phys. Rev. Lett. **43**, 126 (1979).

[84] F. Robicheaux, J. Phys. B **38**, 333 (2005).

[85] A. Reinhard, T. Cubel Liebisch, K. C. Younge, P. R. Berman, and G. Raithel, Phys. Rev. Lett. **100**, 123007 (2008).

[86] T. M. Weber, T. Niederprüm, T. Manthey, P. Langer, V. Guarrera, G. Barontini, and H. Ott, arXiv:1112.5118v1 (2011).

Chapter 4

Additional material

Cooling and trapping of polar molecules in a bilayer configuration using Rydberg atoms[†]

Note added: the following material is the basis of a preprint currently being written

4.1 Introduction

As an alternative way (compared to Chapter 2) to cool polar molecules with Rydberg atoms we aim to understand strong, long-range dipolar interactions between hot polar molecules and a cold gas of Rydberg atoms trapped in two separate two-dimensional layers in order to ensure collisional stability. We show that the molecular kinetic energy can be efficiently transferred from the gas of hot molecules to the cold atoms via the long-range interactions. Moreover, the spatial crystalline structure of the atoms can be used to dynamically tailor the spatial structure of the molecules, which can form atom-molecule bound states over both layer as the steady state of the cooling dynamics.

4.2 The model and energy transfer rates

The setup we have in mind is shown in Fig. 4.1: the molecular and atomic dipoles, d_M and d_A, respectively, are trapped to separate two-dimensional (2D) planes (layer separation ℓ) and polarized perpendicular to the planes, generating intra-plane dipole-dipole interactions

$$V_{AM}(r) = d_A d_M \frac{r^2 - 2\ell^2}{(r^2 + \ell^2)^{5/2}} \tag{4.1}$$

between atoms and molecules and inter-plane dipole-dipole interactions

$$V_{\sigma\sigma}(r) = \frac{d_\sigma d_\sigma}{r^3} \tag{4.2}$$

[†] The work presented in this outlook has been done in close collaboration with M. Baranov, G. Pupillo and P. Zoller. The author of the present thesis did the main calculations, in particular all atomic physics calculations and the molecular dynamics simulations.

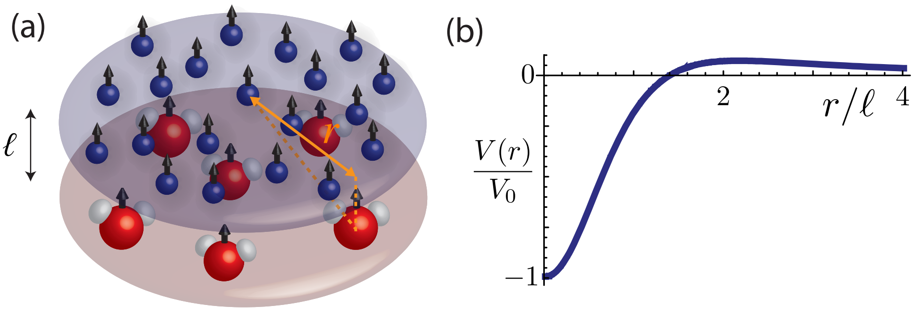

Figure 4.1. *(a) Schematics of the setup: Atoms (blue) are confined in the upper layer and interact with molecules (red and white) in the lower layer. (b) Bilayer interaction potential between atoms and molecules of Eq.* (4.1).

between two atoms ($\sigma = A$) or two molecules ($\sigma = M$) in the same layer. Here $r_{i\sigma,j\sigma'} = |\mathbf{r}_{i,A} - \mathbf{r}_{j,M}|^2$. Microscopically, interaction between atoms and molecules are induced by driving both of them with the same AC-microwave, which drives transitions between the ro-vibrational ground state $|0\rangle$ and the first excited rotational state $|1\rangle$ of the molecules and also between two Rydberg states $|r\rangle$ and $|s\rangle$, see Fig. 4.2. We choose two Rydberg states such that their energy difference approximately matches the rotational energy splitting of the molecule. This induces oscillating dipole moment d_0 and d_m in both, atoms and molecules, respectively, proportional to their transition dipole moment.

We assume that the molecules and the atoms are initially in a hot and cold gas phase, respectively. Assuming two-body collisions only, the kinetic theory of the thermal equilibration between atoms and molecules is well captured by the following quantum Boltzmann equation (BE)

$$\begin{aligned}\frac{\partial n_M(\mathbf{p})}{\partial t} = \int d\mathbf{q}\, d\mathbf{q}' d\mathbf{p}\, \Gamma_{AM}(\mathbf{q}'\mathbf{p}';\mathbf{q}\mathbf{p})\, \{n_M(\mathbf{p}')1 \pm n_A(\mathbf{q})]n_A(\mathbf{q}') - n_M(\mathbf{p})[1 \pm n_A(\mathbf{q}')]n_A(\mathbf{q})\} \\ \times(2\pi)^2\delta(\mathbf{p}+\mathbf{q}-\mathbf{p}'-\mathbf{q}')(2\pi)\delta(\epsilon_p+\epsilon_q-\epsilon_{p'}-\epsilon_{q'}),\end{aligned} \tag{4.3}$$

with $n_M(\mathbf{p})$ $[n_A(\mathbf{p})]$ the distribution function for molecules (atoms), $\Gamma_{AM}(|\mathbf{p}'-\mathbf{p}|) \propto |\tilde{V}_{AM}(|\mathbf{p}'-\mathbf{p}|)|^2$, and $\tilde{V}_{AM}(|\mathbf{q}|) = -2\pi d_A d_M |\mathbf{q}| e^{-|\mathbf{q}|\ell}$ the Fourier transform of the inter-plane interactions. We numerically solve the BE in the limit of a classical Boltzmann distribution for both species, by performing molecular dynamics simulations for up to a few hundred atoms and several tens of dipolar molecules. A characteristic result for the energy loss of a hot molecule as a function of time is shown in Fig. 4.4(left). The figure shows a rapid decay of the kinetic energy of the molecule, to a final situation where $E_{\rm kin}$ fluctuates about a small value, signaling a small finite temperature.

An analytical insight into the numerical results is obtained by approximating the scattering event as that of a fast molecule on an atom at rest, which is valid for fast-moving molecules with velocity $v_M \gg \frac{\hbar}{m_M\ell}$, with ℓ the characteristic size of the molecule-atom interaction. We estimate the average energy loss per collision by computing the differential cross section in the first order Born approximation $d\sigma/d\theta = \tilde{V}_{AM}(|\mathbf{k}|)^2/(8\pi|\mathbf{k}|)$ in the small-angle limit and by averaging over angles as

$$-\frac{dE_M}{dt} = n_A v_M \int d\theta \frac{d\sigma}{d\theta}\frac{\hbar^2 k^2}{2m_A} \simeq \frac{3\pi d_A^2 d_M^2 n_A}{2\ell^5 m_A v_M}. \tag{4.4}$$

We then obtain the following estimate for the temperature decrease as a function of time t for a

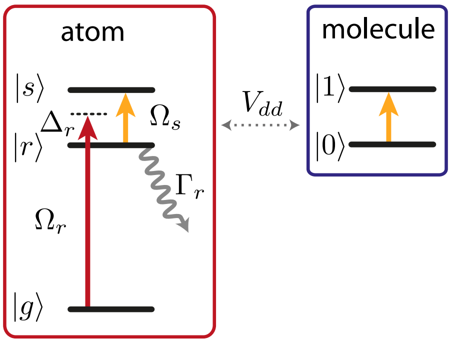

Figure 4.2. *Internal level schemes for atoms (left) and molecules (right).*

molecule scattering on a gas of (non-interacting) Rydberg atoms

$$E_M(t)/E_0 = (1-\gamma t)^{2/3}\,, \tag{4.5}$$

with

$$\gamma = \frac{9\pi}{4\sqrt{2}\hbar} n_A a_A a_M \sqrt{\frac{m_A}{m_M}} \left(\frac{\hbar^2}{m_A \ell^2}\right)^{5/2} E_0^{-3/2} \tag{4.6}$$

the energy transfer rate, where $E_0 \equiv E_M(t=0)$ is the initial energy of the molecule and $a_\nu = m_\nu d_\nu^2/(4\pi\epsilon_0\hbar^2)$ the dipolar length. We note that $\gamma \sim \ell^{-5}$ is very sensitive to the layer separation.

4.3 Implementation using Rydberg atoms and polar molecules

4.3.1 Atomic layer

Hamiltonians

The atomic setup we have in mind is shown in Fig. 4.2. The atomic ground state $|g\rangle$ is weakly coupled by a off-resonant laser light to one of the latter Rydberg states, inducing a tunable dipole moment in the atomic ground state $d_{\tilde{g}} = (\Omega_r/2\Delta_r)^2\, d_0$.

We consider a model atom consisting of a ground state $|g\rangle$ and two Rydberg states $|r\rangle$ and $|s\rangle$. The Rydberg states are coupled by a microwave field with Rabi frequency Ω_s and detuning $\Delta_s \ll \Omega_s$ from the transition $|r\rangle$-$|s\rangle$, see Chapter 3for details. This induces an oscillating dipole moment proportional to the transition dipole moment d_0. With a second laser with Rabi frequency Ω_r and large detuning $\Delta_r \gg \Omega_r$ from the $|g\rangle - |r\rangle$ transition we weakly dress the atomic ground state with the Rydberg state $|r\rangle$. This leads to effective ground state atoms $|\tilde{g}\rangle = |g\rangle + (\Omega_r/2\Delta_r)|r\rangle$ with a tunable dipole moment $d_{\tilde{g}} = (\Omega_r/2\Delta_r)d_0$. The Hamiltonian for this model atom reduces to

$$\begin{aligned} H^{(i)} =& -\Delta_r \sigma_{rr}^{(i)} - (\Delta_r + \Delta_s)\sigma_{ss}^{(i)} \\ &+ \frac{\Omega_r}{2}(\sigma_{rg}^{(i)} + \sigma_{gr}^{(i)}) + \frac{\Omega_s}{2}(\sigma_{sr}^{(i)} + \sigma_{rs}^{(i)}), \end{aligned} \tag{4.7}$$

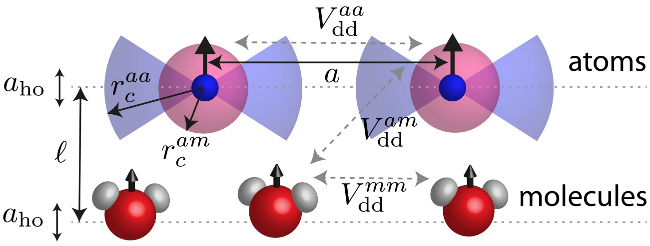

Figure 4.3. *Bilayer scheme and hierarchy of length scales*

where the operator $\sigma_{\alpha\beta}^{(i)} = |\alpha\rangle\langle\beta|$, $i \in \{1, 2\}$, and $\Delta_s = \omega_{Ls} - \omega_s$ is the detuning of the microwave laser from the $(|r\rangle - |s\rangle)$-resonance.

The interactionHamiltonian, accounting for the dipole-dipole interaction of two Rydberg-dressed atoms separated by a distance $|\mathbf{r}_i - \mathbf{r}_j|$, reduces to

$$H_{\rm int}^{(ij)} = \frac{d_0^2}{4\pi\epsilon_0}\frac{1 - 3\cos^2\vartheta}{|\mathbf{r}_i - \mathbf{r}_j|^3}\left[\sigma_{sr}^{(i)}\sigma_{rs}^{(j)} + \sigma_{rs}^{(i)}\sigma_{sr}^{(j)}\right], \tag{4.8}$$

where $\mathbf{d}_0 = \langle s|\hat{\mathbf{d}}|r\rangle$ is the transition dipole moment between the Rydberg states. With ϑ we denote the angle between the direction of polarization and the relative position of the particles. We assume a linear-polarized microwave field which aligns the dipoles of the atoms perpendicular to the plane and thus $\vartheta = \pi/2$ which ensures purely repulsive interactions.

In the case of a near resonant microwave field, i.e. $\Omega_s \gg \Delta_s$ and a far detuned dressing laser, i.e. $\Omega_r \ll \Delta_r$, we find for the energy of the potential surface which asymptotically connects to the energy of both atoms in the dressed ground state

$$E_{gg}^{aa} = \frac{2\alpha^2}{(1-\alpha^2)^4}\left(\frac{\Omega_r}{2\Delta_r}\right)^4 V(r), \tag{4.9}$$

where $\alpha = \Omega_s/2\Delta_r$ and $V(r) = d_0^2/r^3$, which is valid for distances larger than the resonant Condon point

$$r_c^{aa} = \sqrt[3]{\frac{1}{1-\alpha^2}\frac{d_0^2}{8\pi\epsilon_0\Delta_r}}. \tag{4.10}$$

derived in Chapter 3.

For an atomic density n_A with a mean inter-particle distance $a = (4/3)^{1/4}/\sqrt{n_A}$ we have the following hierarchy of length scales

$$a > r_c^{aa} > r_{\rm ryd} \qquad \text{and} \qquad \ell > a_{\rm ho}, \tag{4.11}$$

where $r_{\rm ryd} \sim a_0 n^2$ is the size of the Rydberg atom with a_0 Bohr's radius and $a_{\rm ho} = \sqrt{\hbar^2/2m\omega_\perp}$ is the harmonic oscillator length of the trap, illustrated in Fig. 4.3.

Laser cooling

In the semiclassical approximation, valid for $v_A\Gamma_e \ll \lambda$ and $2\pi/\lambda \ll \delta\mathbf{p}$ with λ and $\delta\mathbf{p}$ the laser wavelength and the momentum spread of the distribution, we can define a phase space density $u(\mathbf{r}_1, \mathbf{p}_1, \mathbf{r}_2, \mathbf{p}_2, t) = \mathrm{tr}\{W\}$, with W the two-particle Wigner function, for which we obtain a Fokker-Planck equation in the low saturation limit (derivation see Chapter 3)

$$\begin{aligned} \dot{u} &= \sum_{i=1,2}\Big[-\frac{\mathbf{p}_i}{m}\cdot\partial_{\mathbf{r}_i}u + \beta_d\hat{\mathbf{k}}_e\cdot\partial_{\mathbf{p}_i}(\mathbf{p}_i u)\cdot\hat{\mathbf{k}}_e \\ &\quad +\frac{D_d}{2}(\hat{\mathbf{k}}_e\cdot\partial_{\mathbf{p}_i})^2u + \frac{D_d}{6}\partial^2_{\mathbf{p}_i}u\Big] \\ &\quad -\mathbf{f}_{12}\cdot(\partial_{\mathbf{p}_1}-\partial_{\mathbf{p}_2})u + D_{f_{12}}[\hat{\mathbf{f}}_{12}\cdot(\partial_{\mathbf{p}_1}-\partial_{\mathbf{p}_2})]^2u \end{aligned} \tag{4.12}$$

where we defined the saturation parameter $s = \left(\frac{\Omega_e}{2}\right)^2/\left(\Delta_e^2+\left(\frac{\gamma_e}{2}\right)^2\right) \ll 1$, the damping constant $\beta_d = 2s\gamma_e\Delta_e\hbar k_e^2/\left[m\left(\Delta_e^2+\left(\frac{\gamma_e}{2}\right)^2\right)\right]$, the diffusion constants $D_d = s\gamma_e\hbar^2k_e^2$ and $D_{f_{12}} = s\gamma_e f_{12}^2/\left(\Delta_e^2+\left(\frac{\gamma_e}{2}\right)^2\right)$, and the force $\mathbf{f}_{12} = -\mathbf{f}_{21} = -\nabla_1 E_{gg}^{aa}$. Here we have neglected those terms that can be canceled when counter-propagating lasers are applied. The first two lines in Eq. (4.12) describe standard laser cooling of two independent atoms, where the damping terms and the diffusion terms accounts for cooling and heating. The third line is new, where the first two terms describe the interaction force between the two atoms and the third term is an additional cross diffusion induced by fluctuation of the force.

We use a Langevin equation to simulate the dynamics of atoms,

$$\begin{aligned} \dot{r}_{i,\alpha} &= p_{i,\alpha}/m, \\ \dot{p}_{i,\alpha} &= -\beta p_{i,\alpha} + \sum_{j\neq i} f_{ij,\alpha}(r_{ij}) + \sum_j A_{ij}E_{j,\alpha}(t) \end{aligned} \tag{4.13}$$

where $\alpha = x, y$, β is a damping constant, A_{ij} is the diffusion constant and $E_{j,\alpha}$ are the fluctuation forces with zero mean value and δ correlations in time. We assume $A_{ii} = \sqrt{D}$ and $A_{ij(i\neq j)} = \sqrt{D_{ij}}$ with D and D_{ij} the diffusion constants. In the current work, we assume $D \gg D_{ij}$, so that the diffusion caused by fluctuations of the interaction force is small. If D_{ij} and the f_{ij} are zero, Eq. (2) can be used to describe cooling of independent atoms, where an effective temperature can be defined as $T_{\text{eff}} = D/(2\beta)$. In the simulation, we first consider $E_{gg}^{aa} \sim 1/r^3$, which is the asymptotic form of the realistic potential and neglect the off-diagonal diffusion terms D_{ij} for simplicity.

Decay from Rydberg states - lifetime

The tuneability of the interaction strength, c.f. Eq. (4.9) comes with the price of a finite lifetime of the dressed ground state atoms $\Gamma_{\tilde{g}} = (\Omega_r/2\Delta_r)\Gamma_r$. Population of intermediate states after spontaneous emission from the Rydberg states will lead to particle loss and heating which strongly depends on the atomic density. For a maximum density of $n_A \lesssim 1/(r_c^{aa})^2$ the half-life was estimated about $\tau_{\tilde{g}} = \Gamma_{\tilde{g}}^{-1}$, which can be strongly increased by reducing the density and active laser cooling of the atoms.

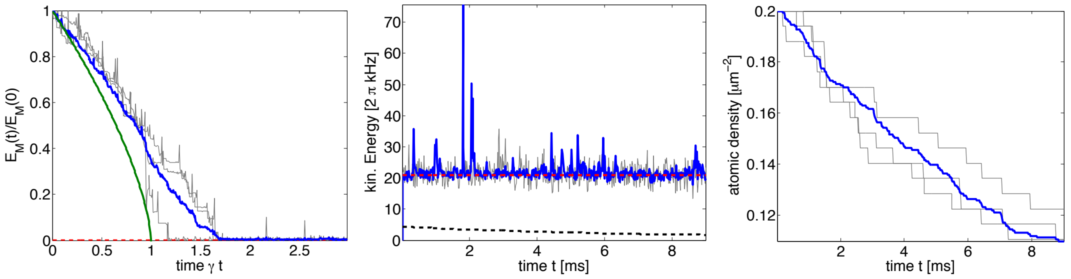

Figure 4.4. *(left) kinetic energy of the molecule: Blue line is the average over 50 runs of simulations. Thin black line is a single trajectory. Green line is the analytic result for non-interacting atoms neglecting decay from the Rydberg states. (middle) atomic energy: Blue line is the average over 50 runs of simulations. Thin black line is a single trajectory. Red-dashed line is the Doppler-temperature* T_D *and black-dashed line is the melting temperature* $T_{\rm melt}$. *(right) Atomic density: Blue line is the average over 50 runs of simulations. Thin black line is a single trajectory.*

4.3.2 Atom-Molecule interaction:

Our starting point is the following model Hamiltonian for two species of dipoles d_A and d_M confined to parallel planes separated by a distance ℓ

$$H = T_A + T_M + \sum_{i,j;\sigma\neq\sigma'} \frac{d_\sigma d_{\sigma'}(|\mathbf{r}_{i,\sigma}-\mathbf{r}_{j,\sigma'}|^2 - 2\ell^2)}{(|\mathbf{r}_{i,\sigma}-\mathbf{r}_{j,\sigma'}|^2+\ell^2)^{5/2}}. \tag{4.14}$$

Here $T_\sigma = \sum_i \mathbf{p}_{i,\sigma}^2/2m_\sigma$ is the kinetic energy Hamiltonian with $\mathbf{p}_{i,\sigma}$ ($\mathbf{r}_{i,\sigma}$) the momentum (position) of the ith-dipole in the plane ($\sigma = A, M$). The latter interaction is valid for distances larger than the atom-molecules Condon point (c.f. Fig. 4.3)

$$r_c^{am} = \sqrt[3]{\frac{d_0 d_m}{4\pi\epsilon_0\Delta_r}}, \tag{4.15}$$

which must be smaller than the interlayer separation, i.e. $r_c^{am} < \ell$.

In order to get insight into the scaling we approximate $\ell \sim r_c^{am}$ and $\sqrt{n_A} \sim 1/r_c^{aa}$ and find

$$\gamma < \frac{9\pi}{16} 2^{1/6}(4\pi\epsilon_0)^{1/3} \frac{d_M^{1/3}}{d_r} \frac{\Omega_r^4}{\Delta_r^{5/3}} \frac{\sqrt{m_M}}{m_A} E_0^{-3/2}. \tag{4.16}$$

It is worth noticing that $\gamma \sim 1/d_r$ which comes from the fact that increasing d_r increases the layer separation required and decreases the maximum atomic density allowed. Since $d_r \sim ea_0n^2$ it is favorable to use states with a low principal n quantum number in order to have a large energy transfer rate. The inverse is true regarding the lifetime of the atomic layer which is proportional to the lifetime of the chosen Rydberg state, i.e. $\tau_{\tilde{g}} \sim n^3$. We therefore have to tradeoff between $1/\gamma \sim n^2 < \tau_{\tilde{g}} \sim n^3$ in order to cool the molecules faster than the lifetime of the atomic layer.

4.4 Simulation results

4.4.1 Numbers

We perform a semi-classical molecular dynamics simulation for 67 atoms and one molecule in a box with hard walls. The atomic density is $n_A = 2 \cdot 10^{11}/\mathrm{m}^2$, which corresponds to a mean inter particle separation of $a = (4/3)^{1/4}/\sqrt{n_A} = 2.4\,\mu\mathrm{m}$. The size of the Rydberg atom for $n = 50$ is $r_{\mathrm{ryd}} = 3/2a_0n^2 = 200$ nm. As an example we consider Rubidium atoms and use the Rydberg states 49p and 50s, which have a transition dipole moment of $d_0 = 5.9$ kD. The latter is coupled to the ground state using a laser with Rabi frequency $\Omega_r/2\pi = 100$ MHz and detuning $\Delta_r/2\pi = 500$ MHz. For $\alpha = 0.45$ ($\Omega_{\mathrm{MW}}/2\pi = 450$ MHz) we obtain dressed ground state atoms with a dipole moment of $d_{\tilde{g}} = 60$ D and a lifetime of $\tau_{\tilde{g}} = 6.3$ ms. The resonant Condon point for the atom-atom interaction is $r_c^{aa} = 1.9\,\mu$m and the melting temperature $T_{\mathrm{melt.}} = 0.2\,\mu$K. The atoms are therefore in a gas phase. We take into account decay from the Rydberg states including spontaneous emission and blackbody radiation for $T = 300$ K.

For the model molecule we assume a dipole moment of $d_m = 2.5$ D and a mass of $m_M = 100$ amu. For a layer separation of $\ell = 400$ nm and an initial energy of $E_0 = 240\,\mu$K this results in a cooling rate of $\gamma^{-1} = 3.1$ ms and an atom-molecule Condon radius of $r_c^{am} = 165.4$ nm. The atoms are confined by an harmonic potential with $\omega_\perp/2\pi = 30$ kHz resulting in a saddle-point energy barrier of $V_{\mathrm{sp}} = 31.65\,\mu$K and a critical loss radius of $r_{\mathrm{crit.}} = 1\,\mu$m. Atoms which get closer than this distance are lost. The harmonic oscillator length is $a_{\mathrm{ho}} = 44$ nm. We perform active laser cooling on the atoms with a cooling rate $\beta/2\pi = 50$ kHz and a diffusion rate D such that the resulting Doppler temperature is $k_BT_D = D/2\beta = k_B\,1\,\mu$K.

4.4.2 Results

Fig. 4.4(left) shows the molecular kinetic energy averaged over 50 runs of simulations as a function of time for the parameters discussed above. The green line is the analytic result of Eq. (4.5). The time to cool the molecules in the simulation takes longer by a factor of ~ 1.7 due to atom-atom interactions and the loss of particles, which results in a time-dependent cooling rate γ. The loss of particles is shown in Fig. 4.4(right): After the time $\tau_{\tilde{g}} = 6.3$ ms approximately 35 % of the atoms are lost. Fig.4.4(middle) show the mean kinetic energy averaged over the 67 particles of the simulation as a function of time. The red-dashed line corresponds to the Doppler temperature T_D, while the black-dashed line is the melting temperature of the atomic crystal. Since, $T_D > T_{\mathrm{melt.}}$ the atoms are in a gas phase.

4.4.3 Atom - molecule bound states

Due to the attractive part of the inter-layer interaction of Eq. (4.14) there is the possibility that the molecule gets trapped and forms a quasi-bound state together with the atom over both layers, illustrated in Fig. 4.5. The potential is given by

$$V_{\mathrm{bound}}(\rho)/V_0 \approx 3\left(\frac{\rho}{\ell}\right)^2 - 1, \quad \text{with} \quad V_0 = \frac{d_{\tilde{g}}d_M}{2\pi\epsilon_0\ell_0^3}, \tag{4.17}$$

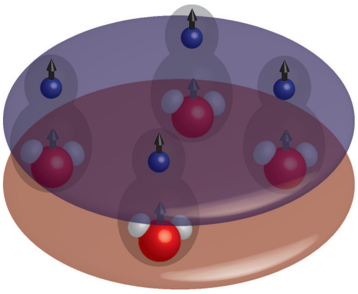

Figure 4.5. *Illustration of an atom-molecule bound states*

which is in lowest order quadratic with a frequency of $\omega_{\text{bound}} = \sqrt{6V_0/m\ell_0^2}$. The potential has a zero-crossing at $\rho_0 = \sqrt{2}\ell$ and a maximum at $\rho_{\text{max}} = 2\ell$, with $V(\rho_{\text{max}}) = 2V_0/25\sqrt{5} \approx 0.04V_0$.

For the parameters discussed above we find $V_0 = 33.9\,\mu\text{K} > T_D$, which is smaller than the final equilibrium temperature of the molecules and $\omega_{\text{bound}} = 2\pi \times 50$ kHz $= 2.5\,\mu$K.

Part II

Quantum computation with Rydberg ions

CHAPTER 5

PUBLICATION

Parallel execution of quantum gates in a long linear ion chain via Rydberg mode shaping[†]

Phys. Rev. A **87**, 052304, (2013)

Weibin Li[1], Alexander. W. Glaetzle[2], Rejish Nath[2], Igor Lesanovsky[1]

[1]*School of Physics and Astronomy, The University of Nottingham, Nottingham, NG7 2RD, United Kingdom*

[2]*Institute for Theoretical Physics, University of Innsbruck,*
and Institute for Quantum Optics and Quantum Information of the Austrian Academy of Sciences,
A-6020 Innsbruck, Austria

We present a mechanism that permits the parallel execution of multiple quantum gate operations within a single long linear ion chain. Our approach is based on large coherent forces that occur when ions are electronically excited to long-lived Rydberg states. The presence of Rydberg ions drastically affects the vibrational mode structure of the ion crystal, giving rise to modes that are spatially localized on isolated subcrystals which can be individually and independently manipulated. We theoretically discuss this Rydberg mode shaping in an experimentally realistic setup and illustrate its power by analyzing the fidelity of two conditional phase flip gates executed in parallel. The ability to dynamically shape vibrational modes on the single-ion level might find applications in quantum simulators and quantum computation architectures.

5.1 Introduction

The ability to execute multiple quantum operations in parallel is believed to be a fundamental requirement for achieving large-scale quantum computation [1–3]. Among the many types of systems being considered for the physical implementation of a quantum processor [4], trapped ions have attracted much attention for the astonishingly high degree of experimental control that can be gained

---

[†] The author of the present thesis contributed to this publication through discussions on the derivation and interpretation of the results, in particular on the microwave coupling scheme. The detailed derivations and numerical calculations have been performed by WL and IL.

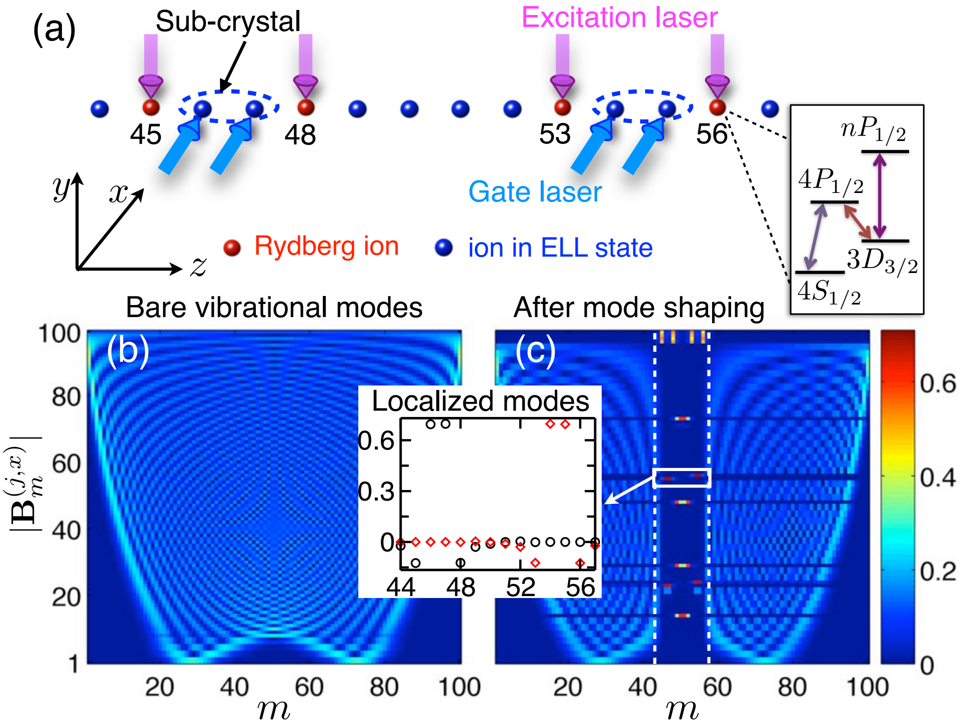

Figure 5.1. *(Color online) (a) Level structure of Ca$^+$ and schematics of the envisioned setup. Red and blue symbols refer to ions in Rydberg states and ions in electronically low-lying (ELL) states, respectively. subcrystals of ion pairs are isolated within a linear crystal formed by 100 ions by the excitation of selected ions to the Rydberg $nP_{1/2}$ state (here the 45th, 48th and 53rd, 56th). Using laser-induced spin-dependent forces, quantum gates can be executed on the two subcrystals in parallel. (b) Vibrational modes of a crystal formed by 100 ions in ELL states. Depicted is the modulus of the normal mode matrix $\mathbf{B}_m^{(j,x)}$ where j (m) refers to the mode (ion) index (see text for further detail). (c) Vibrational modes in the presence of four Rydberg ions. The white dashed lines delimit the region corresponding to the ions that are shown in panel (a). The Rydberg ions drastically reshape the vibrational mode structure, leading to the emergence of modes that are localized on the two subcrystals (see inset).*

over their internal and external degrees of freedom [3]. One strategy for achieving parallelism is to build many local quantum processors. Current proposals envision setups where ions are confined in spatially separated wells provided by arrays of microtraps [5] or by traps with segmented electric field electrodes [6]. Few ions trapped within a given well form one of many local quantum processors that can be operated independently and in parallel [7]. Information can be exchanged among different local processors by rearranging the potential landscape such that previously disconnected ions have common vibrational modes. Such rearrangement is usually achieved by switching voltages applied to the ion trap electrodes [6]. In spite of the availability of microstructured arrays it remains a challenge to obtain fast switching times and a high spatial resolution of the local electric fields that would grant a manipulation of the potential landscape down to the level of a single ion.

In this work we introduce a scheme that permits the execution of multiple quantum gates in parallel on a long linear ion crystal. The method relies on the shaping of the vibrational crystal modes through the laser excitation of selected ions into electronically excited Rydberg states. Strong coherent forces acting on these excited ions [8, 9] effectively break the long crystal into small subcrystals in the sense that vibrational modes emerge which are strongly localized on only a few ions. We illustrate the power of this Rydberg mode shaping by thoroughly analyzing the fidelity of two two-qubit conditional phase flip (CPF) gates that are executed in parallel on different subcrystals belonging to the same ion chain. A feature of our scheme is that decoupling between the localized modes and the remaining spectator modes permits us not only to achieve a high gate fidelity but also to drastically reduce the complexity of gate optimization protocols [10–12]. In view of the intrinsic stability of ion crystals [13], the ability to address single ions individually by lasers [14] and the long lifetime of Rydberg states, we believe that this dynamical mode shaping is particularly useful in digital quantum simulations [15] as these strongly benefit from the availability of robust parallelization approaches.

5.2 Setup and idea

Before providing details let us briefly outline the setup we have in mind. We consider a long linear crystal of 100 $^{40}\mathrm{Ca}^+$ ions which is realized within a quartic electric potential (see details below). This choice is motivated by the proposal discussed in Ref. [13], which envisages the implementation of an ion quantum processor where a long ion chain is divided into two parts: Quantum computation is carried out in the central region where ions are nearly uniformly spaced. The remaining outer ions are continuously Doppler cooled to prevent heating. To describe the internal structure of the ions we consider the four states depicted in Fig. 5.1(a). The electronically low-lying (ELL) S, P, and D states are employed in numerous ion trap experiments for the storage, manipulation, and read-out of quantum information [3]. Furthermore, we consider the Rydberg state nP_J (with $J = 1/2$ and the principal quantum number n) which is excited from the $3D_{3/2}$ state via a single photon transition [14, 16].

We envisage Rydberg excitations to be carried out in the central region of the ion chain and in Fig. 5.1(a) we illustrate a situation where four Rydberg ions enclose two pairs of ions in ELL states. Those ion pairs will form the subcrystals on which we are going to execute quantum gates in parallel. The underlying physical mechanism which we aim to exploit for this purpose becomes apparent in Figs. 5.1(b) and (c). Here we show the absolute values of the normal mode matrix of the vibrational crystal modes which provide a measure on how much each ion contributes to a vibrational mode. In Fig. 5.1(b), which shows the case in which all ions are in ELL states, we see that, in general, many ions contribute to each normal mode. Compared to this, the presence of Rydberg ions leads to a drastic change of the mode structure as can be seen in Fig. 5.1(c). The reason is rooted in the large polarizability $\mathcal{P}_{nP}$ of Rydberg states [9], which modifies the local trapping potential, leading essentially to a constriction of the ion chain at positions where Rydberg ions are excited. The selective Rydberg ion excitation thus creates localized modes, primarily occupying the two isolated subcrystals composed by ions in ELL states. This Rydberg mode shaping permits the parallel execution of quantum gates on the two subcrystals. This is similar in spirit to the idea underlying segmented ion traps [17, 18]. The advantage of our approach is that due to the availability of single ion laser addressing it fundamentally permits the control of the potential landscape on the smallest achievable length scale, namely on the level of single ions.

5.3 Implementation

5.3.1 A long linear ion crystal

Let us now provide a more detailed discussion of the practical implementation of the above idea. To achieve a long ion crystal we consider an ion trap formed by the time-dependent electric potential:

$$\Phi(\mathbf{r},t) = \Phi_{\mathrm{rf}}(\mathbf{r},t) + \Phi_{\mathrm{st}}(\mathbf{r}). \tag{5.1}$$

Here

$$\Phi_{\mathrm{rf}}(\mathbf{r},t) = \alpha \cos \Omega t (x^2 - y^2) \tag{5.2}$$

is the potential of a radio-frequency (rf) field with gradient α and frequency Ω and

$$\Phi_{\mathrm{st}}(\mathbf{r}) = \beta_2 \frac{2z^2 - r^2}{2} + \beta_4 \left[z^4 - 3z^2 r^2 + \frac{3}{8} r^4 \right], \tag{5.3}$$

with $r^2 = x^2 + y^2$, is a quartic static electric potential whose parameters β_j $(j = 2, 4)$ depend on the specifics of the field-generating electrodes, i.e., the gradient and higher derivatives of the field. Recently, similar potentials have been realized experimentally [17, 18]. For a sufficiently fast rf frequency drive [19] an ion of mass M experiences the ponderomotive potential

$$V_{\mathrm{p}}(\mathbf{r}) = e \left[\frac{e\alpha^2}{M\Omega^2} r^2 + \Phi_{\mathrm{st}}(\mathbf{r}) \right]. \tag{5.4}$$

Within this trap an ion chain is formed along the z axis provided that $\alpha \gg \{|\beta_2|, \beta_4 l_s^2\} > 0$ $(\beta_2 < 0)$. Here $l_s = [e/(8\pi\epsilon_0|\beta_2|)]^{1/3}$ is the typical length scale associated with $V_{\mathrm{p}}(\mathbf{r})$ and e and ϵ_0 are the elementary charge and the vacuum permittivity, respectively. In addition, the tuning of the parameters β_2 and β_4 permits us to achieve a long ion crystal in which the equilibrium positions of ions in ELL states are approximately evenly spaced [13]. The equilibrium positions of the long ion crystal is determined by a parameter $k_4 = 2\beta_4 l_s^2/|\beta_2|$. In the following we set $k_4 = 1.343$ as this choice minimizes fluctuations of the nearest-neighbor separation within the central region of the ion chain [13].

In Ref. [9] we showed that ions excited to the $nP_{1/2}$-Rydberg state experience not only the ponderomotive potential but are also subject to an additional radial potential that is proportional to the Rydberg polarizability $V_{\mathrm{a}}(\mathbf{r}) \approx -e^2\alpha^2\mathcal{P}_{nP}r^2$, where $\mathcal{P}_{nP} \approx -0.25 \times n^7$ (in atomic units). There are also small corrections to the trapping potential along the z axis but those are negligible in this linear ion trap. The ratio of the radial trap frequencies experienced by an ion in the Rydberg/ELL state is approximately given by

$$\frac{\omega_{\mathrm{Ryd}}}{\omega_{\mathrm{ELL}}} = \sqrt{1 - M\Omega^2\mathcal{P}_{nP}} \tag{5.5}$$

In practice, ratios on the order of 2 and larger can be achieved. In the following we show that this is already sufficient for a Rydberg ion to effectively introduce a constriction of the linear ion chain which strongly affects the vibrational mode structure. Note, that such state-dependent trap frequency change has also been theoretically reported for Rydberg atoms in inhomogeneous magnetic fields [20].

5.3.2 Collective modes and mode shaping

Let us now demonstrate the mode shaping considering the transverse phonon modes along the x axis as an example. The treatment of the y phonons is done accordingly. The phonon Hamiltonian is [7] $H_\mathrm{v} = \sum_{j=1}^{N} \hbar\omega_j (b_j^\dagger b_j + 1/2)$. Here $b_j^\dagger$ (b_j) is the creation (annihilation) operator of the jth phonon, whose frequency ω_j is calculated by diagonalizing the Hessian matrix $[\sum_m \mathcal{H}_{mn} \mathbf{B}_m^{(j,x)} = (\omega_j/\omega_s)^2 \mathbf{B}_n^{(j,x)}]$ with

$$\mathcal{H}_{mn} = \begin{cases} \left[\frac{\omega_m^{(x)}}{\omega_s}\right]^2 + \frac{1}{2} - \frac{3k_4}{2} z_m^2 - \sum\limits_{k\neq m}^{N} \frac{1}{|z_k - z_m|^3}, & n = m \\ \frac{1}{|z_m - z_n|^3}, & n \neq m \end{cases}$$

and $\mathbf{B}_m^{(j,x)}$ denoting the eigenvectors. The parameters z_m are the z component of the equilibrium position of the mth ion and $\omega_m^{(x)}$ is the state-dependent trapping frequency of the mth ion along the x axis; i.e., $\omega_m^{(x)} = \omega_\mathrm{Ryd}(\omega_\mathrm{ELL})$ if the ion is in the Rydberg (ELL) state. For convenience, we have defined a reference frequency $\omega_s = \sqrt{2e|\beta_2|/M}$ and scaled length with l_s such that the Hessian is dimensionless.

We start with a simple situation where in our chain of 100 ions the 45th and 56th are excited to the Rydberg state. The resulting change of the mode structure becomes directly apparent in the modulus of $\mathbf{B}_m^{(j,x)}$ which is depicted in Fig. 5.2(a). Compared to the situation without mode shaping [Fig. 5.1(b)], the striking difference is that the 46th to 55th ions constitute a virtually isolated subcrystal hosting a series of *spatially localized modes*. The energies of these local modes are shown in Fig. 5.2(b) where we also undertake a comparison to the mode energies obtained by considering exclusively the subcrystal, i.e., a truncated linear crystal composed of only 10 ions. Note, that although we are considering here a case in which the subcrystal ions are symmetrically positioned around the center of the ion crystal, our observations remain true also in asymmetric situations. To effectively create subcrystals with localized modes we require that $(\omega_\mathrm{Ryd}/\omega_s)^2 \gg \max(\mathcal{H}_{mn})$ $(m \neq n)$ with $\max(\mathcal{H}_{mn})$ being the maximum of the off-diagonal matrix elements of the Hessian. This condition means that the energy of vibrational modes to which Rydberg ions participate significantly is much larger than the energy of the collective modes of ions in ELL states.

5.3.3 Parallel conditional phase gates

Let us return to this initial example in which we had two subcrystals composed by the ion pairs $\{46, 47\}$ and $\{54, 55\}$. Each of the subcrystals hosts two localized vibrational modes. The eigenvector corresponding to the localized mode with higher energy is displayed in the inset of Fig. 5.1(c). In the following we show that with these local modes, we can execute two two-qubit gates in parallel. Specifically, we discuss a σ^z-type [24] two-qubit CPF gate. Qubits are encoded in two ELL states of an ion, denoted by $|\uparrow\rangle$ and $|\downarrow\rangle$. These can be hyperfine states as discussed in Refs. [25, 26] or states coupled by optical quadrupole transitions as, e.g., in Ref. [27]. The CPF gate is implemented by a laser-induced coupling [see gate lasers in Fig. 5.1(a)] between the qubit states and the vibrational crystal modes/phonons. This results in a "spin-dependent" force [25–27] whose action is described by the spin-phonon Hamiltonian [11, 28]

$$H_\mathrm{I} = \sum_{m,j=1}^{N} \hbar\Omega_m(t)\sigma_m^z \eta^{(j)} \mathbf{B}_m^{(j,x)} (b_j^\dagger e^{i\omega_j t} + \mathrm{h.c.}). \tag{5.6}$$

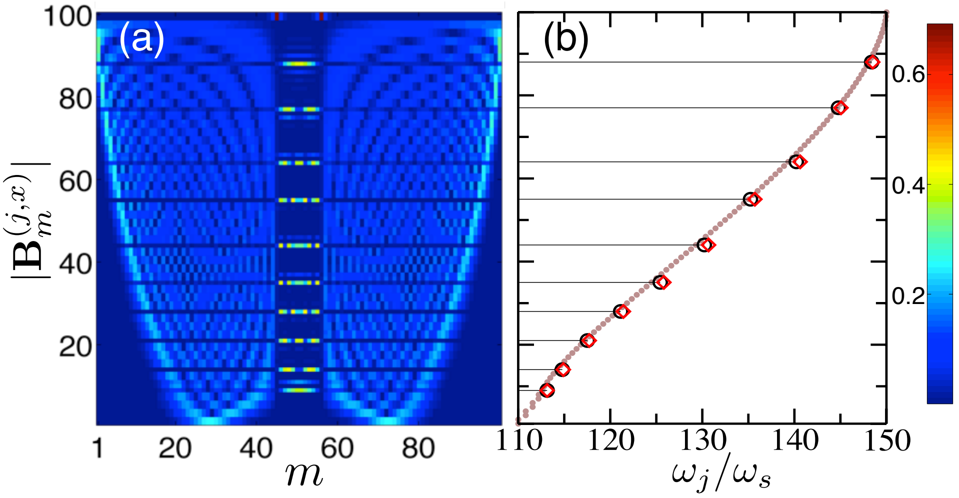

Figure 5.2. *(Color online) (a) Modulus of the eigenvector* $\mathbf{B}_m^{(j,x)}$ *when ions 45 and 56 are in the Rydberg state. Localized modes reside on ions in ELL states forming the subcrystal delimited by the two Rydberg ions. Panel (b) shows the corresponding eigenenergy of the localized modes obtained from the full (circles) and truncated (diamonds) calculations. The largest discrepancy between these calculations is about* 0.3%*. The dots show the (quasi continuous) energy spectrum of the ion chain without mode shaping. In all the calculations we use* $\omega_{\mathrm{ELL}}/\omega_s = 150$ *and* $\omega_{\mathrm{Ryd}}/\omega_s = 198.5$.

Here $\Omega_m(t)$ is the time-dependent Rabi frequency of the gate laser that addresses the mth ion and $\eta^{(j)} = k_{\mathrm{L}}\, l_j$ is the corresponding Lamb-Dicke parameter, with k_{L} being the modulus of the laser wave vector and $l_j = \sqrt{\hbar/2M\omega_j}$ being the oscillator length associated with the jth phonon mode. The CPF gate is conducted by switching the gate lasers on for a given time τ during which the Rabi frequencies $\Omega_m(t)$ are varied. Using the Magnus formula [29], the evolution operator due to H_{I} is then given by

$$U(\tau) = \exp\left[i\sum_m Q_m(\tau)\sigma_m^z + i\sum_{mn}\phi_{mn}(\tau)\sigma_m^z\sigma_n^z\right]. \tag{5.7}$$

The first term in the exponential characterizes the residual coupling of the mth qubit with the phonon modes and depends on $Q_m(\tau) = \sum_j[\alpha_m^{(j)}(\tau)b_j^\dagger + \text{h.c.}]$, where $\alpha_m^{(j)}(\tau)$ is a parameter that characterizes the coupling strength. The second term gives rise to a phonon-induced spin-spin coupling between the mth and nth qubit, thereby effectuating a CPF gate. A perfect CPF gate is realized when $\phi_{mn}(\tau) = \pi/8$ and $\alpha_m^{(j)}(\tau) = 0$. As shown in Refs. [10–12] this can be achieved via optimizing the time-dependent profile of the Rabi frequencies $\Omega_m(t)$. Such optimization is challenging since, in general, many phonon modes contribute even when only a single CPF gate operation is conducted within a long ion chain. Rydberg mode shaping has the potential to drastically reduce the complexity of such optimization procedure as even in long crystals only few vibrational modes actually couple to the qubit ions located on a subcrystal.

Let us now analyze the performance of two CPF gates that are executed in parallel on the two subcrystals depicted in Fig. 5.1(a). To assess the performance of the gate operation, we use the high-energy mode [inset of Fig. 5.1(c)] as "quantum bus". The gate lasers are switched on for a time $\tau = 8\tau_{\mathrm{b}}$, where $\tau_{\mathrm{b}} = 2\pi/\omega_{\mathrm{b}}$ is the oscillation period of the bus mode and the Rabi frequency is assumed to follow $\Omega_m(t) = \Omega_0 \sin(\nu t)$ (as also discussed in Ref. [26]). We optimize the fidelity with respect to the parameter ν of this simple ansatz. Imposing a two-qubit phase shift $\phi_{mn}(\tau) = \pi/8$ fixes the value of the amplitude Ω_0 (for more detail see Ref. [28]). The qubits are prepared in a product state,

$$|\Psi(0)\rangle = (|\psi_{m_1}\rangle \otimes |\psi_{n_1}\rangle) \otimes (|\psi_{m_2}\rangle \otimes |\psi_{n_2}\rangle)\,, \tag{5.8}$$

with $|\psi_m\rangle = (|\uparrow_m\rangle + |\downarrow_m\rangle)/\sqrt{2}$ and $\{m_j, n_j\}$ being indices of ions forming the jth subcrystal. Ideally, the output state after the parallel execution of the two CPF gates is

$$|\Psi(\tau)\rangle = \exp[i\frac{\pi}{4}(\sigma^z_{m_1}\sigma^z_{n_1} + \sigma^z_{m_2}\sigma^z_{n_2})]|\Psi(0)\rangle. \tag{5.9}$$

However, due to the residual phonon-qubit coupling this state will be only reached with a certain probability, which we characterize through the fidelity

$$F = \langle\Psi(\tau)|\mathrm{Tr}_{\mathrm{v}}\rho(\tau)|\Psi(\tau)\rangle \tag{5.10}$$

Here, $\rho(t) = U(t)\rho(0)U^\dagger(t)$, with $\rho(0) = \rho_{\mathrm{v}}\otimes|\Psi(0)\rangle\langle\Psi(0)|$ and Tr_{v} denotes the trace over the vibrational modes whose density matrix is ρ_{v}. For calculating the fidelity we assume the following sequence: The ions are initially in ELL states and the phonon density matrix ρ_{v} is a thermal distribution. Rydberg ions are subsequently excited via protocol that is highly nonadiabatic with respect to the phonons; i.e., the phonon density matrix is unchanged. In Appendix 5.A we provide more detail on such protocol. The gate fidelity is then calculated via a transformation that expresses ρ_{v} in terms of the shaped vibrational modes [9]. The exact details of the calculation are provided in Appendix 5.B.

Let us first consider a situation in which the two CPF gates start simultaneously. We find that the highest achievable fidelity within our simple ansatz is $F_{\max} \approx 99.95\%$. As shown in Fig. 5.3(a), this maximum occurs at $\nu\tau = 2\pi \times K$ (with K an integer). At these points the bus modes almost entirely return to their initial states [11, 30]. The fact that such a high fidelity is achievable within this simple ansatz is a direct consequence of the fact that the Rydberg ions delimiting the subcrystal lead to a dramatic reduction of the number of vibrational modes that couple to the qubit ions. This reduction is clearly shown by the data presented in Fig. 5.3(a). Without this Rydberg mode shaping the highest fidelity that we can achieve is 93%.

The power of the mode shaping becomes even more apparent when introducing a start time delay t_{d} of the second CPF gate with respect to the first one. $F_{\max}$ slightly decreases with growing t_{d} but always remains above 98%, as shown in Fig. 5.3(b). This demonstrates that the two CPF gates can be operated essentially independently. In the absence of mode shaping, however, $F_{\max}$ quickly drops with increasing t_{d} reaching a minimal value of $\approx 36.1\%$.

Finally, let us discuss additional sources that would influence the gate fidelity. First, the fidelity will be, in principle, reduced by the radiative decay of the Rydberg state. This is mitigated by the fact that CPF gates are inherently fast [28] and that Rydberg states are long lived. For example, choosing the $60P_{1/2}$ state, we obtain a Rydberg lifetime $\approx$ 270 μs and with the trap parameters $\alpha = 7 \times 10^8$ V/m^2, $\Omega = 2\pi \times 25.2$ MHz, and $\beta_2 = -2.09 \times 10^3$ V/m^2 we obtain a gate time $\tau \approx 3.7$ μs. Taking into account the Rydberg excitation time, the gate fidelity will be modified by an overall factor, about $0.982^{N_{\mathrm{Ryd}}}$, with N_{Ryd} the number of Rydberg ions that are excited during the gate operation. However, in principle, the gate operations can be accelerated by using a more sophisticated optimization protocol [13], and furthermore, optimized gate schemes can be imagined in which the Rydberg ions do not stay permanently excited. Second, infidelities are caused by other factors, such

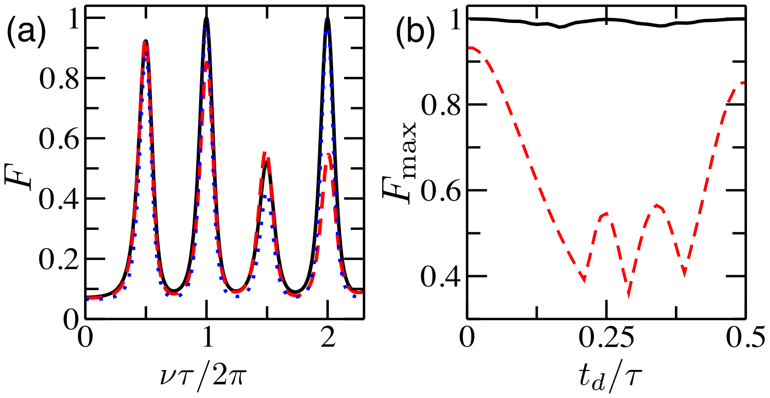

Figure 5.3. *(Color online) (a) Fidelity of the two CPF gates. The solid (dotted) curve is the result calculated using all (only the four localized) modes. The dashed curve corresponds to the gate fidelity without mode shaping, where the bus mode is the highest energy mode [Fig. 5.2(b)], whose average phonon number is* 3.25*. In the calculations, we assume that all phonon modes when the ions are in the ELL states have the same temperature. (b) Maximal fidelity vs. delay time.* $F_{\max}$ *is found by maximizing the fidelity over* ν *within the range shown in (a). The solid (dashed) curve stands for the calculation with (without) mode shaping.*

as the anharmonicity of the ionic motion and corrections beyond the Lamb-Dicke limit. These have been investigated in detail by Lin *et al.* in Ref. [13] and their contributions have been found to be marginal.

5.4 Summary and outlook

In conclusion, we showed that the transverse vibrational modes of a linear ion chain can be shaped by the selective excitation of Rydberg ions leading to the emergence of strongly localized modes. This Rydberg mode shaping can potentially be applied for implementing quantum simulation and processing schemes within a single large (possibly three-dimensional) ion crystal. One can envisage a scheme where dedicated ions are not used as qubits but only for segmenting the crystal. When excited they give rise to local modes that permit the parallel manipulation of sets of qubits. When deexcited the nonlocal character of the vibrational modes is restored permitting the entanglement of more distant qubits.

A drawback of the current scheme is that the gate execution follows the Rydberg excitation. This means that Rydberg ions are excited throughout the entire duration of the gate sequence which consequently leads to a reduced fidelity. A future goal is therefore to devise optimized control sequences which reduce the Rydberg excitation time but at the same time make use of the existence of localized modes. In addition, the Rydberg mode shaping is particularly applicable for parallel execution of multiple quantum gates with the Mølmer-Sørensen scheme [30]. If, instead, the gate is based on the Cirac-Zoller scheme [31], where phonons need to be cooled to the ground state initially, the consequent gate error will be severe as phonons can be significantly excited after the Rydberg excitation (see Appendix 5.B).

Acknowledgment

We thank Peter Zoller for initial discussions which stimulated this work. We thank C. Ates and S. Genway for careful reading of the manuscript. Discussions with all members of the R-ION consortium are kindly acknowledged. This work is funded through EPSRC and the ERA-NET CHIST-ERA (R-ION consortium).

5.A Excitation of Rydberg ions

For the practical application of the mode shaping it is crucial to excite ions to the Rydberg state with high fidelity, which can be a challenge if the trapping potentials of ELL and Rydberg states are very different: In general, the (reduced) density matrix of the ion to be excited is given by $|3D_{3/2}\rangle\langle 3D_{3/2}| \otimes \rho_D$, where ρ_D is the density matrix of the external degrees of freedom. The Rydberg excitation needs to take the ion to the state $|nP_{1/2}\rangle\langle nP_{1/2}| \otimes \rho_P$ as the shaped modes are only present if the electronic population of the ion is entirely transferred to $|nP_{1/2}\rangle$. Note that the density matrix of the external degrees of freedom can, in general, change during the excitation process, e.g., due to nontrivial Franck-Condon factors which arise from the different potential shapes in low-lying and Rydberg states [9]. There are a number of strategies to perform the transfer with high fidelity: For example, one can cool all phonon modes to the ground state, such that the initial state ρ_D is precisely known. The excitation laser pulse (frequency, strength, and duration) can then be optimized to achieve perfect electronic state transfer. Alternatively, one can use a broad band laser excitation that does not resolve the individual phonon modes [32] and thus performs the transfer independently of the phonon state. Both methods, however, are rather challenging with current technology [14, 16, 19]. A currently feasible alternative is to remove the difference in the trapping potentials during the excitation process by altering the polarizability of Rydberg states through the application of a microwave field (MW), which creates dressed states of tuneable polarizability. The Rydberg excitation is then no longer different than the excitation of ELL states. After the excitation has been carried out the MW is switched off in a way that is adiabatic on electronic timescales but can be highly non adiabatic on the timescale of the phonon dynamics.

The scheme works as follows. Together with Rydberg laser, we apply a MW field that couples the Rydberg $|nP_{3/2}(1/2)\rangle$ (denoted by $|P\rangle$) with a nearby s-state $|n'S_{1/2}(1/2)\rangle$ (denoted by $|S\rangle$). The corresponding ion-field interaction is given by

$$V(t) = -eE_0 \cos\omega_0 t\, z - eE_1 \cos\omega_1 t\, z, \tag{5.11}$$

where E_0 (E_1) is the laser (MW) electric field and ω_0 (ω_1) is the Rydberg laser (MW) frequency. Both the Rydberg laser and the MW field are linearly polarized along the z axis. The field-free Rydberg energies are ϵ_S and ϵ_P, respectively. To be concrete we also assume $\epsilon_S < \epsilon_P$. To proceed, it is convenient to transform into the interaction picture. Using the unitary operator $U_\mathrm{i} = |D\rangle\langle D| + e^{i\omega_0 t}|P\rangle\langle P| + e^{i(\omega_0-\omega_1)t}|S\rangle\langle S|$ and in rotating-wave approximation, we obtain the Hamiltonian ($\hbar = 1$)

$$\begin{aligned} H &= \Delta_S|S\rangle\langle S| + \Delta_P|P\rangle\langle P| + H_\mathrm{L}, \qquad (5.12)\\ H_\mathrm{L} &= \frac{\Omega_\mathrm{L}}{2}(|P\rangle\langle D| + h.c) + \frac{\Omega_\mathrm{MW}}{2}(|S\rangle\langle P| + h.c.), \end{aligned}$$

where $\Delta_S = \epsilon_S - (\omega_0 - \omega_1)$ and $\Delta_P = \epsilon_P - \omega_0$. $\Omega_\mathrm{L} = -eE_0\langle P|z|D\rangle$ and $\Omega_\mathrm{MW} = -eE_1\langle S|z|P\rangle$.

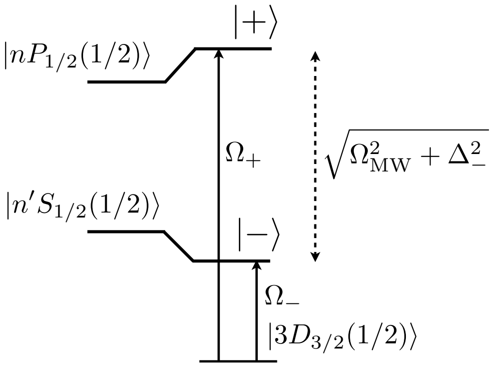

Figure 5.4. *Level scheme used in the Rydberg excitation. A strong MW field results in a large Autler-Townes splitting [33] between the two dressed states.*

We consider a strong MW field, $\Omega_{\mathrm{MW}} \gg \Omega_0$, for which it is convenient to use the dressed state in order to describe dynamics of the Rydberg states. By diagonalizing the part of Hamiltonian (5.12) that contains the MW coupling part, the dressed states are given by

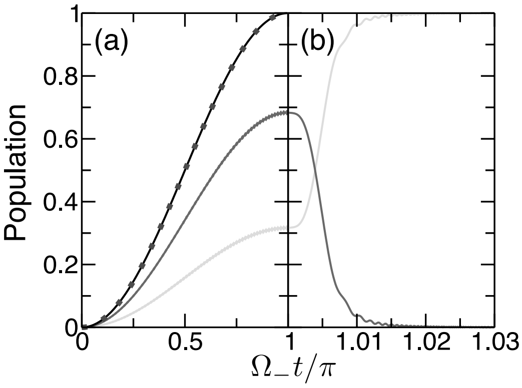

Figure 5.5. *(a) Carrier resonant transition of the $|-\rangle$ state. The black (dotted) curves are solutions of the Hamiltonian Eq. (5.12) [Hamiltonian Eq. (5.14)]. The gray and dark-gray curve correspond to the probability of the $|P\rangle$ and $|S\rangle$ state. The parameters are: $\Omega_- = 2\pi \times 1$ MHz, $\Omega_{\mathrm{MW}} = 2\pi \times 400$ MHz, $\Delta_S = 2\pi \times 136.074$ MHz and $\Delta_P = 2\pi \times 293.957$ MHz. These parameters lead to a vanishing polarizability of the dressed $|-\rangle$ state. (b) Adiabatic evolution of the population in the P and S state. The change rate is $c = \Omega_{\mathrm{MW}}/4.7$.*

$$|\pm\rangle = N_\pm \left(C_\pm|P\rangle + |S\rangle\right), \tag{5.13}$$

where $C_\pm = \frac{\Delta_- \pm \sqrt{\Omega^2_{\mathrm{MW}}+\Delta^2_-}}{\Omega_{\mathrm{MW}}}$ with $\Delta_\pm = \Delta_P \pm \Delta_S$ and $N_\pm$ is the normalization constant. The dressed state energy is $E_\pm = \frac{\Delta_+}{2} \pm \frac{1}{2}\sqrt{\Omega^2_{\mathrm{MW}} + \Delta^2_-}$. With the dressed state at hand, the Hamiltonian Eq. (5.12) becomes

$$\begin{aligned} H &\approx E_+|+\rangle\langle+| + E_-|-\rangle\langle-| + H'_{\mathrm{L}}, \qquad (5.14)\\ H'_{\mathrm{L}} &= -\frac{1}{2}(\Omega_-|-\rangle\langle D| + h.c.) + \frac{1}{2}(\Omega_+|+\rangle\langle D| + h.c.), \end{aligned}$$

with $\Omega_\pm = \frac{\Omega_{\mathrm{MW}}}{2\sqrt{\Omega_{\mathrm{MW}}^2+\Delta_-^2}N_\pm}\Omega_{\mathrm{L}}$. Thus, the low-lying D state is now coupled with the two dressed states. Here the large energy splitting allows us to address the dressed states individually with the Rydberg laser.

The polarizability of the dressed state is $\mathcal{P}_\pm = N_\pm^2(C_\pm^2\mathcal{P}_{nP} + \mathcal{P}_{n'S})$. As $\mathcal{P}_{n'S} > 0$ for high-lying Rydberg states, the polarizability of the dressed state vanishes under certain conditions. For example, for $n' = n$, $\mathcal{P}_\pm = 0$ when $|C_\pm| \approx 0.68$, which can be realized by controlling the MW frequency and/or Rabi frequency. On the other hand, when $\mathcal{P}_\pm = 0$, the trapping potential of the Rydberg ion in the dressed state becomes identical with that of the ions in ELL states. In this case the Franck-Condon factors [9] become trivial and the laser excitation is not different than transitions driven among ELL states. In Fig. 5.5(a) we demonstrate the $|-\rangle$ state excitation. After a π pulse, the ion is excited to the $|-\rangle$ state.

Once the state $|-\rangle$ is excited, the Rydberg laser is switched off and also the MW is switched off such that $|-\rangle$ is adiabatically transferred to the state $|P\rangle$. As an example, we show in Fig. 5.5(b) a case in which the MW detuning is changed according to $\Delta_{SP}(t) = (\Delta_S - \Delta_P)[1 - c^2t^2]$. The Rydberg ion is fully populating the P state after about 13 ns.

5.B Calculation of the gate fidelity

As shown in the previous section, the Rydberg excitation can be performed on a timescale that is highly non adiabatic with respect to the vibrational dynamics. In the extreme case the spatial wave function of the ion does not change, i.e., is frozen, in the course of the Rydberg excitation. In this section, we show how for this case the gate fidelity can be calculated by using a Duschinsky transformation that connects the phonon modes before the Rydberg excitation (bare phonon modes) to the shaped phonon modes.

Let us first describe the normal coordinate Q_g and canonical momentum $\mathcal{P}_g$ of the bare mode using the corresponding phonon creation and annihilation operators [7],

$$\begin{aligned} Q_g &= \mathbf{L}_g(\mathcal{A}_\dagger + \mathcal{A}), && (5.15)\\ \mathcal{P}_g &= \mathbf{P}_g(\mathcal{A}_\dagger - \mathcal{A}), && (5.16)\end{aligned}$$

where $\mathcal{A}_\dagger$ and $\mathcal{A}$ are both column vectors, $\mathcal{A}_\dagger = (a_1^\dagger, a_2^\dagger, \cdots, a_N^\dagger)^{\mathrm{t}}$ and $\mathcal{A} = (a_1, a_2, \cdots, a_N)^{\mathrm{t}}$, with N the total number of ions and t to be the transpose operation. a_p ($a_p^\dagger$) is the annihilation (creation) operator of the pth bare phonon mode. $\mathbf{L}_g$ and $\mathbf{P}_g$ are diagonal matrices, whose matrix elements are $\mathbf{L}_g(p,p) = \sqrt{\hbar/2M\tilde{\omega}_p}$ and $\mathbf{P}_g(p,p) = i\sqrt{\hbar M\tilde{\omega}_p/2}$, where $\tilde{\omega}_p$ is the pth phonon frequency of the bare mode. Similarly, we obtain the result of normal coordinate Q_e and momentum $\mathcal{P}_e$ of the Rydberg shaped mode

$$\begin{aligned} Q_e &= \mathbf{L}_e(\mathcal{B}_\dagger + \mathcal{B}), && (5.17)\\ \mathcal{P}_e &= \mathbf{P}_e(\mathcal{B}_\dagger - \mathcal{B}), && (5.18)\end{aligned}$$

where $\mathcal{B}_\dagger = (b_1^\dagger, b_2^\dagger, \cdots, b_N^\dagger)^{\mathrm{t}}$, $\mathcal{B} = (b_1, b_2, \cdots, b_N)^{\mathrm{t}}$, $\mathbf{L}_e(p,q) = \sqrt{\hbar/2M\omega_p}$, and $\mathbf{P}_e(p,q) = i\sqrt{\hbar M\omega_p/2}$ when $p = q$ and zero otherwise.

We now find the Duschinsky transformation between the bare and Rydberg modes. The displacement of the ions around their equilibrium positions is denoted by a column vector $\mathcal{X} = (x_1, x_2 \cdots, x_N)^{\mathrm{t}}$.

Table 5.1. *The 4-qubit basis*

$\|1\rangle = \|\uparrow\uparrow\uparrow\uparrow\rangle$	$\|2\rangle = \|\downarrow\uparrow\uparrow\uparrow\rangle$	$\|3\rangle = \|\uparrow\downarrow\uparrow\uparrow\rangle$	$\|4\rangle = \|\uparrow\uparrow\downarrow\uparrow\rangle$
$\|5\rangle = \|\uparrow\uparrow\uparrow\downarrow\rangle$	$\|6\rangle = \|\downarrow\downarrow\uparrow\uparrow\rangle$	$\|7\rangle = \|\downarrow\uparrow\downarrow\uparrow\rangle$	$\|8\rangle = \|\downarrow\uparrow\uparrow\downarrow\rangle$
$\|9\rangle = \|\uparrow\downarrow\downarrow\uparrow\rangle$	$\|10\rangle = \|\uparrow\downarrow\uparrow\downarrow\rangle$	$\|11\rangle = \|\uparrow\uparrow\downarrow\downarrow\rangle$	$\|12\rangle = \|\downarrow\downarrow\downarrow\uparrow\rangle$
$\|13\rangle = \|\downarrow\downarrow\uparrow\downarrow\rangle$	$\|14\rangle = \|\downarrow\uparrow\downarrow\downarrow\rangle$	$\|15\rangle = \|\uparrow\downarrow\downarrow\downarrow\rangle$	$\|16\rangle = \|\downarrow\downarrow\downarrow\downarrow\rangle$

We can obtain that $\mathcal{Q}_g = \mathbf{A}\mathcal{X}$ and $\mathcal{Q}_e = \mathbf{B}\mathcal{X}$, where $\mathbf{A}$ ($\mathbf{B}$) is the eigenvector of the bare (Rydberg) mode. Applying the Duschinsky transformation, one finds $\mathcal{Q}_e = \mathbf{T}\mathcal{Q}_g$ with $\mathbf{T} = \mathbf{B}\mathbf{A}^{-1}$. Similarly, one obtains $\mathcal{P}_e = \mathbf{T}\mathcal{P}_g$.

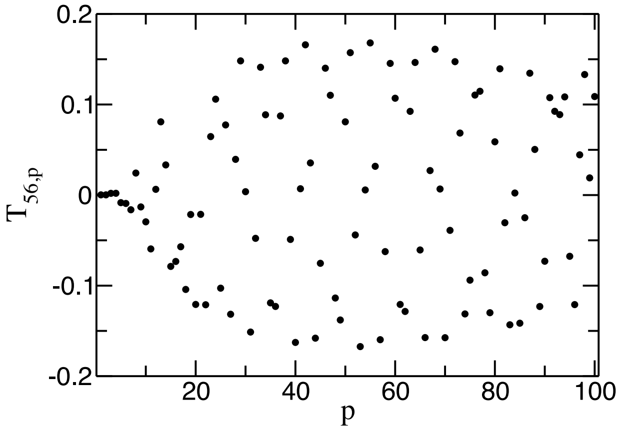

Figure 5.6. **T** *matrix elements corresponding to one of the localized mode (mode index 56, see Fig. 1c) and the bare mode. The mode vector is shown in Fig. 1b (bare mode) and the inset of Fig. 1c (localized mode).*

With Eqs. (5.15)-(5.18) and the Duschinsky transformation, we can find the transformation between the phonon operators of the Rydberg and bare mode,

$$\mathcal{B}_\dagger = \frac{1}{2}\left[\mathcal{T}_+\mathcal{A}_\dagger + \mathcal{T}_-\mathcal{A}\right], \tag{5.19}$$

$$\mathcal{B} = \frac{1}{2}\left[\mathcal{T}_-\mathcal{A}_\dagger + \mathcal{T}_-\mathcal{A}\right], \tag{5.20}$$

where $\mathcal{T}_\pm = (\mathbf{L}_e^{-1}\mathbf{T}\mathbf{L}_g \pm \mathbf{P}_e^{-1}\mathbf{T}\mathbf{P}_g)$. This relation allows us to express the gate evolution operator Eq. (5.7) in the main text in terms of the phonon operators of the bare mode,

$$\begin{aligned} U(\tau) &= \exp\left[-i(\mathbf{C}_g\mathcal{A}_\dagger + \mathbf{C}_g^*\mathcal{A} + \sum_{m,n=1}^{4}\phi_{mn}\sigma_m^z\sigma_n^z)\right], \qquad (5.21) \\ &= \exp\left[-i\sum_{p=1}^{N}(\mathbf{c}_p a_p^\dagger + \mathbf{c}_p^* a_p) + i\sum_{m,n=1}^{4}\phi_{mn}\sigma_m^z\sigma_n^z\right], \end{aligned}$$

where $\mathbf{C}_g = \mathrm{Re}(\mathbf{C}_e)\mathbf{L}_e^{-1}\mathbf{T}\mathbf{L}_g + i\mathrm{Im}(\mathbf{C}_e)\mathbf{P}_e^{-1}\mathbf{T}\mathbf{P}_g$ and $\mathbf{c}_p = \sum_{m=1}^{4}\mathbf{C}_g(m,p)$. $\mathbf{C}_e$ is a diagonal matrix characterizing the residual phonon-qubit coupling, whose diagonal matrix elements are $\mathbf{C}_e(p,p) =$

Index	n=1	n=2	n=3	n=4
m=1	-2.8 (-2.8)	$\pi/8$ ($\pi/8$)	4.5×10^{-4} (3.0×10^{-4})	3.1×10^{-4} (2.8×10^{-4})
m=2	$\pi/8$ ($\pi/8$)	-2.8 (-2.8)	7×10^{-4} (2.8×10^{-4})	4.5×10^{-4} (3.0×10^{-4})
m=3	4.5×10^{-4} (3.0×10^{-4})	7×10^{-4} (3.8×10^{-4})	-2.8 (-2.8)	$\pi/8$ ($\pi/8$)
m=4	3.1×10^{-4} (2.8×10^{-4})	4.5×10^{-4} (3.0×10^{-4})	$\pi/8$ ($\pi/8$)	-2.8 (-2.8)

Table 5.2. *The spin-spin phase ϕ_{mn}. Data in the parentheses corresponds to the ϕ_{mn} without mode shaping.*

$\sum_{m=1}^{4} \alpha_m^{(p)} \sigma_m^z$ with $\alpha_m^{(p)}(\tau) = \int_0^\tau \Omega_m(t) \mathbf{B}_m^{(p)} \eta^{(p)} e^{i\omega_p t} dt$, where $\mathbf{B}_m^{(p)}$ is the pth mode vector of the mth ion and $\eta^{(p)} = k_\mathrm{L} l_p$ is the corresponding Lamb-Dicke parameter. Here $\Omega_m(t) = \Omega_0 \sin(\nu t)$ is the time-dependent Rabi frequency of the gate laser that addresses the mth ion. The spin-spin phase is $\phi_{mn}(\tau) = \int_0^\tau dt' \int_0^{t'} dt \sum_p \Omega_m(t')\Omega_n(t) \mathbf{B}_m^{(p)} \mathbf{B}_n^{(p)} \eta^{(p)} \eta^{(p)} \sin[\omega_p (t' - t)]$. For convenience, we have denoted the index of the qubit ions (the 46th, 47th, 54th, and 55th ion in the 100-ion chain) with $m\,(n) = 1,\, 2,\, 3,\, 4$.

Equation (5.21) permits us to calculate the gate fidelity conveniently as the bare phonon modes are initially in a thermal state ρ_v. The qubits are in a product state $|\Psi(0)\rangle = (|\psi_{m_1}\rangle \otimes |\psi_{n_1}\rangle) \otimes (|\psi_{m_2}\rangle \otimes |\psi_{n_2}\rangle)$ with $|\psi_m\rangle = (|\uparrow_m\rangle + |\downarrow_m\rangle)/\sqrt{2}$ and $\{m_j, n_j\}$ being indices of ions forming the jth subcrystal. Ideally, the output state after a gate time τ is $|\Psi(\tau)\rangle = \exp[i\pi/4(\sigma_{m_1}^z \sigma_{n_1}^z + \sigma_{m_2}^z \sigma_{n_2}^z)]|\Psi(0)\rangle$. The actual gate performance is characterized by the gate fidelity $F = \langle \Psi(\tau)|\mathrm{Tr}_\mathrm{v} \rho(\tau)|\Psi(\tau)\rangle = 1/256 \sum_{j,k=1}^{16} \langle j|\rho(\tau)|k\rangle$. Here $|j\rangle$ ($j = 1, \cdots, 16$) is the four-qubit basis (a full list of $|j\rangle$ is given in Table 5.1), with $\sigma_m^{(z)}|j\rangle = \sigma_m^j |j\rangle$ and $\rho(t) = U(t)\rho(0)U^\dagger(t)$ with $\rho(0) = \rho_\mathrm{v} \otimes |\Psi(0)\rangle\langle\Psi(0)|$. Tr_v denotes the trace over the vibrational modes. After some math, the gate fidelity is found explicitly as

$$F = \frac{1}{256} \sum_{j,k=1}^{16} \varphi_{jk} \times \exp\left[\frac{1}{2} \sum_{p=1}^{N} \left(c_p^j c_p^{k*} - c_p^{j*} c_p^k - |c_p^j - c_p^k|^2 \coth\frac{\gamma_p}{2} \right)\right], \tag{5.22}$$

where $\mathbf{c}_p|j\rangle = c_p^j|j\rangle$ and $\gamma_p = \hbar\omega_p/k_B T$ is the temperature factor (k_B the Boltzman constant, T phonon temperature) and

$$\begin{aligned} \varphi_{jk} &= \exp\left[\frac{i\pi}{4}(\sigma_{m_1}^k \sigma_{n_1}^k - \sigma_{m_1}^j \sigma_{n_1}^j + \sigma_{m_2}^k \sigma_{n_2}^k - \sigma_{m_2}^j \sigma_{n_2}^j) \right. \\ &+ \left. i \sum_{m,n=1}^{4} (\phi_{mn} \sigma_m^j \sigma_n^j - \phi_{mn}^* \sigma_m^k \sigma_n^k) \right], \end{aligned} \tag{5.23}$$

The gate error here is mainly caused by the spin-phonon coupling, i.e., the c_p^j term in Eq. (5.22). We illustrate this with an example when $\nu\tau/2\pi = 1$ [see Fig. 3(a)]. We assume that initially all the bare modes share a same temperature T, in which the average phonon number of the highest energy mode is 3.25. The temperature factor is roughly $\gamma_p \sim 0.2$. The gate fidelity is calculated under two different situations, i.e., without and with Rydberg mode shaping. When the gate is performed with the bare mode, we find that $0 < |c_p^j| < 3.9 \times 10^{-2}$. Note that the total number of coefficients c_p^j is 16×100 and that it is therefore impractical to list all of them here. While applying the mode shaping, $0 < |c_p^j| < 2.2 \times 10^{-3}$. Therefore, the maximal $|c_p^j|$ in the presence of the mode shaping is one order of magnitude smaller than that of the bare mode case. In both cases, $|\varphi_{jk}| \approx 1$ (the numerical value of the spin-spin phase ϕ_{mn} is given in Table 5.B), which results from the optimization of the laser Rabi frequency Ω_0 [13]. With these data we find the gate fidelity $F = 0.85$ (in case of the bare mode) and $F = 0.9995$ (in case of the mode shaping), respectively.

Bibliography

[1] D. P. DiVincenzo, Fortschritte der Physik, **48**, 771 (2000).

[2] A. M. Steane, Quantum Inf. Comput. **7**, 171 (2007).

[3] H. Häffner, C. Roos, and R. Blatt, Phys. Rep. **469**, 155 (2008).

[4] M. A. Nielsen and I. L. Chuang, *Quantum Computation and Quantum Information* (Cambridge University Press, 2000).

[5] J. I. Cirac and P. Zoller, Nature **404**, 579 (2000).

[6] D. Kielpinski, C. Monroe, and D. J. Wineland, Nature **417**, 709 (2002).

[7] D. James, Appl. Phys. B **66**, 181 (1998).

[8] M. Müller, L. Liang, I. Lesanovsky, and P. Zoller, New J. Phys. **10**, 093009 (2008).

[9] W. Li and I. Lesanovsky, Phys. Rev. Lett. **108**, 023003 (2012).

[10] J. J. García-Ripoll, P. Zoller, and J. I. Cirac, Phys. Rev. Lett. **91**, 157901 (2003).

[11] J. J. García-Ripoll, P. Zoller, and J. I. Cirac, Phys. Rev. A **71**, 062309 (2005).

[12] L. M. Duan, Phys. Rev. Lett. **93**, 100502 (2004).

[13] G. Lin, S. Zhu, R. Islam, K. Kim, M. Chang, S. Korenblit, C. Monroe, and L. Duan, EPL **86**, 60004 (2009).

[14] F. Schmidt-Kaler, T. Feldker, D. Kolbe, J. Walz, M. Müller, P. Zoller, W. Li, and I. Lesanovsky, New J. Phys. **13**, 075014 (2011).

[15] J. T. Barreiro, M. Müller, P. Schindler, D. Nigg, T. Monz, M. Chwalla, M. Hennrich, C. F. Roos, P. Zoller and R. Blatt, Nature **470**, 486 (2011).

[16] D. Kolbe, M. Scheid, and J. Walz, Phys. Rev. Lett. **109**, 063901 (2012).

[17] M. Harlander, R. Lechner, M. Brownnutt, R. Blatt, and W. Hänsel, Nature **471**, 200 (2011).

[18] K. R. Brown, C. Ospelkaus, Y. Colombe, A. C. Wilson, D. Leibfried, and D. J. Wineland, Nature **471**, 196 (2011).

[19] D. Leibfried, R. Blatt, C. Monroe, and D. Wineland, Rev. Mod. Phys. **75**, 281 (2003).

[20] B. Hezel, I. Lesanovsky, and P. Schmelcher, Phys. Rev. Lett. **97**, 223001 (2006).

[21] J. P. Schiffer, Phys. Rev. Lett. **70**, 818 (1993).

[22] E. Shimshoni, G. Morigi, and S. Fishman, Phys. Rev. Lett. **106**, 010401 (2011).

[23] C. Marquet, F. Schmidt-Kaler, and D. James, Appl. Phys. B **76**, 199 (2003).

[24] C. Schneider, D. Porras, and T. Schaetz, Rep. Prog. Phys. **75**, 024401 (2012).

[25] D. Leibfried, B. DeMarco, V. Meyer, D. Lucas, M. Barrett, J. Britton, W. M. Itano, B. Jelenkovic, C. Langer, T. Rosenband, and D. J. Wineland, Nature **422**, 412 (2003).

[26] P. J. Lee, K. Brickman, L. Deslauriers, P. C. Haljan, L. Duan, and C. Monroe, J. Opt. B **7**, S371 (2005).

[27] K. Kim, C. F. Roos, L. Aolita, H. Häffner, V. Nebendahl, and R. Blatt, Phys. Rev. A **77**, 050303 (2008).

[28] S. L. Zhu, C. Monroe, and L. M. Duan, Phys. Rev. Lett. **97**, 050505 (2006).

[29] S. Blanes and F. Casas, Phys. Rep. **470**, 151 (2009).

[30] A. Sørensen and K. Mølmer, Phys. Rev. Lett. **82**, 1971 (1999).

[31] J. I. Cirac and P. Zoller, Phys. Rev. Lett. **74**, 4091 (1995).

[32] J. F. Poyatos, J. I. Cirac, R. Blatt and P. Zoller, Phys. Rev. A **54**, 1532 (1996).

[33] S. H. Autler and C. H. Townes, Phys. Rev.**100**, 703 (1955).

Part III

Quantum many-body physics with Rydberg atoms - anisotropic interactions involving Rydberg *p*-states

CHAPTER 6

PREPRINT

Quantum Spin Ice and dimer models with Rydberg atoms[†]

Phys. Rev. X **4** 041037 (2014-11-25)

A. W. Glaetzle[1,2], M. Dalmonte[1,2], R. Nath[1,2,3], I. Rousochatzakis[4], R. Moessner[4], and P. Zoller[1,2]

[1] *Institute for Quantum Optics and Quantum Information of the Austrian Academy of Sciences, A-6020 Innsbruck, Austria*
[2] *Institute for Theoretical Physics, University of Innsbruck, A-6020 Innsbruck, Austria*
[3] *Indian Institute of Science Education and Research, Pune 411 008, India*
[4] *Max Planck Institute for the Physics of Complex Systems, D-01187 Dresden, Germany*

Quantum spin ice represents a paradigmatic example on how the physics of frustrated magnets is related to gauge theories. In the present work we address the problem of approximately realizing quantum spin ice in two dimensions with cold atoms in optical lattices. The relevant interactions are obtained by weakly admixing van der Waals interactions between laser admixed Rydberg states to the atomic ground state atoms, exploiting the strong angular dependence of interactions between Rydberg p-states together with the possibility of designing step-like potentials. This allows us to implement Abelian gauge theories in a series of geometries, which could be demonstrated within state of the art atomic Rydberg experiments. We numerically analyze the family of resulting microscopic Hamiltonians and find that they exhibit both classical and quantum order by disorder, the latter yielding a quantum plaquette valence bond solid. We also present strategies to implement Abelian gauge theories using both s- and p-Rydberg states in exotic geometries, e.g. on a 4-8 lattice.

6.1 Introduction

The ice model has been fundamental in furthering our understanding of collective phenomena in condensed matter and statistical physics: in 1935 Pauling provided an explanation of the ‘zero-point

---

[†] The author of the present thesis was strongly involved in doing the calculation presented in this work and in writing the manuscript. In particular, he preformed the atomic physics calculation deriving the van der Waals interactions. The detailed numerical simulation of the many-body dynamics have been performed by IR and RM.

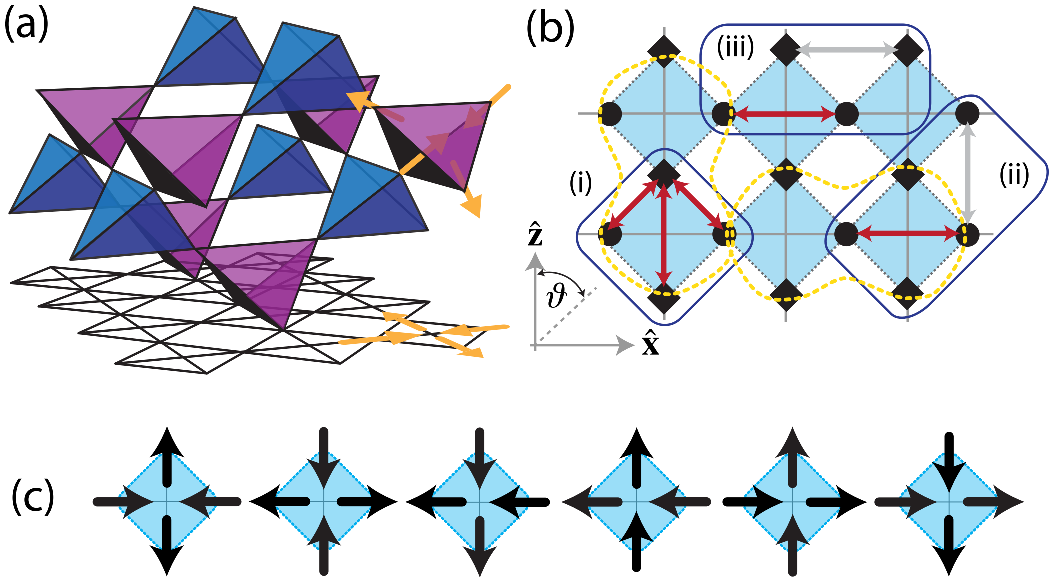

Figure 6.1. *(a) In spin ice materials the magnetic moments (yellow arrows) of rare-earth ions are located on the corners of a pyrochlore lattice, which is a network of corner-sharing tetrahedra. They behave as almost perfect Ising spins and point along the line from the corner to the centre of the tetrahedron, either inward or outward. Due to the different Ising-axes of the spins this results in an effectively antiferromagnetic interaction which is frustrated. (b) Projecting the 3D pyrochlore lattice onto a 2D square lattice yields a checkerboard lattice where tetrahedrons are mapped onto crossed-plaquettes (light-blue). Interactions between two spins located on ● or ■ lattice sites have to be (i) step-like as a function of the distance, (ii) anisotropic and (iii) require a bipartite labelling of the lattice sites. (c) Degenerate ground state configurations of spins on a crossed-plaquette. They obey the ice-rules, which enforce two spins pointing inward and two spins pointing outward at each vertex.*

entropy' of water ice [1] as measured by Giauque and Stout [2], while Lieb demonstrated with his exact solution of the ice model in two dimension [3] that there exist phase transitions with critical exponents different from those of Onsager's solution of the Ising model. The experimental discovery [4] of a classical spin version of the ice model [5] has in turn generated much interest in the magnetism community [6–9].

More recently, quantum ice models [10–14] have attracted a great deal of attention in the context of phases exhibiting exotic types of orders, such as resonating valence bond liquids [15, 16] or quantum Coulomb phases [12, 17–19]. They form part of a broader family of models, which also includes quantum dimer models or other quantum vertex models [20], in which locally a hard constraint is imposed, such as the ice rules defined below. Such a constraint can then endow the configuration space with additional structure – most prominently, an emergent gauge field which can be the basis of the appropriate effective description at low energies [20–22]. This is an important phenomenon as it is perhaps the simplest way of obtaining gauge fields as effective degrees of freedom in condensed matter physics. More broadly, this is part of a long-running search for magnetic materials hosting quantum spin liquids [7].

In the present work we address the problem of physically realizing models of quantum spin ice and quantum dimer models in two spatial dimensions with ultracold atoms in optical lattices. Our proposal builds on the recent experimental advances, and opportunities in engineering many-body interactions with laser excited Rydberg states [23–37]. In particular, this will allow us to develop a Rydberg toolbox for the complex interactions required in 2D quantum ice models [8]. Our investigation also fits into the broader quest for the realization of synthetic gauge fields with cold atoms. While much effort is being devoted to the generation of static gauge fields [38], e.g. on optical flux lattices, here we follow the strategy of generating a *dynamical* gauge field [12, 17–19, 21, 22, 39–42] emerging upon imposition of the ice rule.

While in condensed matter systems the interactions underlying ice and spin ice arise naturally in a 3D context [see Fig. 6.1(a)], the 2D quantum ice on a square lattice requires a certain degree of fine tuning of the relevant interactions [see Fig. 6.1(b)]. In 3D spin ice materials, for example, the ions of magnetic rare-earth atoms reside on a pyrochlore lattice, representing a network of corner-sharing tetrahedra. Magnetic interactions in combination with crystal fields give rise to a low energy manifold of states on each tetrahedron consisting of six configurations, in which two spins point inward and two spins point outward [compare Fig. 6.1(c)]. In a similar way, in water ice each O^{2-} atom in a tetrahedrally coordinated framework has two protons attached to it, giving rise to a manifold of energetically degenerate configurations. 2D models of ice and spin ice can be understood as projection of the pyrochlore on a square lattice (see Fig. 6.1), where again the low energy configurations of spins residing on the links obey the “ice rule” two-in and two-out at each vertex. While these 2D ice models play a fundamental role in our theoretical understanding of frustrated materials, a physical realization requires a precise adjustment of the underlying interactions – different local configurations which are symmetry distinct need to be at least approximately degenerate; the required fine-tuning however needs to be delicately directionally dependent, as in the pure ice model, the ratio of some interactions between different pairs of equidistant spins vanishes, see Fig. 6.1(b). Things are not all hopeless, however, as there exist a number of settings in which partial progress has been made to realizing such models. In two dimensions, artificial structures using nanomagnetic [43] or colloidal arrays [44] have been proposed, including strategies for tuning the interactions appropriately [45]. The present proposal with Rydberg atoms is unique, however, as it combines both the possibilities of engineering the complex interactions using Rydberg interactions with the accessibility of the quantum regime in cold atom experiments.

Alkali atoms prepared in their electronic ground state can be excited by laser light to Rydberg states, i.e. states of high principal quantum number n [46–49]. These Rydberg atoms interact strongly via the van der Waals interaction exhibiting the remarkable scaling $V_{\mathrm{VdW}} \sim n^{11}$, and which exceed typical ground state interactions of cold atoms by several orders of magnitude. In an atomic ensemble the large level shifts associated with these interactions implies that only a single atom can be excited to the Rydberg state, while multiple excitations are suppressed within a blockade radius determined by the van der Waals interactions and laser parameters [50, 51]. This blockade mechanism results in novel collective and strongly correlated many-particle phenomena such as the formation of super-atoms, and Rydberg quantum crystals [46–49]. In present experiments the emphasis is on *isotropic* van der Waals interactions [23–36], which, for example, can be obtained by exciting Rydberg s-states using a two-photon excitation scheme. In contrast, we will be interested below in excitations of Rydberg p-states, where the van der Waals interactions can be highly *anisotropic*,as discussed in Ref. [52–55]. Below we will discuss in detail the controllability of the shape and range of these anisotropic interactions via atomic and laser parameters for the case of Rb atoms. In the present context this will provide us with the tools to engineer the required complex interaction patterns for 2D quantum spin ice and dimer models. The setup we will discuss will consist of cold atoms in optical lattices, where the strong Rydberg interactions are weakly admixed to the atomic ground states [56–60], thus effectively dressing ground state atoms to obtain the complex interactions in atomic Hubbard models required for the realization of 2D quantum spin ice and dimer models.

We then proceed to numerically analyze the family of Hamiltonian realizable with this toolbox. We verify that it contains two phases exhibiting distinct types of order by disorder [61, 62]. Most remarkably, quantum order by disorder – due to the presence of quantum dynamics in the ice model – realizes the plaquette valence bond solid as an unusual non-Néel phase of a frustrated magnet. This terminates when classical degeneracy lifting takes over.

The latter phase is conventional in that it is diagnosed by a conventional spin order parameter, which would manifest itself in a Bragg peak in the structure factor. By contrast, the valence bond solid would be diagnosed by higher order ‘string’ correlators, and is thus fundamentally different from some other instances of quantum order by disorder, where finally the mechanism, but not quite so much the order parameter, is exotic [62, 63]. Notably, precisely such order parameters have become accessible to experimental measurements recently [64], so that our proposal not only covers the setting for realizing quantum order by disorder, but also the means for detecting it.

In addition, at finite temperature, we find that the classically ordered state, even in the absence of quantum dynamics, melts into a classical version of a Coulomb phase, namely a Coulomb gas in which thermally activated plaquettes violating the ice rule play the role of positive and negative charges. As these interact via an entropic two-dimensional (logarithmic) Coulomb law, this phase is only marginally confined [65, 66].

While throughout the paper we will be mostly interested in quantum ice models, which require the development of advanced interaction-pattern design, we will also discuss a second strategy to implement constrained dynamics, and in particular quantum dimer models, with Rydberg atoms. It relies on combining simple interaction patterns, such as the ones generated by s-states, with complex lattice structures, which can be realized either via proper laser combination or by the recently developed optical lattice design with digital micromirror devices [67]. These models extend the class of dynamical gauge fields in AMO systems to non hyper-cubic geometries. Overall, the ability to synthetically design Abelian dynamical gauge fields with discrete variables also establishes interesting connections with high energy physics, where these theories are usually refereed as quantum link models [68, 69]. Within this context, the key developments in engineering pure gauge theories can be combined with other schemes, where dynamical matter is included, which have already been proposed in the context of cold atom gases [69].

The paper is structured as follows. In Sec. 6.2, we briefly provide the background on quantum ice models needed for digesting the remainder of the material. Sec. 6.3 outlines the implementation of a family of model Hamiltonians approximating the quantum ice model using atoms in optical lattices weakly admixed with a Rydberg p-state. Our model Hamiltonians are then analyzed for their phase diagram in Sec. 6.4. Sec. 6.5 presents strategies to implement simpler Abelian gauge theories using both s- and p-Rydberg states in exotic geometries, e.g. a 4-8 lattice. The paper closes with a summary and outlook in Sec. 6.6.

6.2 The quantum ice model

This section provides a brief overview over the statistical mechanics of the ice model, the emergence of a gauge field, and the challenges in realizing such a model experimentally.

6.2.1 The configuration space: ice rules and emergent gauge fields

The ice model on the square lattice, also known the six-vertex model or simply square ice [3], has Ising degrees of freedom residing on the *links* of a square lattice. They can either be thought of as 'fluxes', $\left\{\hat{S}_i^z\right\}$, pointing in either of the directions along the bond i, see layer (i) of Fig. 6.2(a); or equivalently can be mapped onto spins $\left\{S_i^z\right\}$ which point up or down depending on the direction of the flux [see layer (ii) of Fig. 6.2(a)].

Only configurations satisfying the ice rule are permitted, which stipulate that the spins on each vertex add up to zero – there are $\binom{4}{2} = 6$ ways of arranging this, see panel (i) of Fig. 6.2(b). The number of configurations satisfying the ice rule grows exponentially with the size of the system – for a lattice of N spins, there are $(4/3)^{\frac{3N}{4}}$ ice states [3].

The origin of the emergent gauge field is transparent in flux language, where it implies that the lattice divergence of the flux field vanishes: defining the x(y) component of a two-dimensional vector flux $\mathbf{b}$ to be the flux along the corresponding links emanating from a vertex in the positive x(y) direction, one has

$$\nabla \cdot \mathbf{b} = 0 \Rightarrow \ \mathbf{b} = \nabla \times \mathbf{a}. \tag{6.1}$$

Note that a gauge field $\mathbf{a}$ has appeared naturally as a consequence of enforcing the ice rule, just as it does in magnetostatics, where Maxwell's law for the magnetic field $\nabla \cdot \mathbf{B} = 0$ leads to the introduction of the familiar vector potential $\mathbf{A}$.

In the present example in two dimensions, where the flux is a two component vector $\mathbf{b}$, and the scalar constraint $\nabla \cdot \mathbf{b} = 0$ fixes one degree of freedom, $\mathbf{a}$ only has one physical degree of freedom left – it can be thought of as a scalar, usually referred to as a height: $\mathbf{a} = h\mathbf{z}$ 'in the z-direction' [65, 66]. Defects in this height field – forbidden in the six vertex model but allowed when violating the ice rule comes only with a finite energy penalty – are then known as charges or monopoles, which carry a gauge charge with respect to the emergent gauge field.

Having enforced the ice rule, the natural degree of freedom is thence an *emergent* gauge field $\mathbf{a}$ – it is in this way that gauge fields quite generically emerge in condensed matter physics, with a constraint arising either from the need to satisfy a dominant term in the Hamiltonian, or a microscopic relation on the local Hilbert space [20].

6.2.2 Realization, and fine-tuning in $d = 2$

The ice rule on a given vertex involves four spins, but it can be enforced via a pairwise interaction: if all four spins on a vertex interact antiferromagnetically *and equally* – described by the Hamiltonian

$$H_{\text{ice}} = V \sum_{i,j \in +} S_i^z S_j^z, \tag{6.2}$$

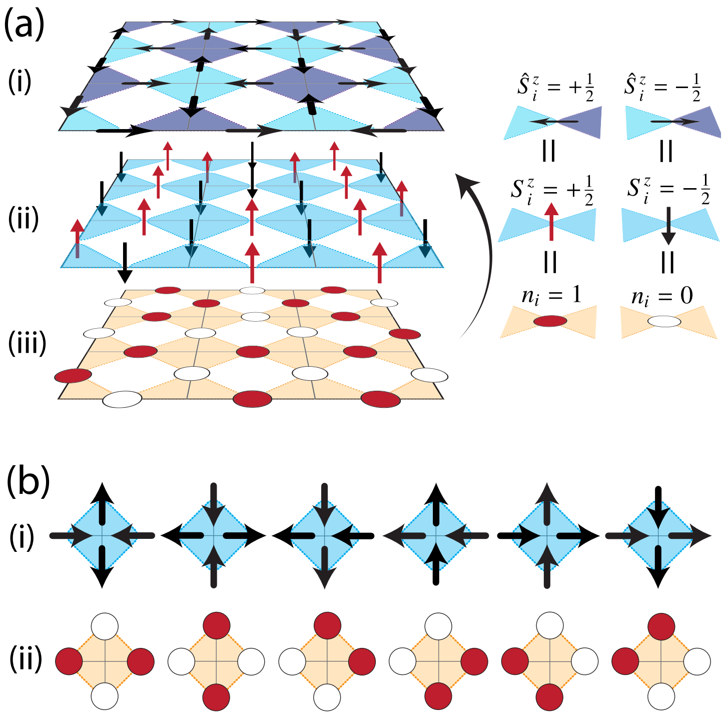

Figure 6.2. *(a) The spins of the 2D ice model on a checkerboard lattice can be interpreted as (i) "fluxes",* $\{\hat{S}_i^z\}$*, pointing either inward or outward of a specific crossed plaquette. This requires a bipartite labeling of the plaquettes (light blue and light magenta plaquettes) since an outward pointing flux vector corresponds to an inward pointing flux vector for the neighboring plaquette. (ii) They can be interpreted as spins,* $\{S_i^z\}$ *aligned perpendicular to the plane, pointing either up (red arrows) or down (black arrows). In the right inset we identify a spin pointing up,* $S_i^z = +\frac{1}{2}$*, with a flux vector pointing from the magenta to the blue plaquette,* $\hat{S}_i^z = +\frac{1}{2}$ *and vice versa. (iii) Spins,* $\{S_i^z\}$*, can be mapped onto hard-core bosons,* $n_i \in \{0, 1\}$*. Here, e.g. a particle (red circle),* $n_i = 1$*, corresponds to a spin pointing upward,* $S_i^z = +\frac{1}{2}$*, while an empty lattice site (white circle),* $n_i = 0$*, corresponds to a spin pointing downward,* $S_i^z = -\frac{1}{2}$*. (b) The six ice-rule states correspond to vertex configurations with two hard-core bosons and two empty lattice sites.*

where + denotes a crossed plaquette in 2D or a tetrahedron in 3D – the resulting ground states are those which obey the ice rules, see panel (i) of Fig. 6.2(b). In three dimensions, equality of the pairwise interactions can be symmetry-generated – by placing the spins on the corners of a tetrahedron, any antiferromagnetic interaction depending only on the distance between the spins will yield the ice rule. By contrast, in two dimensions, a tetrahedron becomes a square with interactions also across the diagonal (Fig. 6.1), which are no longer symmetry equivalent to those along the edges [70].

In particular, interactions, $V_{ij}(\mathbf{r})$, between two spins i and j located on the bonds of a checkerboard lattice separated by a distance $\mathbf{r}$, have to fulfill three demanding properties [see Fig. 6.1(b)] in order to map onto the Spin ice Hamiltonian of Eq. (6.2)

1. **Anisotropy:** Interactions have to be *strongly anisotropic*. This is illustrated in panel (ii) of Fig. 6.1(b). Particles which belong to the same vertex interact strongly (red arrow), while

particles which do not belong to the same vertex do not interact (gray arrow). Thus, for ● particles in panel (ii) one needs an interaction which satisfied $V_{\bullet\bullet}(\vartheta = 0) = 0$ (gray arrow) and $V_{\bullet\bullet}(\vartheta = \pi/2) = \tilde{V}_0$ (red arrow), where the angle ϑ is defined in the inset.

2. **Step-like potentials:** All four particles which belong to the same vertex (enclosed by light blue squares) interact with the same strength $\tilde{V}_0$, independent of their distance, either a or $a\sqrt{2}$, where a is the lattice spacing. Obviously, an interaction of the form $1/|\mathbf{r}|^\alpha$ would not suffice. It is therefore necessary to have *step-like potentials* which fulfill $V_{ij}(|\mathbf{r}| < r_c) = \tilde{V}_0 \neq 0$ and $V_{ij}(|\mathbf{r}| > r_c) = 0$ for $\sqrt{2}a < r_c < 2a$.
3. **Bipartite-lattice structure:** Furthermore, panel (iii) of Fig. 6.1(b), shows that the desired interaction properties cannot be satisfied by a homogeneous interaction pattern, but require a bipartite structure [squares and circles in Fig. 6.1(b)] where the angular dependence on the interaction depends on the lattice bipartition. For example, in the last paragraph we enforced that $V_{\bullet\bullet}(\vartheta = 0) = 0$ [see panel (ii)] but the opposite is true for ■ particles, see panel (iii). Here, $V_{\blacksquare\blacksquare}(\vartheta = \pi/2) = 0$ but $V_{\blacksquare\blacksquare}(\vartheta = 0) = \tilde{V}_0$. On top of that, mixed interactions between ● and ■ particles on the 45 degree lines should obey $V_{\bullet\blacksquare}(\vartheta = \pm\pi/4) = \tilde{V}_0$ in order to ensure that all six possible interactions at a specific vertex are the same, see panel (i).

It is these three countervailing requirements that we manage to satisfy approximately by using Rydberg dressed atoms to engineer an appropriate quantum Hamiltonian (Sec. 6.3).

6.2.3 Adding quantum dynamics, and quantum order by disorder

While the properties of the two-dimensional ice model were broadly understood a long time ago, the question what a quantum version of it would look like was not posed until much later [10]. Unlike in, say, a transverse field Ising model, where the simplest quantum dynamics consists of reversing a single spin, the ice model does not permit such single-site configuration changes, as these would lead to a violation of the ice rule.

The smallest cluster which may flip consists of a closed flux loop around an empty square plaquette, denoted by $\square$ (see Fig. 6.3),

$$H_\square = -t \sum_{\substack{j\,\square\,k \\ i\quad\; l}} \left(S_i^+ S_j^- S_k^+ S_l^- + \text{h.c.} \right) \tag{6.3}$$

and this will be the second ingredient that our work will implement (Sec. 6.3). What this amounts to in the language of gauge theory is the addition of a field conjugate to the height/gauge field $\mathbf{a} = h\mathbf{z}$ – or in more familiar parlance of electromagnetism, the appearance of an (emergent) magnetic field alongside an (emergent) electric one [22].

In two dimensions, adapting a celebrated result by Polyakov (which does not apply straightforwardly as it is based on Lorentz invariance which does not hold *a priori* for our emergent field), it is known that the (emergent) electromagnetism is confining. As a consequence, the emergent excitations cannot spread freely over the system, being bounded by an effective string tension due to the gauge fields. Concretely, one finds a phenomenon known as order by disorder [62]. The quantum dynamics mixes the degenerate ice states into a superposition to form the quantum ground state. Even though

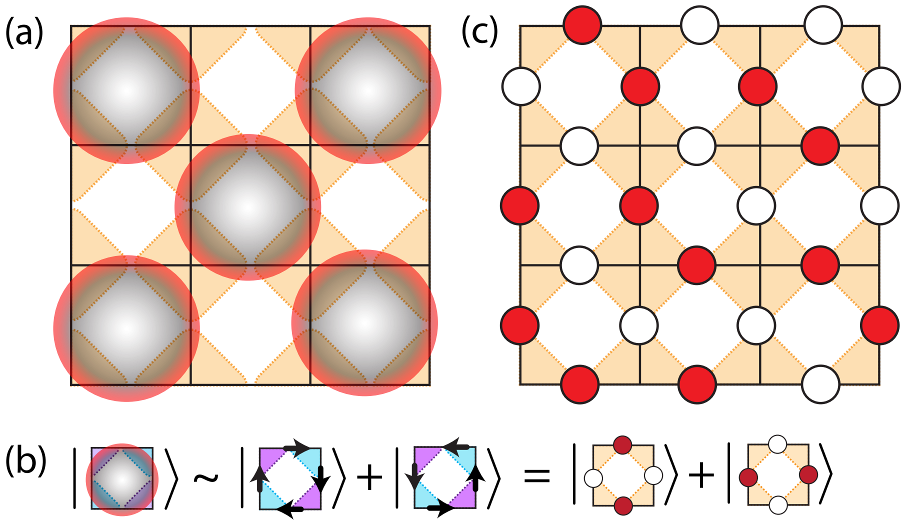

Figure 6.3. *(a) Cartoon state of a plaquette RVB solid. An alternating pattern of plaquettes (shaded red circles) are resonating, i.e., they are in an eigenstate* $|\circledcirc\rangle$ *[see panel (b)] of the plaquette Hamiltonian of Eq.* (6.3), $H_\square|\circledcirc\rangle = -t|\circledcirc\rangle$. *The GS in the thermodynamic limit is two-fold degenerate, reflecting the different coverings of the square lattice with alternating plaquettes. (c) cartoon of one of the degenerate ground states with* $(-\pi/2, \pi/2)$ *order. Along the bottom-left / top-right diagonal, there is antiferromagnetic order. Along the other, the order has a double period,* $\uparrow\uparrow\downarrow\downarrow$.

the quantum dynamics induces fluctuations ('disorder'), the resulting ground state exhibits long-range order. This order takes the form known as a plaquette valence bond solid (Fig. 6.3) [71], which breaks translational symmetry. Such valence bond solids occur frequently in the theory of quantum magnets, but they are not commonly realized in experiment.

In Sec. 6.4, we show that the model Hamiltonian we provide a recipe for does exhibit this kind of order-by-disorder plaquette phase, and we discuss how to detect this kind of exotic order. In addition, we find that for weak quantum dynamics, a different, classical type of symmetry-breaking occurs (see in Fig. 6.3(c)). This happens because different ice states are only approximately degenerate for our engineered Hamiltonian, and the residual energy differences are sufficient to select a particular ordered configuration.

6.2.4 Relation between quantum ice, Bose-Hubbard models and dimer models

As a starting point for our implementation, we will consider a hard-core extended Bose-Hubbard Hamiltonian on a 2D checkerboard lattice:

$$H = -J_h \sum_{\langle i,j \rangle} \left(b_i^\dagger b_j + \text{h.c.} \right) + \sum_{i,j} \tilde{V}_{ij} n_i n_j. \tag{6.4}$$

Here, $b_i^\dagger$ (b_i) is an operator that creates (annihilates) a hard-core boson on site i which obey an on-site contained $b_i^2 = b_i^{\dagger 2} = 0$. The rate J_h is the nearest neighbor (NN) hopping amplitude and V describes a repulsion between all atoms sitting close to the same vertex. The operator $n_i = b_i^\dagger b_i$

counts the number of bosons at site i and can be either zero or one, $n_i \in \{0, 1\}$. The summation runs over nearest neighbors only. The hard-core boson model can be mapped to a spin-1/2 model using the transformation [72] $b_i^\dagger \to S_i^+$, $b_i \to S_i^-$, $n_i \to S_i^z + 1/2$, $J_h \to J_\perp$ and $V_{ij} \to J_{ij}$, which yields

$$H = -J_\perp \sum_{\langle ij \rangle} \left(S_i^+ S_j^- + \text{h.c.} \right) + \sum_{\langle ij \rangle} J_{ij} \left(S_i^z + \frac{1}{2} \right) \left(S_j^z + \frac{1}{2} \right). \tag{6.5}$$

Expanding the last term gives the two-body interaction proportional to $J_{ij} S_i^z S_j^z$ and an additional magnetic field term proportional to $J_{ij} S_i^z$ which is constant after fixing an initial number of particles. This will fix the gauge sector in the gauge theory description [20].

In order to implement the constrained model of Eq. (6.2) we demand (i) *anisotropic* and (ii) *step-like* interactions between (iii) *two species* of particles, as discussed in Sec 6.2.2, that is $\tilde{V}_{ij}$ has to fulfill

$$\sum_{ij} \tilde{V}_{ij} n_i n_j = \tilde{V}_0 \sum_{+} \sum_{i,j \in +} n_i n_j, \tag{6.6}$$

with $\tilde{V}_0$ a constant interaction between all particles belonging to the same vertex denoted by +. Under this assumptions, in the limit $\tilde{V}_0 \gg J_h$ the Bose-Hubbard Hamiltonian of Eq. (6.4) maps onto the spin ice Hamiltonian of Eq. (6.2). The specific form of V_{ij} ensures that all six interactions between particles which belong to the same vertex are equal and interactions between particles which do not belong to the same vertex vanish. In the case of total half-filling of the initial bosons, $N = L/2$, one has $\sum_i S_i^z = 0$: this fixes the effective dynamics on the aforementioned ice manifold of interest. In the case different initial fillings are considered, one has access to different quantum dynamics: a notable case is the $N = L/4$ case, which defines a constrained dynamics on a manifold where a single boson sits close to each vertex [10]. The effective description is then the same of hard-code quantum dimer models on a square lattice.

6.3 Quantum ice with Rydberg-dressed atoms: exploiting p-states

We now turn to the realization of the extended 2D Bose Hubbard Hamiltonian of Eq. (6.4) with cold atoms in optical lattices. The key challenge is the implementation of the interactions $\tilde{V}_{ij}$ with constraints represented in Eq. (6.6). We will show below that this can be achieved via the very anisotropic Rydberg interactions involving laser excited p-states of Rubidium atoms.

6.3.1 Single-particle Hamiltonian on a bi-partite lattice

In our setup we consider Rubidium ^{87}Rb atoms prepared in an internal ground state, which we choose as $|g\rangle \equiv |F = 2, m_F = 2\rangle$. The atoms are trapped in a 2D square optical lattice in the xz-plane created by two pairs of counter propagating laser beams of wavelength λ and wave vector $k = 2\pi/\lambda$, and strongly confined in the y-direction by an additional laser. (We note that these external coordinates should not be confused with the internal spin coordinates, e.g. in Eq. (6.2) and Fig. 6.2). By tilting the laser beams by an angle α we can adjust the lattice spacing in the xz-plane to any value $a = \lambda/[2\sin(\alpha/2)] \geq \lambda/2$ [73] (see below). Quantum tunneling allows the atoms to hop between different lattice sites, thus realizing the kinetic energy term with hopping amplitude J_h of the single band

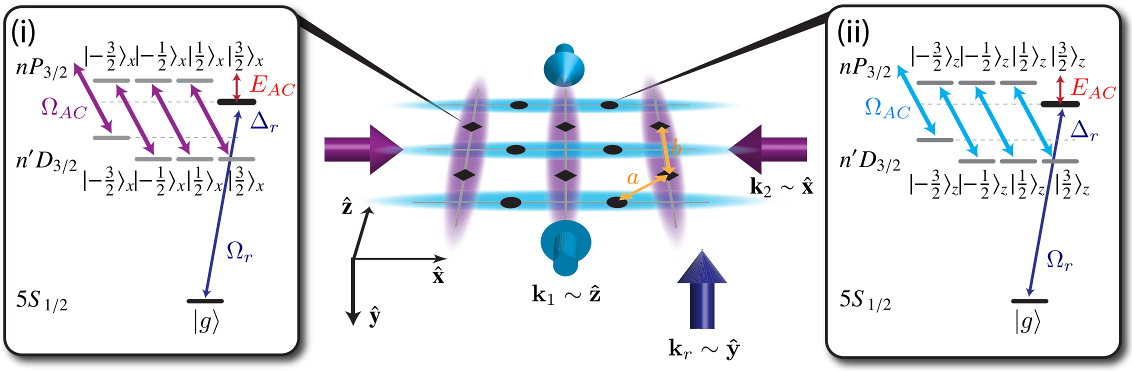

Figure 6.4. *We consider ^{87}Rb atoms loaded in a square optical lattice with lattice spacing a and lattice sites labeled alternating as ● and ■. Additional AC Stark lasers (magenta and light blue arrows) with wave vectors $\mathbf{k}_1 = \pm 2\pi/\lambda_{AC}\,\hat{\mathbf{z}}$ and $\mathbf{k}_2 = \pm 2\pi/\lambda_{AC}\,\hat{\mathbf{x}}$, respectively, form two pairs of standing waves each with periodicity $b = \lambda_{AC}/2$, which are rotated by 45 degrees with respect to the initial lattice. In order to create local quantization axes along $\hat{\mathbf{z}}$ or $\hat{\mathbf{x}}$ for ● or ■ lattice sites, respectively, we require that that atoms located a ● lattice site only feel the intensity maxima of the light blue laser with $\mathbf{k}_1 \sim \mathbf{z}$, while ■ lattice site only feel the intensity maxima of the magenta laser with $\mathbf{k}_2 \sim \hat{\mathbf{x}}$. This can be achieved by adjusting the initial trapping lattice by tilting the corresponding trapping lasers with an angle α such that $a = \lambda/[2\sin(\alpha/2)] \geq \lambda/2$ [73] in order to fulfill $b = \sqrt{2}a$. The two AC Stark lasers have a polarization σ_+ and resonantly couple the $n^2P_{3/2}$ manifold to a lower lying $n'D_{3/2}$ manifold thereby inducing an AC Stark shift on each Zeeman m-level in the $n^2P_{3/2}$ manifold except for the maximum stretched $|n^2P_{3/2}, 3/2\rangle_{z,x}$ states. This locally isolates the $|n^2P_{3/2}, 3/2\rangle_z$ and $|n^2P_{3/2}, 3/2\rangle_x$ state at lattice sites ● and ■, respectively, in energy by at least E_{AC} (see left and right panels). A global Rydberg laser (dark blue arrow) with detuning $\Delta_r \ll E_{AC}$ propagating along the y-direction then selectively admixes the states $|n^2P_{3/2}, 3/2\rangle_z$ and $|n^2P_{3/2}, 3/2\rangle_x$ at lattice sites ● and ■, respectively, to the ground state $|g\rangle$.*

Hubbard model (6.4). Furthermore, we work in the hardcore boson limit, i.e. $U \gg J_h$, in which multiple occupancy in a single site is energetically prohibited.

As already discussed in the context of Fig. 6.1(b) we want to distinguish between ● and ■ sites in the 2D lattice. This bipartite labelling of the optical lattice is essential for realizing the complex interaction pattern $\tilde{V}_{\bullet\bullet}$, $\tilde{V}_{\bullet\blacksquare}$ and $\tilde{V}_{\blacksquare\blacksquare}$ discussed in Sec. 6.2.2, which underlies the second term of the extended Bose Hubbard Hamiltonian (6.4). In our scheme, we assume that atoms on lattice sites ● are excited by laser light to the Rydberg $^2\mathrm{P}_{3/2}$-state $|r_\bullet\rangle = |n^2P_{3/2}, m = 3/2\rangle_z$, whereas atoms at sites ■ are excited to $|r_\blacksquare\rangle = |n^2P_{3/2}, m = 3/2\rangle_x$. Here the subscripts x and z indicate the *different local quantization axes* for the ● and ■ sites. Note that the Rydberg states of interest are the *stretched states* of the fine structure manifold, i.e. states with maximum $m = 3/2$ value for the given angular momentum $j = 3/2$. We will show in the next section that the van der Waals interactions between these polarized Rydberg p-states realize naturally the complex interaction pattern required by Eq. (6.6) for quantum spin ice. By weakly admixing these Rydberg states to the atomic ground state with a laser [see Sec. 6.3.3], the ground state atoms will inherit these interaction patterns, thus realizing the interaction term in the extended Bose Hubbard Model of Eq. (6.4), including the constraints enforced by the interactions satisfying Eq. (6.6).

It is essential in our scheme that we energetically isolate the stretched states $|n^2P_{3/2}, m = 3/2\rangle_{x,z}$

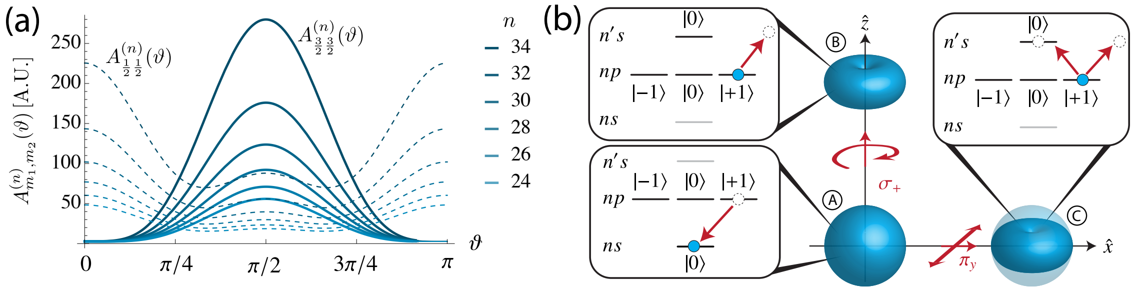

Figure 6.5. *(a) Angular part, $A^{(n)}_{m_1,m_2}(\vartheta)$, of the van der Waals interaction, $V^{(n)}_{m_1,m_2}(r,\vartheta) = \langle m_1, m_2|\hat{V}_{\mathrm{vdW}}|m_1, m_2\rangle = (n - \delta_{n\ell j})^{11} A^{(n)}_{m_1,m_2}(\vartheta)/r^6$, between a pair of ^{87}Rb atoms in the $|3/2, 3/2\rangle_z \equiv |n^2P_{3/2}, 3/2\rangle_z \otimes |n^2P_{3/2}, 3/2\rangle_z$ state (solid lines) and in the $|1/2, 1/2\rangle_z \equiv |n^2P_{3/2}, 1/2\rangle_z \otimes |n^2P_{3/2}, 1/2\rangle_z$ state (dashed lines). We plot the angular part of the rescaled interaction energy, $A^{(n)}_{m_1,m_2}$ as a function of the angle ϑ for various values of the principal quantum number n in atomic units. Here, $A^{(n)}_{3/2,3/2}$ (solid lines) corresponds to the angular part of the interaction, $V_{\bullet\bullet}$, between two atoms excited to the $|r_\bullet\rangle$ Rydberg state and shows a characteristic $\sim \sin^4\vartheta$ shape due to the dominant $S_{1/2}$-channel. Residual interactions at $\vartheta = 0$ are very small and arise from channels coupling to virtual D-states. (see Tab. 6.1). (b) The angular characteristic of the interaction between two atoms both in the "stretched" Rydberg state, $|r_\bullet\rangle = |n^2P_{3/2}, 3/2\rangle_z = |np, 1\rangle_z|\frac{1}{2}\frac{1}{2}\rangle_z$, can be qualitatively understood from its angular part $|np, 1\rangle_z$ and the dominating S-channel: atom A prepared in a $|np, 1\rangle_z$ state can make a virtual transition to a lower-lying $|ns, 0\rangle_z$ state (red arrow in the lower left panel) while emitting a photon. If this photon propagates along the z-direction it has polarization σ_+ and cannot be absorbed by atom B. Therefore, atom A and atom B will not interact, i.e. $V_{\bullet\bullet}(\vartheta = 0) = 0$. If this photon propagates alone the x-direction it is linear polarized with a polarization vector along the y-direction. In the frame of atom C this photon will drive both σ_+- and σ_--transitions and thus can be absorbed. Hence, atom A can interact with atom C, i.e. $V_{\bullet\bullet}(\vartheta = \pi/2) \neq 0$.*

from the other m-states in the given fine structure manifold. This is necessary to protect these states from mixing with other Zeeman m-levels. Such unwanted couplings can be induced by van der Waals interactions (see Sec. 6.3.2 below), or via the light polarization of the Rydberg laser. This energetic protection requires an (effective) *local magnetic field*, which for the ● and ■ sites points in the x and z-direction, respectively. Strong local fields with spatial resolution on the scale given by the lattice spacing can be obtained via AC Stark shifts, combining the m-dependence of atomic AC tensor polarizabilities with spatially varying polarization gradients. Fig. 6.4 outlines a scheme, where we superimpose two pairs of counter propagating laser beams of wavelength λ_{AC} (light blue and magenta arrows). They create a standing wave pattern (light blue and magenta gradients), such that ● lattice sites only see the intensity maxima of the standing wave propagating along the z-direction (light blue laser), while ■ lattice sites see the intensity maxima of the standing wave propagating along the x-direction (magenta laser).

The AC Stark lasers have polarization σ_+ and resonantly couple the $nP_{3/2}$ manifold to a lower lying $n'D_{3/2}$ manifold (see magenta and blue arrows in the left and right panels of Fig. 6.4, respectively). This induces an AC-Stark shift on each Zeeman m-level in the $n^2P_{3/2}$ manifold. The Rabi frequency is proportional to $\Omega_{AC} \sim \sqrt{(m - \frac{3}{2})(m + \frac{5}{2})} \langle nP_{3/2}||r||n'D_{3/2}\rangle \mathcal{E}$ with $\mathcal{E}$ the electric field strength of the

AC Stark lasers. In this configuration the stretched states $|n^2P_{3/2}, m = 3/2\rangle_{z,x}$ of interest are not affected by the AC Stark lasers. The minimum shift (as a function of $m \neq 3/2$) is denoted E_{AC}, which has to obey $E_{\mathrm{AC}} \gg V_{\mathrm{off}}$ and $E_{\mathrm{AC}} \gg \Delta_r$ in order to suppress mixing between different m-states due to van der Waals interactions and the excitation laser. Here, V_{off} is the largest off-diagonal van der Waals matrix element in the $n^2P_{3/2}$ manifold (see App. 6.C).

The AC Stark lasers will create an additional trapping potential, $V_{AC}(\mathbf{r}_i)|g\rangle\langle g|_i$, for ground state atoms with minima not commensurate with the initial trapping lattice. In order to not distort the desired lattice structure this additional potential must not be larger than the initial lattice potential, see App. 6.A.

It is then possible to dress the ground state atoms with either the $|r_\bullet\rangle = |n^2P_{3/2}, m = 3/2\rangle_z$ or the $|r_\blacksquare\rangle = |n^2P_{3/2}, m = 3/2\rangle_x$ Rydberg state by a single, global laser with Rabi frequency Ω_r and detuning Δ_r propagating in the direction perpendicular to the plane, i.e. $\mathbf{k}_r \sim \mathbf{y}$ (dark blue arrow in Fig. 6.4). In the local x- and z-basis this laser will couple to all four $|m\rangle_{z,x}$ levels with different weights (see App. 6.B). Since the states $|m \neq 3/2\rangle_{z,x}$ are energetically separated by at least E_{AC} from the $|m = 3/2\rangle$ state a laser with detuning $\Delta_r \ll E_{\mathrm{AC}}$ and wave vector $\mathbf{k} \sim \mathbf{y}$ will selectively admix the states $|3/2\rangle_z$ and $|3/2\rangle_x$ at lattice sites ● and ■, respectively, to the ground state $|g\rangle$ with an effective Rabi frequency $\Omega_r' = \Omega_r/(2\sqrt{2})$. The single particle Hamiltonian describing the laser dressing in a frame rotating with the laser frequency for an atom i then becomes

$$H_i = -\Delta_r |r_{\alpha_i}\rangle\langle r_{\alpha_i}|_i + \frac{1}{2}\Omega_r' \left(|g\rangle\langle r_{\alpha_i}|_i + |r_{\alpha_i}\rangle\langle g|_i\right), \tag{6.7}$$

where $\alpha_i \in \{\bullet, \blacksquare\}$ depends on the lattice site of the i-th atom. In the weakly-dressing regime, $\Delta_r \gg \Omega_r$, the new dressed ground states are $|\bullet\rangle_i \equiv |g\rangle_i + \Omega_r/(2\Delta_r)|r_\bullet\rangle_i$ or $|\blacksquare\rangle_i \equiv |g\rangle_i + \Omega_r/(2\Delta_r)|r_\blacksquare\rangle_i$ if $\alpha_i = \bullet$ or $\blacksquare$, respectively. Thus, each ground state atom gets a small admixture of one of the Rydberg states, depending on the sublattice. Due to the weak admixture of the Rydberg states, the dressed ground states get a comparatively small decay rate $\tilde{\Gamma} = (\Omega_r/2\Delta_r)^2\Gamma$, where Γ is the decay rate of the bare Rydberg state, which has to be much smaller than the relevant system energy scales discussed below.

6.3.2 Interactions between *p*-states

Below we will consider the van der Waals interactions, $V_{\bullet\bullet}$, $V_{\bullet\blacksquare}$ and $V_{\blacksquare\blacksquare}$, between pairs of atoms prepared in the bare Rydberg states $|r_\bullet\rangle = |n^2P_{3/2}, m = 3/2\rangle_z$ and $|r_\blacksquare\rangle = |n^2P_{3/2}, m = 3/2\rangle_x$. For Rubidium atoms excited to Rydberg p-states, these van der Waals forces are strongly anisotropic [52–55]. Fig. 6.5(a) shows the angular part of the van der Waals interaction, $V_{\bullet\bullet}$, for different n-values, which is in very good approximation proportional to

$$V_{\bullet\bullet}(r, \vartheta) \sim \frac{(ea_0)^4 n^{11}}{r^6} \sin^4\vartheta, \tag{6.8}$$

while the actual strength depends on the principal quantum number n and scales as n^{11} away from the Förster resonance at $n = 38$. A detailed discussion of this scaling behavior and of the resonance origin can be found in Ref. [54]. Similarly, one finds for the interaction between $|r_\blacksquare\rangle = |n^2P_{3/2}, m = 3/2\rangle_x$ Rydberg states

$$V_{\blacksquare\blacksquare}(r, \vartheta) \sim \frac{(ea_0)^4 n^{11}}{r^6} \cos^4\vartheta, \tag{6.9}$$

Channel		$C_6^{(\nu)}$ [A.U.]		$\langle \frac{3}{2}\frac{3}{2}\lvert\mathcal{D}_\nu(\vartheta)\rvert\frac{3}{2}\frac{3}{2}\rangle$
ν	$n = 28$	$n = 30$	$n = 32$	
$S_{1/2} + S_{1/2}$	5.07×10^{17}	1.60×10^{18}	4.88×10^{18}	$\sin^4\vartheta/4$
$S_{1/2} + D_{3/2}$	1.60×10^{16}	3.72×10^{16}	8.15×10^{16}	$(2 + \cos 2\vartheta)\sin^2\vartheta/50$
$S_{1/2} + D_{5/2}$	1.62×10^{16}	3.76×10^{16}	8.26×10^{16}	$(209 + 84\cos 2\vartheta + 27\cos 4\vartheta)/2400$
$D_{3/2} + D_{3/2}$	-2.71×10^{15}	-5.85×10^{15}	-1.20×10^{16}	$(5 + 2\cos 2\vartheta + \cos 4\vartheta)/1250$
$D_{3/2} + D_{5/2}$	-2.43×10^{15}	-5.20×10^{15}	-1.06×10^{16}	$(358 + 186\cos 2\vartheta - 27\cos 4\vartheta)/15000$
$D_{5/2} + D_{5/2}$	-2.15×10^{15}	-4.56×10^{15}	-9.16×10^{15}	$3(1745 - 876\cos 2\vartheta + 27\cos 4\vartheta)/20000$

Table 6.1. *Two atoms both in the $|r_\bullet\rangle = |n^2P_{3/2}, 3/2\rangle_z = |np, 1\rangle_z|\frac{1}{2}\frac{1}{2}\rangle_z$ state can couple to six channels. Each channel ν has a characteristic angular dependency $(\mathcal{D}_\nu)_{\frac{3}{2}\frac{3}{2}}$ which contributes with weight $C_6^{(\nu)}$. The total interaction can be obtained by summing over all channels, i.e. $V_{\bullet\bullet}(r, \vartheta) = 2\sum_\nu C_6^{(\nu)}\langle\frac{3}{2}\frac{3}{2}|\mathcal{D}_\nu(\vartheta)|\frac{3}{2}\frac{3}{2}\rangle/r^6$. It turns out that two atoms in the $|r_\bullet\rangle$ Rydberg state dominantly couple to the $S_{1/2} + S_{1/2}$ channel with a characteristic angular dependence $\sim \sin^4\vartheta$.*

which can be obtained by rotating the coordinate system by $\pi/2$. Mixed interactions such as

$$V_{\bullet\blacksquare}(r, \vartheta) \sim \frac{(ea_0)^4 n^{11}}{r^6}\left(3\sin 2\vartheta + 2\right)^2, \tag{6.10}$$

are shown in Fig. 6.16 (App. 6.D) and have two asymmetric maxima at $\vartheta = \pm\pi/4$. The Rydberg states $|r_\bullet\rangle$ and $|r_\blacksquare\rangle$ therefore realize the desired angular interaction properties as discussed in Sec. 6.2.2. Together with the possibility of creating soft-core potentials (see the following subsection), the anisotropy of these interactions leads naturally to the desired interaction pattern illustrated in Fig. 6.1(b) and demanded by Eq. (6.6). These interactions underly our realization of the Bose Hubbard Hamiltonian (6.4).

We now detail the physical mechanism which generates these anisotropic interactions, and describe how to derive the aforementioned results. Van der Waals interactions between two atoms i and j prepared in a given Rydberg state arise from the exchange of virtual photons: atom i in a Rydberg state $|r_i\rangle$ can for example virtually undergo a dipole allowed transition to a lower-lying electronic state $|\alpha\rangle$ while emitting a photon. If this virtual photon reaches atom j during its lifetime, it can excite the second atom to an electronic state $|\beta\rangle$. This then leads to correlated oscillations of instantaneously induced dipoles in both atoms which give rise to the non-retarded van der Waals force [74]. For the familiar case of s-states these interactions are isotropic, $V_{\mathrm{VdW}}(r) = C_6/r^6$ with the van der Waals coefficient C_6 scaling as $C_6 \sim n^{11}$ [52–55]. Here, n is the principal quantum number and r the distance between atoms. These van der Waals interactions between Rydberg states exceed ground state interactions by several orders of magnitude and have been observed and explored in recent experiments [23–37].

In the case of Rydberg p-states, the angular distribution of these emission and absorption processes of virtual photons in combination with the angular momentum structure of the atomic orbitals leads to nontrivial anisotropic van der Waals interactions [52–55]. We now focus on the van der Waals interaction $V_{\bullet\bullet}$, between both atoms in the $|r_\bullet\rangle = |n^2P_{3/2}, m = 3/2\rangle_z$ Rydberg state with quantization axis along the z-direction. Mixed interactions, $V_{\bullet\blacksquare}$, and interactions between both atoms in the $|r_\blacksquare\rangle = |n^2P_{3/2}, m = 3/2\rangle_x$ Rydberg state, $V_{\blacksquare\blacksquare}$, will be derived in App. 6.C. The latter can simply

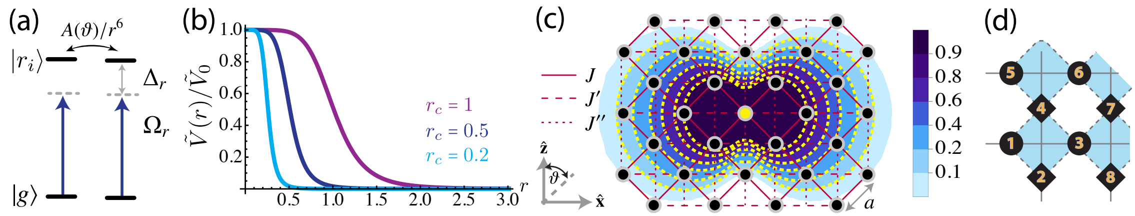

Figure 6.6. *(a) Qualitative sketch of the energy levels (black lines) and lasers (thick solid dark-blue arrows) required for the Rydberg dressing scheme. The ground state $|g\rangle$ of each atom is off-resonantly coupled to a Rydberg state $|r_i\rangle$ with a c.w. laser of Rabi frequency Ω_r and detuning Δ_r (see also Fig. 6.4). Pairwise interactions between the energetically well-isolated Rydberg states can be anisotropic, i.e. $V_{ij}(\mathbf{r}) = A(\vartheta)/r^6$. (b) Energy eigenvalues $\tilde{V}(\mathbf{r})$ of Eq. (6.14) (dressed Born-Oppenheimer potential surfaces) of Rydberg-dressed ground state atoms for different values of the Condon radius r_c defined in Eq. (6.15). The potential has a step-like shape and saturates for small distances at $\tilde{V}_0$, while the onset of the steep slope is given by r_c. (c) Contour plot of the dressed ground state interaction $\tilde{V}_{ij}(\mathbf{r})/\tilde{V}_0$ between the atom in the middle (yellow circle) and the surrounding atoms (black circles) arranged on a square lattice all in the $|r_\bullet\rangle$ Rydberg state. In this case $A(\vartheta) \sim \sin^4\vartheta$ which gives rise to a figure-eight shaped interaction plateau (yellow dashed lines). Residual interactions along $\vartheta = 0$ come from virtual transitions to D-states (see Sec. 6.3.2). (d) Labeling of the lattice sites for the example of Sec. 6.3.4.*

be obtained by rotating the xz-plane by 90 degrees, i.e. $V_{\blacksquare\blacksquare}(r,\vartheta) = V_{\bullet\bullet}(r,\vartheta-\pi/2)$, while in order to calculate mixed interactions one has to calculate off-diagonal matrix elements in the $n^2P_{3/2}$ manifold.

In general, van der Waals interactions arise as a second order process from dipole-dipole interaction, $\hat{V}_{\mathrm{dd}}^{(ij)}(\mathbf{r}) = \left(\mathbf{d}^{(i)}\cdot\mathbf{d}^{(j)} - 3(\mathbf{d}^{(i)}\cdot\mathbf{n})(\mathbf{d}^{(j)}\cdot\mathbf{n})\right)/r^3$, where V_{dd} couples the initial Rydberg states $|r_i, r_j\rangle$ to virtual intermediate states $|\alpha,\beta\rangle$ and back. Here, $\mathbf{d}^{(i)}$ is the dipole operator of the i-th atom and $\mathbf{r} = r\mathbf{n} = (r,\vartheta,\varphi)$ is the relative distance between atom i and atom j with $\mathbf{n}$ a unit vector and (r,ϑ,φ) the spherical coordinates. It is convenient to rewrite the latter expression in a spherical basis [75]

$$\hat{V}_{\mathrm{dd}}^{(ij)}(\mathbf{r}) = -\sqrt{\frac{24\pi}{5}}\,\frac{1}{r^3}\sum_{\mu,\nu} C^{1,1;2}_{\mu,\nu;\mu+\nu}\, Y_2^{\mu+\nu}(\vartheta,\varphi)^*\, d_\mu^{(i)} d_\nu^{(j)}, \tag{6.11}$$

with $d_\mu^{(i)}$ the spherical components ($\mu,\nu \in \{-1,0,1\}$) of $\mathbf{d}^{(i)}$, $C^{j_1,j_2;J}_{m_1,m_2;M}$ the Clebsch-Gordan coefficients, and Y_l^m the spherical harmonics.

Due to the dipole selection rules, states in the $n^2P_{3/2}$ manifold can only couple to states in a $n'S_{1/2}$, $n'D_{5/2}$ or $n'D_{3/2}$ manifold. It turns out that for ^{87}Rb the dominating channel is $P_{3/2} + P_{3/2} \longrightarrow S_{1/2} + S_{1/2}$, which can be explicitly seen from Table 6.1 for various n levels. In order to simplify the following discussion we will first focus on this channel and neglect all other channels including $D_{3/2}$ and $D_{5/2}$ states which lead to small imperfections discussed in App. 6.C.

For a single atom, the $|n^2P_{3/2}, \frac{3}{2}\rangle$ state is a *stretched-state* which reads in the uncoupled basis $|n^2P_{3/2}, \frac{3}{2}\rangle \equiv |np, 1\rangle \otimes |\frac{1}{2}, \frac{1}{2}\rangle$. Thus, it can be factorized into an angular and a spin degree of freedom. Since the dipole-dipole interaction, $\hat{V}_{\mathrm{dd}}(\mathbf{r})$, does not couple spin degrees of freedom, the angular dependence of the van der Waals interaction is determined solely by the angular part of the wave function, which is $|np, 1\rangle$.

Figure 6.5(b) illustrates the interaction between two atom initially prepared in a $|np, 1\rangle$ state as a function of ϑ for $\vartheta = 0$ (atom A and B) and $\vartheta = \pi/2$ (atom A and C). We first consider atom A in the lower left corner of Fig. 6.5(b). Initially prepared in a $|np, 1\rangle$ state it can make a virtual transition to a lower-lying $|ns, 0\rangle$ state [red arrow in the lower left panel of Fig. 6.5(b)] while emitting a photon. The corresponding angular distribution of the spontaneously emitted photon has the same characteristic as light emitted by a classical dipole tracing out a circular trajectory in the x-y plane [75]. In general, it is elliptically polarized with cylindrical symmetry, but in particular there are two specific directions:

(i) light emitted along the z direction ($\vartheta = 0$) is circularly polarized, rotating in the same way as the dipole. Thus, a photon emitted in the z direction has polarization σ_+ and carries one unit of angular momentum such that the total angular momentum of the combined system atom-photon is conserved. A second atom, labeled as atom B in Fig. 6.5(b), located on the z axis ($\vartheta = 0$) cannot absorb this photon [see red arrow in the upper left panel of Fig. 6.5(b)], since only a $|n's, 0\rangle$ state is available. The same result can be derived from Eq. (6.11), which for $\vartheta = 0$ simplifies to

$$\hat{V}_{\mathrm{dd}}^{(ij)}(\vartheta = 0) = -\frac{2}{r^3}\sum_{\mu}\frac{d_{\mu}^{(i)}d_{-\mu}^{(j)}}{(1-\mu)!(1+\mu)!}, \tag{6.12}$$

and couples only states with initial magnetic quantum number m_1, m_2 to states with $m_1 \pm 1, m_2 \mp 1$, such that the total angular momentum $M = m_1 + m_2$ is conserved. Therefore, the dipole-dipole matrix element vanishes, $\langle np1, np1|\hat{V}_{\mathrm{dd}}^{(AB)}(\vartheta = 0)|ns0, n's0\rangle = 0$, and hence atoms A and B do not interact.

(ii) light emitted into the x-y plane ($\vartheta = \pi/2$) is linearly polarized, with a polarization vector lying in the x-y plane and perpendicular to the emission direction. A third atom, labeled as atom C in Fig. 6.5(b), located on the x axis is able to absorb this linearly polarized photon emitted by atom A, which in the frame of atom C corresponds to a superposition of σ_+ and σ_- polarized light [see red arrows in the right panel of Fig. 6.5(b)]. For $\vartheta = \pi/2$, Eq. (6.11) contains a sum over $\cos[\frac{\pi}{2}(\mu + \nu)]$, and the only non-vanishing combinations for $\mu = -1$ are $\nu = \pm 1$. Thus, the dipole matrix element $\langle np1, np1|\hat{V}_{\mathrm{dd}}^{(AC)}(\vartheta = \pi/2)|ns0, n's0\rangle$ is non zero and atom A and C will interact.

In general, for the dominant channel $P_{3/2} + P_{3/2} \longrightarrow S_{1/2} + S_{1/2}$ only the term $d_{-1}^{(1)}d_{-1}^{(2)}$ with $\mu = \nu = -1$ in Eq. (6.11) can contribute to the dipole-dipole matrix element and thus the van der Waals interaction between both atoms in a $n^2P_{3/2}, m = 3/2$ states becomes $V_{\frac{3}{2},\frac{3}{2}}^{(n)}(r, \vartheta, \varphi) \sim (Y_2^{-2})^2 \sim \sin^4\vartheta$ for this channel. Residual interactions at $\vartheta = 0$ and π come from couplings to $D_{3/2,5/2}$ channels which are small, see Tab. 6.1. Thus, using Rubidium $n^2P_{3/2}$ states with $m_j = 3/2$ allows an almost perfect realization of an anisotropic interaction with vanishing interaction along one axis and large interaction along a perpendicular axis. Note that interactions between two atoms in a $|n^2P_{3/2}, m = 3/2\rangle$ are negative (attractive) for $n > 38$ and positive (repulsive) for $n < 38$, where a Förster resonance at $38P_{3/2} + 38P_{3/2} \longrightarrow 38S_{1/2} + 39S_{1/2}$ changes the sign of the interaction [52–55]. Figure 6.5(a) shows the result of the the full calculation of the van der Waals interactions between $n^2P_{3/2}, 3/2$ states including all channels and summing over n' and n'' levels between $n \pm 10$. The full calculation agrees well with the simplified picture discussed above and illustrated in Fig. 6.5(b) since the dominating channel is the one coupling to $S_{1/2}$ states. Moreover, it is in full agreement with previous studies on anisotropic interactions between Rb Rydberg states [54].

6.3.3 Soft-core potentials

In the previous section we showed how to engineer the anisotropic part of the interactions required by Eq. (6.6). We now briefly review how to create soft-core potentials by weakly admixing the Rydberg

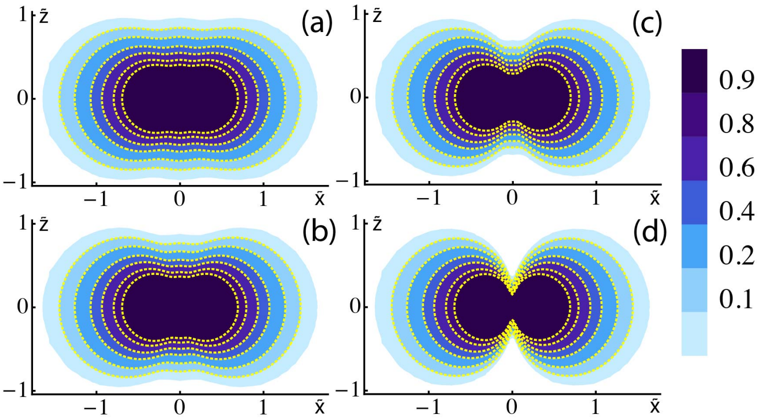

Figure 6.7. *Soft core potentials (in units of $\tilde{V}_0$) of Eq.* (6.14) *between* $n^2P_{3/2}$, $m_j = 3/2$ *Rydberg states with (a)* $n = 25$, $A(\frac{\pi}{2}, 0) = 2\pi \times 6.3$ *MHz* μm^6 *(b)* $n = 30$, $A(\frac{\pi}{2}, 0) = 2\pi \times 114.8$ *MHz* μm^6, *(c)* $n = 36$, $A(\frac{\pi}{2}, 0) = 2\pi \times 4.8$ *GHz* μm^6 *and (d)* $n = 38$, $A(\frac{\pi}{2}, 0) = 2\pi \times 390.0$ *GHz* μm^6. *Here,* $\tilde{x} = x/r_c(\frac{\pi}{2}, 0)$ *and* $\tilde{z} = z/r_c(\frac{\pi}{2}, 0)$ *are dimensionless, with* r_c *defined in Eq.* (6.15). *Residual interactions along the z-direction come from virtual transitions to D-channels and depend on the principal quantum number n, see Tab. 6.1.*

states to the atomic ground state [56, 59]. This guarantees that interactions between atoms sitting on a square lattice at different distances a and $\sqrt{2}a$ experience the same interaction potential [76], as required by Eq. (6.6) and illustrated in Fig. 6.1(b).

The single atom configuration we have in mind was introduced in Sec. 8.B and is governed by the Hamiltonian of Eq. (6.7). Pairwise interactions [see panel (a) of Fig. 6.6] between N atoms both excited to the Rydberg states $|r_i\rangle|r_j\rangle$ are described by

$$H_{ij}(\mathbf{r}_{ij}) = V_{ij}(\mathbf{r})|r_i\rangle\langle r_i| \otimes |r_j\rangle\langle r_j|, \tag{6.13}$$

where $V_{ij}(\mathbf{r}_{ij}) = A_{ij}(\vartheta_{ij}, \varphi_{ij})/r_{ij}^6$ is the van-der-Waals interaction potential between the Rydberg states of atom i and atom j discussed in the previous section and $(r_{ij}, \vartheta_{ij}, \varphi_{ij})$ are the spherical coordinates of the relative vector.

Following the s-state case [57–60], Brillouin-Wigner perturbation theory up to fourth order in the small parameter $\Omega_r/(2\Delta_r) \ll 1$ results in a sum of binary interaction between the dressed ground state atoms of the form

$$\tilde{V}_{ij} = 2\Delta_r \left(\frac{\Omega_r}{2\Delta_r}\right)^4 \frac{r_c^6(\vartheta_{ij}, \varphi_{ij})}{r_c^6(\vartheta_{ij}, \varphi_{ij}) + r_{ij}^6}, \tag{6.14}$$

with

$$r_c(\vartheta_{ij}, \varphi_{ij}) = \left(\frac{A_{ij}(\vartheta_{ij}, \varphi_{ij})}{2|\Delta_r|}\right)^{1/6} \tag{6.15}$$

being the Condon radius. In the case of p-Rydberg states, where the interactions are *anisotropic*, the Condon radius depends on the angular pattern of the van der Waals interaction $A(\vartheta, \varphi)$ which can be tuned by choosing a particular Rydberg state. Additionally, the Condon radius can be scaled by changing the detuning Δ_r of the dressing laser. Figure 6.6(b) shows typical examples of the dressed ground state potential, $\tilde{V}_{ij}$, for red detuning $\Delta_r < 0$ and repulsive interactions $V_{ij} > 0$, for different Condon radii, r_c. For large distances, $r \gg r_c$, the dressed ground state potential is proportional to the Rydberg interaction, $\tilde{V}_{ij} = \Omega_r^4/(2\Delta_r)^4 V_{ij} \sim 1/r_{ij}^6$, reduced by a factor $[\Omega_r/(2\Delta_r)]^4$ arising from the small probability to excite both atoms to the Rydberg state. However, for small distances, $r < r_c$, when two atoms are within the Condon radius, the excitation to the Rydberg states becomes ineffective due to the large total detuning $|\Delta_r| + V_{ij}$ (Dipole blockade), and the effective ground state interaction, $\tilde{V}_{ij} \approx \tilde{V}_0[1 - (r/r_c)^6]$ for $r < r_c$, saturates at a constant value $\tilde{V}_0 = \Omega_r^4/(2\Delta_r)^3$, which is independent of the strength or form of the Rydberg-Rydberg interactions. The presence of a plateau at short distances, $r < r_c$ and a rapid decrease of the potential at $r \sim r_c$, where $\tilde{V}_{ij} \sim 1/r_{ij}^6$, allows to engineer approximately equal interactions between atoms within r_c independent of their specific distance. At the same time, long-range interactions, between e.g. next-nearest-neighbors (NNN), are substantially suppressed.

Combining the step-like ground state potentials of Eq. (6.14) with anisotropic interactions discussed in the previous section leads to figure-eight shaped plateau potentials shown in Fig. 6.6(c). Here, atoms (black circles) interact with J, J' and J'' along the ± 45-degree lines, the x-axis and the z-axis, respectively, with the atom in the middle (yellow circle). It is possible to tune the interaction strength J, J' and J'' over a large range by e.g. changing the detuning, Δ_r, or the principal quantum number, n, of the Rydberg state. In particular one can realize an interaction pattern where atoms sitting at different distances, a and $\sqrt{2}a$, interact with equal strength, that is $J \approx J'$, while $J'' \ll J$, thus realizing a frustrated $J - J'$ model. Note that the interaction symmetry in this case is triangular on top of an square lattice.

6.3.4 Explicit numbers and discussion of imperfections

As an explicit example we consider the $29\,{}^2P_{3/2}$ Rydberg manifold of ^{87}Rb. We resonantly couple the $29\,{}^2P_{3/2}$ manifold to the lower-lying $7\,{}^2D_{3/2}$ manifold, as illustrated in Fig. 6.4 ($n = 29$ and $n' = 7$), with a laser of wavelength $\lambda_{AC} = 3.296\,\mu$m. This results in a lattice spacing $a = \lambda_{AC}/(2\sqrt{2}) = 1.16\,\mu$m which can be adjusted by tilting the trapping lasers by an angle $\alpha = 39$ degrees (see Sec. 8.B).

For the van der Waals interactions between the Rydberg states $|r_\bullet\rangle = |29\,{}^2P_{3/2}, 3/2\rangle_z$ and $|r_\blacksquare\rangle = |29\,{}^2P_{3/2}, 3/2\rangle_x$ we find

$$\begin{aligned}
V_{\bullet\bullet}(r,\vartheta) &= 2\pi \times \frac{25.4 - 31.9\cos 2\vartheta + 8.2\cos 4\vartheta}{(r/\mu\mathrm{m})^6}\,\mathrm{MHz},\\
V_{\blacksquare\blacksquare}(r,\vartheta) &= 2\pi \times \frac{25.4 + 31.9\cos 2\vartheta + 8.2\cos 4\vartheta}{(r/\mu\mathrm{m})^6}\,\mathrm{MHz},\\
V_{\bullet\blacksquare}(r,\vartheta) &= 2\pi \times \frac{16.8 - 8.2\cos 4\vartheta + 20.3\sin 2\vartheta}{(r/\mu\mathrm{m})^6}\,\mathrm{MHz},
\end{aligned} \tag{6.16}$$

including all channels of Tab. 6.1 and summing over ±10 n-values (see App. 6.C and 6.D). They are plotted in Fig. 6.5(a) and Fig. 6.16. The largest off-diagonal matrix element coupling different Zeeman m-levels is $V_{\mathrm{off}}(a) = \langle \tfrac{3}{2}\tfrac{3}{2}|\hat{V}_{\mathrm{vdW}}(a,\pi/2)|\tfrac{1}{2}\tfrac{1}{2}\rangle = 2\pi{\times}11.2\,\mathrm{MHz}$. Using an AC Stark laser with power $P = 1.0$ mW focused on a area $A = 50\,\mu\mathrm{m}^2$ yields a Rabi frequency $\Omega_{AC} = 2d_{7D-29P}\mathcal{E}_{AC}/\hbar = 2\pi \times 205.5$ MHz, where $d_{7D-29P} = \langle 7D_{3/2}, 3/2|d|29P_{3/2}, 1/2\rangle = 0.065\,ea_0$ is the smallest transition dipole moment and $\mathcal{E}_{AC} = \sqrt{2P/c\epsilon_0 A}$ is the electric field strength. The AC Stark lasers will create an additional ground

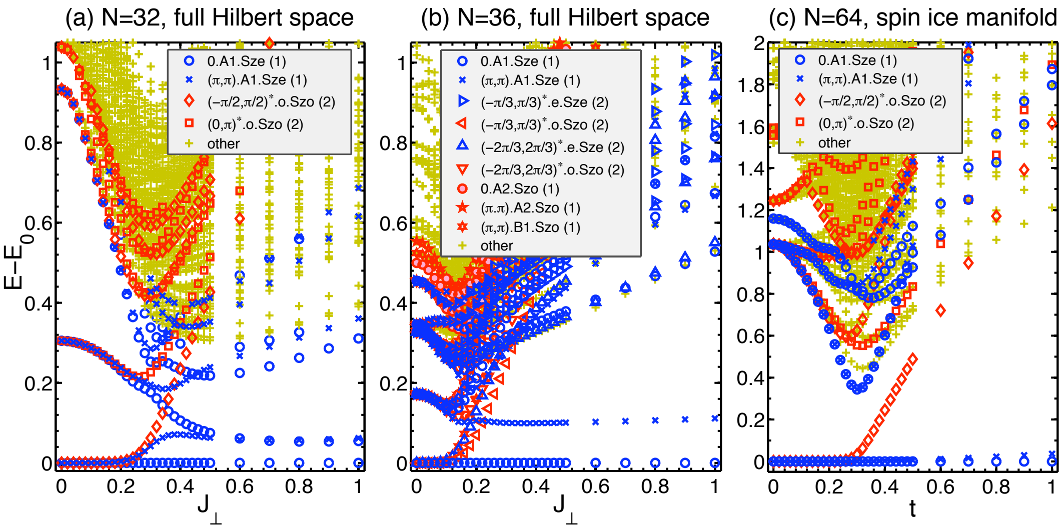

Figure 6.8. *(a-b) Low energy spectra of H (in units of $\tilde{V}_0$) versus $J_\perp$ for N=32 (a) and 36 (b), in the total magnetization sector $S_z = 0$ and for cutoff $J_c = 0.001$. (c) Low energy spectra of the constrained, spin-ice model H_2 versus t for 64 sites. The eigenstates are labeled by linear momentum* **k**, *the irreducible representations of the point group of* **k** *(the point group of the model is C_{2v}), and parity under spin inversion ("Sze" and "Szo" stand for even and odd parity, respectively). Numbers inside parentheses give the multiplicity of each energy level.*

state potential with depth $V_{AC} = 2\pi \times 27.8$ kHz thus the initial trapping potential, V_{trap}, must be larger than V_{AC}, see App. 6.A.

Adjusting the detuning Δ_r of the Rydberg laser allows to tune the length scale and the imperfections in Eq. (6.14). These are (i) small long-range interactions between nearest-neighbor lattice sites and (ii) deviations form the constraint model of Eq. (6.6). Here, for example we use $\Delta_r = 2\pi \times 400$ kHz which yields the following interaction pattern between particles labeled in Fig. 6.6(d): $\tilde{V}_{14}/\tilde{V}_0 = \tilde{V}_{23}/\tilde{V}_0 = 0.96$, $\tilde{V}_{13}/\tilde{V}_0 = \tilde{V}_{24}/\tilde{V}_0 = 0.80$, $\tilde{V}_{12}/\tilde{V}_0 = \tilde{V}_{34}/\tilde{V}_0 = 0.70$ around a vertex and small imperfect interactions between different vertices, e.g. $\tilde{V}_{15}/\tilde{V}_0 = \tilde{V}_{28}/\tilde{V}_0 = 0.09$ and next-nearest-neighbor interactions e.g. $\tilde{V}_{16}/\tilde{V}_0 = \tilde{V}_{27}/\tilde{V}_0 = 0.12$ or $\tilde{V}_{18}/\tilde{V}_0 = \tilde{V}_{25}/\tilde{V}_0 = 0.01$.

By varying the Rabi frequency of the Rydberg laser $\Omega_r = 2\pi \times (120, 160, 200)$ kHz one obtains $\epsilon = \Omega_r/2\Delta_r = (0.15, 0.20, 0.25)$ which gives rise to an effective ground state interaction $\tilde{V}_0 = \Omega_r^4/8\Delta_r^3 = 2\pi \times (405, 1280, 3125)$ Hz. This is much larger than the effective decay rate from the dressed ground state $\tilde{\Gamma} = \epsilon^2\Gamma = 2\pi \times (74, 132, 206)$ Hz, and larger than a corresponding tunneling rate between the minima. Here, $\Gamma = 2\pi \times 3.3$ kHz is the decay rate form the Rydberg states.

There is an ample choice in the parameter regimes available as a function of the n-level. Away from the Förster resonance at $n = 38$, it is possible to engineer infra-red lattices which allow for comparable timescales between the interactions induced by the dressing, and the tunneling matrix elements of the atoms on the original square lattice. Going higher in n, closer to the Förster resonance, allows faster timescales and slower decays: however, in this case the infra-red laser has a strong influence on the underlying lattice, excluding the possibility of using conventional single particle tunneling to induce quantum fluctuations. On the other hand, one can profit here from the richness of the Rydberg manifolds involved, realizing the hopping matrix element as a spin-exchange coupling between different atoms sitting at different potential minima [1]. In both cases above, the interaction pattern will depend on the specific targeted n, as discussed in Sec. 6.3.2. As the qualitative (and in many respects quantitative, as indicated in Table 6.1 and Fig. 6.7) shape of the interactions will be very similar in the interval of interest $n = 25 - 37$, we will focus in the following on a single case sample to underpin the stability of the many-body effects we are interested in.

6.4 Numerical results

In this section, we consider the properties of the approximate realization of the quantum spin ice model Hamiltonian proposed above. We demonstrate that, as a function of the strength of the quantum dynamics, the ground state has two regimes reflecting two distinct forms of ordering (Sec. 6.4.2). One, stabilized via a quantum order by disorder mechanism, generates the above mentioned plaquette phase for sufficiently strong quantum dynamics. As it is weakened, there is a transition into a phase with classical ordering, which is stabilized by the long-range parts of the dipolar couplings and which breaks translational symmetry in a different way. In addition, we show that even without quantum dynamics, there is an interesting thermal phase transition to an approximate realization of a (classical) Coulomb phase, with only a very small density of defects (plaquettes violating the ice rule) of around 5% (Sec. 6.4.3). We discuss signatures of these items in various quantities, in particular proposing a simple correlation function in which the quantum plaquette order will be visible, and which should be accessible in cold atom experiments via *in-situ* parity measurements [33, 77, 78].

6.4.1 General definitions and conventions

We begin with some general definitions and technical details of our numerical study. We consider both the unconstrained spin-1/2 model H from by Eq. (6.5), as well as the projected model H_2 inside the spin ice manifold:

$$\begin{aligned} H &= \sum_{i<j} J_{ij} S_i^z S_i^z + J_\perp \sum_{\langle ij \rangle} \left(S_i^+ S_j^- + S_i^- S_j^+ \right) \\ H_2 &= \sum_{i<j} J_{ij} S_i^z S_j^z - t \sum_{{}_i^j\square_l^k} \left(S_i^+ S_j^- S_k^+ S_l^- + h.c. \right) . \end{aligned}$$

Here $\langle ij \rangle$ denote nearest-neighbor (NN) sites on the 2D checkerboard lattice, and $(ijkl)$ label clockwise the four sites around empty square plaquettes. Note that only the empty plaquettes with alternating up-down spins (or ‘flippable’ plaquettes) contribute to the second term of H_2. In our Exact Diagonalizations (ED) we have considered finite-size clusters with periodic boundary conditions and N=16, 32, 36, 64 and 72 sites, see details in App. 6.E. To treat these clusters with ED, we exploit translational symmetry, point group operations (the model has C_{2v} symmetry), as well as spin inversion ($S_z \rightarrow -S_z$) inside the total magnetization sector $S_z = 0$. Consequently, the eigenstates are labeled by linear momentum $\mathbf{k}$, the irreducible representations of the point group of $\mathbf{k}$, and the parity under spin inversion.

---

[1] A. W. Glaetzle, *et. al., in preparation*

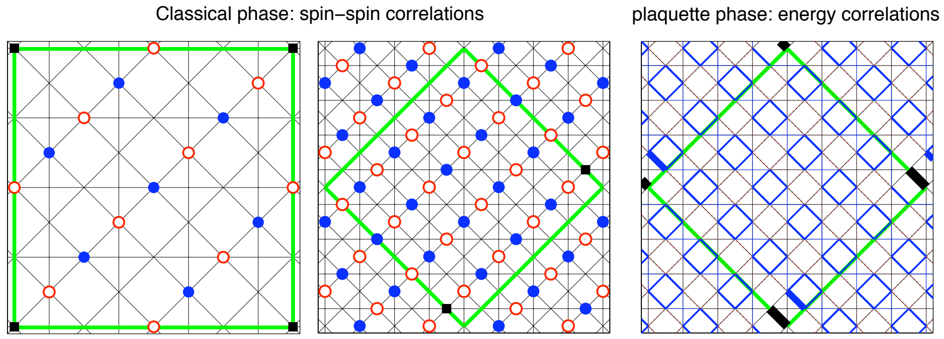

(a) N=32, full Hilbert space, $J_\perp$=0.1 (b) N=64, spin–ice manifold, t=0.1 (c) N=64, spin–ice manifold, t=1

Figure 6.9. *Ground state diagnostics of the classical (a-b) and the QM plaquette (c) phases: Spin-spin correlation profiles (of the type* $\langle S^z_i S^z_j\rangle$*, where i is the reference site, indicated by filled black square) in the ground state of (a) H for N=32 and* $J_\perp = 0.1$*, and (b)* H_2 *for N=64 and* $t = 0.1$*. Filled blue (open red) circles corresponds to positive (negative) amplitude. (c) Connected energy correlation profiles (of the type* $\langle S^z_i S^z_j S^z_k S^z_l\rangle - \langle S^z_i S^z_j\rangle\langle S^z_k S^z_l\rangle$*, where the reference bond* (ij) *is indicated by the thick black segment) in the ground state of* H_2 *for N=64 and* $t = 1$*. Solid blue (dashed red) bonds indicate positive (negative) amplitudes, while the width of each bond scales with the magnitude. All data correspond to the symmetry sector "0.A1.Sze" and are taken for cutoff* $J_c = 0.001$.

We note that, whereas the quantum phase is quite robust, the classical phase is considerably less so, reflecting the many nearly-degenerate classical ice states. We illustrate this in App. 6.F by imposing a variable cut-off on the long-range aspect of the dipolar couplings J_{ij}: by neglecting terms weaker than a cutoff J_c, we find a set of states with different classical orders, which settle down into the correct ground state without truncation for J_c no larger than 0.001.

6.4.2 The two zero-temperature phases: Low-energy spectroscopy and ground state diagnostics

Figure 6.8 shows the low energy spectra of H as a function of $J_\perp$ for N=32 (a) and N=36 (b), and that of H_2 as a function of t for N=64 (c). All spectra correspond to the total magnetization sector $S_z = 0$ and a cutoff value of $J_c = 0.001$. In all spectra, there is a manifold of low-lying states that is well separated from higher-energy excitations. Provided they become degenerate in the thermodynamic limit, these states are the finite-size fingerprints of the spontaneously symmetry broken phases [79–83]: their multiplicities and symmetry content reveal the nature of the ground state. The structure of the low-lying energy states show consistently two qualitatively different phases. One, which is adiabatically connected to the classical limit $J_\perp = 0$, and the other which is stabilized for large enough $J_\perp$ or t.

We begin with the classical phase, focusing on the N=32 (a) and N=64 (c) results first. Here we find four low-lying states which become exactly degenerate as $J_\perp \to 0$. We find translational symmetry breaking with ordering wavevector $\mathbf{Q} = (-\frac{\pi}{2}, \frac{\pi}{2})$, as illustrated in Fig. 6.3(c). The nature of this phase is revealed by the spin-spin correlation profiles of Figs. 6.9(a-b), with alternating up-down spins along one of the two diagonal directions of the lattice. The vanishing of correlations on

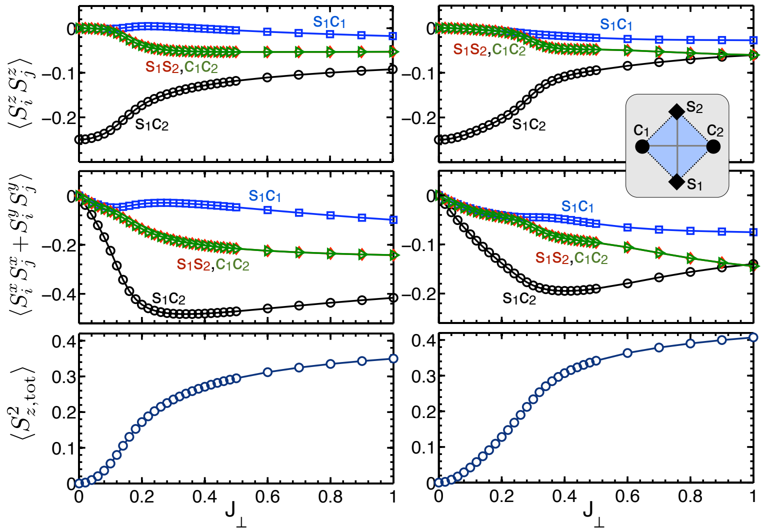

Figure 6.10. *Various expectation values in the ground state of H for N=16 (left column) and 32 (right column), for cutoff* $J_c = 0.001$. *The first two panels in each column show the NN spin-spin correlations for all symmetry inequivalent bonds (inset) in the longitudinal and transverse (xy) channel. The bottom panels show the square of the total magnetization per crossed plaquette, which is a measure of the weight from states outside the spin ice manifold.*

every second diagonal line arises due to the existence of two states compatible with the non vanishing correlations on the other diagonals. For a finite cluster, these appear with equal weight and thus average out, while in the thermodynamic limit, symmetry breaking selects either one of the two spontaneously. Finally, the N=36 cluster cannot accommodate the $\mathbf{Q} = (-\frac{\pi}{2}, \frac{\pi}{2})$ phase (see App. 6.F), which is why the low-lying sector of Fig. 6.8(b) has a different structure (and, in fact, higher ground state energy per site, see Table 6.2).

Turning to the quantum phase, the N=32 and 64-site spectra give the onset of this phase around $J_\perp \simeq 0.23$ and $t \simeq 0.28$, respectively. Beyond this point, the spin structure factor (not shown) is completely structureless, indicative of the absence of magnetic (classical) ordering. Since the imperfections in the present spin-ice model are expected to become irrelevant for large enough $J_\perp$, this phase must be the plaquette phase of the pure spin-ice model [11, 71] and the pure Heisenberg model [84]. The standard diagnostic for this phase is the dimer-dimer (or energy-energy) correlations, and indeed the correlation profiles of Fig. 6.9(c) show a strong $\mathbf{Q} = (\pi, \pi)$ response within one sublattice of empty plaquettes. This is consistent with the structure of the low-lying spectra which show two low-lying states with momenta $\mathbf{k} = 0$ and (π, π) which come almost on top of each other for N=64, see Fig. 6.8(c). Note that for N=32, there is a third low-lying state (with $\mathbf{k} = 0$) which is however not related to the physics at the thermodynamic limit but it is specific to the special topology of this cluster [2].

Further information about the two phases is given in Fig. 6.10, which shows the GS expectation values of the longitudinal and transverse NN spin-spin correlations for all symmetry-inequivalent

---

[2] Such "extra" low-lying states are also present in the pure Heisenberg model and are related to extra symmetries of the 32-site cluster [84]

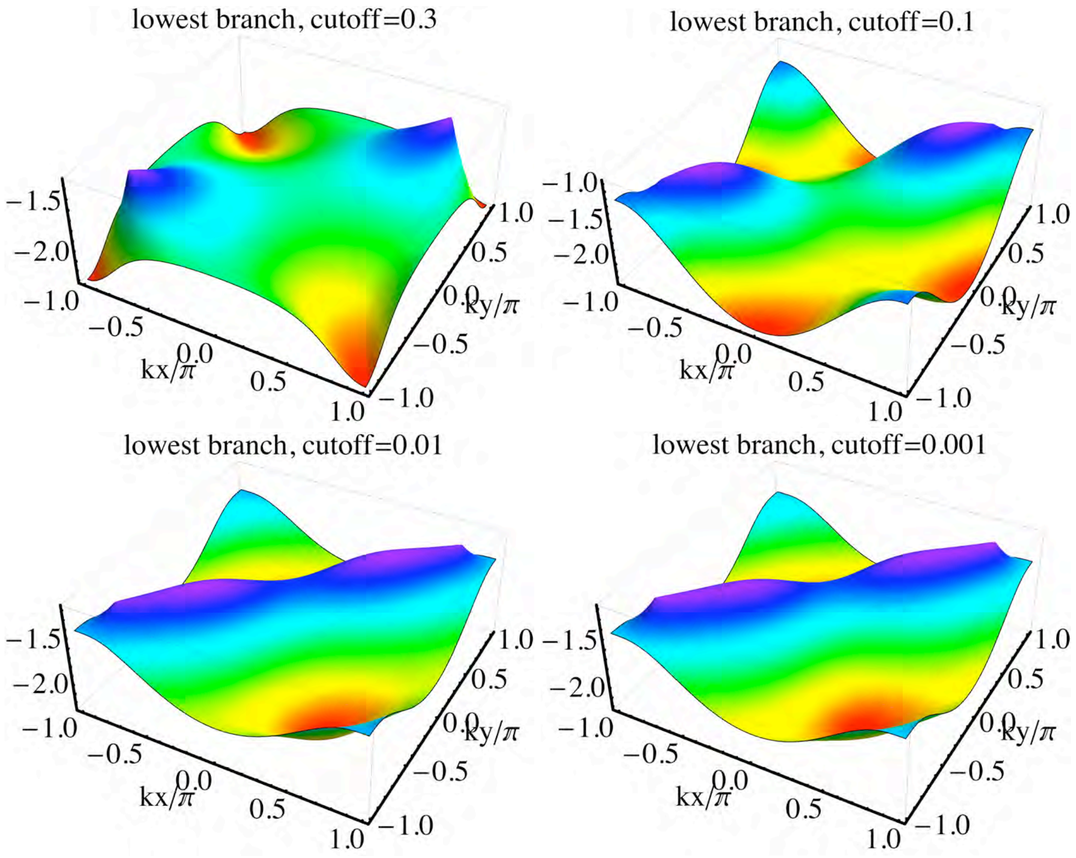
lowest branch, cutoff=0.3

lowest branch, cutoff=0.1

lowest branch, cutoff=0.01

lowest branch, cutoff=0.001

Figure 6.11. *Dispersion of the lowest eigenvalue* $\lambda_1(\mathbf{k})$ *(in units of* $\tilde{V}_0$*) of the dipolar interaction matrix* $\mathbf{\Lambda}(\mathbf{k})$ *(in the thermodynamic limit) for four different values of cutoffs.*

bonds, as well as the square magnetization of crossed plaquettes. The former describe how the energy is distributed over the bonds and over the different directions in spin space, while the latter is a measure of the admixture from states outside the spin ice manifold. First, the NN correlations show that the spins fluctuate mostly along the z-axis for small $J_\perp$, as expected. More importantly, most of the energy comes from antiferromagnetic bonds along one of the two diagonal directions (bonds labeled 's_1c_2' in the inset of Fig. 6.10), which is a clear signature of the presence of strongly asymmetric spin-spin correlations in this regime. This asymmetry, which is inherited by the point group symmetry (C_{2v}) of the model, is more directly revealed in the spin structure factor discussed above. Second, the qualitative change in the behavior of the NN correlations around $J_\perp \sim 0.2$, reflects the presence of the phase transition in this region. Finally, the square of the total magnetization per crossed plaquette reveals that the spin-ice manifold remains well protected up to relatively high $J_\perp$.

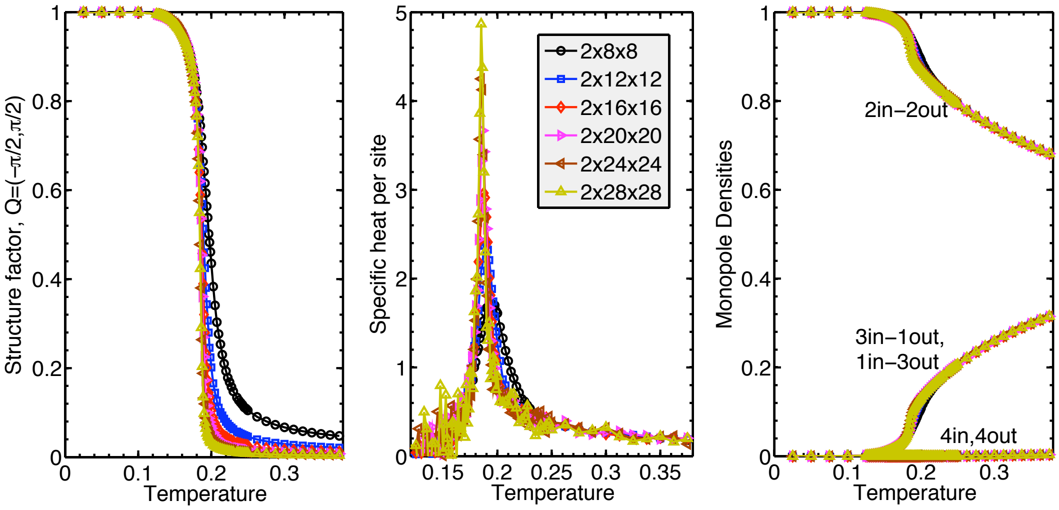

Figure 6.12. *Temperature dependence of the structure factor* $\mathcal{S}(\mathbf{Q})$ *(left), the specific heat per site, in units of Boltzmann's constant* k_B *(middle) and the monopole densities for systems up to N=2x28x28 sites, for* $J_\perp = 0$ *and cutoff* $J_c = 0.001$*. Temperature is given in units of* $\tilde{V}_0$*.*

6.4.3 Further insights in the classical limit $J_\perp = 0$

Momentum space minimization

The nature of the classical phase and the role of the dipolar couplings can be understood in more detail by a closer examination of the limit $J_\perp = 0$ using a classical minimization treatment in momentum space [85–88]. The checkerboard lattice has a square Bravais lattice with two sites per unit cell. In the following, sites are labeled as $i \to (\mathbf{R}, \alpha)$, where $\mathbf{R}$ gives the position of the unit cell, and $\alpha = 1$-2. For $J_\perp = 0$, we can replace $S_i^z \to \frac{1}{2}\sigma_i$, where $\sigma_i = \pm 1$. The total energy then reads $E = \frac{1}{4}E'$, where

$$E' = \frac{1}{2} \sum_{\mathbf{R}\mathbf{R}',\alpha\alpha'} J_{\mathbf{R}\alpha,\mathbf{R}'\alpha'} \sigma_{\mathbf{R},\alpha} \sigma_{\mathbf{R}',\alpha'} .$$

Using $\sigma_{\mathbf{R},\alpha} = \frac{1}{\sqrt{N_{uc}}} \sum_{\mathbf{k}} e^{i\mathbf{k}\cdot\mathbf{R}} \sigma_{\mathbf{k},\alpha}$, where $N_{uc} = N/2$ is the number of unit cells, and $J_{\mathbf{R}\alpha,\mathbf{R}'\alpha'} = J_{\mathbf{R}-\mathbf{R}',\alpha\alpha'}$ (from translational invariance), yields

$$E' = \frac{1}{2} \sum_{\mathbf{k}} \sum_{\alpha\alpha'} \sigma_{\mathbf{k},\alpha} \Lambda_{\alpha\alpha'}(\mathbf{k}) \sigma_{-\mathbf{k},\alpha'},$$

where the 2×2 interaction matrix $\mathbf{\Lambda}(\mathbf{k})$ is given by

$$\Lambda_{\alpha\alpha'}(\mathbf{k}) \equiv \sum_{\mathbf{r}} J_{\mathbf{r},\alpha\alpha'} e^{-i\mathbf{k}\cdot\mathbf{r}} .$$

Let us denote by $\lambda_{1,2}(\mathbf{k})$ and $\mathbf{v}_{1,2}(\mathbf{k})$ the eigenvalues and the corresponding (normalized) eigenvectors of $\mathbf{\Lambda}(\mathbf{k})$, with $\lambda_1(\mathbf{k}) \leq \lambda_2(\mathbf{k})$. Minimizing $\lambda_1(\mathbf{k})$ over the entire BZ of the model provides a lower bound for the energy [85–88]. The corresponding eigenvector is a faithful ground state provided it satisfies the spin length constraint at all sites.

The minimization can be done both for the infinite lattice and for the finite lattices studied by ED by simply scanning through the allowed momenta of each cluster. The latter are discussed in App. 6.F and are useful for clarifying the various finite-size effects in our ED data. Here we focus on the infinite lattice case. Figure 6.11 shows the momentum dependence of the low-energy branch $\lambda_1(\mathbf{k})$ for cutoff values J_c =0.3, 0.1, 0.01 and 0.001. For $J_c = 0.3$, which amounts to keeping only the dominant, NN couplings (i.e. three couplings per site), the minimum sits at $\mathbf{Q}=(\pi,\pi)$ and corresponds to the well-known Néel phase with AFM correlations along both the horizontal and the vertical directions of the lattice. This phase is stabilized by the imbalance in the NN imperfections, which favors the first two vertex configurations in Fig. 2(b). However, further-neighbor interactions destabilize the Néel phase and lead to a different minimum. For $J_c = 0.1$, which amounts to keeping seven interactions per site, the minimum of $\lambda_1(\mathbf{k})$ now sits at the two M points of the BZ, $\mathbf{Q}=(\pi,0)$ and $(0,\pi)$, which correspond to a stripy AFM alignment of the spins in the horizontal or the vertical direction of the lattice.

Lowering J_c further shifts the minimum to two incommensurate (IC) positions, $\pm\mathbf{Q}_{IC}$, which are extremely close to the commensurate $\pm(-\pi/2,\pi/2)$ points. For example, for $J_c = 0.01$ (12 interactions/site), $J_c = 0.001$ (31 interactions/site) and $J_c = 10^{-6}$ (299 couplings/site), the minima sit respectively at $\mathbf{Q}_{IC}=0.473(-\pi,\pi)$, $0.457(-\pi,\pi)$ and $0.462(-\pi,\pi)$. At the same time, the corresponding eigenvector $\mathbf{v}_1(\mathbf{Q}_{IC})$ cannot be used to construct a state satisfying the spin length constraint at all sites of the system simultaneously. This means that the present method cannot deliver the true ground state of the system and that $\lambda_1(\mathbf{Q}_{IC})$ serves only as a lower energy bound.

Physically, the system may accommodate the tendency for incommensurate correlations by forming long-wavelength modulations of the local $(-\pi/2,\pi/2)$ order parameter, in analogy e.g. to the anisotropic Ising model with competing interactions (the so-called ANNNI model) [89–92]. We should remark however that the energy landscape around the IC minimum is very flat and its distance from $(-\frac{\pi}{2},\frac{\pi}{2})$ is very small, so in principle such discommensurations (if any) should appear at much longer distances than the ones considered in our finite-lattice calculations, and indeed the length scales over which cold atom realizations are uniform (in both density and interaction patterns) on account of the parabolic confining potential. To confirm this point we have performed classical Monte Carlo (CMC) simulations on $N=2\times L\times L$-site clusters with periodic boundary conditions, see details in App. 6.G. All results up to $L = 36$ give consistently the $(-\frac{\pi}{2},\frac{\pi}{2})$ state without any sign of domain-wall discommensurations, implying that at least for these distances the system locks-in to the closest commensurate $\mathbf{Q} = (-\pi/2,\pi/2)$ phase.

Thermal phase transition into a classical Coulomb phase

Given the finite energy gap above the commensurate $\mathbf{Q}=(-\frac{\pi}{2},\frac{\pi}{2})$ state at $J_\perp = 0$ (see Fig. 6.8), one expects that this phase survives against thermal fluctuations up to a finite temperature T_C. To confirm this picture, and to find the numerical value of T_C, we have performed classical MC simulations at finite temperatures. The first two panels of Fig. 6.12 show the T-dependence of the structure factor $\mathcal{S}(\mathbf{Q})$ at $\mathbf{Q} = (-\pi/2,\pi/2)$, and the specific heat per site for systems up to N=2x28x28 sites. The results demonstrate clearly the thermal phase transition, with $T_C \simeq 0.185$. The third panel shows the T-dependence of the three different types of crossed plaquette configurations: the ice-rule 2in-2out states, and the defected 3up-1down (or 3down-1up) states and 4-in (or 4-out) states. The defects are almost entirely of the 3up-1down type, but their density remains very small up to the transition temperature (about 5%). So the classical phase gives way to a Coulomb gas [65, 66], an approximate realization of a classical Coulomb phase, with only a very small density of defects. This phase is marginally confined on account of the logarithmic nature of the interactions between the defects; given the non-vanishing defect density above T_C, their correlations are expected to exhibit a screened (Debye) form [93].

6.5 Quantum dimer models with Rydberg atoms: beyond quantum ice

6.5.1 Simple interactions, complicated lattices

As we have shown in the spin ice example, weakly Rydberg-dressed atoms in optical lattices provide a perfect platform to investigate quantum magnetism in AMO settings. The procedure can be extended to a series of 2D and 3D models using isotropic interactions, either using s- (whose corresponding frozen regimes have already been accessed in a series of experiments [23–37, 94]) or p-states (with out-of-plane polarization in the 2D case) combined with complicated lattice structures. This way, the complication of realizing fine-tuned interaction pattern is transferred to a complicated lattice geometry, which might be realized provided the correspondent light-pattern is realizable.

The fundamental features of those *complicated* lattices is the fact that *sharp* plateau, isotropic interactions, are sufficient to define a classical limit where there is a set of degenerate classical ground states, increasing extensively with system size. Given the shape of the interactions, one can identify the possible lattices as follows. First, we define as b the largest distance between sites belonging to the same simplices [8] (or *gauge cell*), that is, the unit cell where the Gauss law of interest is defined (in the spin ice case, these are the squares with crosses). Secondly, we define as c the smallest distance between sites which do not belong to the same gauge cell. It is then clear that, in the case where $b < c$, a plateau interaction of range $b < r_{bc} < c$ can generates the desired constraint in each gauge cell. In case this is not true (like, e.g., in the square ice case), additional features are needed such as angular dependence.

Some examples of the lattices which satisfy the previous property are illustrated in Fig. 6.13, together with the corresponding gauge cells. The list includes several 2D lattices which have already been realized in AMO settings, such as the Kagome lattice with triangular gauge cells (but not with hexagonal gauge cells), the Ruby lattice and the Honeycomb lattice. In the 3D case, a simple example is the pyrochlore lattice, already discussed in Ref. [39] in the context of polar gases. Interestingly, in this former case, dipolar interactions behave in a very similar manner to simple plateau-like ones due to their symmetry content [95].

Once taken at filling factor of an integer number of particles per gauge cell for the underlying Bose-Hubbard Hamiltonian, all of those lattices generate in perturbation theory quantum dimer or quantum loop models [8]. These are naturally described by emergent gauge theories: however, the gauge symmetry itself is not always straightforwardly determined given the gauge symmetry of the microscopic constituents [3]. The procedure to derive the proper dimer model dynamics given a lattice

---

[3] This is the case, e.g., of the Kagome Bose-Hubbard model with the hexagonal cell as gauge cell, where the proper low-energy theory is a $\mathbb{Z}_2$ gauge theory which can undergo deconfinement, and thus stabilize a spin-liquid phase.

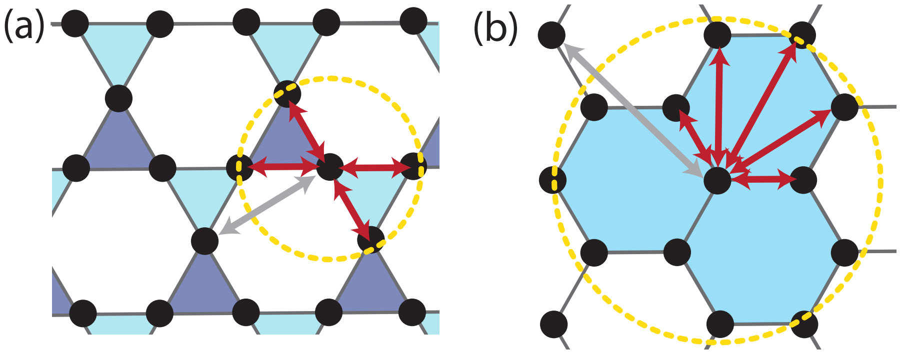

Figure 6.13. *Lattices possessing the properties discussed in Sec. 6.5.1: Panel (a) shows a kagome lattice with triangles as gauge cells (shaded area) and panel (b) a honeycomb lattice with hexagons as gauge cells. In both cases, the maximal intraplaquette euclidean distance (yellow dashed circle) is smaller than the minimal interplaquette distance (gray arrow). The radius of the needed plateau-like interaction is described by the yellow circles.*

and an Ising constraint is outlined in Ref. [8]. Below, we illustrate a simple example of how complicated lattices can meet simple interactions to let a quantum dimer model emerge by focusing on the concrete example of the 4-8 lattice.

6.5.2 Emergent quantum dimer dynamics on a 4-8 lattice from an XXZ model

The 4-8 lattice (also known as CAVO lattice) [96] represents a useful example to illustrate how the combination of a complicated lattice with simple Ising interactions can lead to intriguing quantum dynamics. The lattice structure for the underlying bosons we start from is the squagome lattice [97, 98], illustrated in Fig. 6.14: once the triangles are identified as the gauge cells, it is easy to see that $b = a$, $c = \sqrt{2}a$, so that a plateau interaction of range $1 < r/a < \sqrt{2}$ can indeed enforce constraints on the gauge cells. Since each site is shared by 3 gauge cells, a filling fraction of $n = 1/3$ atoms per site, combined with the plateau interactions, will generate a degenerate manifold $\mathcal{H}_{4-8}$ of classical ground states where for each triangle a single site is occupied [see Fig.6.14(b)].

When formulated in spin language with $S^z_j = n_j - 1/2$, the Hamiltonian

$$H^{Is}_{4-8} = J_z \sum_{\triangle} \sum_{\{i,j\}\in\triangle} S^z_j S^z_i \tag{6.17}$$

has (trivially) a set of $U(1)$-like conserved charges at each triangle, that is:

$$G_\triangle = \sum_{j\in\triangle} S^z_j + 1/2, \quad G_\triangle|\psi\rangle = 0 \qquad \forall|\psi\rangle \in \mathcal{H}_{4-8}. \tag{6.18}$$

Once an additional, small term inducing quantum fluctuations is introduced:

$$H^{Ex}_{4-8} = J \sum_{\square} \sum_{\{i,j\}\in\square} S^+_j S^-_i + \tilde{J} \sum_{\bigcirc} \sum_{\{i,j\}\in\bigcirc} S^+_j S^-_i \tag{6.19}$$

tunneling between the different classical degenerate minima becomes possible within perturbation theory, while still preserving the set of conserved charges in Eq. (6.18). Notice that we used two

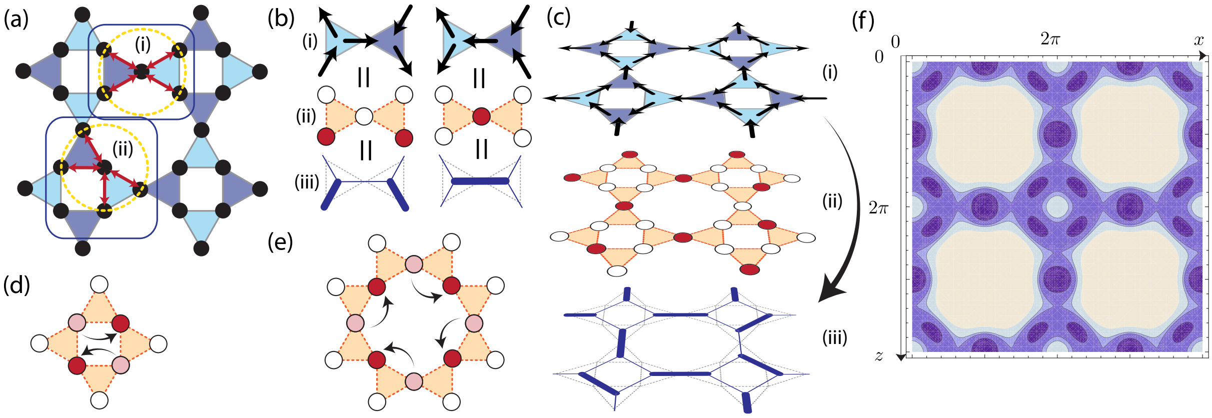

Figure 6.14. *Configuration space of the squagome lattice and gauge invariant dynamics: (a) Atoms are disposed on a squagome pattern (filled-black circles) and interact with NN atoms (red arrows) which all are the same distance apart (yellow dashed circle). Triangular gauge cell are indicated as shaded areas in light blue and violet in an alternating pattern. Panel (b) describes possible gauge invariant configurations [from Eq.* (6.18)*], where a configuration with (i) two flux vectors pointing outwards (inwards) on a light blue (violet) gauge cell map onto a configuration (ii) where a single site on each triangle is occupied (red circle) and two lattice sites are unoccupied (white circles). Here, an arrow pointing from a violet triangle to a light blue triangle corresponds to an occupied lattice site and vice versa to an empty lattice site. (iii) This can be further mapped to a quantum dimer model on the 4-8 lattice. The new sites are defined at the centre of each triangle: the bond variable between them is either empty (thin blue line) or a dimer (thick blue line), depending on the original occupation of the site shared by the triangles. Panel (c) illustrates a full gauge invariant configuration. Quantum fluctuations induce non-trivial dynamics around both the square (d) and octagonal plaquettes (e), described by Eqs.* (6.20) *and* (6.21)*. Panel (f) shows the optical lattice pattern of Eq.* (6.22) *as described in the text. Darker areas correspond to deeper potentials.*

different matrix elements for particle tunneling around the squares (J) and around the octagons ($\tilde{J}$). Two kind of moves are allowed. At second order, two particles sitting along a diagonal of a square plaquette can resonantly flip to sit on the other diagonal:

$$H^{\square} \simeq -\frac{J^2}{J_z}(S_1^+ S_2^- S_3^+ S_4^- + \text{h.c.}) \tag{6.20}$$

where we have numbered the sites of the square plaquette in clockwise order. The next non-vanishing contribution takes place at fourth order, where particles sitting at the edges of each octagonal plaquette can re-arrange via an extended ring-exchange:

$$H^{\octagon} \simeq -3\frac{\tilde{J}^4}{J_z^3}(S_1^+ S_2^- S_3^+ S_4^- S_5^+ S_6^- S_7^+ S_8^- + \text{h.c.}). \tag{6.21}$$

where we have numbered the sites of the octagonal plaquette in clockwise order. The two terms are illustrated in Fig. 6.14(d)-(e). We now reformulate the problem in terms of dimer models, which allows to set up a proper description in terms of effective degrees of freedom. In order to do that, we follow the procedure exemplified in Ref. [8, 99–101], and illustrated in Fig. 6.14(b)-(c): we define a new lattice, the so called simplex lattice, whose vertices are the middle points of each gauge cell, and whose bonds connect vertices of gauge cells which share a single site: each bond sits on a vertex of the original lattice. Then, we introduce dimer variables on the bonds as follows: *i)* if a bond sits on a site which is occupied by a boson, we draw a dimer, *ii)* if not, we leave the bond empty. This way, the Gauss law of Eq. (6.18) is easily reformulated as a conservation law of a single dimer at each vertex.

The lattice on the top of which the quantum dimer model is defined is then a 4-8 lattice: as it is bipartite, the corresponding low-energy theory is a $U(1)$ gauge theory, which can then display different confined phases as a function of the two kinetic energy terms for the dimers $H^{\octagon}$ and $H^{\square}$. This setup might constitute then a perfect setting for the investigation of the competition between different RVB solid orders and the transitions between them. The corresponding periodic structure can be either realized using digital-micromirror-devices (DMD) [67], or by using an optical potential of the form

$$V(x,z) = 4V_1(x+z, x-z) + V_2(x,z), \tag{6.22}$$

where

$$V_1(x,z) = \cos(\pi x)^2 + \cos(\pi z)^2 - 2\cos(0.55)\cos(\pi x)\cos(\pi z) \tag{6.23}$$

is a 2D lattice created by two 1D standing waves with phase difference $\phi = 0.55$ and anti-parallel polarizations $\mathbf{e}_1 \cdot \mathbf{e}_2 = -1$. The second 2D lattice is created by lasers with three times the frequency and orthogonal polarization,

$$V_2(x,z) = \cos(3\pi x)^2 + \cos(3\pi z)^2. \tag{6.24}$$

Both lattices are rotated by 45 degrees, respectively. The full lattice structure is illustrated in Fig. 6.14(f), and realizes the squagome lattice potential of interest.

6.6 Conclusions and Outlook

In summary, we have shown how dynamical gauge fields emerging from frustration can be ideally realized in cold atom systems by employing optical lattices combined with Rydberg interactions. This allows to probe gauge theory phenomena in a variety of models. In particular, we analyzed in detail the case of quantum square ice, a paradigmatic example of frustrated statistical mechanics, both at the few- and at the many-body level.

From the atomic physics side, the key element of our implementation is the tunable interaction pattern generated by Rydberg p-states and local polarizations due to tensor polarizabilities. Prominent atomic physics features can be exploited in order to generate (repulsive) anisotropic interactions that allow to enforce the complex gauge constraints of square ice models. The possibility of generating such anisotropic interaction patterns enriches the cold atom Hubbard toolbox of yet another potential feature, which can find different applications in many-body physics even beyond engineering complicated and fine tuned lattice constraints. It paves the way toward the realization of different constrained dynamics, in particular, quantum dimer models on complicated lattices.

From the many-body side, we have provided numerical evidence that typical imperfections generated by the Rydberg interactions still allow the observation of a non-trivial state of matter, a plaquette valence bond crystal. Moreover, we have shown how a cold atom suited detection technique can be identified, by performing parity measurements along the plaquettes, which directly identifies the spontaneous symmetry breaking of a discrete lattice symmetry. Even in the absence of quantum dynamics, the engineered interactions stabilize a magnetically ordered state with a large unit cell at low temperature, which gives way to a classical Coulomb gas, a marginally confining two-dimensional Coulomb phase with a small but nonzero density of charges in the form of thermally activated plaquettes violating the ice rule.

Different directions can be pursued further following the lines discussed here. A first, interesting extension would be to understand whether different kinds of anisotropic interactions can play a significant role in engineered Ising constraints in cold atom systems. In particular, anisotropic interactions between Rydberg d-states of ^{87}Rb atoms have been recently demonstrated in Ref. [37]: as their angular dependence differs from the one discussed here, it can constitute yet another tool in order to realize complicated, fine-tuned interaction patterns. Secondly, the present proposal, which generates pure gauge theories, can be combined in a modular way with previous ones [102] in such a way that either fermionic or bosonic matter can be included into the dynamics. This would extend the toolkit of quantum simulation of lattice gauge theories within the quantum link model formalism. From the one hand side, quantum simulation of QED$_3$ models with different flavor degrees of freedom could be foreseen [103]. From the other hand side, the combination of bosonic fields, as e.g. in Ref. [102], with the current proposal would allow for the exploration of the Fradkin-Shenker scenario of Higgs physics in 2D [104], and possibly in more exotic geometries. Finally, cold atom realizations can also provide a suitable platform for the investigation of *dynamical* effects in quantum dimer models and gauge theories in general; it'd be interesting to see whether simple observables and experimental procedures can be implemented, to described complex many-body phenomena such as string dynamics [105] in the presence of static charges [40], or the dynamical properties of thermally activated monopoles on top of a vacuum state.

Acknowledgments

We thank T. Pfau for stimulating discussions in the initial stage of this work. We also thank I. Bloch, Ch. Groß, M. Hennrich, A. Läuchli, E. Rico and F. Schreck for helpful discussions. Furthermore, discussions with all members of the R-ION and UQUAM consortium are kindly acknowledged. This project was supported in parts by the ERC Synergy Grant UQUAM, SIQS, the SFB FoQuS (FWF Project No. F4006-N16), and the ERA-NET CHIST-ERA (R-ION consortium). R.M. acknowledges the Helmholtz Virtual Institute ”New States of Matter and Their Excitations”.

6.A Effect of the AC-Stark lasers on the ground state

The AC Stark lasers introduced in Sec. 8.B will create an additional trapping potential, $V_{AC}(\mathbf{r}_i)|g\rangle\langle g|_i$, for ground state atoms with minima not commensurate with the initial trapping lattice. In order to not distort the desired lattice structure this additional potential must not be larger than the initial trapping potential. The dominant effect comes from a second order Stark effect by off-resonantelly coupling the $5S$ state to the first excited state $5P$ and is given by $V_{AC} = \Omega^2_{5s5p}/(2\Delta_{5s5p})$ with Rabi frequency $\Omega_{5s5p} = 2d_{5s5p}\mathcal{E}/\hbar$ and detuning $\Delta_{5s5p} = 2\pi c(\lambda^{-1}_{5s5p} - \lambda^{-1}_{AC})$. Here, $d_{5s5p} = \langle 5S|d|5P\rangle$ is the

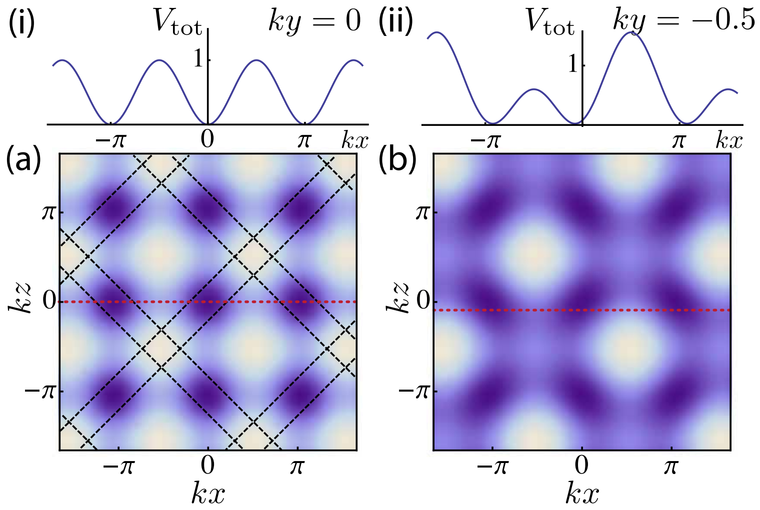

Figure 6.15. *Contour plots of the total trapping potential, $V_{\text{tot}}(x, z)$. (a) without the AC Stark potential ($\alpha = 0$) and (b) with the AC Stark potential ($\alpha = 1$). Black dashed lines in (a) show the 0.9 level lines of the AC Stark potential, V_{AC}. The insets (i) and (ii) show the 1D potential along the red dotted lines for (i) $ky = 0$ and (ii) $ky = -0.5$.*

transition dipole matrix element and λ_{5s5p} the transition wavelength. Fig. 6.15(a) shows the desired trapping lattice created by two counter propagating laser beams which form a ground state potential $V_{\text{trap}}(z, x) = \cos^2 kz + \cos^2 kx$. The dashed black lines indicate the 0.9 level lines of the AC-Stark potential $V_{AC}(z, x) = \cos^2[k_{AC}(x - y)/\sqrt{2}] + \sin^2[k_{AC}(x + y)/\sqrt{2}]$ with $k_{AC} = k/\sqrt{2}$. The maxima are localized at the ● and ■ lattice sites, respectively, as required in Sec. 8.B. Fig. 6.15(b) shows the total potential, $V_{\text{tot}} = V_{\text{trap}} + \alpha V_{AC}$, in the case of equal strength, i.e. $\alpha = 1$. The insets on top show the 1D potential along the (i) $ky = 0$ and (ii) $ky = -0.5$ lines [red dotted lines in Fig. 6.15(a) and (b)]. In the case of equal strength of the trapping lattice and additional lattice created by the AC-Stark lasers the potential minima are still located at the same position, but slightly elongated. Note that the potential barrier between neighboring lattice sites is about 1/2 smaller than without the additional AC Stark laser. This will lead to higher tunneling rates compared to the case without the AC Stark laser.

6.B Global Rydberg laser excitation

In the following we show that it is possible to weakly admix the locally polarized Rydberg states of Sect. 8.B to the electronic ground state $|g\rangle$ using a *single* laser with a wave vector $\mathbf{k} \sim \mathbf{y}$ and polarization σ_+ (see Fig. 6.4)

$$H_L = \frac{\Omega_R}{2}\left[|g\rangle_y\, {}_y\langle n^2P_{3/2}, 3/2| + \text{h.c.}\right]. \tag{6.25}$$

In the local x- and z- basis this laser will couple to all four m_j-levels with different weights, i.e.

$$|\tfrac{3}{2}\rangle_y = \frac{1}{2\sqrt{2}}\left[|\tfrac{3}{2}\rangle_z + i\sqrt{3}|\tfrac{1}{2}\rangle_z - \sqrt{3}|-\tfrac{1}{2}\rangle_z - i|-\tfrac{3}{2}\rangle_z\right], \tag{6.26}$$

$$|\tfrac{3}{2}\rangle_y = \frac{1}{2\sqrt{2}}\left[e^{-3i\pi/4}|\tfrac{3}{2}\rangle_x + \sqrt{3}e^{-i\pi/4}|\tfrac{1}{2}\rangle_x + \sqrt{3}e^{i\pi/4}|-\tfrac{1}{2}\rangle_x + e^{3i\pi/4}|-\tfrac{3}{2}\rangle_x\right]. \tag{6.27}$$

where we used the irreducible representation of a rotation in the $j = 3/2$ subspace, $D[\mathcal{R}(\alpha,\beta,\gamma)] = e^{-i\alpha J_z}e^{-i\beta J_y}e^{-i\gamma J_z}$.

Since the states $|m \neq 3/2\rangle_{z,x}$ are energetically separated by at least E_{AC} from the $|m = 3/2\rangle$ state a laser with detuning $\Delta_R \ll E_{\mathrm{AC}}$ and wave vector $\mathbf{k} \sim \mathbf{y}$ will selectively admix the states $|3/2\rangle_z$ and $|3/2\rangle_x$ at lattice sites ● and ■, respectively, to the ground state $|g\rangle$ with an effective Rabi frequency $\Omega_R/(2\sqrt{2})$.

6.C Van der Waals interactions

In this appendix we briefly summarize the technical details in order to calculate the angular dependent van der Waals interactions of Sec. 6.3.2. Due to the odd parity of the electric dipole operators $d_\mu^{(i)}$ and $d_\nu^{(j)}$, the dipole-dipole interaction, V_{dd}, of Eq. (6.11) can only couple states with initial angular (total) momentum ℓ (j) to states with new angular (total) momentum $\ell \pm 1$ (j or $j \pm 1$). Therefore, the number of possible "channels" $n\ell jm_1 + n\ell jm_2 \longrightarrow n'\ell' j'm' + n''\ell'' j''m''$ for which the matrix element $\langle n\ell jm_1; n\ell jm_2|V_{\mathrm{dd}}^{(ij)}|n'\ell' j'm'; n''\ell'' j''m''\rangle$ is non-zero are limited. While there is no selection rule for possible final principal quantum numbers n' and n'' which solely determine the overall strength of the matrix element, the dipole-dipole matrix element is only non-zero if the magnetic quantum numbers and the spherical component of the dipole operator fulfill $m_1 + \mu = m'$ and $m_2 + \nu = m''$. If the energy difference $\delta_{\alpha\beta} = E(\alpha) + E(\beta) - 2E(n\ell j)$, between the initial states $n\ell j$ and the intermediate states $\alpha \equiv n_\alpha \ell_\alpha j_\alpha m_\alpha$ and $\beta \equiv n_\beta \ell_\beta j_\beta m_\beta$ of the atoms is larger than the dipole-dipole matrix element connecting those states the dominant interaction is of van der Waals type which arises from V_{dd} in second order perturbation

$$\hat{V}_{\mathrm{vdW}} = \hat{P}_{12} \sum_{\alpha\beta} \frac{\hat{V}_{\mathrm{dd}} \hat{Q}_{\alpha,\beta} \hat{V}_{\mathrm{dd}}}{\delta_{\alpha\beta}} \hat{P}_{34}. \tag{6.28}$$

Here, $\hat{V}_{\mathrm{vdW}}$ is an operator acting in the degenerate manifold of magnetic sublevels with $\hat{P}_{ij} = |n\ell jm_i, n\ell jm_j\rangle\langle n\ell jm_i, n\ell jm_j|$ a projector into the $n\ell j$-manifold and $\hat{Q}_{\alpha,\beta} = |\alpha,\beta\rangle\langle\alpha,\beta|$ a projector on a specific state in the complementary space. The sum is over all two-atom energy levels, where the indices $\alpha \equiv n_\alpha \ell_\alpha j_\alpha m_\alpha$ and $\beta \equiv n_\beta \ell_\beta j_\beta m_\beta$ denote a full set of quantum numbers that specify the states. Due to the electric dipole selection rules discussed above this sum can be split up into channels denoted by $\nu = (\ell_\alpha, j_\alpha; \ell_\beta, j_\beta)$. Eq. (8.8) can be written as $\hat{V}_{\mathrm{vdW}} = \sum_\nu C_6^{(\nu)} \mathcal{D}_\nu(\vartheta, \varphi)/r^6$, where $C_6^{(\nu)}$ contains the radial part of the matrix elements

$$C_6^{(\nu)} = \sum_{n_\alpha, n_\beta} \frac{\mathcal{R}_1^\alpha \mathcal{R}_2^\beta \mathcal{R}_3^\alpha \mathcal{R}_4^\beta}{\delta_{\alpha\beta}} \tag{6.29}$$

which accounts for the overall strength of the interaction and is independent of the magnetic quantum numbers. Here, $\mathcal{R}_i^j = \int dr r^2 \psi_{n_i,\ell_i,j_i}(r)^* r \psi_{n_j,\ell_j,j_j}(r)$ is the radial integral calculated with radial wave functions $\psi_{n_j,\ell_j,j_j}(r)$ obtained using the model potential from [106]. The matrix

$$\mathcal{D}_\nu(\vartheta, \varphi) = \hat{P}_{12} \sum_{m_\alpha, m_\beta} \mathcal{M}_\nu \hat{Q}_{\alpha,\beta} \mathcal{M}_\nu \hat{P}_{34} \tag{6.30}$$

on the other hand is a matrix in the subspace of magnetic quantum numbers which contains the relative angles between the two atoms ($s = 1/2$)

$$\begin{aligned}\langle m_1, m_2|\mathcal{M}_\nu|m_\alpha, m_\beta\rangle =& (-)^{s-m_1}\sqrt{\prod_{i=1,\alpha}(2\ell_i+1)(2j_i+1)}\begin{Bmatrix}\ell_1 & \ell_\alpha & 1\\ j_\alpha & j_1 & s\end{Bmatrix}\begin{pmatrix}\ell_\alpha & 1 & \ell_1\\ 0 & 0 & 0\end{pmatrix}\\ &\times(-)^{s-m_2}\sqrt{\prod_{i=2,\beta}(2\ell_i+1)(2j_i+1)}\begin{Bmatrix}\ell_2 & \ell_\beta & 1\\ j_\beta & j_2 & s\end{Bmatrix}\begin{pmatrix}\ell_\beta & 1 & \ell_2\\ 0 & 0 & 0\end{pmatrix}\\ &\times\left(-\sqrt{\frac{24\pi}{5}}\sum_{\mu,\nu}C^{1,1;2}_{\mu,\nu;\mu+\nu}\begin{pmatrix}j_\alpha & 1 & j_1\\ m_\alpha & \mu & -m_1\end{pmatrix}\begin{pmatrix}j_\beta & 1 & j_2\\ m_\beta & \nu & -m_2\end{pmatrix}Y_2^{\mu+\nu}(\vartheta,\varphi)^*\right).\end{aligned} \tag{6.31}$$

As an example we show the $\mathcal{D}_1$ matrix for the first channel $P_{3/2} + P_{3/2} \longrightarrow S_{1/2} + S_{1/2}$

$$\mathcal{D}_1 = \begin{pmatrix} \frac{1}{4}\sin^4\vartheta & -\frac{1}{2\sqrt{3}}\cos\vartheta\sin^3\vartheta & \frac{\sin^2\vartheta}{24\sqrt{3}}(3\cos 2\vartheta+1) & 0\\ -\frac{1}{2\sqrt{3}}\cos\vartheta\sin^3\vartheta & \frac{1}{12}\left(\sin^4\vartheta+\sin^2 2\vartheta\right) & -\frac{1}{9}\cos\vartheta\sin\vartheta & \frac{\sin^2\vartheta}{24\sqrt{3}}(3\cos 2\vartheta+1)\\ \frac{\sin^2\vartheta}{24\sqrt{3}}(3\cos 2\vartheta+1) & -\frac{1}{9}\cos\vartheta\sin\vartheta & \frac{1}{864}(12\cos 2\vartheta-27\cos 4\vartheta+47) & -\frac{\sin 2\vartheta}{24\sqrt{3}}(3\cos 2\vartheta+1)\\ 0 & \frac{\sin^2\vartheta}{24\sqrt{3}}(3\cos 2\vartheta+1) & -\frac{\sin 2\vartheta}{24\sqrt{3}}(3\cos 2\vartheta+1) & \frac{1}{144}(3\cos 2\vartheta+1)^2 \end{pmatrix} \tag{6.32}$$

in the subspace of states $|\frac{3}{2},\frac{3}{2}\rangle$, $|\frac{3}{2},\frac{1}{2}\rangle$, $|\frac{3}{2},-\frac{1}{2}\rangle$ and $|\frac{3}{2},-\frac{3}{2}\rangle$ where the first atom is fixed in the $m = 3/2$ state. In general one has to diagonalize the operator $\hat{V}_{\mathrm{vdW}}$ in the degenerate Zeeman subspace in order to obtain the new eigenenergies and eigenstates in the presence of interactions. If an external electric or magnetic field separates an initial two atom state $|m_1, m_2\rangle$ from all other Zeeman sublevel such that the energy difference is larger than the vdW coupling matrix elements then it is possible to simply take expectation values of $V^{(n)}_{m_1,m_2}(\mathbf{r}) = \langle m_1, m_2|\hat{V}_{\mathrm{vdW}}|m_1, m_2\rangle$ in order to obtain the interaction potential of two atoms initially in the $|m_1, m_2\rangle$ state.

6.D Mixed interactions

In the following we show how to calculate the mixed interactions, $V_{\bullet\blacksquare}(r,\vartheta)$, introduced in Sec. 6.3.2 between the *locally* polarized Rydberg states $|\bullet\rangle \equiv |n^2P_{3/2}, 3/2\rangle_{\mathbf{z}}$ and $|\blacksquare\rangle \equiv |n^2P_{3/2}, 3/2\rangle_{\mathbf{x}}$. Here, the indices z and x denote the local quantization axis of the state. In the following we work in the z-basis. Rotating the latter state into the z basis using the irreducible representation $D^{(3/2)}[\mathcal{R}(\hat{\mathbf{y}},\pi/2)]^{-1}$ of a rotation around $\mathbf{y}$ by an angle of $\pi/2$ in the $j = \frac{3}{2}$ space yields

$$|\blacksquare\rangle = \frac{1}{2\sqrt{2}}\left[|\tfrac{3}{2}\rangle_{\mathbf{z}} - \sqrt{3}|\tfrac{1}{2}\rangle_{\mathbf{z}} + \sqrt{3}|-\tfrac{1}{2}\rangle_{\mathbf{z}} - |-\tfrac{3}{2}\rangle_{\mathbf{z}}\right], \tag{6.33}$$

where $|m\rangle_{\mathbf{z}} \equiv |n^2P_{3/2}, m\rangle_{\mathbf{z}}$. The state $|\blacksquare\rangle = |n^2P_{3/2}, 3/2\rangle_{\mathbf{x}} = \sum_m c_m|n^2P_{3/2}, m\rangle_{\mathbf{z}}$ is thus a superposition of different m_j-states in the z basis. Interactions between two atoms in a $|\blacksquare\bullet\rangle$ or $|\blacksquare\blacksquare\rangle$ state can be calculated by evaluating the corresponding matrix elements of Eq. (8.8) which requires to compute van der Waals interactions between atoms in different m_j states, e.g.

$$\langle\bullet\blacksquare|V_{\mathrm{vdW}}|\bullet\blacksquare\rangle = \sum_{m,m'} c_{m'}c^*_m\langle\tfrac{3}{2}, m|V_{\mathrm{vdW}}|\tfrac{3}{2}, m'\rangle. \tag{6.34}$$

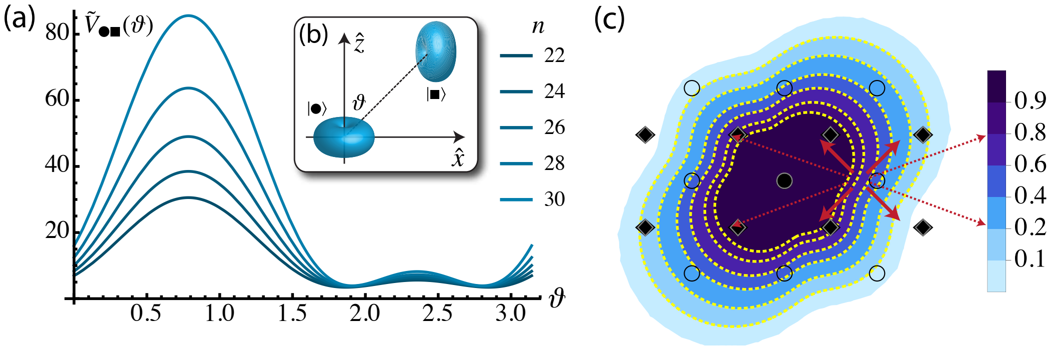

Figure 6.16. *(a) Angular part, $A^{(n)}_{\bullet\blacksquare}(\vartheta)$, of the van der Waals interaction, $V^{(n)}_{\bullet\blacksquare}(r,\vartheta) = (n-\delta_{n\ell j})^{11}A^{(n)}_{\bullet\blacksquare}(\vartheta)/r^6$, between a pair of ^{87}Rb atoms in the $|r_\bullet\rangle = |n^2P_{3/2},3/2\rangle_z$ and $|r_\blacksquare\rangle = |n^2P_{3/2},3/2\rangle_x$ Rydberg states of ^{87}Rb (solid lines). We plot the rescaled interaction energy, $A^{(n)}_{\bullet\blacksquare}(\vartheta)$ as a function of the angle ϑ for various values of the principal quantum number n, with δ the quantum defect. (b) Cartoon of the states and definition of the angle ϑ. (c) Contour plot of the effective interaction $\tilde{V}^{(n)}_{\bullet\blacksquare}(r,\vartheta)/\tilde{V}_0$ between the dressed ground state atom $|\bullet\rangle$ in the middle and the NN $|\blacksquare\rangle$ atoms (red arrows) the NNN $|\blacksquare\rangle$ atoms (red dotted arrows).*

The angular dependence of the van der Waals interaction between two Rydberg atoms in a $|\bullet\bullet\rangle$ or in a $|\blacksquare\blacksquare\rangle$ state, $V_{\bullet\bullet}(r,\vartheta) = V_{\blacksquare\blacksquare}(r,\vartheta-\pi/2) \sim \sin^4\vartheta/r^6$ are the same up to a rotation by 90 degrees and show the typical anisotropic behavior discussed in Sec. 6.3.2 [see solid lines in Fig. 6.5(a)] On the other hand, the angular dependence of the mixed interactions between two Rydberg atoms in a $|\blacksquare\bullet\rangle$ state, shown in Fig. 6.16(a), exhibits two asymmetric maxima at $\vartheta = \pm\pi/4$. The asymmetry arises from off-diagonal matrix elements, e.g. $\langle\frac{3}{2},\frac{1}{2}|\hat{V}_{\mathrm{vdW}}|\frac{3}{2},-\frac{1}{2}\rangle \sim \sin 2\vartheta$. Note that the actual strength of the interaction only affects the Condon radius, r_c [see Eq. (6.15)], but not the energy shift $\tilde{V}_0$ or $r \to 0$. Panel (c) of Fig. 6.16 shows a contour plot of the mixed interaction,$\tilde{V}_{\bullet\blacksquare}/\tilde{V}_0$ of Eq. (6.14), between the dressed ground state atoms $|\bullet\rangle$ in the middle and the surrounding $|\blacksquare\rangle$ atoms. Interactions with the neighboring $|\blacksquare\rangle$ atoms (red solid arrows) are strong, $\sim \tilde{V}_0$, while interactions with next-nearest-neighbor $|\blacksquare\rangle$ atoms (red dotted arrows) are strongly suppressed due to the plateau structure of the potential.

6.E Finite-size clusters

In our Exact Diagonalizations we have considered the following checkerboard clusters with periodic boundary conditions:

N	$\mathbf{T}_1$	$\mathbf{T}_2$	$\mathbf{G}_1$	$\mathbf{G}_2$	$\mathcal{D}^{S_z=0}_{\mathrm{full}}$	$\mathcal{D}_{\text{spin-ice}}$
16	$(2,2)$	$(-2,2)$	$(\frac{\pi}{2},\frac{\pi}{2})$	$(-\frac{\pi}{2},\frac{\pi}{2})$	12870	90
32	$(4,0)$	$(0,4)$	$(\frac{\pi}{2},0)$	$(0,\frac{\pi}{2})$	601080390	2970
36	$(3,3)$	$(-3,3)$	$(\frac{\pi}{3},\frac{\pi}{3})$	$(-\frac{\pi}{3},\frac{\pi}{3})$	9075135300	6840
64	$(4,4)$	$(-4,4)$	$(\frac{\pi}{4},\frac{\pi}{4})$	$(-\frac{\pi}{4},\frac{\pi}{4})$	1832624140942590534	2891562
72	$(6,0)$	$(0,6)$	$(\frac{\pi}{3},0)$	$(0,\frac{\pi}{3})$	442512540276836779204	16448400

where N is the number of lattice sites, $\mathbf{T}_{1,2}$ are the spanning vectors of the cluster, $\mathbf{G}_{1,2}$ are the reciprocal vectors, $\mathcal{D}^{S_z=0}_{\mathrm{full}}$ is the size of the full Hilbert space in the total magnetization $S_z = 0$ sector, and $\mathcal{D}_{\text{spin-ice}}$ is the dimensionality of the spin ice manifold. Note that, in order to evaluate J_{ij} across the periodic boundaries in a consistent manner [4], we keep the maximum amplitude among the set $\{J_{i,j+\epsilon_1\mathbf{T}_1+\epsilon_2\mathbf{T}_2}, \epsilon_{1,2}=-1,0,1\}$, where $\mathbf{T}_1$ and $\mathbf{T}_2$ are the spanning vectors of the cluster.

6.F Classical Minimization

Table 6.2 summarizes the main results from the classical minimization procedure of Sec. 6.4.3 for the finite clusters considered in our ED study but also for the thermodynamic limit (last line). The main findings are as follows:

(i) $J_c = 0.3$*, all clusters* — Here the minimum sits at $\mathbf{Q} = (\pi,\pi)$, with $\mathbf{v}_1(\mathbf{Q}) = \frac{1}{\sqrt{2}}(1,1)$ and $\lambda_1(\mathbf{Q}) < \lambda_2(\mathbf{Q})$. The minimum energy is achieved by

$$\sigma_{\mathbf{k},\alpha} = \sqrt{2N_{uc}}\, v_{1\alpha}(\mathbf{Q})\delta_{\mathbf{k},\mathbf{Q}} \Rightarrow \sigma_{\mathbf{R},\alpha} = \sqrt{2}\, v_{1\alpha}(\mathbf{Q})e^{i\mathbf{Q}\cdot\mathbf{R}}$$

where $N_{uc}=N/2$ stands for the number of unit cells, and the constants have been chosen to satisfy the spin length constraint. The energy is given by $E'/N_{uc}=\lambda_1(\mathbf{Q})$.

(ii) $J_c = 0.1$*, all clusters except N=36* — Here we have two optimal wavevectors $\mathbf{Q}_1 = (0,\pi)$ and $\mathbf{Q}_2=(\pi,0)$ with $\lambda_1(\mathbf{Q}_1) = \lambda_1(\mathbf{Q}_2)$ and $\mathbf{v}_1(\mathbf{Q}_1)=(1,0)$, $\mathbf{v}_1(\mathbf{Q}_2)=(0,1)$, and $\lambda_1(\mathbf{Q}_j)<\lambda_2(\mathbf{Q}_j)$. Then the solutions that satisfy the spin length constraint are

$$\sigma_{\mathbf{R},1} = \pm e^{i\mathbf{Q}_1\cdot\mathbf{R}}, \quad \sigma_{\mathbf{R},2} = \pm e^{i\mathbf{Q}_2\cdot\mathbf{R}}$$

i.e., we have four ground states, with energy $E'/N_{uc}=\lambda_1(\mathbf{Q}_1)$.

(iii) $J_c \leq 0.01$*, all clusters except N=36 and 72* — Here the minima sit at $\pm\mathbf{Q} = \pm(-\frac{\pi}{2},\frac{\pi}{2})$ with eigenvectors $\mathbf{v}_1(\mathbf{Q})=(1,\mp i)/\sqrt{2}$, and again $\lambda_1(\mathbf{Q})<\lambda_2(\mathbf{Q})$. Let us try the ansatz:

$$\begin{aligned}
\sigma_{\mathbf{k},\alpha} &= \frac{\sqrt{N_{uc}}}{\sqrt{2}}\Big(v_{1\alpha}(\mathbf{Q})\delta_{\mathbf{k},\mathbf{Q}} + v^*_{1\alpha}(\mathbf{Q})\delta_{\mathbf{k},-\mathbf{Q}}\Big)\\
\Rightarrow \sigma_{\mathbf{R},\alpha} &= \frac{1}{\sqrt{2}}\Big[v_{1\alpha}(\mathbf{Q})e^{i\mathbf{Q}\cdot\mathbf{R}} + v_{1\alpha}(-\mathbf{Q})e^{-i\mathbf{Q}\cdot\mathbf{R}}\Big]\\
&= \sqrt{2}\,\mathrm{Re}[v_{1\alpha}(\mathbf{Q})e^{i\mathbf{Q}\cdot\mathbf{R}}] = \Big(\cos(m-n)\frac{\pi}{2},\ \sin(m-n)\frac{\pi}{2}\Big)
\end{aligned}$$

where we labeled $\mathbf{R}=n\mathbf{e}_x + m\mathbf{e}_y$, and n, m are integers. This ansatz does not satisfy the spin length constraint at all sites. Another ansatz is $\sigma_{\mathbf{R},\alpha} = \Big(-\sin(m-n)\frac{\pi}{2},\ \cos(m-n)\frac{\pi}{2}\Big)$, which results from the first ansatz by replacing $\mathbf{v}_1(\mathbf{Q}) \to i\mathbf{v}_1(\mathbf{Q})$. To get a solution that satisfies the spin constraint we

---

[4] It is not enough to choose the minimum distance as a criterion, since it may happen that the distance between i and j and e.g. that between i and $j+\mathbf{T}_1$ is the same but the corresponding amplitudes are not the same.

combine the two:

$$\begin{aligned}
\sigma_{\mathbf{k},\alpha} &= \frac{\sqrt{N_{uc}}}{\sqrt{2}}\Big((\epsilon_1 + i\epsilon_2)v_{1\alpha}(\mathbf{Q})\delta_{\mathbf{k},\mathbf{Q}} + (\epsilon_1 - i\epsilon_2)v^*_{1\alpha}(\mathbf{Q})\delta_{\mathbf{k},-\mathbf{Q}}\Big) \\
\Rightarrow \sigma_{\mathbf{R},\alpha} &= \frac{1}{\sqrt{2}}\Big[(\epsilon_1 + i\epsilon_2)v_{1\alpha}(\mathbf{Q})e^{i\mathbf{Q}\cdot\mathbf{R}} + (\epsilon_1 - i\epsilon_2)v_{1\alpha}(-\mathbf{Q})e^{-i\mathbf{Q}\cdot\mathbf{R}}\Big] = \sqrt{2}\,\mathrm{Re}[(\epsilon_1 + i\epsilon_2)v_{1\alpha}(\mathbf{Q})e^{i\mathbf{Q}\cdot\mathbf{R}}] \\
&= \Big(\epsilon_1\cos(m-n)\frac{\pi}{2} - \epsilon_2\sin(m-n)\frac{\pi}{2},\ \epsilon_1\sin(m-n)\frac{\pi}{2} + \epsilon_2\cos(m-n)\frac{\pi}{2}\Big)
\end{aligned}$$

where $\epsilon_{1,2} = \pm 1$, i.e. we have four possible solutions, all with energy $E'/N_{uc} = \lambda_1(\mathbf{Q})$.

All remaining cases— Here we cannot satisfy the spin length constraint. This is what happens e.g. for N=36 and $J_c \leq 0.1$, for N=72 and $J_c \leq 0.01$, and for $N = \infty$ and $J_c \leq 0.01$. In these cases, $\lambda_1(\mathbf{Q})$ serves only as a lower bound of the energy (see comparison with ED data in Table 6.2). From these results we can infer that the best choice for the cutoff is 0.001, and the best finite size cluster for the investigation of the $t = 0$ ground states is the N=64 cluster, whose ground state energy per unit cell, $E'/N_{uc} = -2.108984$, is very close to the one for $N = \infty$ ($E'/N_{uc} = -2.11938$). The next good cluster (again in terms of energy) is N=32 which has $E'/N_{uc} = -2.056628$.

6.G Technical details on classical Monte Carlo simulations

Low energy configurations are generated by thermal annealing consisting of a million sweeps per site, using a combination of single-spin flip and long-loop updates. The former can annihilate all types of defects (3up-1down, 3down-1up, 4up, and 4down) but suffers from very low acceptance ratios at low temperatures, while the loop updates have much higher acceptance ratios (~16%) and can annihilate all defects except the 3up-1down (or 3down-1up). So combining both types of updates gives sufficiently large acceptance ratios and can annihilate all defects.

6.H Energy scales and possible effects of dissipation

Here, we briefly comment on other possible imperfection of Rydberg experiments.

6.H.1 Energy scales and state preparation

The large energy scales provided by dressed Rydberg interactions allow to engineer RVB plaquette solids with gaps of order of few hundred Hz. Those are one order of magnitude larger than typical exchange energy scales currently employed in bosonic cold atom experiment, allowing for the investigation of ground state physics within current temperature regimes.

Beyond a direct cooling within the gauge invariant manifold protected by such energy scales, the plaquette RVB solid can also be reached via an adiabatic ramp. A first possibility consists of starting directly in the solid phase at $J_\perp = 0$, and switching on the tunnelling adiabatically (which corresponds to lowering the optical lattice potential). The ramp has to be performed sufficiently slowly with respect to the energy gap in Fig. 6.8 in order to limit the number of proliferating defects. Alternatively, adiabatic engineering of small RVB samples has already been experimentally demonstrated in coupled double-well systems [107]: starting from such a state, one could melt the different RVB cells following a similar procedure as in Ref. [108], that is, merging the different cells by using an additional pair of superlattice potentials in the $x-y$ plane. A possible drawback is represented by spontaneous emission described in Sec. 6.3 which, despite being strongly suppressed by the dressing technique, might still play a detrimental role in establishing the correct ground state physics. A straightforward way to further minimise the effects of losses would be to address Rydberg p-states with higher principal quantum number n, as interactions ($\sim n^{11}$) and decay times ($\sim n^3$) both scale favourably as a function of the principal quantum number. We comment below on the expected influence of gauge variant dissipative dynamics.

For, e.g., $n = 32$, the diagonal interaction between both atoms in the $m_j = 3/2$ state is $V_{\frac{3}{2}\frac{3}{2}}(a) = 2\pi \cdot 150.53\,\text{MHz}$ while the largest off-diagonal matrix element is $V_{\text{off}}(a) = 2\pi \cdot 65.40\,\text{MHz}$. Using an AC-Stark laser with $P = 10\,\text{mW}$ one obtains a Rabi frequency of $\Omega_{AC} = 2\pi{\cdot}325\,\text{MHz} \gg V_{\text{off}}(a)$ on the $32P_{3/2} - 7D_{3/2}$ transition. The same laser creates an AC-Stark effect on the ground state 5S of $V_{AC} = 2\pi \cdot 279.5\,\text{kHz}$, which has to be smaller than the actually lattice trapping the atoms, V_{trap}. The optimal dressed potentials (with respect to NNN imperfections) is obtained with a detuning $\Delta_r = 2\pi{\cdot}2475\,\text{kHz}$ (which sets the Condon radius of the step-like interaction) of the Rydberg laser coupling $5S - 32P$. The decay rate of $32P$ is $\Gamma = 2\pi \cdot 2.4$ kHz. With a Rabi frequency of $\Omega_r = 2\pi \cdot (500, 625, 750)$ kHz one obtained $\epsilon = \Omega/2\Delta = (0.10, 0.13, 0.15)$. The effective decay rate is $\epsilon^2\Gamma = 2\pi \cdot (24, 38, 55)$ Hz and the soft-core potential is $\tilde{V}_0 = \epsilon^3\Omega = 2\pi \cdot (515, 1258, 2610)$ Hz. While in this specific case, direct tunneling will be suppressed due to deep lattice potential, one could nevertheless demonstrate experimentally the classical order-by-disorder mechanism discussed in Sec. 6.5, or exploit internal spin-exchange within the Rydberg manifold [5].

6.H.2 Effects of spontaneous emission

The influence of dissipative dynamics which explicitly violates Gauss constraints has been numerically investigated in Ref. [109] for a series of both Abelian and non-Abelian discrete gauge theories in one dimension. In particular, when the energy scales of dissipative and coherent dynamics are well separate, the influence of dissipative effects is quantitatively negligible as long as low-order observables, such as, e.g., correlation functions, are considered (as is the case here). Due to the stability of the plaquette order (protected by a large energy gap) with respect to Hamiltonian imperfection, we expect a similar stability in the gauge theory studied here. A detailed numerical study on the specific model could shed further light on the effects of spontaneous emission, furthering the understanding on how the low-energy physics affects the open system dynamics (along the lines discussed in Ref. [110]).

Bibliography

[1] L. Pauling, Journal of the American Chemical Society **57**, 2680 (1935).

[2] W. F. Giauque and M. F. Ashley, Physical Review **43**, 81 (1933); W. F. Giauque and J. W. Stout, Journal of the American Chemical Society **58**, 1144 (1936).

---

[5] A. W. Glaetzle, *et. al.*, *in preparation*

[3] E. Lieb, Physical Review Letters **18**, 692 (1967).

[4] M. J. Harris, S. T. Bramwell, D. F. McMorrow, T. Zeiske, and K. W. Godfrey, Physical Review Letters **79**, 2554 (1997).

[5] P. W. Anderson, Physical Review **102**, 1008 (1956).

[6] S. T. Bramwell and M. J. P. Gingras, Science **294**, 1495 (2001).

[7] L. Balents, Nature **464**, 199 (2010).

[8] C. Lacroix, P. Mendels, and F. Mila, *Introduction to Frustrated Magnetism: Materials, Experiments, Theory*, Springer Series in Solid-State Sciences (Springer, Berlin, Heidelberg, 2011).

[9] C. Castelnovo, R. Moessner, and S. L. Sondhi, Nature **451**, 42 (2008).

[10] R. Moessner and S. L. Sondhi, Phys. Rev. B **63**, 224401 (2001).

[11] R. Moessner, O. Tchernyshyov, and S. L. Sondhi, Journal of statistical physics **116**, 755 (2004).

[12] M. Hermele, M. P. A. Fisher, and L. Balents, Physical Review B **69**, 064404 (2004).

[13] A. Banerjee, S. V. Isakov, K. Damle, and Y. B. Kim, Physical Review Letters **100**, 047208 (2008).

[14] N. Shannon, O. Sikora, F. Pollmann, K. Penc, and P. Fulde, Physical Review Letters **108**, 067204 (2012).

[15] R. Moessner and S. L. Sondhi, Phys. Rev. Lett. **86**, 1881 (2001).

[16] G. Misguich, D. Serban, and V. Pasquier, Phys. Rev. Lett. **89**, 137202 (2002).

[17] R. Moessner and S. L. Sondhi, Physical Review B **68**, 184512 (2003).

[18] C. L. Henley, Phys. Rev. B **71**, 014424 (2005).

[19] C. L. Henley, Annual Review of Condensed Matter Physics, Vol 1 **1**, 179 (2010).

[20] R. Moessner and K. S. Raman, in *Introduction to Frustrated Magnetism: Materials, Experiments, Theory* (Springer Berlin Heidelberg, Berlin, Heidelberg, 2011) pp. 437–479.

[21] C. Castelnovo, R. Moessner, and S. L. Sondhi, Annual Review of Condensed Matter Physics **3**, 35 (2012).

[22] E. Fradkin, *Field Theories of Condensed Matter Systems*, Advanced Books Classics Series (Perseus Books, 1997).

[23] R. Heidemann, U. Raitzsch, V. Bendkowsky, B. Butscher, R. Löw, and T. Pfau, Physical Review Letters **100**, 033601 (2008).

[24] W. Anderson, J. Veale, and T. Gallagher, Physical Review Letters **80**, 249 (1998).

[25] C. S. Hofmann, G. Günter, H. Schempp, N. L. M. Müller, A. Faber, H. Busche, M. Robert-de Saint-Vincent, S. Whitlock, and M. Weidemüller, Frontiers of Physics , 1 (2013).

[26] D. Maxwell, D. J. Szwer, D. Paredes-Barato, H. Busche, J. D. Pritchard, A. Gauguet, K. J. Weatherill, M. P. A. Jones, and C. S. Adams, Physical Review Letters **110**, 103001 (2013).

[27] A. Schwarzkopf, D. A. Anderson, N. Thaicharoen, and G. Raithel, Physical Review A **88**, 061406 (2013).

[28] H. Schempp, G. Günter, M. Robert-de Saint-Vincent, C. S. Hofmann, D. Breyel, A. Komnik, D. W. Schönleber, M. Gärttner, J. Evers, and S. Whitlock, Physical Review Letters **112**, 013002 (2014).

[29] A. Tauschinsky, R. M. T. Thijssen, S. Whitlock, H. B. van Linden van den Heuvell, and R. J. C. Spreeuw, Physical Review A **81**, 063411 (2010).

[30] J. D. Carter and J. Martin, Physical Review A **88**, 043429 (2013).

[31] H. Kübler, J. P. Shaffer, T. Baluktsian, R. Löw, and T. Pfau, Nature Photonics **4**, 112 (2010).

[32] Y. O. Dudin and A. Kuzmich, Science (New York, N.Y.) **336**, 887 (2012).

[33] P. Schauß, M. Cheneau, M. Endres, T. Fukuhara, S. Hild, A. Omran, T. Pohl, C. Gross, S. Kuhr, and I. Bloch, Nature **491**, 87 (2012).

[34] L. Li, Y. O. Dudin, and A. Kuzmich, Nature **498**, 466 (2013).

[35] M. Ebert, A. Gill, M. Gibbons, X. Zhang, M. Saffman, and T. G. Walker, Physical Review Letters **112**, 043602 (2014).

[36] M. M. Valado, N. Malossi, S. Scotto, D. Ciampini, E. Arimondo, and O. Morsch, Physical Review A **88**, 045401 (2013).

[37] D. Barredo, S. Ravets, H. Labuhn, L. Béguin, A. Vernier, F. Nogrette, T. Lahaye, and A. Browaeys, arXiv.org (2014), 1402.4077v1 .

[38] J. Dalibard, F. Gerbier, G. Juzeliūnas, and P. Öhberg, Reviews of Modern Physics **83**, 1523 (2011).

[39] S. Tewari, V. W. Scarola, T. Senthil, and S. Das Sarma, Physical Review Letters **97**, 200401 (2006).

[40] D. Banerjee, M. Bögli, M. Dalmonte, E. Rico, P. Stebler, U. J. Wiese, and P. Zoller, Physical Review Letters **110**, 125303 (2013).

[41] L. Tagliacozzo, A. Celi, A. Zamora, and M. Lewenstein, Annals of Physics **330**, 160 (2013).

[42] E. Zohar, J. I. Cirac, and B. Reznik, Physical Review Letters **110**, 125304 (2013).

[43] C. Nisoli, R. Moessner, and P. Schiffer, Reviews of Modern Physics **85**, 1473 (2013).

[44] A. Libál, C. Reichhardt, and C. Reichhardt, Physical Review Letters **97**, 228302 (2006).

[45] G. Möller and R. Moessner, Physical Review Letters **96**, 237202 (2006).

[46] T. F. Gallagher, *Rydberg Atoms*, Cambridge Monographs on Atomic, Molecular and Chemical Physics (Cambridge University Press, 2005).

[47] M. Saffman, T. G. Walker, and K. Mølmer, Reviews of Modern Physics **82**, 2313 (2010).

[48] D. Comparat and P. Pillet, Journal of the Optical Society of America B **27**, A208 (2010).

[49] R. Löw, H. Weimer, J. Nipper, J. B. Balewski, B. Butscher, H. P. Büchler, and T. Pfau, Journal of Physics B: Atomic, Molecular and Optical Physics **45**, 113001 (2012).

[50] D. Jaksch, J. I. Cirac, P. Zoller, R. Côté, and M. D. Lukin, Physical Review Letters **85**, 2208 (2000).

[51] M. D. Lukin, M. Fleischhauer, R. Côté, L. M. Duan, D. Jaksch, J. I. Cirac, and P. Zoller, Physical Review Letters **87**, 037901 (2001).

[52] T. G. Walker and M. Saffman, Physical Review A **77**, 032723 (2008).

[53] T. G. Walker and M. Saffman, Journal of Physics B: Atomic, Molecular and Optical Physics **38**, S309 (2005).

[54] A. Reinhard, T. Liebisch, B. Knuffman, and G. Raithel, Physical Review A **75**, 032712 (2007).

[55] K. Singer, J. Stanojevic, M. Weidemüller, and R. Côté, Journal of Physics B: Atomic, Molecular and Optical Physics **38**, S295 (2005).

[56] L. Santos, G. V. Shlyapnikov, P. Zoller, and M. Lewenstein, Physical Review Letters **85**, 1791 (2000).

[57] J. Honer, H. Weimer, T. Pfau, and H. P. Büchler, Physical Review Letters **105**, 160404 (2010).

[58] G. Pupillo, A. Micheli, M. Boninsegni, I. Lesanovsky, and P. Zoller, Physical Review Letters **104**, 223002 (2010).

[59] N. Henkel, R. Nath, and T. Pohl, Physical Review Letters **104**, 195302 (2010).

[60] T. Macrì and T. Pohl, Physical Review A **89**, 011402 (2014).

[61] Villain, J., Bidaux, R., Carton, J.-P., and Conte, R., Journal de Physique **41**, 1263 (1980).

[62] E. F. Shender, JETP **56**, 178 (1982).

[63] T. Yildirim, A. B. Harris, and E. F. Shender, Phys. Rev. B **58**, 3144 (1998).

[64] M. Endres, M. Cheneau, T. Fukuhara, C. Weitenberg, P. Schauß, C. Gross, L. Mazza, M. C. Banuls, L. Pollet, I. Bloch, and S. Kuhr, Science **334**, 200 (2011).

[65] B. Nienhuis, in *Phase Transitions and Critical Phenomena, Vol. 11*, edited by C. Domb, M. Green, and J. L. Lebowitz (Academic Press, London, 1987).

[66] C. Zeng and C. L. Henley, Phys. Rev. B **55**, 14935 (1997).

[67] T. Fukuhara, A. Kantian, M. Endres, M. Cheneau, P. Schauß, S. Hild, D. Bellem, U. Schollwöck, T. Giamarchi, C. Gross, I. Bloch, and S. Kuhr, Nature Physics **9**, 235 (2013).

[68] D. Banerjee, F.-J. Jiang, P. Widmer, and U. J. Wiese, Journal of Statistical Mechanics: Theory and Experiment **2013**, P12010 (2013).

[69] U. J. Wiese, Annalen der Physik **525**, 777 (2013).

[70] R. Moessner and J. T. Chalker, Phys. Rev. B **58**, 12049 (1998).

[71] N. Shannon, G. Misguich, and K. Penc, Phys. Rev. B **69**, 220403 (2004).

[72] S. Sachdev, *Quantum Phase Transitions* (Cambridge University Press, 2001).

[73] M. Viteau, M. G. Bason, J. Radogostowicz, N. Malossi, D. Ciampini, O. Morsch, and E. Arimondo, Physical Review Letters **107**, 060402 (2011).

[74] P. W. Milonni, *The quantum vacuum: an introduction to quantum electrodynamics* (Academic Press, 1994).

[75] J. Schwinger, L. L. J. Deraad, and K. A. Milton, *Classical Electrodynamics*, Advanced book program (Westview Press, 1998).

[76] A. Dauphin, M. Müller, and M. A. Martin-Delgado, Physical Review A **86**, 053618 (2012).

[77] W. S. Bakr, J. I. Gillen, A. Peng, S. Fölling, and M. Greiner, Nature **462**, 74 (2009).

[78] J. F. Sherson, C. Weitenberg, M. Endres, M. Cheneau, I. Bloch, and S. Kuhr, Nature **467**, 68 (2010).

[79] P. W. Anderson, *Basic Notions of Condensed Matter Physics, Frontiers in Physics, Vol. 55* (Benjamin Cummings, London, 1984).

[80] B. Bernu, C. Lhuillier, and L. Pierre, Phys. Rev. Lett. **69**, 2590 (1992); B. Bernu, P. Lecheminant, C. Lhuillier, and L. Pierre, Phys. Rev. B **50**, 10048 (1994).

[81] C. Lhuillier, eprint arXiv:cond-mat/0502464 (2005).

[82] G. Misguich and P. Sindzingre, Journal of Physics: Condensed Matter **19**, 145202 (2007).

[83] I. Rousochatzakis, A. M. Läuchli, and R. Moessner, Phys. Rev. B **85**, 104415 (2012).

[84] J. B. Fouet, M. Mambrini, P. Sindzingre, and C. Lhuillier, Phys. Rev. B **67**, 054411 (2003).

[85] J. M. Luttinger and L. Tisza, Physical Review **70**, 954 (1946).

[86] E. F. Bertaut, J. Phys. Chem. Solids **21**, 256 (1961).

[87] D. B. Litvin, Physica **77**, 205 (1974).

[88] T. A. Kaplan and N. Menyuk, Philos. Mag. **87**, 3711 (2007).

[89] R. J. Elliott, Physical Review **124**, 346 (1961).

[90] M. Fisher and W. Selke, Physical Review Letters **44**, 1502 (1980).

[91] P. Bak, Reports on Progress in Physics **45**, 587 (1982).

[92] W. Selke, Physics Reports **170**, 213 (1988).

[93] W. Krauth and R. Moessner, Phys. Rev. B **67**, 064503 (2003).

[94] C. Carr, R. Ritter, C. G. Wade, C. S. Adams, and K. J. Weatherill, Physical Review Letters **111**, 113901 (2013).

[95] S. V. Isakov, R. Moessner, and S. L. Sondhi, Physical Review Letters **95**, 217201 (2005).

[96] J. Richter, J. Schulenburg, and A. Honecker, in *Quantum Magnetism*, edited by U. Schollwöck, J. Richter, D. Farnell, and R. Bishop (Springer Berlin Heidelberg, 2004) pp. 85–153.

[97] R. Siddharthan and A. Georges, Phys. Rev. B **65**, 014417 (2001); P. Tomczak and J. Richter, Physical Review B **54**, 9004 (1996).

[98] I. Rousochatzakis, R. Moessner, and J. van den Brink, Phys. Rev. B **88**, 195109 (2013).

[99] D. C. Cabra, M. D. Grynberg, P. Holdsworth, A. Honecker, P. Pujol, J. Richter, D. Schmalfuß, and J. Schulenburg, Physical Review B **71**, 144420 (2005).

[100] D. L. Bergman, R. Shindou, G. A. Fiete, and L. Balents, Phys. Rev. B **75**, 094403 (2007).

[101] I. Rousochatzakis, A. M. Läuchli, and F. Mila, Physical Review B **77**, 094420 (2008).

[102] D. Banerjee, M. Dalmonte, M. Müller, E. Rico, P. Stebler, U. J. Wiese, and P. Zoller, Physical Review Letters **109**, 175302 (2012).

[103] P. A. Lee, N. Nagaosa, and X.-G. Wen, Rev. Mod. Phys. **78**, 17 (2006).

[104] E. Fradkin and S. Shenker, Phys. Rev. D **19**, 3682 (1979).

[105] Y. Wan and O. Tchernyshyov, Physical Review Letters **108**, 247210 (2012).

[106] M. Marinescu, H. Sadeghpour, and A. Dalgarno, Physical Review A **49**, 982 (1994).

[107] S. Nascimbène, Y.-A. Chen, M. Atala, M. Aidelsburger, S. Trotzky, B. Paredes, and I. Bloch, Phys. Rev. Lett. **108**, 205301 (2012), 1202.6361 .

[108] S. Trebst, U. Schollwoeck, M. Troyer, and P. Zoller, Phys. Rev. Lett. **96**, 250402 (2006), cond-mat/0506809 .

[109] K. Stannigel, P. Hauke, D. Marcos, M. Hafezi, S. Diehl, M. Dalmonte, and P. Zoller, Phys. Rev. Lett. **112**, 120406 (2014), 1308.0528 .

[110] J. Schachenmayer, L. Pollet, M. Troyer, and A. J. Daley, Phys. Rev. A **89**, 011601 (2014), 1305.1301 .

Table 6.2. *Results for the classical ground state at $t = 0$ from the classical minimization method of Sec. 6.4.3, and Exact Diagonalizations (ED). Here N_{ints} is the total number of interaction terms (of the type $S_i^z S_j^z$) in the Hamiltonian, $\mathbf{Q}$ is the minimum of $\lambda_1(\mathbf{k})$ over the BZ, $\mathbf{v}_1(\mathbf{Q})$ and $\lambda_1(\mathbf{Q})$ are the corresponding eigenvector (dashes indicate when the eigenvectors $\mathbf{v}_1(\mathbf{Q})$ cannot satisfy the spin length constraint) and eigenvalue, respectively. The last line for each given N gives the corresponding ground state energies per unit cell (multiplied by a factor of 4 to account for the unit spin length) as found by ED. Bold numbers indicate the cases with $N_{ints}(N) < N_{ints}(\infty)$ (for the given cutoff J_c) due to the finite size, showing that it is not safe to decrease the cutoff further.*

N		cutoff=0.3	0.1	0.01	0.001
16	N_{ints}/N	3	**5**	**6.5**	**7.5**
	$\mathbf{Q}$	(π,π)	$(0,\pi), (\pi,0)$	$\pm(-\pi/2,\pi/2)$	$\pm(-\pi/2,\pi/2)$
	$\mathbf{v}_1(\mathbf{Q})$	$(1,1)/\sqrt{2}$	$(1,0), (0,1)$	$(1,\mp i)/\sqrt{2}$	$(1,\mp i)/\sqrt{2}$
	$\lambda_1(\mathbf{Q})$	-2.211504	-1.97784	-2.011411	-1.995727
	ED	-2.21150	-1.97784	-2.011411	-1.995727
32	N_{ints}/N	3	7	**10.5**	**15.5**
	$\mathbf{Q}$	(π,π)	$(0,\pi), (\pi,0)$	$\pm(-\pi/2,\pi/2)$	$\pm(-\pi/2,\pi/2)$
	$\mathbf{v}_1(\mathbf{Q})$	$(1,1)/\sqrt{2}$	$(1,0), (0,1)$	$(1,\mp i)/\sqrt{2}$	$(1,\mp i)/\sqrt{2}$
	$\lambda_1(\mathbf{Q})$	-2.211504	-2.271598	-2.089309	-2.056628
	ED	-2.21150	-2.271598	-2.089309	-2.056628
36	N_{ints}	3	7	**11.5**	**16.5**
	$\mathbf{Q}$	(π,π)	$\pm(-\pi,\pi/3)$	$\pm(\pi/3,-\pi/3)$	$\pm(\pi/3,-\pi/3)$
	$\mathbf{v}_1(\mathbf{Q})$	$(1,1)/\sqrt{2}$	—	—	—
	$\lambda_1(\mathbf{Q})$	-2.211504	-2.03528	-1.95403	-1.94119
	ED	-2.21150	-1.8845151	-1.8803936	-1.8731703
64	N_{ints}/N	3	7	12	**25.5**
	$\mathbf{Q}$	(π,π)	$(0,\pi), (\pi,0)$	$\pm(-\pi/2,\pi/2)$	$\pm(-\pi/2,\pi/2)$
	$\mathbf{v}_1(\mathbf{Q})$	$(1,1)/\sqrt{2}$	$(1,0), (0,1)$	$(1,\mp i)/\sqrt{2}$	$(1,\mp i)/\sqrt{2}$
	$\lambda_1(\mathbf{Q})$	-2.211504	-2.271598	-2.166198	-2.108984
	ED	-2.21150	-2.271598	2.166198	-2.108984
72	N_{ints}/N	3	7	12	**27.5**
	$\mathbf{Q}$	(π,π)	$(0,\pi), (\pi,0)$	$\pm(2\pi/3,-\pi/3)$	$\pm(2\pi/3,-\pi/3)$
	$\mathbf{v}_1(\mathbf{Q})$	$(1,1)/\sqrt{2}$	$(1,0), (0,1)$	—	—
	$\lambda_1(\mathbf{Q})$	-2.211504	-2.271598	-2.075198	-2.03849
	ED	-2.21150	-2.271598	-2.04433866	-2.0137376
∞	N_{ints}/N	3	7	12	31
	$\mathbf{Q}$	(π,π)	$(0,\pi), (\pi,0)$	$\pm 0.473296(-\pi,\pi)$	$\pm 0.4573374(-\pi,\pi)$
	$\mathbf{v}_1(\mathbf{Q})$	$(1,1)/\sqrt{2}$	$(1,0), (0,1)$	—	—
	$\lambda_1(\mathbf{Q})$	-2.21150	-2.27159	-2.17273	-2.11938
	$\lambda_1(\frac{-\pi}{2},\frac{\pi}{2})$	-1.93452	-1.93452	-2.16620	-2.10609

Chapter 7

Preprint

Dynamical preparation of laser-excited anisotropic Rydberg crystals[†]

arXiv:1408.0662

B. Vermersch[1,2], M. Punk[1,2], A. W. Glaetzle[1,2], C. Gross[3] and P. Zoller[1,2]

[1] *Institute for Quantum Optics and Quantum Information, Austrian Academy of Sciences, 6020 Innsbruck, Austria*
[2] *Institute for Theoretical Physics, University of Innsbruck, 6020 Innsbruck, Austria* [3] *Max-Planck-Institut für Quantenoptik, 85748 Garching, Germany*

We describe the dynamical preparation of anisotropic crystalline phases obtained by laser-exciting ultracold Alkali atoms to Rydberg p-states where they interact via anisotropic van der Waals interactions. We develop a time-dependent variational mean field ansatz to model large, but finite two-dimensional systems in experimentally accessible parameter regimes, and we present numerical simulations to illustrate the dynamical formation of anisotropic Rydberg crystals.

7.1 Introduction

Highly excited Rydberg states of atoms have unique properties. This includes the size of the Rydberg orbitals scaling as n^2, the polarizabilities as n^7 and a long lifetime as n^3 with n the principal quantum number. These properties are also manifest in interactions between Rydberg states, e.g. in van der Waals (vdW) interactions $\propto n^{11}/r^6$, which can be controlled and tuned via external fields. Exciting ground state atoms with a laser to Rydberg states thus provides a means to study many body systems with strong, long-range interactions [1, 2]. With the atomic ground state and the Rydberg state defining an effective spin-1/2, we can describe the many body dynamics in terms of a model of interacting spins [3–5], reflecting the competition between the laser excitation and vdW interactions, at least in the short time limit where the motion of the atoms can be neglected (the so-called frozen gas regime).

The study of quantum phases of a laser excited Rydberg gas of alkali atoms, including its dynamical preparation, has so far focused on isotropic vdW interactions, corresponding to Rydberg

---

[†] The author of the present thesis contributed to the full quantum treatment of the problem in terms of the derivation of the coupled Liouville-equations and did the molecular dynamics simulations of the collisional process.

s-states excited in a two-photon process. This includes theoretical studies [6–11] and experimental observations [12, 13] of Rydberg crystals due to the Rydberg blockade mechanism [14–20], and their melting with increasing laser intensity to a quantum-disordered phase [21, 22]. The steady state of the system has also been studied in presence of dissipation [23–26]. With the availability of UV laser sources also Rydberg p-states can be excited in a single photon transition, leading to anisotropic vdW interactions [27, 28]. The goal of this paper is to investigate the quantum phases and their dynamical preparation with a laser pulse protocol for these anisotropic interactions. We are interested in 2D systems with a relatively high density of excitations involving a larger number of atoms, and in particular in the dynamical formation of anisotropic Rydberg crystals. Our studies are performed within a time-dependent variational mean field ansatz, beyond what can be accessed by exact diagonalization techniques.

7.2 Model and Method

7.2.1 Laser excited interacting Rydberg atoms as an anisotropic spin model

We are interested in the quantum dynamics and the quantum phases of a gas of laser excited Rydberg atoms, interacting via *anisotropic* vdW interactions. The setup we have in mind is represented in Fig. 7.1. We assume that the atoms are trapped in a 2D square lattice with exactly one atom per lattice site, as obtained in a Mott insulator phase. The atoms are initially prepared in the ground state, denoted by $|\downarrow\rangle$, and coherently excited by a laser to a Rydberg state $|\uparrow\rangle$ with Rabi frequency Ω and laser detuning Δ [see Fig. 7.1(a)]. Two atoms i and k both excited to the Rydberg state $|\uparrow\rangle$ and located at positions $\mathbf{r}_i$ and $\mathbf{r}_k$, respectively, interact via vdW interactions $V(\mathbf{r}_i - \mathbf{r}_k) = C_6(\theta_{i,k})/|\mathbf{r}_i - \mathbf{r}_k|^6$. These vdW interactions exceed typical ground state interactions of cold atoms by several orders of magnitude. We are interested in a situation where the vdW interaction has a non-trivial angular dependence $C_6(\theta_{i,k})$. Such an angular dependence arises, for example, in laser excitation to higher angular momentum states, e.g. to Rydberg p-states, as opposed to excitation of s-states where the interactions are isotropic [27]. In the remainder of this paper we will illustrate the anisotropic interactions by explicitly considering the stretched state $|n^2P_{3/2}, m_j = 3/2\rangle$ of Rubidium for which the $C_6(\theta_{i,k})$ is dominated by a term proportional to $\sin^4\theta_{i,k}$ [28]. Interactions are therefore much stronger along the x direction compared to the z direction [see Fig. 7.1(b)]. The atomic physics underlying this interaction will be discussed in detail in Sec. 7.3 below.

In its simplest form the dynamics of the driven Rydberg gas can be described by an interacting system of pseudospin-1/2 particles

$$H = \frac{\hbar}{2}\sum_{i=1}^{N}\left(\Omega\sigma_x^{(i)} - \Delta\sigma_z^{(i)}\right) + \frac{1}{2}\sum_{i=1}^{N}\sum_{k=1,k\neq i}^{N}\frac{C_6(\theta_{i,k})P_iP_k}{|\,\mathbf{r}_i - \mathbf{r}_k\,|^6} \tag{7.1}$$

where $\sigma_x^{(i)} = |\uparrow\rangle_i\langle\downarrow| + |\downarrow\rangle_i\langle\uparrow|$ and $\sigma_z^{(i)} = |\uparrow\rangle_i\langle\uparrow| - |\downarrow\rangle_i\langle\downarrow|$ correspond to the local Pauli matrices and $P_i = |\uparrow\rangle_i\langle\uparrow|$ is the projection operator on the Rydberg level. We note that in this model atoms are assumed to be pinned to the lattice sites, which is referred to as the *frozen gas approximation* [2]. For isotropic interactions spin models of this type have been discussed in previous theoretical work [6–11], and have been the basis for interpreting experiments [12, 13].

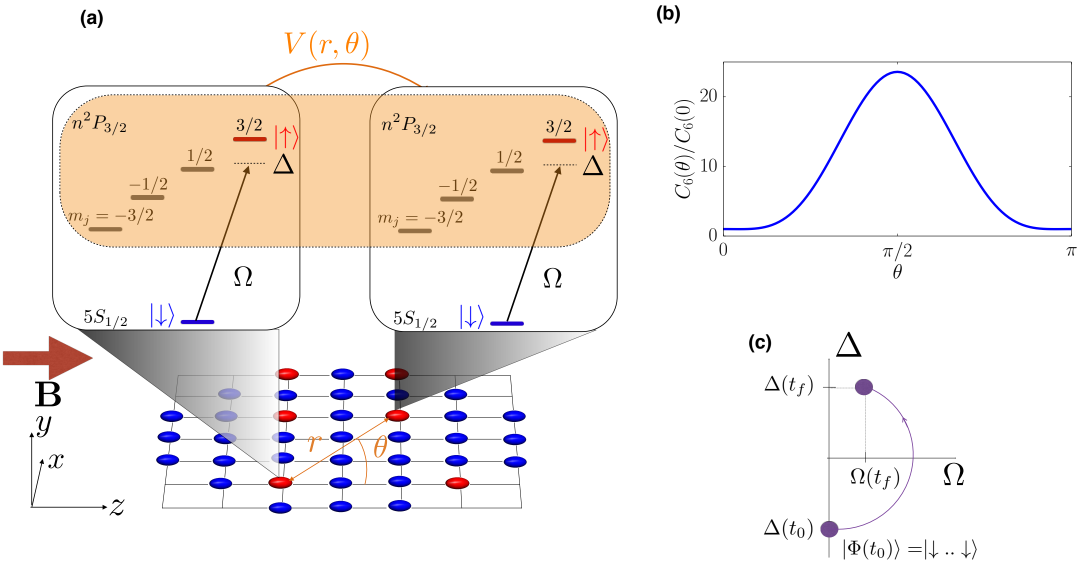

Figure 7.1. *(a) Setup: The ground state atoms $|\downarrow\rangle$ are placed in a square optical lattice and are excited to a Rydberg state $|\uparrow\rangle$ via a homogeneous laser beam with Rabi frequency Ω and detuning Δ. The vdW interaction V between two Rydberg atoms i and k is a function of their relative distance $|\mathbf{r}_i - \mathbf{r}_k|$ but also of the angle $\theta_{i,k}$ between their relative vector and the magnetic field B which is set along the z direction of the lattice. The details of these interactions in the fine structure manifold $n^2P_{3/2}$, in the presence of the magnetic field are discussed in Sec. 7.3. (b) Example of angular dependence of the C_6 coefficient obtained for a Rydberg state of Rubidium $|25P_{3/2}, m_j = 3/2\rangle$. (c) Example of sweep path: initially the atoms are prepared in the ground state $|\downarrow\rangle$ with a negative detuning $\Delta(t_0) < 0$. The Rabi frequency Ω and the laser detuning Δ are then slowly varied to reach the final state of the preparation at time t_f.*

The modeling of the laser excited Rydberg gas as a coherent spin dynamics governed by the Hamiltonian Eq. (7.1) is valid for *sufficiently short times*. First, as we noted above, the model Eq. (7.1) ignores the motion of the atoms: laser excited Rydberg atoms are typically not trapped by the optical lattice for the ground state atoms, and there will be (large) mechanical forces associated with the vdW interactions. In addition, Rydberg states have a finite life time, scaling as $\tau \sim n^3$ ($\tau \sim n^5$) for low (high) angular momentum states with n the principal quantum number, and black body radiation can drive transitions between different Rydberg states, further decreasing the lifetime by approximately a factor of two [29]. The regime of validity has been analyzed in detail in [30]: there the long time dynamics of laser excited Rydberg gas including motion and dissipation was treated, including the validity of the frozen gas approximation and the cross over regime.

We emphasize that the various quantum phases predicted by the spin model Eq. (7.1) as a function of the laser parameters and interactions, and their preparation in an experiment, can only be understood in a dynamical way. In an experiment all atoms are initially prepared in their atomic ground state, $|\Phi(t_0)\rangle = |G\rangle \equiv |\downarrow\rangle_1 \dots |\downarrow\rangle_N$, which is the ground state of the many-body Hamiltonian Eq. (7.1) for $\Omega = 0$ and $\Delta < 0$. Preparation of the ground state of the spin Hamiltonian Eq. (7.1) for a given Ω and Δ can thus be understood in the sense of adiabatic state preparation, where starting from an initial time t_0 with laser parameters $\Omega(t_0) = 0$ and $\Delta(t_0) < 0$ we follow the evolution of the many body state for a parameter trajectory to the final time t_f with $\Omega(t_f) = \Omega$ and $\Delta(t_f) = \Delta$, see Fig. 7.1(c). This dynamical preparation of many-body states and quantum phases of the spin-model Eq. (7.1) in a time-dependent mean field ansatz, in particular in the anisotropic case, will be a central question to be addressed below.

While our focus below will be on the anisotropic model, we find it worthwhile to summarize the basic properties and signatures of the quantum phases (ground states) of the spin model Eq. (7.1) for isotropic interactions. Even for this case, the ground-state phase diagram of the Hamiltonian Eq. (7.1) is rather complicated. In the so-called *classical limit*, $\Omega \to 0$, where all terms in the Hamiltonian Eq. (7.1) commute, the ground-state corresponds to the minimum energy configuration of classical charges on a square lattice interacting via a $1/r^6$ potential, and Δ serves as a chemical potential [31]. As noted above, for $\Delta < 0$ this corresponds to the state $|G\rangle$ with all atoms in the ground state. For $\Delta > 0$ a finite density of excited Rydberg atoms is energetically favorable and the competition between the laser detuning and the vdW interactions results in a complex crystalline arrangement with a typical distance between excited atoms set by the length scale $\ell \equiv [C_6/(\hbar\Delta)]^{1/6}$. In two dimensions the Rydberg atoms ideally want to form a triangular lattice to maximize their distance, which will compete with the square optical lattice for the setup of Fig. 7.1. An exact solution of this classical commensurability problem is not known except in one dimension, where all possible commensurate crystalline phases form a complete devil's staircase [32]. In analogy to the 1D case we expect a plethora of different crystalline phases in two dimensions, which are stable over some part of the phase diagram and which break the lattice symmetries in different ways [31, 33, 34].

Away from the classical limit, $\Omega \neq 0$, the crystalline states of Rydberg atoms are expected to be stable for sufficiently small Ω. By increasing Ω quantum fluctuations will eventually melt the crystalline phases and we reach a quantum disordered phase. The nature of the corresponding quantum phase-transition has been studied in one dimension [21, 22] and remains an open issue in higher dimensions.

Concerning anisotropic interactions, it is natural to expect that the angular dependence of the vdW coefficient, $C_6(\theta_{i,k})$, is responsible for the presence of an anisotropic crystalline phase at small Ω. In summary, our goal below is to describe the dynamical formation of such crystals in large but finite systems similar to realistic experimental situations, where finite size effects still play an important role, and to compare the final state to the ground state of the system in order to assess the fidelity of the dynamical preparation. To this end, we developed an approach based on a time-dependent variational principle which proved very useful to describe the crystalline states for isotropic as well as anisotropic interactions with a large number of excitations, i.e. in a parameter regime where an exact solution cannot be applied.

7.2.2 Time dependent variational ansatz for many-body systems

In the following we present our variational ansatz and the corresponding equations of motion which we use to describe the dynamical preparation of Rydberg crystals governed by Eq. (7.1). The simplest variational ansatz which is able to describe crystalline states of Rydberg atoms takes the most general product state form

$$|\Phi(t)\rangle = \bigotimes_{i=1}^{N} \left[\alpha_i(t)\,|{\downarrow}\rangle_i + \beta_i(t)\,|{\uparrow}\rangle_i\right], \tag{7.2}$$

where N denotes the number of atoms and the coefficients α_i and β_i obey the normalization condition $|\alpha_i|^2 + |\beta_i|^2 = 1$. Crystalline phases correspond to states where the probability $|\beta_i|^2$ to find an atom in the Rydberg state at lattice site i is spatially modulated and its Fourier components serve as an infinite set of order parameters. In contrast, in the quantum disordered phase the Rydberg density is homogeneous and $|\beta_i|^2$ is equal on all lattice sites i.

Equilibrium properties of the variational ansatz

Before deriving equations of motion for the time dependent variational parameters $\alpha_i(t)$ and $\beta_i(t)$ we discuss equilibrium properties of our variational ansatz. Note that the ansatz Eq. (7.2) captures the exact ground- and excited states of our model Hamiltonian [equation Eq. (7.1)] in the classical limit $\Omega \to 0$, where all eigenstates are product states. In the general case $\Omega > 0$, it is an approximation and its validity will be discussed at the end of this subsection. In principle we find the variational ground-state by minimizing the expectation value of the Hamiltonian with respect to the variational parameters α_i and β_i. In the ground-state these parameters can be chosen to be real and the variational ground-state energy, $E = \langle\Phi|H|\Phi\rangle$, can be expressed as function of the probabilities $p_i = |\beta_i|^2$ as

$$\begin{aligned} E(p_i) &= -\hbar\Omega \sum_i \sqrt{p_i(1-p_i)} - \hbar\Delta \sum_i (p_i - \frac{1}{2}) \\ &\quad + \frac{1}{2} \sum_{k \neq i} V(\mathbf{r}_i - \mathbf{r}_k) p_i p_k \end{aligned} \tag{7.3}$$

with $V(\mathbf{r}_i - \mathbf{r}_k) = C_6(\theta_{i,k})/|\mathbf{r}_i - \mathbf{r}_k|^6$. Finding all solutions of the corresponding mean-field equations $\partial E(p_i)/\partial p_i = 0$ in the thermodynamic limit is an impossible task, however. For this reason we do not attempt to make predictions about the phase diagram of Eq. (7.1) in the thermodynamic limit and rather focus on experimentally relevant systems with a finite but large number of atoms instead.

There is one notable exception, however: we can make a statement about the melting transition between the quantum disordered phase at large Ω and the adjacent crystalline phase within our variational (mean-field) approach. In the thermodynamic limit, the quantum disordered phase has a homogeneous Rydberg density $f_R := p_i \equiv p$ and we can determine at which point the homogeneous solution becomes unstable to density modulations. Linearizing the mean-field equations in small perturbations around the homogeneous solution we find the condition

$$1 + \frac{\hbar^2\Omega^2}{[(V_0 f_R - \hbar\Delta)^2 + \hbar^2\Omega^2)]^{3/2}} \min_{\mathbf{k}}(V_{\mathbf{k}}) = 0\,, \tag{7.4}$$

where $V_{\mathbf{k}} = \sum_i e^{\mathrm{i}\mathbf{k}\cdot\mathbf{R}_i} V(\mathbf{R}_i)$ are Fourier components of the interaction potential (note that the density f_R of Rydberg excitations depends on Ω and Δ). We note that an expansion in small density modulations around the homogeneous solution implicitly assumes that the melting transition is continuous. It is possible that this transition could be first order, however. In order to rule out a discontinuous melting transition we minimized the variational energy Eq. (7.3) numerically on a lattice with $N = 441$ sites and found that the melting transition is indeed continuous.

The momentum $\mathbf{k}_0$ at which the interaction potential $V_{\mathbf{k}}$ is minimal determines the wave-vector at which density modulations form in the crystalline phase. In the isotropic case this minimum is at $\mathbf{k}_0 = (k_0^x, k_0^z) = (\pi/a, \pi/a)$, where a is the lattice constant of the optical lattice. If one approaches the crystalline phase from the quantum disordered phase, the leading instability is thus always towards a crystalline state with Neel-type order, which breaks a Z_2 lattice symmetry. Only at smaller Ω more complicated crystalline states appear, which are most likely separated by first order phase transitions. Consequently, within our variational approach the quantum phase transition between the disordered and the crystalline phase is always in the Ising universality class for isotropic interactions, independent of Ω and Δ.

For an anisotropic interaction potential with angular dependence $C_6(\theta_{i,k})$, present for example between $|\uparrow\rangle = |n^2P_{3/2}, m_j = 3/2\rangle$ states of Rubidium as discussed in Sec. 7.3, the minimum is at a wave-vector $\mathbf{k}_0 = (\pi/a, 0)$. Again, if we approach the crystalline phase from the quantum-disordered regime, crystalline order will form only in x-direction with a period of two lattice spacings, whereas no crystalline order is present in z-direction. This transition is again continuous. The system thus decouples into an array of quasi one dimensional Rydberg gases. Upon further decreasing Ω, we expect a transition to a state with incommensurate, floating crystalline order in z-direction, in analogy to one-dimensional systems [21, 22]. The system remains long-range ordered in x-direction, however, and finally settles into a commensurate, genuinely two-dimensional crystalline state at sufficiently small Ω. We leave a detailed investigation of this two-step directional melting transition open for future study.

The phase boundary obtained from Eq. (7.4) is shown in Fig. 7.2 for both isotropic as well as anisotropic interactions with the angular dependence represented in Fig. 7.1(b). As in the anisotropic case the interactions are much stronger in the x direction compared to the z-direction, the corresponding phase-boundary significantly differs from the isotropic curve and is very close to the one obtained for a one-dimensional system. Note that the mean-field phase boundary has an unphysical re-entrance behavior at negative detunings. This is because our variational ansatz vastly overestimates the ground-state energy in the quantum disordered phase at finite Ω, where pair-correlations are important.

Indeed, our product ansatz of Eq. (7.2) does not describe correlations between local density fluctuations of Rydberg atoms

$$\langle \delta P_i \delta P_k \rangle = \langle P_i P_k \rangle - \langle P_i \rangle \langle P_k \rangle \,, \tag{7.5}$$

and thus $\langle \delta P_i \delta P_k \rangle_\Phi \equiv 0$ for our variational wave-function. Deep in the crystalline phase these correlations are weak and decay exponentially with distance, however. We can give an upper bound on the strength of such density density correlations and consequently make a statement about the validity of our ansatz by estimating the strength of local density fluctuations

$$\langle \delta P_i{}^2 \rangle = \langle P_i \rangle (1 - \langle P_i \rangle) \,. \tag{7.6}$$

Accordingly, density-density correlations are negligible deep in the crystal, where $\langle P_i \rangle$ is either close to zero or one. As a consequence we expect our ansatz to be valid also at finite Ω as long as we are deep in the crystalline phase. At sufficiently large Ω, where the system enters the quantum disordered phase and quantum correlations become predominant, our ansatz is not a good approximation for the exact ground-state wave function.

Time-dependent variational ansatz and Euler-Lagrange equations

One of the main goals of our paper is to describe the dynamical formation of crystalline states of Rydberg excitations in a large but finite system during a slow change of the laser parameters. For this

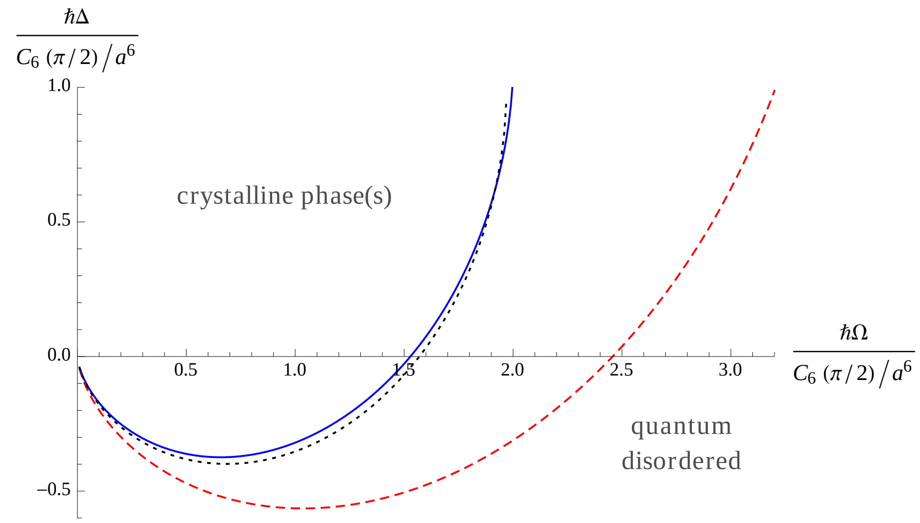

Figure 7.2. *Mean-field phase boundary between the quantum-disordered and crystalline phase(s) obtained from Eq. (7.4). The blue solid line represents the case of anisotropic interactions with the angular dependence $C_6(\theta)$ of Rubidium $|nP_{3/2}, m_j = 3/2\rangle$ atoms [see Fig. 7.1(c)]. The red dashed line shows the phase boundary for isotropic interactions. For comparison, the black dotted line represents the mean-field phase boundary of a one-dimensional system.*

reason we incorporate our ansatz into a time-dependent variational approach, where the formation of Rydberg excitations is described by the time evolution of the variational coefficients $\alpha_i(t)$ and $\beta_i(t)$ and governed by the Hamiltonian Eq. (7.1). Considering an initial condition where all atoms are in the ground state $|G\rangle$, i.e. $\alpha_i(t_0) = 1$ $(\forall i \in \{1, \ldots, N\})$ and $\Omega(t_0) = 0$, $\Delta(t_0) < 0$, we use the time-dependent variational principle (TDVP) [35] to derive the equations of motion for the variational coefficients during a slow change of Ω and Δ as in typical dynamical state preparation schemes [8, 9, 13]. The TDVP states that the time-evolution of the variational coefficients satisfy the least action principle which means that they can be derived using the Euler-Lagrange equations:

$$\begin{aligned}\frac{d}{dt}\left(\frac{\partial L}{\partial \dot{\alpha}_i^*}\right) &= \frac{\partial L}{\partial \alpha_i^*}\\ \frac{d}{dt}\left(\frac{\partial L}{\partial \dot{\beta}_i^*}\right) &= \frac{\partial L}{\partial \beta_i^*}\end{aligned}$$

where L is the Lagrangian

$$L = \frac{i\hbar}{2}\langle\Phi|d_t\Phi\rangle - \frac{i\hbar}{2}\langle d_t\Phi|\Phi\rangle - \langle\Phi|H|\Phi\rangle.$$

leading to a set of $2N$ non-linear coupled equations

$$\begin{aligned}i\hbar\dot{\alpha}_i &= \frac{\hbar\Omega}{2}\beta_i + \frac{\hbar\Delta}{2}\alpha_i\\ i\hbar\dot{\beta}_i &= \frac{\hbar\Omega}{2}\alpha_i - \frac{\hbar\Delta}{2}\beta_i + \sum_{k\neq i}\frac{C_6(\theta_{i,k})}{|\mathbf{r}_i - \mathbf{r}_k|^6}|\beta_k|^2\beta_i.\end{aligned} \tag{7.7}$$

We note that these equations conserve the norm of the wavefunction for all times, i.e. $|\alpha_i(t)|^2+|\beta_i(t)|^2 = 1$. If Ω and Δ do not evolve in time, the expectation value of the energy $E = \langle\Phi|H|\Phi\rangle$ is also a conserved quantity. However, this is not the case for a *dynamical* state preparation and the final energy depends crucially on the parameter trajectory.

In a perfectly adiabatic situation we would obtain the variational ground-state for $\Omega(t_f)$ and $\Delta(t_f)$ at the end of the time evolution. Since our sweep protocols are limited to timescales smaller than the lifetime of the Rydberg state, the preparation will not be perfectly adiabatic and we discuss deviations from adiabaticity in subSec. 7.4.1. We note that given the phase diagram shown in Fig. 7.2 and the typical parameter sweep we consider [Fig. 7.1(b)], the system has to undergo a quantum phase transition from the quantum disordered phase to the crystalline phase at some point in the preparation which may reduce the adiabaticity of the preparation significantly. In the finite systems that we consider in the rest of this work, a finite-size gap is always present which reduces this problem, however.

Finally, we note that our ansatz Eq. (7.2) is particularly suited to study the experimentally relevant situation where the Rydberg laser is switched off at the end of the parameter sweep $\Omega(t_f) = 0$, because it captures the exact ground- and excited states of the Hamiltonian Eq. (7.1) in the classical limit $\Omega = 0$, as discussed above. In subSec. 7.4.1 we also estimate the typical Rabi frequency Ω at which our ansatz fails by comparing our approach to the exact solution of the Schrdinger equation.

In the next section, we explain in detail the implementation of the model Hamiltonian Eq. (7.1) with Rydberg atoms excited to $|\uparrow\rangle = |n^2P_{3/2}, m_j = 3/2\rangle$ Rydberg states in order to provide realistic parameters for our numerical Sec. 7.4.

7.3 Anisotropic interactions for Rydberg atoms in p-states

In the following we discuss the derivation of our model Hamiltonian [equation Eq. (7.1)] from a microscopic Hamiltonian,

$$H_{\text{mic}} = \sum_{i=1}^{N} \left[H_A^{(i)} + H_L^{(i)} \right] + \frac{1}{2} \sum_{i=1}^{N} \sum_{k=1,k\neq i}^{N} H_V^{(i,k)}. \tag{7.8}$$

describing vdW interactions between N alkali atoms laser excited to the $|\uparrow\rangle \equiv |nP_{3/2}, m_j = 3/2\rangle$ Rydberg state. We first focus on the Rydberg manifold and their interactions and then discuss the laser excitations. The first term of Eq. (7.8),

$$H_A^{(i)} = \sum_{m_j} \left[\hbar\omega_{nP_{3/2}} + \mu_B g_j B_z m_j \right] |m_j\rangle\langle m_j|, \tag{7.9}$$

accounts for the energies of the Zeeman sublevels $|m_j\rangle \equiv |nP_{3/2}, m_j\rangle$ with $m_j \in \{-3/2, \ldots, 3/2\}$ as illustrated in Fig. 7.1. Here, $\hbar\omega_{nP_{3/2}}$ is the energy difference between the atomic ground state, $5S_{1/2}$, and the $nP_{3/2}$ Rydberg manifold in the absence of external fields. The second term of $H_A^{(i)}$ describes the lifting of the energy degeneracy of the $nP_{3/2}$ Rydberg manifold due to a magnetic field $\mathbf{B} = B\mathbf{e}_z$ (see Fig. 7.1), with $\mu_B/h = 1.4$ MHz/G the Bohr magneton and g_j the Lande factor for $j = 3/2$. Note, that the quantization axis of the corresponding eigenstates is given by the direction of the magnetic field, $\mathbf{B}$, and is aligned *in plane* along the z-axis, see Fig. 7.1. In order to neglect higher order shifts and to prevent mixing between different fine-structure manifolds the energy shifts $\Delta E_{m_j} = \mu_B g_j B_z m_j$ have to be much smaller than the fine-structure splitting $E_{nP_{3/2}} - E_{nP_{1/2}}$ of the Rydberg manifolds. Typically, the fine structure splitting is of the order of tens of GHz, e.g. 7.9 GHz for $n = 25$.

Away from Foerster resonances two laser excited Rydberg atoms dominantly interact via van der Waals interactions [1, 2]. In general, these van der Waals interactions, $\hat{V}_{\mathrm{vdW}}$, will mix different Zeeman sublevels $|m_j\rangle$ in the $nP_{3/2}$ manifold [36]. Let us denote by $\hat{P} = \sum_{i,j} |m_i, m_j\rangle\langle m_i, m_j|$ a projection operator into the $nP_{3/2}$ manifold, then the dipole-dipole interactions $\hat{V}_{\mathrm{dd}}$ will couple to intermediate states, $\hat{Q}_{\alpha,\beta} = |\alpha,\beta\rangle\langle\alpha,\beta|$, which have an energy difference $\delta_{\alpha\beta}$. In second order perturbation this gives rise to

$$\hat{V}_{\mathrm{vdW}} = \hat{P} \sum_{\alpha\beta} \frac{\hat{V}_{\mathrm{dd}} \hat{Q}_{\alpha,\beta} \hat{V}_{\mathrm{dd}}}{\delta_{\alpha\beta}} \hat{P}, \tag{7.10}$$

where $\hat{V}_{\mathrm{vdW}}$ is understood as an operator acting in the manifold of Zeeman sublevels We note, that in the absence of an external magnetic field, $\mathbf{B} \to 0$, the new eigenenergies obtained from diagonalizing $\hat{V}_{\mathrm{vdW}}$ are isotropic.

Anisotropic van der Waals interactions can be obtained by lifting the degeneracy between the Zeeman sublevels e.g. with a magnetic field. For distances large enough, such that the off-diagonal vdW coupling matrix elements of Eq. (8.8) are much smaller than the energy splitting between the Zeeman sublevels, it is possible to simply consider interactions between $|nP_{3/2}, m_j = 3/2\rangle$ states and neglect transitions to different m_j levels. Typically, for Rydberg p-states the off-diagonal vdW matrix elements are of the same order as the diagonal interaction matrix elements. Pairwise interactions between two atoms excited to the $|\uparrow\rangle = |nP_{3/3}, m_j = 3/2\rangle$ state are then described by the Hamiltonian

$$H_V^{(i,k)} = V(\mathbf{r}_i - \mathbf{r}_k)\, |\uparrow\rangle_i\langle\uparrow| \otimes |\uparrow\rangle_k\langle\uparrow|, \tag{7.11}$$

where $V(\mathbf{r}_i - \mathbf{r}_k) = \langle \frac{3}{2}, \frac{3}{2} | \hat{V}_{\mathrm{vdW}} | \frac{3}{2}, \frac{3}{2} \rangle = C_6(\theta_{i,k})/|\mathbf{r}_i - \mathbf{r}_k|^6$ the van der Waals interaction potential, giving rise to the second term of Eq. (7.1). Here, $\theta_{i,k} = \sphericalangle(\mathbf{B}, \mathbf{r}_i - \mathbf{r}_k)$ is the angle between the relative vector and the quantization axis given by the magnetic field direction $\mathbf{B}$ (see Fig. 7.1).

The second term of Eq. (7.8), $H_L^{(i)}$, accounts for the laser excitation of Rubidium ^{87}Rb atoms prepared in their electronic ground state, which we choose as $|\downarrow\rangle = |5^2S_{1/2}, F = 2, m_F = 2\rangle$, to the $|\uparrow\rangle = |nP_{3/2}, m_j = 3/2\rangle$ Rydberg states. This can be done using a single-photon transition with Rabi frequency Ω, scaling as $\Omega \sim n^{-3/2}$. Using a UV laser source it is possible to obtain Rabi frequencies of several MHz in order to excite Rydberg states around $n \sim 30$. The single particle Hamiltonian governing the laser excitation of atom i is

$$H_L^{(i)}(t) = \frac{\hbar\Omega}{2} \left(|\uparrow\rangle_i\langle\downarrow|\, e^{i(\mathbf{k}_L\cdot\mathbf{r_i} - \omega_L t)} + |\downarrow\rangle_i\langle\uparrow|\, e^{-i(\mathbf{k}_L\cdot\mathbf{r_i} - \omega_L t)} \right), \tag{7.12}$$

where $\omega_L = \omega_{nP_{3/2}} + \Delta E_{3/2}/\hbar + \Delta$ is the laser frequency detuned by Δ from the atomic transition (including the magnetic field splitting) and $\mathbf{k}_L$ is the wave vector of the laser. Unwanted couplings to Zeeman levels with $m_j \neq 3/2$ due to the laser can be prevented by using a detuning $|\Delta| \ll |\Delta E_{3/2} - \Delta E_{1/2}|$ or by using circular polarized light propagating along the quantization axis, i.e. $\mathbf{k_L} \sim \hat{\mathbf{z}}$, which couples $|\downarrow\rangle$ only to the $m_j = 3/2$ state. In a frame rotating with the laser frequency and after absorbing the position dependent phase into $|\uparrow\rangle_i \to e^{-i\mathbf{k}_L\cdot\mathbf{r_i}}\, |\uparrow\rangle_i$ one obtains the first term of Eq. (7.1).

As an example, we consider the $n = 25$ Rydberg state, i.e. $|\uparrow\rangle \equiv |25P_{3/2}, m_j = \frac{3}{2}\rangle$. For the corresponding diagonal van der Waals matrix element we obtain using the model potential from [37]

$$C_6(\theta) = \left(6.33 \sin^4\theta - 0.267 \sin^2\theta + 0.269\right) h\,\mathrm{MHz}\,\mu\mathrm{m}^6. \tag{7.13}$$

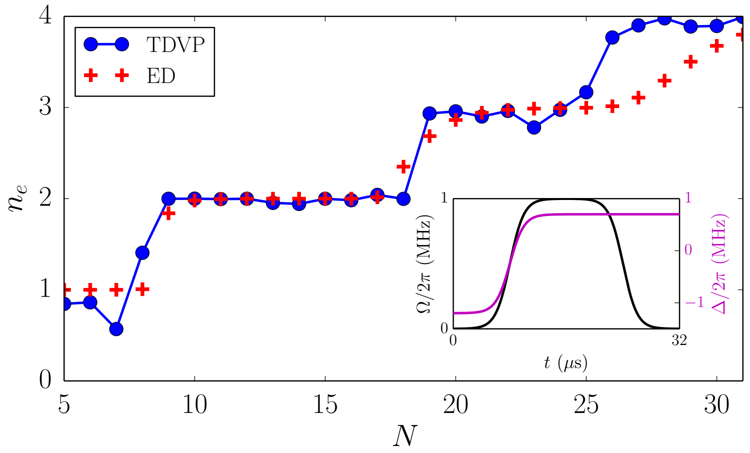

Figure 7.3. *Number of excitations n_e of the final state of the preparation as a function of the number N of atoms obtained after a sweep time of* 32 μs *with* $\Omega(t_f) = 0$, $\Delta(t_f)/(2\pi) = 0.7$ *MHz and a Rydberg state* $|43S_{1/2}, m_j = \frac{1}{2}\rangle$. *Blue circles represent our variational approach, red crosses the exact solution obtained by the Schrdinger equation and the same sweep. Inset: Laser parameters* $\Omega/(2\pi)$ *and* $\Delta/(2\pi)$ *as a function of time* t *used for the dynamical state preparation.*

Thus, $C_6(\pi/2) = 6.35\, h\, \mathrm{MHz}\, \mu\mathrm{m}^6$ and $C_6(0) = 0.269\, h\, \mathrm{MHz}\, \mu\mathrm{m}^6$. The dominant $\sim \sin^4\theta$ term arises from dipole-dipole transitions to $nS_{1/2}$ states, while residual interactions at $\theta = 0$ and deviations from the $\sim \sin^4\theta$ shape originate from couplings to D-channels as discussed in [27]. The lifetime of the Rydberg state is $\tau \approx 29\,\mu$s [29].

We finally note that it is also possible to switch from the anisotropic configuration defined above to an isotropic configuration where the angle θ is fixed to a constant value $\frac{\pi}{2}$. In this configuration, the magnetic field is rotated from the z to the y-direction (see Fig. 7.1) and the Rydberg state which is excited by the laser $|\uparrow\rangle$ is in this case $|n^2P_{3/2}, m_j = \frac{3}{2}\rangle_y$.

7.4 Numerical results

In the following we present our numerical results obtained by propagating the equations of motion Eq. (7.7) along different parameter trajectories $(\Omega(t), \Delta(t))$ in order to describe the dynamical state preparation of Rydberg crystalline phases. To this end we first estimate the domain of validity of our approach based on the TDVP comparing in the case of small systems our results to the exact diagonalization (ED) solution which is obtained from the Schrdinger equation. We then present the results of our approach for large systems ($N > 500$) with large densities of Rydberg excitations where ED techniques cannot be applied.

7.4.1 Validity of the variational approach for small systems

It is instructive to start by considering small systems where an exact numerical solution is available which allows us to estimate the validity of our approach. The first situation we have in mind is

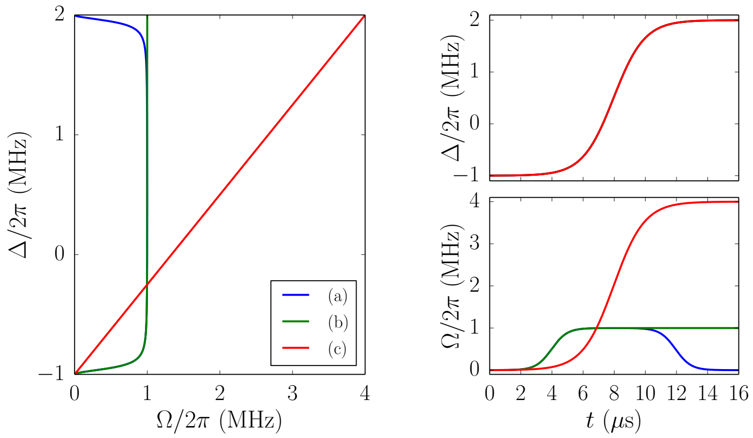

Figure 7.4. *The three different parameter sweep paths (a), (b), (c), corresponding to the final Rabi frequencies $\Omega(t_f)/2\pi = 0, 1$ and 4 MHz. The left plot shows the three paths in parameter space, whereas the right plots show how the parameters evolve as a function of time. Initially, all atoms are in the ground state with $\Omega(t_0) = 0$ and $\Delta(t_0)/(2\pi) = -1$ MHz.*

the classical limit ($\Omega = 0$) of the model Eq. (7.1) for a one-dimensional system where the number of excitations takes the form of the stair case as a function of the number of atoms N [32]. As its existence was recently demonstrated experimentally [13] we consider as a first illustration of our approach the same parameters as in [13] with the notable exception that we choose a larger sweep time $t_f = 32\,\mu$s instead of $t_f = 4\,\mu$s in order to describe the dynamical preparation of states which are as close as possible to the ground state of the system. We now test our approach by comparing the exact number of excitations n_e for theses parameters, obtained after a truncation of the Hilbert space [8] , to the one corresponding to our variational ansatz. The result is shown in Fig. 7.3 as a function of the number of atoms N where the laser sweep is represented in the inset. Our approach describes very well the excitation stair case and apart from some defects (for example for $N = 8$) compares very well with the exact solution (red crosses). We finally emphasize that as the sweep time is increased, our solution converges towards the exact classical ground state, as expected.

Our approach describes the key feature of the one-dimensional system but as it relies on a mean-field approximation of the many-body Hamiltonian Eq. (7.1), its domain of validity may strongly depend on the dimension of the system. As a second illustration of our variational approach we consider, therefore, a small two-dimensional system of $N = 16$ atoms, in an isotropic configuration where an ED solution based on the truncation of the Hilbert space is still available.

Our goal here is to show the influence of the final Rabi frequency $\Omega(t_f)$ on the validity of our approach. To this end, we consider three different sweeps of the Rabi-frequency Ω and detuning Δ along the paths shown in Fig. 7.4 corresponding to three final Rabi frequencies $\Omega(t_f)/(2\pi) = 0, 1, 4$ MHz at a positive detuning $\Delta(t_f)/(2\pi) = 2$ MHz. In all three cases we start at a negative detuning $\Delta(t_0)/(2\pi) = -1$ MHz and zero Rabi frequency and compute the mean distribution of excited Rydberg atoms at the end of the sweep, which is given by $|\beta_i|^2$. We choose a lattice spacing $a = 532$ nm and the Rydberg level $|\uparrow\rangle = |25P_{3/2}, m_j = 3/2\rangle$ corresponding to a C_6 coefficient Eq. (7.13) where due to the isotropic configuration considered here, the angle θ is fixed to $\frac{\pi}{2}$. The sweep time is $t_f = 16\,\mu s$ which is lower than the lifetime of the Rydberg excitations $\tau \approx 29\,\mu$s [29].

Fig. 7.5 shows final distributions of Rydberg atoms computed using our TDVP approach (upper

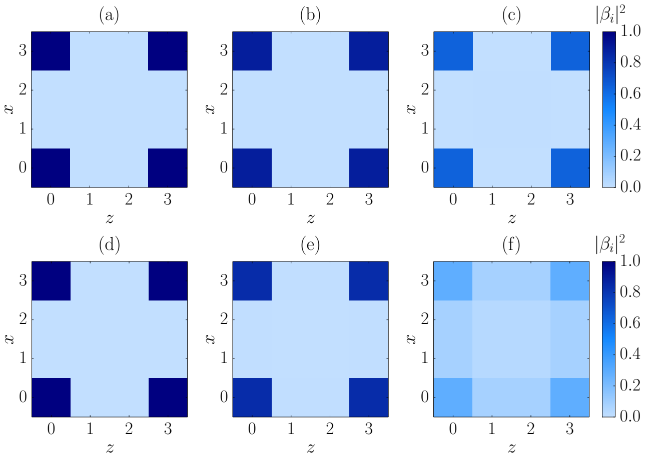

Figure 7.5. *Comparison of TDVP with ED. Upper panel: distribution of Rydberg atoms for isotropic interactions after the three parameter sweeps shown in Fig. 7.4 using the TDVP approach. Lower panel: same as in the upper panel but calculated using ED. For small final Rabi frequencies the results obtained by both approaches are basically indistinguishable. The corresponding energies per particle are* $E = 0.603, 0.556, 0.204\,h$ *MHz for (a), (b), (c) in the upper panel and* $E = 0.602, 0.548, -0.049\,h$ *MHz for (d), (e), (f) in the lower panel.*

panel) as well as ED (lower panel) for the three sweeps (a) (b) (c). Note that in contrast to the 1D case, the variational ansatz describes the sweep to the classical limit $\Omega(t_f) = 0$ perfectly well, even though our approach propagates the wave-function through the non-classical region $\Omega > 0$, where our ansatz is not strictly valid. In a perfectly adiabatic situation corresponding to $t_f \to \infty$, the final state obtained with our time-dependent variational approach would coincide with the variational ground state, which is the exact ground state in this case. The fact that our results for a finite sweep time compare very well with the exact solution suggests that deviations from adiabaticity are negligible. For such a small system size, the competition between the laser excitation and the vdW interactions results in a regular pattern of four Rydberg atoms placed at the corners of the system. We also obtain a good agreement for $\Omega(t_f)/(2\pi) = 1$ MHz and the corresponding pattern is not modified compared to the classical limit. However, for $\Omega(t_f)/(2\pi) = 4$ MHz, our ansatz overestimates the ground state energy considerably, even though the distribution of excitations looks similar to the exact result. It is also instructive to study how the system behaves during the sweep. Fig. 7.6s (a) and (b) show a comparison of Rydberg density f_R and energy as function of time during the parameter sweep for the three sweep protocols shown in Fig. 7.4. Again a substantial difference between TDVP and ED is only visible for sweeps to large final Rabi frequencies.

The results shown in Fig. 7.5 and Fig. 7.6(b),(c) allow to assess the validity of our approach for a realistic dynamical state preparation. We are also interested in estimating the typical value of the parameters Ω, Δ where our ansatz can describe the ground state of the model Eq. (7.1), regardless of the details of the dynamical state preparation. To this end we consider a very large sweep time $t_f = 150\,\mu$s to ensure that the equations of motion Eq. (7.7) lead to the formation of the variational ground state whereas the solution obtained with ED results in the exact ground state. We then estimate the regime of validity of the variational ground state as follows: we compute the Rydberg density at the end of the parameter sweep using both TDVP and ED and plot the relative difference of f_R between the two approaches as a function of the final Rabi frequency $\Omega(t_f)$ at the end of the sweep.

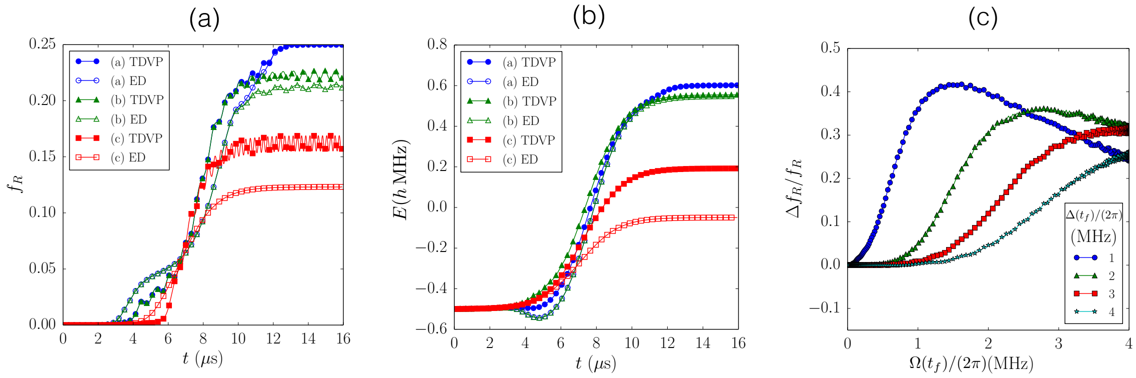

Figure 7.6. *Comparison between TDVP and ED. (a) density of Rydberg atoms f_R as a function time t during the sweep for the three paths shown in Fig. 7.4. (b) Energy as function of sweep time. (c) graph shows the difference in the Rydberg density $\Delta f_R/f_R$ after an adiabatic parameter sweep as calculated from TDVP with respect to ED as a function of the final $\Omega(t_f)/(2\pi)$ and for four different final detunings $\Delta(t_f)/(2\pi) = 1, 2, 3, 4$ MHz. For $\Delta(t_f)/(2\pi) = 2$ MHz the difference Δf_R of the Rydberg density between the two methods starts to deviate from zero if $\Omega(t_f)/(2\pi) \gtrsim 1$ MHz, indicating the breakdown of our variational approach.*

Results are shown in Fig. 7.6(c) for four different final detunings Δ. We see that for a final detuning $\Delta(t_f)/(2\pi) = 2$ MHz the difference $\Delta f_R/f_R$ starts to deviate from zero if the sweep protocol samples Rabi frequencies which are larger than $\Omega(t_f)/(2\pi) > 1$ MHz. Accordingly, for $\Delta/(2\pi) = 2$ MHz our variational ansatz is correct as long as $\Omega/(2\pi) \lesssim 1$ MHz. We note, however, that this criterion was obtained for a small system and potentially depends on system size.

7.4.2 Isotropic Rydberg crystals

Now that we have assessed the regime of validity of our ansatz and checked in particular that it can quantitatively describe the dynamical preparation of Rydberg crystals in small two dimensional systems, let us now present our results for large system sizes where an exact numerical treatment is not possible.

We first describe the formation of Rydberg crystals in an isotropic configuration. In analogy to the experimental setup [13], we start from a circular (cookie shaped) distribution of $N = 777$ ground-state atoms considering the three sweeps path shown in Fig. 7.4 keeping the other parameters of the last subsection unchanged.

Let us first comment on our choice of sweep paths (Fig. 7.4). In order to prepare a state which is as close as possible to the variational ground-state, it is particularly important to circumvent the region around the critical point $\Omega = 0, \Delta = 0$ [7] during the sweep into the crystalline phase. Indeed we found that the energy of the final state increases substantially if the initial negative detuning is chosen too small. On the other hand, if the initial detuning is too large, the length of the sweep path in parameter space is long and the rate of change of the parameters during the same sweep time is increasing such that the sweep becomes less adiabatic again. This is shown in Fig. 7.7 where we plot the energy of the final state obtained for $\Omega(t_f) = 0$ and $\Delta(t_f)/(2\pi) = 2$ MHz as a function of the initial detuning, for different sweep times. We found that the optimal choice of the initial detuning is $\Delta(t_0)/(2\pi) = -1$

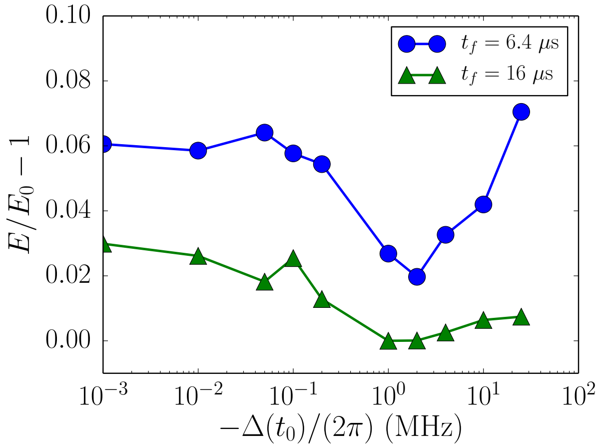

Figure 7.7. *Influence of the sweep time t_f and of the initial detuning $\Delta(t_0)$ on the energy E at the end of the sweep for the case of isotropic interactions and $\Omega(t_f) = 0$ and $\Delta(t_f)/(2\pi) = 2$ MHz. E_0 represents the minimum of the energy obtained for $t_f = 16\ \mu s$ and $\Delta(t_0)/(2\pi)$= -1 MHz which corresponds to the first path in Fig. 7.4. The results show that the fidelity to stay in the ground-state during the parameter sweep decreases if $\Delta(t_0)$ is too small or the sweep time is too short.*

MHz. In this case our sweeps are almost adiabatic in the sense that the energy of the states at the end of the sweeps is less than three percent above the ground-state energy which we found by an independent optimization of the variational wave-functions using a homotopy-continuation method [38].

Results for the final distribution of Rydberg excitations at the end of the sweep are shown in Fig. 7.8. We note that for all three sweep protocols we obtain a single crystalline pattern which respects the symmetries of the cookie-shaped atom distribution. The shape of the crystal is pinned by boundary effects and the variational ground-state that we find is non-degenerate and unique. This is in contrast to experiments, where different symmetry-related, almost degenerate crystal configurations are observed from shot to shot [13]. Also note that our equations of motion for the variational parameters Eq. (7.7) preserve symmetries during time evolution. If degenerate, symmetry related ground states exist for a given set of parameters Δ and Ω, the time evolution passes through a bifurcation point, which signals the presence of the phase transition to the crystalline state. At this point tiny numerical errors will pick out one of the degenerate ground states. It is important to emphasize, however, that we always found a unique, symmetric variational ground-state for the parameters considered here.

Ideally, the first sweep to a final Rabi frequency $\Omega(t_f) = 0$ shown in Fig. 7.4(a) prepares the ground-state of the classical Ising model, if the sweep were perfectly adiabatic. In this case the arrangement of excited Rydberg atoms would correspond to the minimum energy configuration of classical charges with a $1/r^6$ potential and the probability to be in the Rydberg state is either zero or one in this limit. From Fig. 7.8(a) one can see that the probability to be in the Rydberg state is ~ 0.8 rather than 0 or 1 on some sites, indicating deviations from adiabaticity. Nevertheless, a crystalline arrangement of Rydberg atoms is clearly visible. The average density of Rydberg atoms is $f_R = 0.09$ in this case, which is in accordance with an average distance between two excitations on the order of $\left[C_6\left(\frac{\pi}{2}\right)/\hbar\Delta\right]^{1/6} \approx 2-3$.

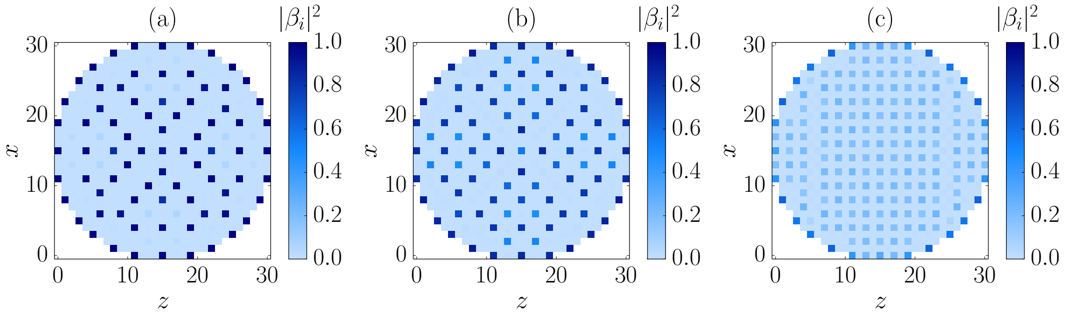

Figure 7.8. *Distribution of Rydberg excitations at the end of the three parameter sweep protocols (a), (b), (c) shown in Fig. 7.4 for the case of isotropic interactions. Plotted is the probability $|\beta_i|^2$ to be in the Rydberg state on each lattice site. The corresponding energies per lattice site are $E = 0.86, 0.82, 0.52\,h\,MHz$. The crystalline arrangement of Rydberg atoms is clearly visible. In the classical limit $\Omega \to 0$ (left) the excitation probabilities are close to either zero or one, whereas quantum superpositions with intermediate values of $|\beta_i|^2$ appear at finite Ω (middle, right).*

For the case of sweeps to finite final Rabi frequencies $\Omega(t_f)$ away from the classical limit [figures 7.8(b) and (c)], quantum superpositions between ground-state and excited atoms are present, and the probability to be in the Rydberg state is thus no longer restricted to zero or one. For increasing final Ω quantum fluctuations are stronger and the average number of Rydberg excitations increases, while the average excitation probability decreases. At large enough Ω the crystalline arrangement finally melts and one enters a quantum disordered regime where the average excitation probability is equal on all lattice sites. This trend is visible in panel (c).

Note that the complex crystalline arrangement of Rydberg atoms is strongly dependent on the size and of the shape of the system. In an infinite system the excited atoms would ideally maximize their average distance, which would result in a triangular lattice of Rydberg atoms. Due to the underlying square optical lattice strong commensurability issues arise, however, in particular if the average distance between excitations is on the order of a few lattice spacings. We observe that the crystalline structure is strongly pinned by boundary effects in our case and the crystalline structures in the classical limit thus do not resemble those which supposedly exist in the thermodynamic limit [31].

7.4.3 Anisotropic Rydberg crystals

We now describe the preparation of anisotropic Rydberg crystals. In this case, the magnetic field is set along the z-direction of the optical lattice, as shown in Fig. 7.1(a), keeping the other parameters such as sweep paths, atom distribution and the Rydberg level unchanged. Accordingly, the interaction between Rydberg atoms is anisotropic and stronger in x- than in z-direction.

Results for the three sweep paths are presented in the upper panel of Fig. 7.9. As in the isotropic case, the crystal progressively melts as Ω is increased. Note, however, that the anisotropy is visible in all cases and the crystalline structure melts first in the weakly interacting z-direction while translational symmetry is still broken in the strongly interacting x-direction. Again, we observe that the form of the Rydberg crystal is strongly pinned by boundary effects, similar to the isotropic case.

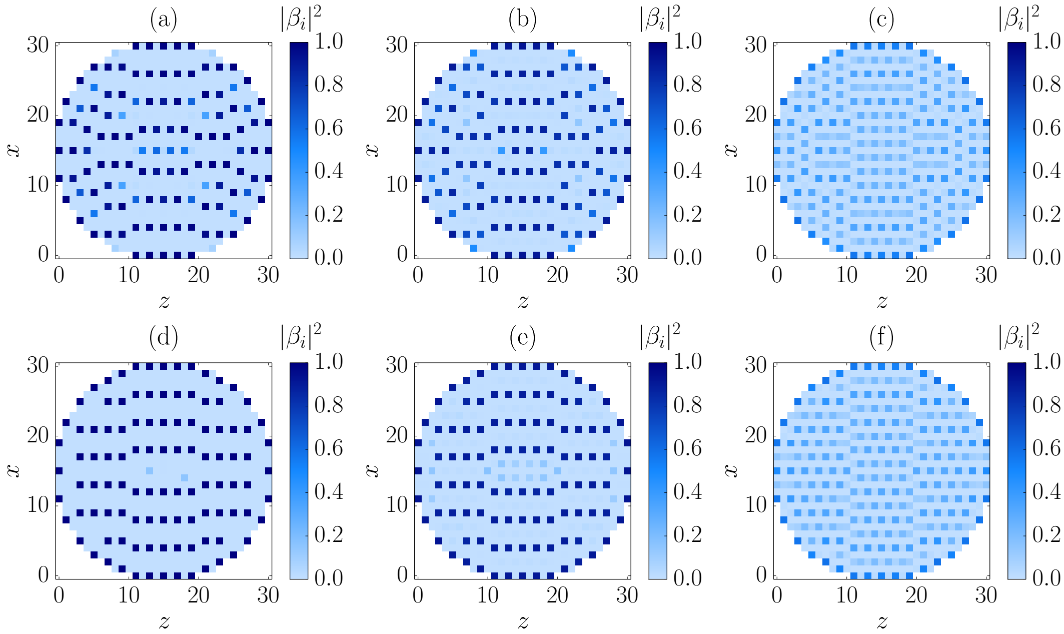

Figure 7.9. *Upper panel: distribution of Rydberg excitations at the end of the three parameter sweep protocols (a), (b), (c) shown in Fig. 7.4 for the case of anisotropic interactions. Corresponding energies per lattice site are* $E = 0.79, 0.74, 0.30\,h$ *MHz. Lower panel: distribution of Rydberg excitations obtained after a direct minimization of the variational ground-state energy. The Rabi frequencies and detunings match the parameters at the end of the sweep protocols in the upper panel. Corresponding ground-state energies per particle are* $E = 0.77, 0.72, 0.29\,h$ *MHz. Defects in the crystalline arrangement due to the small non-adiabaticity of the sweep protocols are clearly visible in the left panel.*

In the classical limit $\Omega = 0$, we find an anisotropic crystal with an average distance between excitations on the order of $\left[C_6\left(\frac{\pi}{2}\right)/\hbar\Delta\right]^{1/6} \approx 3$ in the $x-$direction and of $\left[C_6\left(0\right)/\hbar\Delta\right]^{1/6} \approx 1-2$ in the $z-$direction. Again, the results for the sweep to the classical limit $\Omega(t_f) = 0$ indicate that the preparation was not perfectly adiabatic. Indeed, the excitation probabilities differ from 0 or 1 at the end of the parameter sweep, as in the case of isotropic interactions. The deviations from adiabaticity are even more pronounced for anisotropic interactions, as we find non-classical excitation probabilities on the order of ~ 0.5 in this case. This can be attributed to the fact that the excitation gaps are smaller compared to the case of isotropic interactions, due to the substantially weaker interaction in z-direction.

In order to estimate the fidelity of the dynamic state preparation scheme we plot the distribution of Rydberg atoms obtained after a direct minimization of the ground-state energy within our variational ansatz in the lower panel of Fig. 7.9. Comparing this to the distributions obtained after the parameter sweep it is apparent that a number of defects are created due to the not fully adiabatic sweep protocol. Again, the crystalline arrangement is not strongly affected by the rather short sweep time, however.

7.5 Conclusion and outlook

In the present work we have developed a time dependent mean field theory to model the dynamical preparation of anisotropic Rydberg crystals with atoms in 2D optical lattices. In addition we have presented results of numerical simulations relevant for experimentally realistic system sizes, in the limit of patterns with a large number of Rydberg excitations.

We note that the anisotropic character of the vdW interactions has been seen experimentally in a recent Rydberg-blockade experiment involving Rydberg s and d-states [39]. In contrast to the present work, where we considered the anisotropic vdW interactions between single Zeeman levels of the Rydberg states, i.e. in the limit of large Zeeman splitting, in these experiments vdW couplings involving transitions between Zeeman levels can be important. This interplay leads to several new physical phenomena, which will be presented in a future work.

Acknowledgment

We thank W. Lechner, T. Lahaye, A. Browaeys and I. Bloch for interesting discussions. Work at Innsbruck is supported by the ERC-Synergy Grant UQUAM and SFB FOQUS of the Austrian Science Fund. B. V. acknowledges the Marie Curie Initial Training Network COHERENCE for financial support. M. P. is supported by the Erwin Schrödinger Fellowship No. J 3077-N16 of the Austrian Science Fund (FWF).

Bibliography

[1] M. Saffman, T. G. Walker, and K. Mølmer, Reviews of Modern Physics **82**, 2313 (2010).

[2] R. Löw, H. Weimer, J. Nipper, J. B. Balewski, B. Butscher, H. P. Büchler, and T. Pfau, Journal of Physics B: Atomic, Molecular and Optical Physics **45**, 113001 (2012).

[3] I. Bloch, J. Dalibard, and W. Zwerger, Reviews of Modern Physics **80**, 885 (2008).

[4] I. Bloch, J. Dalibard, and S. Nascimbène, Nature Physics **8**, 267 (2012).

[5] I. M. Georgescu, S. Ashhab, and F. Nori, Reviews of Modern Physics **86**, 153 (2014).

[6] F. Robicheaux and J. Hernández, Physical Review A **72**, 063403 (2005).

[7] H. Weimer, R. Löw, T. Pfau, and H. P. Büchler, Physical Review Letters **101**, 250601 (2008).

[8] T. Pohl, E. Demler, and M. D. Lukin, Physical Review Letters **104**, 043002 (2010).

[9] J. Schachenmayer, I. Lesanovsky, A. Micheli, and A. J. Daley, New Journal of Physics **12**, 103044 (2010).

[10] I. Lesanovsky, Physical Review Letters **106**, 025301 (2011).

[11] M. Gärttner, K. P. Heeg, T. Gasenzer, and J. Evers, Physical Review A **86**, 033422 (2012).

[12] P. Schauß, M. Cheneau, M. Endres, T. Fukuhara, S. Hild, A. Omran, T. Pohl, C. Gross, S. Kuhr, and I. Bloch, Nature **491**, 87 (2012).

[13] P. Schauß, J. Zeiher, T. Fukuhara, S. Hild, M. Cheneau, T. Macrì, T. Pohl, I. Bloch, and C. Gross, , 10 (2014), arXiv:1404.0980 .

[14] D. Jaksch, J. I. Cirac, P. Zoller, S. L. Rolston, R. Côté, and M. D. Lukin, Phys. Rev. Lett. **85**, 2208 (2000).

[15] M. D. Lukin, M. Fleischhauer, R. Cote, L. M. Duan, D. Jaksch, J. I. Cirac, and P. Zoller, Phys. Rev. Lett. **87**, 37901 (2001).

[16] D. Tong, S. M. Farooqi, J. Stanojevic, S. Krishnan, Y. P. Zhang, R. Côté, E. E. Eyler, and P. L. Gould, Physical Review Letters **93**, 063001 (2004).

[17] K. Singer, M. Reetz-Lamour, T. Amthor, L. G. Marcassa, and M. Weidemüller, Physical Review Letters **93**, 163001 (2004).

[18] P. Cheinet, S. Trotzky, M. Feld, U. Schnorrberger, M. Moreno-Cardoner, S. Fölling, and I. Bloch, Physical Review Letters **101**, 090404 (2008).

[19] A. Gaëtan, Y. Miroshnychenko, T. Wilk, A. Chotia, M. Viteau, D. Comparat, P. Pillet, A. Browaeys, and P. Grangier, Nature Physics **5**, 115 (2009).

[20] E. Urban, T. a. Johnson, T. Henage, L. Isenhower, D. D. Yavuz, T. G. Walker, and M. Saffman, Nature Physics **5**, 110 (2009).

[21] H. Weimer and H. P. Büchler, Physical Review Letters **105**, 230403 (2010).

[22] E. Sela, M. Punk, and M. Garst, Physical Review B **84**, 085434 (2011).

[23] M. Höning, D. Muth, D. Petrosyan, and M. Fleischhauer, Physical Review A **87**, 023401 (2013).

[24] I. Lesanovsky and J. P. Garrahan, Physical Review Letters **111**, 215305 (2013).

[25] D. Petrosyan, Physical Review A **88**, 043431 (2013).

[26] M. Hoening, W. Abdussalam, M. Fleischhauer, and T. Pohl, , 1 (2014), arXiv:arXiv:1404.1281v1 .

[27] A. Reinhard, T. Liebisch, B. Knuffman, and G. Raithel, Physical Review A **75**, 032712 (2007).

[28] A. W. Glaetzle, M. Dalmonte, R. Nath, I. Rousochatzakis, R. Moessner, and P. Zoller, **1**, 26 (2014), arXiv:1404.5326 .

[29] I. Beterov, I. Ryabtsev, D. Tretyakov, and V. Entin, Physical Review A **79**, 052504 (2009).

[30] A. Glaetzle, R. Nath, B. Zhao, G. Pupillo, and P. Zoller, Physical Review A **86**, 043403 (2012).

[31] L. Rademaker, Y. Pramudya, J. Zaanen, and V. Dobrosavljević, Physical Review E **88**, 032121 (2013).

[32] P. Bak and R. Bruinsma, Physical Review Letters **49**, 249 (1982).

[33] S. Lee, J.-R. Lee, and B. Kim, Physical Review Letters **88**, 025701 (2001).

[34] W. Zeller, M. Mayle, T. Bonato, G. Reinelt, and P. Schmelcher, Physical Review A **85**, 063603 (2012).

[35] P. Kramer, Journal of Physics: Conference Series **99**, 012009 (2008).

[36] T. Walker and M. Saffman, Physical Review A **77**, 032723 (2008).

[37] M. Marinescu, H. Sadeghpour, and A. Dalgarno, Physical Review A **49**, 982 (1994).

[38] M. Punk, , 5 (2014), arXiv:1405.5894 .

[39] D. Barredo, S. Ravets, H. Labuhn, L. Béguin, A. Vernier, F. Nogrette, T. Lahaye, and A. Browaeys, Phys. Rev. Lett. **112**, 183002 (2014).

CHAPTER 8

PREPRINT

Frustrated Quantum Magnetism with Laser-Dressed Rydberg Atoms[†]

arXiv:1410.3388

A. W. Glaetzle[1,2], M. Dalmonte[1,2], R. Nath[1,2,3], Christian Gross[4], Immanuel Bloch[4,5], and
P. Zoller[1,2]

[1]*Institute for Quantum Optics and Quantum Information of the Austrian Academy of Sciences,
A-6020 Innsbruck, Austria*
[2]*Institute for Theoretical Physics, University of Innsbruck, A-6020 Innsbruck, Austria*
[3]*Indian Institute of Science Education and Research, Pune 411 008, India*
[4]*Fakultät für Physik, Ludwig-Maximilians-Universität München, 80799 Munich, Germany*
[5]*Max-Planck-Institut für Quantenoptik, 85748 Garching, Germany*

We show how a broad class of lattice spin-1/2 models with angular- and distance-dependent couplings can be realized with cold alkali atoms stored in optical or magnetic trap arrays. The effective spin-1/2 is represented by a pair of atomic ground states, and spin-spin interactions are obtained by admixing van der Waals interactions between fine-structure split Rydberg states with laser light. The strengths of the diagonal spin interactions as well as the “flip-flop”, and “flip-flip” and “flop-flop” interactions can be tuned by exploiting quantum interference, thus realizing different spin symmetries. The resulting energy scales of interactions compare well with typical temperatures and decoherence time-scales, making the exploration of exotic forms of quantum magnetism, including emergent gauge theories and compass models, accessible within state-of-the-art experiments.

8.1 Introduction

Understanding exotic forms of quantum magnetism is an outstanding challenge of condensed matter physics [1]. Cold atoms stored in optical or magnetic trap arrays provide a unique platform to realize interacting quantum spins in various lattice geometries with tunable interactions, and thus the

---

[†] The author of the present thesis was strongly involved in doing the calculation presented in this work and in writing the manuscript. In particular, he preformed the atomic physics calculation deriving the van der Waals interactions. This chapter was updated on 13th of Oct 2014.

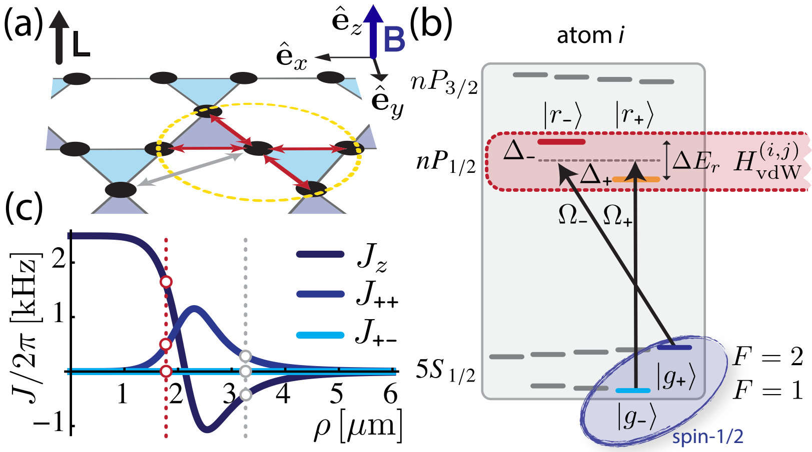

Figure 8.1. *(a) Atoms loaded in a Kagome lattice driven by laser light (L) propagating along the z-axis defined by the magnetic field (B).(b) Atomic level scheme:* ^{87}*Rb atoms with hyperfine ground states* $|g_\sigma\rangle$ *(representing spin-1/2) coupled to* $n^2P_{1/2}$ *Rydberg states with* $\sigma^\pm$ *polarized light and interacting via vdW interactions. (c) Spin interactions* J_α *of Eq.* (8.1) *as a function of distance* ρ *realizing quantum spin ice on a Kagome lattice [10]. Red (gray) dotted lines indicate NN and NNN interactions [red (gray) arrows in panel (a)]. Here* $|r_\pm\rangle = |60^2P_{1/2}, \pm\frac{1}{2}\rangle$ *with Rabi frequencies* $\Omega_- = \Omega_+/4 = 2\pi\times 2.5$ *MHz and detunings* $\Delta_- = -\Delta_+ = 2\pi\times 50$ *MHz (so that* $J_{+-} = 0$ *— see text).*

basic ingredients of competing magnetic orders and frustrated magnetism [2]. A central experimental challenge for the observation of magnetic phases with cold atoms is given by the requirement of ultra-low temperatures (and entropies), as set by the interaction scales of magnetic interactions. For spin models derived from Hubbard dynamics for atoms in optical lattices, this energy scale is set by the super-exchange processes, $J \sim t_H^2/U$, with t_H the hopping amplitude of atoms between lattice sites, and U the onsite interactions, resulting in (rather small) energy scales of a few-tens of Hertz (or few nK) regime [3] (see however [4]). Below we take an alternative route, and show that laser-excited interacting Rydberg atoms [5] provide us not only with a complete toolbox to design and realize the complex spin-1/2 models of interest, but also give rise to energy scales much larger than relevant decoherence rates. In contrast to models where a spin is encoded directly in a Rydberg state [6] we use ground state atoms weakly dressed with Rydberg states by laser light [7], which can be trapped in (large spacing) optical [8] or magnetic lattices [9] of various geometries. This should make phases of exotic quantum magnetism accessible to present atomic experiments.

We are interested in general XYZ spin-1/2 models with both isotropic and anisotropic interactions in 2D, as represented by the Hamiltonian

$$\begin{aligned} H = \sum_{i<j} \Big[& J_z(\mathbf{r}_{ij}) S_z^i S_z^j + J_{\|}(\mathbf{r}_{ij}) S_z^i \\ & + \frac{1}{2}\left(J_{+-}(\mathbf{r}_{ij}) S_+^i S_-^j + J_{++}(\mathbf{r}_{ij}) S_+^i S_+^j + \text{h.c.}\right)\Big], \end{aligned} \tag{8.1}$$

where S_α^j are spin-1/2 operators at the lattice sites $\mathbf{r}_j$. Our goal is to design spin-spin interaction patterns J_α, including nearest-neighbor (NN) and next-nearest-neighbor (NNN) couplings, as a function of $\mathbf{r}_{ij} = \mathbf{r}_i - \mathbf{r}_j$ including the range, angular dependence and strength of the couplings. Below we wish to illustrate the broad tunability offered by our setup in the context of a paradigmatic example illustrated in Fig. 8.1: on a Kagome lattice, different coupling realizations of Eq. (8.1) encompass a variety of physical models, including Kagome quantum spin ice (requiring $J_{+-} = 0$) [10] and extended XYZ models [11]. These models encompass a prototypical feature of frustrated quantum magnets, i.e., the emergence of dynamical gauge fields [1]. The specific form of the underlying gauge theories and the presence of topological spin liquid phases has been actively debated, making the controlled realization of such Hamiltonian dynamics timely matched with current theoretical efforts.

8.2 The model

In our setup we consider single atoms loaded in trap arrays of tunable geometry with spacings on the micrometer scale as demonstrated in recent experiments [8, 9]. We are interested here in alkali atoms, where a pair of states from the two hyperfine manifolds in the atomic ground state represents the effective spin-1/2 [12]. To be specific we consider ^{87}Rb atoms and choose $|g_+\rangle \equiv |5^2S_{1/2}, F = 2, m_F = 2\rangle$ and $|g_-\rangle \equiv |5^2S_{1/2}, F = 1, m_F = 1\rangle$ as our spin-1/2 [see Fig. 8.1(b)].

Interactions between these effective spin states are induced by admixing highly lying Rydberg states to the atomic ground states with laser light, where van der Waals (vdW) interactions provide a strong coupling even at micrometer distances. The key element is the excitation of Rydberg states with finite orbital angular momentum exhibiting fine structure splitting, and it is the combination of the spin-orbit interaction and vdW interactions which provides the mechanism for the spin-spin coupling. As indicated in Fig. 8.1(b), we assume excitations by left and right circularly polarized lasers with propagation direction orthogonal to the lattice plane. In this configuration the ground states are coupled to the two Rydberg Zeeman levels $|r_{\sigma=\pm}\rangle \equiv |n^2P_{1/2}, m_j = \pm\frac{1}{2}\rangle \otimes |m_I = \frac{3}{2}\rangle$. Here, $|m_I = \frac{3}{2}\rangle$ is the maximally polarized nuclear spin state, which remains a spectator in our dynamics [1]. This choice of laser configuration leads to spin couplings $J_\alpha(\rho_{ij})$ with a *purely radial* dependence as a function of the distance $\rho_{ij} = |\mathbf{r}_i - \mathbf{r}_j|$, as shown in Fig. 8.1(c). This illustrates the design of Kagome quantum spin ice ($J_{+-} = 0$) [10] for realistic atomic parameters. As discussed below, an angular dependence of J_α can be obtained by inclining the laser beams [13].

To obtain the desired spin-spin interactions in Eq. (8.1) we consider a pair of atoms and derive by adiabatic elimination of the Rydberg levels the effective Hamiltonian for the ground state spins. Our starting point is the microscopic Hamiltonian, $H_{\mathrm{mic}} = \sum_{i=1}^{2}\left[H_A^{(i)} + H_L^{(i)}\right] + H_{\mathrm{vdW}}$, which is written as the sum of a single atom Hamiltonians including Zeeman split energy levels of the various states, the laser driving and the vdW interaction. In the rotating frame we have $H_A^{(i)} = -\Delta_+|r_+\rangle_i\langle r_+| - \Delta_-|r_-\rangle_i\langle r_-|$ and $H_L^{(i)} = \frac{1}{2}\Omega_+ e^{i\varphi_+}|g_-\rangle_i\langle r_+| + \frac{1}{2}\Omega_- e^{i\varphi_-}|g_+\rangle_i\langle r_-| + \mathrm{h.c.}$, where Δ_σ denotes the laser detunings, Ω_σ the Rabi frequencies and φ_σ local laser phases. Since the derivation of the effective Hamiltonian is invariant under local gauge transformations, in the following we fix $\varphi_\sigma = 0$ without loss of generality.

At the heart of our scheme is the vdW interaction H_{vdW} between the Zeeman sublevels in the $n^2P_{1/2}$ manifold. For the atomic configuration of Fig. 8.1(a) (atoms in the xy-plane and lasers propa-

---

[1] For laser detunings and vdW interactions much larger than the hyperfine splitting we can ignore the hyperfine interactions in the Rydberg state and the nuclear spin becomes a spectator.

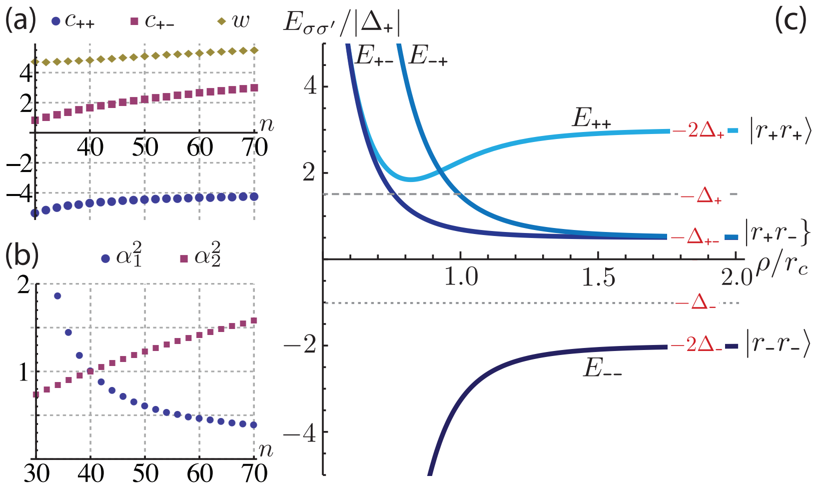

Figure 8.2. *(a) C_6 coefficients c_{++}, c_{+-}, and w of Eq. (8.2) in atomic units for Rb atoms vs. principal quantum number n. (b) Ratios of diagonal and the m-changing C_6. (c) Eigenenergies $E_{\sigma\sigma'}(\rho)$ (8.4) (thick solid lines), energies of states with a single Rydberg excitation in r_+ (gray dashed line) and r_- (gray dotted line) vs. ρ/r_c with $r_c = (c_{++}/2|\Delta_+|)^{1/6}$. Asymptotic energies and eigenstates are indicated on the right.*

gating along z) this vdW interaction has the structure (see SM)

$$H_{\text{vdW}}(\rho) = \begin{pmatrix} V_{++}(\rho) & 0 & 0 & W_{++}(\rho) \\ 0 & V_{+-}(\rho) & W_{+-}(\rho) & 0 \\ 0 & W_{+-}(\rho) & V_{-+}(\rho) & 0 \\ W_{++}(\rho) & 0 & 0 & V_{--}(\rho) \end{pmatrix} \tag{8.2}$$

written in the basis $\{|r_-r_-\rangle, |r_-r_+\rangle, |r_+r_-\rangle, |r_+r_+\rangle\}$ of Rydberg Zeeman states. Here, $V_{\sigma\sigma'}(r) \equiv c_{\sigma\sigma'}/\rho^6$ are the (diagonal) vdW interactions between the pair states $|r_\sigma r_{\sigma'}\rangle$, with $V_{++} = V_{--}$ and $V_{+-} = V_{-+}$. In addition we have "flip-flop" interactions between the states $|r_-r_+\rangle$ and $|r_+r_-\rangle$ and also "flip-flip" and "flop-flop" interactions between the Rydberg states $|r_-r_-\rangle$ and $|r_+r_+\rangle$, with coupling strength W_{+-} and W_{++}, respectively, where $W_{+-}(\rho) = -3W_{++}(\rho) \equiv w/\rho^6$. This arises from the fact that in our configuration the total magnetic quantum number $M = m_j + m_{j'}$ can change by 0 or ±2 [14]. The corresponding C_6-coefficients c_{++}, c_{+-} and w of Rb, which can be attractive or repulsive, are plotted in Fig. 8.2(a) as a function of the principal quantum number n. We emphasize that in writing the time-independent Eq. (8.2) we have assumed $\Delta E_r - (\Delta_+ - \Delta_-) = 0$, corresponding to the energy conservation condition for Raman processes between the spin ground states. We note, however, that Δ_+ and Δ_- can still be chosen independently via an appropriate choice of laser frequencies and Rydberg Zeeman splitting ΔE_r. [2]

---

[2] Away from the energy conservation condition the terms W_{++} in (8.2) will carry a time-depencence $\exp[i2(\Delta E_r - (\Delta_+ - \Delta_-))t]$

8.3 Adiabatic elimination and effective spin Hamiltonian

In the following we will derive the effective spin-spin interactions of Eq. (8.1) by weakly admixing these Rydberg-Rydberg interactions to the ground state manifold with lasers. We note, however, the basic features of these spin-spin interactions can already be identified in H_{vdW}: (strong) diagonal interactions V_{++} and V_{-+} will induce tunable J_z interactions between the dressed ground states $|g_-\rangle$ and $|g_+\rangle$, while the couplings W_{+-} and W_{++} give rise to the J_{+-} and J_{++} spin flips terms, respectively.

In the limit of weak laser excitation we obtain the effective spin-spin interaction between the ground states by treating the laser interactions $H_L^{(1)} + H_L^{(2)}$ as a perturbation. As a first step we diagonalize $H_A^{(1)} + H_A^{(2)} + H_{\mathrm{vdW}}$ as the dominant part of the Hamiltonian in the subspace of two Rydberg excitations. This results in four new eigenstates

$$\begin{aligned} |E_{\sigma\sigma}(\rho)\rangle &= [\cos\chi(\rho)|r_\sigma r_\sigma\rangle + \sigma\sin\chi(\rho)|r_{\bar\sigma} r_{\bar\sigma}\rangle]\,/\,\sqrt{2}, \\ |E_{\sigma\bar\sigma}(\rho)\rangle &= (|r_\sigma r_{\bar\sigma}\rangle + \sigma|r_{\bar\sigma} r_\sigma\rangle)\,/\,\sqrt{2} \end{aligned} \tag{8.3}$$

where $\sigma = +, -$ and we defined $\bar\sigma \equiv -\sigma$ with corresponding eigenenergies

$$\begin{aligned} E_{\sigma\sigma}(\rho) &= V_{++}(\rho) - \Delta_{+-} + \sigma\sqrt{\delta_{+-}^2 + W_{++}(\rho)^2}, \\ E_{\sigma\bar\sigma}(\rho) &= V_{+-}(\rho) - \Delta_{+-} + \sigma W_{+-}(\rho), \end{aligned} \tag{8.4}$$

shown in Fig. 8.2(c). These new eigenenergies can be interpreted as Born-Oppenheimer adiabatic potentials. Here, we used the short hand notation $\Delta_{+-} \equiv \Delta_+ + \Delta_-$, $\delta_{+-} \equiv \Delta_+ - \Delta_-$ and $\tan 2\chi(\rho) = W_{++}(\rho)/\delta_{+-}$. We note that for large distances $E_{++}(\rho \to \infty) = -2\Delta_+$ and $E_{--}(\rho \to \infty) = -2\Delta_-$, corresponding to states $|r_+ r_+\rangle$ and $|r_- r_-\rangle$, respectively, while the states $|r_- r_+\rangle$ and $|r_+ r_-\rangle$ become asymptotically degenerate with energy $E_{+-}(\rho \to \infty) = E_{-+}(\rho \to \infty) = -(\Delta_+ + \Delta_-)$. The ratios $\alpha_1 = W_{+-}/V_{+-}$ and $\alpha_2 = W_{++}/V_{++}$ shown in Fig. 8.2(b) determine the sign of the slope of the new eigenenergies at short distances. In particular, for $n^2P_{1/2}$ states of ^{87}Rb we find that for $n \geq 41$ the eigenenergies $E_{++}(\rho)$, $E_{+-}(\rho)$ and $E_{-+}(\rho)$ are repulsive while $E_{--}(\rho)$ is attractive at short distances [see Fig. 8.2(c)]. For detunings $\Delta_+/\Delta_- < 0$ and $\Delta_+ + \Delta_- < 0$ we avoid resonant Rydberg excitations for all distances, i.e. there are no zero-crossings of $E_{\sigma\sigma'}(\rho)$, and perturbation theory in $\Omega_\sigma/|E_{\sigma'\sigma''}|$ is valid for all ρ.

In 4th order in the small parameter $\Omega_\sigma/|E_{\sigma'\sigma''}| \ll 1$ we obtain an effective spin-spin interaction Hamiltonian $\tilde H = \sum_{\sigma,\sigma'}\left[\tilde V_{\sigma\sigma'}|g_\sigma g_{\sigma'}\rangle\langle g_\sigma g_{\sigma'}| + \tilde W_{\sigma\sigma'}|g_\sigma g_{\sigma'}\rangle\langle g_{\bar\sigma} g_{\bar\sigma'}|\right]$ between the dressed ground states atoms. The diagonal interactions are

$$\begin{aligned} \tilde V_{\sigma\sigma} &= \frac{\Omega_{\bar\sigma}^4}{8\Delta_{\bar\sigma}^3}\frac{V_{++}\left(V_{++} - 2\Delta_\sigma\right) - W_{++}^2}{W_{++}^2 - \left(V_{++} - 2\Delta_+\right)\left(V_{++} - 2\Delta_-\right)}, \\ \tilde V_{+-} &= \frac{\Omega_+^2\Omega_-^2}{16\Delta_+^2\Delta_-^2}\left(\Delta_+ + \Delta_-\right)\frac{V_{+-}\left(\Delta_{+-} - V_{+-}\right) + W_{+-}^2}{\left(\Delta_{+-} - V_{+-}\right)^2 - W_{+-}^2}, \end{aligned} \tag{8.5}$$

which, for small distances, are step-like potentials with $V_{\sigma\sigma'}(\rho \to 0) = -\Omega_{\bar\sigma}^2\Omega_{\bar\sigma'}^2(\Delta_{\bar\sigma}+\Delta_{\bar\sigma'})/(16\Delta_{\bar\sigma}^2\Delta_{\bar\sigma'}^2)$. We have absorbed single particle light shifts in the definition of the detunings (see SM). For the "flip-flop" and "flop-flop" interactions we get

$$\begin{aligned} \tilde W_{+-} &= \frac{\Omega_+^2\Omega_-^2}{16\Delta_+^2\Delta_-^2}\frac{\left(\Delta_+ + \Delta_-\right)^2 W_{+-}}{\left(\Delta_+ + \Delta_- - V_{+-}\right)^2 - W_{+-}^2}, \\ \tilde W_{++} &= -\frac{\Omega_+^2\Omega_-^2}{4\Delta_+\Delta_-}\frac{W_{++}}{W_{++}^2 - \left(V_{++} - 2\Delta_+\right)\left(V_{++} - 2\Delta_-\right)}, \end{aligned} \tag{8.6}$$

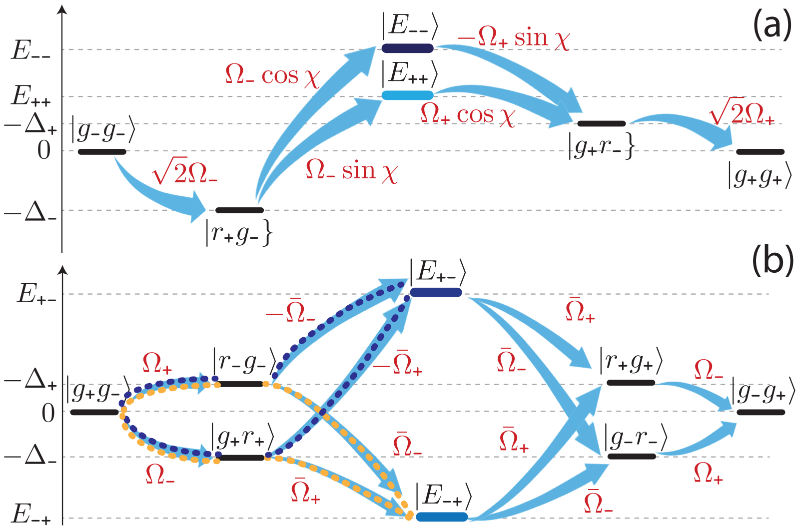

Figure 8.3. *Path of perturbative couplings between the states (a) $|g_+g_+\rangle$ and $|g_-g_-\rangle$ and (b) $|g_+g_-\rangle$ and $|g_-g_+\rangle$ visualizing the perturbative expressions behind J_{++} and J_{+-} of Eqs.* (8.7)*, respectively. The energies $E_{\sigma\sigma'}$ are plotted for a specific interatomic distance ρ (with abbreviation $\bar{\Omega}_\sigma \equiv \Omega_\sigma/\sqrt{2}$). Yellow and blue dotted paths can interfere destructively (see text).*

which are peaked at $R_{+-}^6 = \sqrt{c_{+-}^2 - w_{+-}^2}/|\Delta_+ + \Delta_-|$ and $R_{++}^6 = \sqrt{(c_{++}^2 - w_{++}^2)/(4\Delta_+\Delta_-)}$, respectively, and go to zero for small and large distances. The spin couplings of Eq. (8.1) are then obtained as

$$\begin{aligned} J_{\|}(\mathbf{r}_{ij}) &= \frac{1}{4}\left[\tilde{V}_{++}(\mathbf{r}_{ij}) - \tilde{V}_{--}(\mathbf{r}_{ij})\right], \\ J_z(\mathbf{r}_{ij}) &= \frac{1}{4}\left[\tilde{V}_{--}(\mathbf{r}_{ij}) - 2\tilde{V}_{+-}(\mathbf{r}_{ij}) + \tilde{V}_{++}(\mathbf{r}_{ij})\right], \\ J_{+-}(\mathbf{r}_{ij}) &= 2\tilde{W}_{+-}(\mathbf{r}_{ij}), \text{ and } J_{++}(\mathbf{r}_{ij}) = 2\tilde{W}_{++}(\mathbf{r}_{ij}). \end{aligned} \tag{8.7}$$

Figure 8.1(c) shows a plot of (8.7) for $n = 60\ P_{1/2}$ and a typical set of laser parameters. The diagonal J_z interaction is steplike with a repulsive (antiferromagnetic) soft core at small distances, $\rho < 2\ \mu$m and an attractive (ferromagnetic tail) at long distances. The spin flip term J_{++} is peaked at $\rho \approx 2.5\,\mu$m while $J_{+-} = 0$, thus realizing the Hamiltonian of quantum spin ice on a Kagome lattice [10] at a lattice spacing $a = 1.8\ \mu$m. The lifetime of the $60P_{1/2}$ Rydberg state including blackbody radiation at $T = 300$ K is $\tau_{60} = 133\,\mu$s [15] which yields an effective ground state decay rate of $\Gamma_{\text{eff}} = (\Omega_-/2\Delta_-)^2\tau_{60}^{-1} \approx 2\pi \times 18$ Hz for $\Omega_- = 2\pi \times 5$ MHz and $\Delta_- = 2\pi \times 50$ MHz, which is more than one to two orders of magnitude smaller than typical interaction energy scales shown in Fig. 8.1(c). The fine structure splitting between the $60P_{1/2}$ and $60P_{3/2}$ manifolds is $\Delta E_{FS} \approx 2\pi \times 920$ MHz which is much larger than the Rydberg interactions for distances larger than about 2 μm.

The form and strength of the effective spin-spin interactions of Eqs. (8.5) and (8.6) shown in Fig. 8.1(c), including $J_{+-} = 0$ for $\Delta_+ = -\Delta_-$, can be understood in terms of *quantum interference* of the various paths contributing to the perturbation expressions (8.7). These paths are illustrated in Fig. 8.3: both the states $|g_+g_+\rangle$ and $|g_-g_-\rangle$ (panel a) and also the states $|g_+g_-\rangle$ and $|g_-g_+\rangle$ (panel b) are coupled via four laser photons (blue arrows), giving rise to $\tilde{W}_{++}$ and $\tilde{W}_{+-}$, respectively. In particular, the states $|g_+g_+\rangle$ and $|g_-g_-\rangle$ are coupled either via $|E_{++}\rangle$ or via $|E_{--}\rangle$ with position dependent coupling

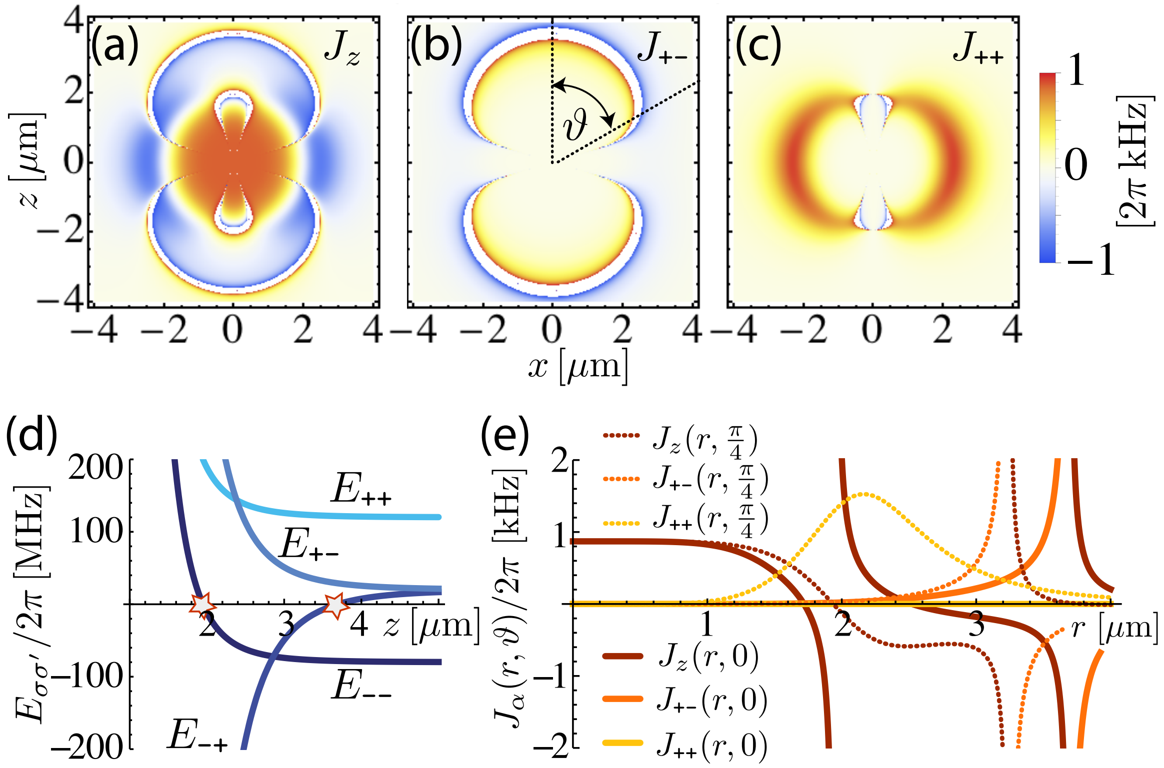

Figure 8.4. *(a-c) Effective spin-spin interactions* J_α (8.1) *as a function of* r *and* ϑ *for a laser propagating along the* z *axes and atoms in the* zx*-plane. Here* $|r_\pm\rangle = |60^2P_{1/2}, \pm\frac{1}{2}\rangle$ *with* $\Omega_- = \Omega_+/2 = 2\pi\times 5$ *MHz and* $(\Delta_-,\Delta_+) = 2\pi\times(-60,40)$ *MHz. (d) Cut through the energy surfaces* $E_{\sigma\sigma'}$ (8.4) *along the* z *axis. In contrast to Fig.* 8.2*(c) resonances appear, indicated with a star where* J_α *becomes singular as shown in panels (a-c). (e) Cut through panels (a-c) for* $\vartheta = 0$ *(solid lines) and* $\vartheta = \pi/8$ *(dotted lines).*

rates $\Omega_\sigma \sin\chi(\rho)$ and $\Omega_\sigma \cos\chi(\rho)$. For large distances $\sin\chi(\rho) \to 0$ and thus $\tilde{W}_{++} \to 0$ while at short distances the "flop-flop" process is suppressed by the large resolvents $E^{-1}_{\sigma\sigma'}$ giving rise to the peaked form of W_{++} as a function of ρ. Panel (b) shows eight possible paths which can couple the $|g_+g_-\rangle$ and $|g_-g_+\rangle$ states. We note that both the two blue and the two yellow dotted paths coupling $|g_+g_-\rangle$ either to $|E_{+-}\rangle$ or to $|E_{-+}\rangle$, respectively, differ only by the energy denominators Δ_+^{-1} or Δ_-^{-1}. Thus, for $\Delta_+ = -\Delta_-$ the two yellow dotted paths and also the two blue dotted paths will *interfere destructively* and the "flip-flop" process vanishes, i.e. $J_{+-} = 2\tilde{W}_{+-} = 0$, as shown in Fig. 8.1(c).

8.4 Anisotropic models

We now turn to a setup with laser propagation direction (z-axis) inclined with respect to the 2D plane containing the trapped atoms. This allows for an *angular dependence* (anisotropy) of the $J_\alpha(\mathbf{r}_{ij})$. In addition, we find as a new feature the appearance of *resonances* in the spin-spin couplings as a function of spatial distance in the lattice. The origin of the anisotropy is the strong dependence of the various vdW interactions matrix elements on the angle ϑ between the z-axis (defined by the laser propagation direction) and the relative vector connecting the two atoms i and j (see SM for details). As an example, we show in Fig. 8.4 the spin-spin interactions for a propagation direction of both lasers parallel to the 2D plane (zx-plane). The anisotropy of the J_α as a function of the angle ϑ is shown in panels (a-c). In particular, $W_{++}(r, \vartheta) \sim \sin^2 \vartheta$, and thus vanishes along the z direction, reflecting the conservation of angular momentum $M = m_j + m'_j$. In addition for $\vartheta \neq \pi/2$ resonances appear at specific interparticle distances, where one of the eigenenergies $E_{\sigma\sigma'}$ (8.4) crosses the energy surface $E = 0$ corresponding to ground state atoms $|g_\sigma, g_{\sigma'}\rangle$ (indicated by the red stars in panel d). This gives rise to clepsydra-shaped resonances in J_α, as shown in panels a-c, which in our perturbative treatment appear as singularities as a function of the distance, with J_α changing sign across the resonance.

8.5 Conclusion and Outlook

We conclude with a perspective on the quantum many-body physics opened by the present work. The toolbox described above, together with techniques of adiabatic state preparation [16] paves the way toward the engineering of frustrated spin models, where different aspects of the interaction pattern can be exploited. First, the independent tunability of both J_{+-} and J_{++} couplings selects a particular spin symmetry, either conserving the total magnetization $\sum_j S^z_j$ or the parity $\prod_j S^z_j$, giving rise to a U(1) or $\mathbb{Z}_2$ symmetry, respectively. This finds immediate application in the context of extended quantum ice models [17], as illustrated in Fig. 8.1 for Kagome quantum spin ice [10]. Within the same geometry, moving away from $\Delta_+ = -\Delta_-$ regime, a finite J_{+-} can be switched on, and extended XYZ models can be realized [11, 18]. The ability of controlling each coupling strength in an angular- and distance-dependent way (c.f. Fig. 8.4) points toward the realization of models displaying intermediate symmetry, such as, e.g., compass models [19]. By properly choosing the lattice spacings on a square lattice, it is possible to single out interactions along one direction of pure zz-type, and of ++ type along the other, thus realizing extended square compass models. The large energy scales provided by the vdW interactions, combined with *in situ* measurement techniques demonstrated in large-spacing lattices [8, 9], make the observation of different physical phenomena encompassed by these models, such as emergent gauge theories and exotic spin liquid states [1], accessible within Rydberg atom experiments.

Acknowledgment

We thank A. Läuchli, M. Lukin, and M. Saffman for stimulating discussions. Furthermore, discussions with all members of the R-ION and UQUAM consortium are kindly acknowledged, in particular with P. Schauß, B. Vermersch and J. Zeiher. This project was supported in parts by the ERC Synergy Grant UQUAM, SIQS, COHERENCE, the SFB FoQuS (FWF Project No. F4006-N16), and the ERA-NET CHIST-ERA (R-ION consortium).

Note added. — In the final stages of the work we have been informed by T. Pohl of related work in the context of spin-1 models.

8.A Van der Waals interactions between $j = 1/2$ Rydberg states

Away from Foerster resonances two laser excited Rydberg atoms dominantly interact via van der Waals interactions [5]. These van der Waals interactions, $H^{(i,k)}_{\mathrm{vdW}}$, will mix different Zeeman sublevels $|m_j\rangle$ in the $nP_{1/2}$ manifold [14]. Let us denote by $\hat{P} = \sum_{i,j} |m_i, m_j\rangle\langle m_i, m_j|$ a projection operator into the $nP_{1/2}$ manifold, then dipole-dipole interactions

$$V^{(i,k)}_{\mathrm{dd}}(\mathbf{r}) = -\sqrt{\frac{24\pi}{5}}\frac{1}{r^3}\sum_{\mu,\nu} C^{1,1;2}_{\mu,\nu;\mu+\nu} Y^{\mu+\nu}_2(\vartheta,\varphi)^* d^{(i)}_\mu d^{(j)}_\nu,$$

will couple states in the $\hat{P}$ manifold to intermediate states, $\hat{Q}_{\alpha,\beta} = |\alpha,\beta\rangle\langle\alpha,\beta|$, which have an energy difference $\delta_{\alpha\beta}$. Here, $\mathbf{d}^{(i)}$ is the dipole operator of the i-th atom and $\mathbf{r} = (r, \vartheta, \varphi)$ is the relative vector between atom i and atom j in spherical coordinates and $d^{(i)}_\mu$ is the μ-th spherical components ($\mu, \nu \in \{-1, 0, 1\}$) of the atomic dipole operator. With $C^{j_1,j_2;J}_{m_1,m_2;M}$ we denote the Clebsch-Gordan coefficients and Y^m_l are spherical harmonics. In second order perturbation theory this gives rise to

$$H^{(i,k)}_{\mathrm{vdW}} = \hat{P}\sum_{\alpha\beta}\frac{V^{(i,k)}_{\mathrm{dd}}\hat{Q}_{\alpha,\beta}V^{(i,k)}_{\mathrm{dd}}}{\delta_{\alpha\beta}}\hat{P}, \tag{8.8}$$

where $H^{(i,k)}_{\mathrm{vdW}}$ is understood as an operator acting in the manifold of Zeeman sublevels.

Due to the odd parity of the electric dipole operators $d^{(i)}_\mu$ and $d^{(j)}_\nu$, the dipole-dipole interaction, V_{dd}, can couple initial $nP_{1/2}$ states only to $n'S_{1/2}$ or $n''D_{3/2}$ states. Therefore, there are four possible channels shown in Tab. 8.1(left) for which the matrix element $\langle nP_{1/2}m_1|\langle nP_{1/2}m_1|V_{\mathrm{dd}}|n', \ell_\alpha, j_\alpha, m_\alpha\rangle|n'', \ell_\beta, j_\beta, m_\beta\rangle$ of Eq. (8.8) is non-zero. Here, $(\ell_{\alpha,\beta}, j_{\alpha,\beta})$ can either correspond to $S_{1/2}$ or $D_{3/2}$ states depending on the channel. While there is no selection rule for possible final principal quantum numbers n' and n'' which solely determine the overall strength of the matrix element, the dipole-dipole matrix element is only non-zero if the magnetic quantum numbers and the spherical component of the dipole operator fulfill $m_1 + \mu = m_\alpha$ and $m_2 + \nu = m_\beta$. The total vdW interaction of Eq. (8.8) can be obtained by summing over all channels ν, that is

$$\hat{V}_{\mathrm{vdW}} = \sum_\nu C^{(\nu)}_6 \mathcal{D}_\nu(\vartheta,\varphi)/r^6. \tag{8.9}$$

Here, $C^{(\nu)}_6$ contains the radial part of the matrix elements

$$C^{(\nu)}_6 = \sum_{n_\alpha,n_\beta}\frac{\mathcal{R}^\alpha_1\mathcal{R}^\beta_2\mathcal{R}^\alpha_3\mathcal{R}^\beta_4}{\delta_{\alpha\beta}} \tag{8.10}$$

which accounts for the overall strength of the interaction and is independent of the magnetic quantum numbers. With $\mathcal{R}^k_i = \int dr r^2 \psi_{n_i,\ell_i,j_i}(r)^* r\, \psi_{n_k,\ell_k,j_k}(r)$ we denote the radial integral. The matrix

$$\mathcal{D}_\nu(\vartheta,\varphi) = \hat{P}_{12}\sum_{m_\alpha,m_\beta}\mathcal{M}_\nu\hat{Q}_{\alpha,\beta}\mathcal{M}_\nu\,\hat{P}_{34} \tag{8.11}$$

on the other hand is a matrix in the subspace of magnetic quantum numbers which contains the relative angles between the two atoms ($s = 1/2$)

$$\begin{aligned}\langle m_1, m_2|\mathcal{M}_\nu|m_\alpha, m_\beta\rangle =& (-)^{s-m_1}\sqrt{(2\ell_1+1)(2j_1+1)(2\ell_\alpha+1)(2j_\alpha+1)}\begin{Bmatrix} \ell_1 & \ell_\alpha & 1 \\ j_\alpha & j_1 & s \end{Bmatrix}\begin{pmatrix} \ell_\alpha & 1 & \ell_1 \\ 0 & 0 & 0 \end{pmatrix} \\ &\times(-)^{s-m_2}\sqrt{(2\ell_2+1)(2j_2+1)(2\ell_\beta+1)(2j_\beta+1)}\begin{Bmatrix} \ell_2 & \ell_\beta & 1 \\ j_\beta & j_2 & s \end{Bmatrix}\begin{pmatrix} \ell_\beta & 1 & \ell_2 \\ 0 & 0 & 0 \end{pmatrix} \\ &\times\left[-\sqrt{\frac{24\pi}{5}}\sum_{\mu,\nu} C^{1,1;2}_{\mu,\nu;\mu+\nu}\begin{pmatrix} j_\alpha & 1 & j_1 \\ m_\alpha & \mu & -m_1 \end{pmatrix}\begin{pmatrix} j_\beta & 1 & j_2 \\ m_\beta & \nu & -m_2 \end{pmatrix} Y_2^{\mu+\nu}(\vartheta,\varphi)^*\right].\end{aligned} \tag{8.12}$$

For the individual channels $\nu \in \{a, b, c, d\}$ of Tab. 8.1 we find

$$\begin{aligned} &\text{(a)} \quad \mathcal{D}_a(\vartheta,\varphi) = \frac{2}{9}\mathbb{I}_4 - \mathcal{D}_0(\vartheta,\varphi), \\ &\text{(b)} \quad \mathcal{D}_b(\vartheta,\varphi) = \frac{4}{9}\mathbb{I}_4 - \mathcal{D}_0(\vartheta,\varphi), \\ &\text{(c, d)} \quad \mathcal{D}_c(\vartheta,\varphi) = \mathcal{D}_d(\vartheta,\varphi) = \mathcal{D}_0(\vartheta,\varphi), \end{aligned} \tag{8.13}$$

with $\mathbb{I}_4$ the 4×4 identity matrix and

$$\mathcal{D}_0(\vartheta,\varphi) = \frac{1}{81}\begin{pmatrix} 3\cos(2\vartheta)+11 & 3e^{-i\phi}\sin(2\vartheta) & 3e^{-i\phi}\sin(2\vartheta) & 6e^{-2i\phi}\sin^2(\vartheta) \\ 3e^{i\phi}\sin(2\vartheta) & 13-3\cos(2\vartheta) & -3\cos(2\vartheta)-5 & -3e^{-i\phi}\sin(2\vartheta) \\ 3e^{i\phi}\sin(2\vartheta) & -3\cos(2\vartheta)-5 & 13-3\cos(2\vartheta) & -3e^{-i\phi}\sin(2\vartheta) \\ 6e^{2i\phi}\sin^2(\vartheta) & -3e^{i\phi}\sin(2\vartheta) & -3e^{i\phi}\sin(2\vartheta) & 3\cos(2\vartheta)+11 \end{pmatrix} \tag{8.14}$$

written in the basis $\{|{-\frac{1}{2}}{-\frac{1}{2}}\rangle, |{-\frac{1}{2}}\frac{1}{2}\rangle, |\frac{1}{2}{-\frac{1}{2}}\rangle, |\frac{1}{2}\frac{1}{2}\rangle\}$ of Zeeman states in the $j = 1/2$ Rydberg manifold. For the special orientations (i) $\vartheta = 0$ we find

$$\mathcal{D}_0(0,0) = \frac{1}{81}\begin{pmatrix} 14 & 0 & 0 & 0 \\ 0 & 10 & -8 & 0 \\ 0 & -8 & 10 & 0 \\ 0 & 0 & 0 & 14 \end{pmatrix} \tag{8.15}$$

and (ii) for $\vartheta = \pi/2$ the matrix simplifies to

$$\mathcal{D}_0(\tfrac{\pi}{2},0) = \frac{1}{81}\begin{pmatrix} 8 & 0 & 0 & 6 \\ 0 & 16 & -2 & 0 \\ 0 & -2 & 16 & 0 \\ 6 & 0 & 0 & 8 \end{pmatrix}. \tag{8.16}$$

The total vdW interaction matrix in the $nP_{1/2}$ subspace becomes

$$H^{(i,k)}_{\mathrm{vdW}} = \frac{2}{9}\left(C_6^{(a)} + 2C_6^{(b)}\right)\mathbb{I}_4 + \left(2C_6^{(c)} - C_6^{(a)} - C_6^{(b)}\right)\mathcal{D}_0, \tag{8.17}$$

where the coefficients $C_6^{(\nu)}$ depend on the principal quantum number n, see Fig. 8.5.

We note that the vdW Hamiltonian describing the interactions between $S_{1/2}$-states can be written in the exact same form as Eq. (8.17). However, the coupling terms, $C_6^{(\nu)}$, correspond to the channels

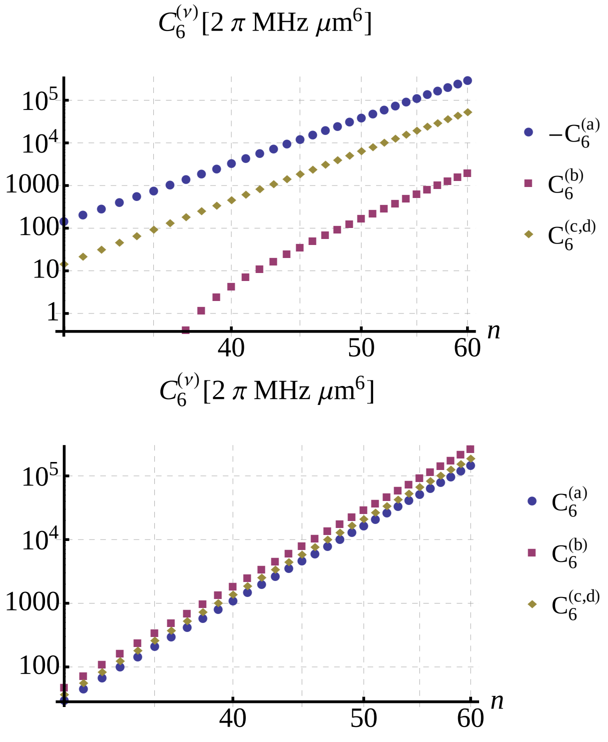

Figure 8.5. *We plot the $C_6^{(\nu)}$ for (left) $nP_{1/2}$ and (right) $nS_{1/2}$ Rydberg states of ^{87}Rb as a function of the principal quantum number n for different channels ν of Tab. 8.1.*

of Tab. 8.1(right). Therefore, the radial matrix elements for $S_{1/2}$ states differ only slightly due to the fine structure splitting ΔE_{FS} between $P_{1/2}$ and $P_{3/2}$ states, see Fig. 8.5(right). In the limit where the fine structure can be neglected compared to other energy scales we find $C_6^{(a)} = C_6^{(b)} = C_6^{(c)} = C_6^{(d)}$ and the vdW interaction of Eq. (8.17) between $nS_{1/2}$ states becomes diagonal, that is $H_{\mathrm{vdW}}^{(i,k)} = (2/3)C_6^{(a)}\mathbb{I}_4$. Thus, there is no vdW mixing between Zeeman sublevels if the fine-structure splitting can be neglected. This can be understood by a simple argument: Since for s-states the different m_j levels are proportional to the electronic spin m_s, that is $|m_j = \pm\frac{1}{2}\rangle = |\ell = 0, m_\ell = 0\rangle \otimes |m_s = \pm\frac{1}{2}\rangle$, and since dipole-dipole interactions cannot mix spin degrees of freedom there cannot be any vdW mixing of Zeeman levels in the absence of fine-structure. The first correction will be proportional to $\sim \Delta E_{FS}/\delta_{\alpha\beta}\mathcal{D}_0$. It is therefore only the spin-orbit coupling in the intermediate $Q_{\alpha,\beta}$ manifold which mixes different Zeeman sublevels in the case of $S_{1/2}$ states.

On the contrary, for $P_{1/2}$ states, the radial coefficients $C_6^{(\nu)}$ differ much more strongly due to the energy difference between d- and s-states and due to the fact that Zeeman sublevels in the $nP_{1/2}$ manifold are already a superposition between $m_s = \pm\frac{1}{2}$ states of the electronic spin. Therefore, mixing of Zeeman sublevels for $nP_{1/2}$ states can be of the same order of magnitude than the diagonal terms and play a significant role. In the special (1D) case $\vartheta = 0$, the doubly excited levels $|\text{-}\frac{1}{2}\text{-}\frac{1}{2}\rangle$ and $|\frac{1}{2}\frac{1}{2}\rangle$ are not coupled to any other doubly excited states which is a consequence of the conservation of the total angular momentum. On the contrary, for $\vartheta = \pi/2$ (atoms polarized perpendicular to the

ν	$(\ell, j) + (\ell, j)$	$\longrightarrow$	$(\ell_\alpha, j_\alpha) + (\ell_\beta, j_\beta)$
(a)	$P_{1/2} + P_{1/2}$	$\longrightarrow$	$S_{1/2} + S_{1/2}$
(b)	$P_{1/2} + P_{1/2}$	$\longrightarrow$	$D_{3/2} + D_{3/2}$
(c)	$P_{1/2} + P_{1/2}$	$\longrightarrow$	$S_{1/2} + D_{3/2}$
(d)	$P_{1/2} + P_{1/2}$	$\longrightarrow$	$D_{3/2} + S_{1/2}$

ν	$(\ell, j) + (\ell, j)$	$\longrightarrow$	$(\ell_\alpha, j_\alpha) + (\ell_\beta, j_\beta)$
(a)	$S_{1/2} + S_{1/2}$	$\longrightarrow$	$P_{1/2} + P_{1/2}$
(b)	$S_{1/2} + S_{1/2}$	$\longrightarrow$	$P_{3/2} + P_{3/2}$
(c)	$S_{1/2} + S_{1/2}$	$\longrightarrow$	$P_{1/2} + P_{3/2}$
(d)	$S_{1/2} + S_{1/2}$	$\longrightarrow$	$P_{3/2} + P_{1/2}$

Table 8.1. *Dipole-dipole interactions can couple $P_{1/2}$ (left) and $S_{1/2}$ (right) states to four channels (a-d).*

plane), the Hamiltonian of Eq. (8.17) reduces to Eq. (8.2) with

$$\begin{aligned} c_{++} &= \frac{2}{81}\left(5C_6^{(a)} + 14C_6^{(b)} + 8C_6^{(c)}\right), \\ c_{+-} &= \frac{2}{81}\left(C_6^{(a)} + 10C_6^{(b)} + 16C_6^{(c)}\right), \\ w_{++} &= -\frac{2}{27}\left(C_6^{(a)} + C_6^{(b)} - 2C_6^{(c)}\right), \\ w_{+-} &= \frac{2}{81}\left(C_6^{(a)} + C_6^{(b)} - 2C_6^{(c)}\right) = -\frac{w_{++}}{3}. \end{aligned} \tag{8.18}$$

shown in Fig. 8.2(a) as a function of the principal quantum number n. In the following sections of this supplemental material, we will consider this particular orientation as it is the simplest configuration of vdW coupling where the doubly laser-excited state $|\text{-}\tfrac{1}{2}\text{-}\tfrac{1}{2}\rangle$ is only coupled to $|\tfrac{1}{2}\tfrac{1}{2}\rangle$.

8.B Laser excitation and hyperfine ground states

The laser Hamiltonian, $H_L^{(i)}$, couples two hyperfine ground states $|g_-\rangle$ and $|g_+\rangle$ to the Zeeman sublevels in the $nP_{1/2}$ Rydberg manifold with detunings Δ_σ and Rabi frequencies Ω_σ ($\sigma = +, -$), respectively, see Fig. 8.1(b). Uncoupling the nuclear spin the hyperfine ground states read

$$\begin{aligned} |g_+\rangle &\equiv |5^2S_{1/2}, F = 2, m_F = 2\rangle = |m_j = \tfrac{1}{2}\rangle|m_I = \tfrac{3}{2}\rangle, \\ |g_-\rangle &\equiv |5^2S_{1/2}, F = 1, m_F = 1\rangle = \frac{1}{2}\left[|m_j = \tfrac{1}{2}\rangle|m_I = \tfrac{1}{2}\rangle - \sqrt{3}|m_j = -\tfrac{1}{2}\rangle|m_I = \tfrac{3}{2}\rangle\right], \end{aligned}$$

where m_I is the projection quantum number of the nuclear spin. Using σ_+ and σ_- polarized light for the transition

$$\begin{aligned} |g_-\rangle &\xrightarrow{\Omega_+,\sigma_+} |nP_{1/2}, m_j = +\tfrac{1}{2}\rangle \otimes |m_I = \tfrac{3}{2}\rangle, \\ |g_+\rangle &\xrightarrow{\Omega_-,\sigma_-} |nP_{1/2}, m_j = -\tfrac{1}{2}\rangle \otimes |m_I = \tfrac{3}{2}\rangle, \end{aligned} \tag{8.19}$$

respectively, couples to two different Rydberg states but both in the same nuclear state. Thus, hyperfine structure can be treated as a spectator in the Rydberg manifold. Neglecting (small) hyperfine interactions, these are closed cycle transitions and do not couple to any other states in the hyperfine manifold. There are several alternative possibilities, e.g.

$$|g_+\rangle \equiv |5^2S_{1/2}, F=2, m_F=1\rangle = \frac{1}{2}\left[\sqrt{3}|m_j=\tfrac{1}{2}\rangle|m_I=\tfrac{1}{2}\rangle + |m_j=-\tfrac{1}{2}\rangle|m_I=\tfrac{3}{2}\rangle\right],$$
$$|g_-\rangle \equiv |5^2S_{1/2}, F=1, m_F=0\rangle = \frac{1}{\sqrt{2}}\left[|m_j=\tfrac{1}{2}\rangle|m_I=-\tfrac{1}{2}\rangle - |m_j=-\tfrac{1}{2}\rangle|m_I=\tfrac{1}{2}\rangle\right],$$

which can be laser excited to specific Rydberg states

$$|g_-\rangle \xrightarrow{\Omega_+,\sigma_+} |nP_{1/2}, m_j=-\tfrac{1}{2}\rangle \otimes |m_I=\tfrac{1}{2}\rangle,$$
$$|g_+\rangle \xrightarrow{\Omega_-,\sigma_-} |nP_{1/2}, m_j=+\tfrac{1}{2}\rangle \otimes |m_I=\tfrac{1}{2}\rangle.$$

8.C Effective ground state potentials

8.C.1 Adiabatic elimination

In the dressing limit, $\Omega_\sigma \ll \Delta_{\sigma'}$, atoms initially in their electronic ground states $|g\rangle_1 \dots |g\rangle_N$ are off-resonantelly coupled to the Rydberg states $|r\rangle_1 \dots |r\rangle_N$ and the new "dressed" ground states inherit a tunable fraction of the Rydberg interaction [7]. The effective interaction potential between N atoms in their dressed ground states, $|\tilde{g}\rangle_1 \dots |\tilde{g}\rangle_N$, can be obtained by diagonalizing the Hamiltonian H_{mic} for a fixed relative position and zero kinetic energy. The total Hamiltonian H_{mic} has block structure

$$H_{\text{mic}} = \begin{pmatrix} \mathbf{H}_0 & \mathbf{\Omega}_1 & 0 & 0 & \\ \mathbf{\Omega}_1^\dagger & \mathbf{H}_1 & \mathbf{\Omega}_2 & 0 & \\ 0 & \mathbf{\Omega}_2^\dagger & \mathbf{H}_2 & \mathbf{\Omega}_3 & \\ 0 & 0 & \mathbf{\Omega}_3^\dagger & \mathbf{H}_3 & \\ & & & & \ddots \end{pmatrix} \tag{8.20}$$

where $\mathbf{H}_n$ governs the dynamics in the subspace with n-Rydberg excitations present, while the $\mathbf{\Omega}_n$ matrices describe the coupling between adjacent sectors n and $n-1$ due to the laser. Only subspaces $\mathbf{H}_{n\geq 2}$ contain the interaction potentials V_{ij} and W_{ij} since we assume that ground and Rydberg states do not interact at long distances.

Adiabatically eliminating (up to fourth order in $\Omega_\sigma/\Delta_{\sigma'} \ll 1$) of the Rydberg states yields an effective interaction in the subspace of hyperfine states

$$\begin{aligned} \tilde{H} = {} & \mathbf{H}_0 + \mathbf{H}_1 - \mathbf{\Omega}_1\mathbf{H}_1^{-1}\mathbf{\Omega}_1^\dagger \\ & + \mathbf{\Omega}_1\mathbf{H}_1^{-1}\mathbf{\Omega}_1\mathbf{H}_1^{-1}\mathbf{\Omega}_1^\dagger\mathbf{H}_1^{-1}\mathbf{\Omega}_1^\dagger \\ & - \mathbf{\Omega}_1\mathbf{H}_1^{-1}\mathbf{\Omega}_2\mathbf{H}_2^{-1}\mathbf{\Omega}_2^\dagger\mathbf{H}_1^{-1}\mathbf{\Omega}_1^\dagger \end{aligned} \tag{8.21}$$

which yields (for two atoms)

$$\tilde{H} = \begin{pmatrix} \tilde{V}_{++} & 0 & 0 & \tilde{W}_{++} \\ 0 & \tilde{V}_{+-} & \tilde{W}_{+-} & 0 \\ 0 & \tilde{W}_{+-}^* & \tilde{V}_{-+} & 0 \\ \tilde{W}_{++}^* & 0 & 0 & \tilde{V}_{--} \end{pmatrix} \tag{8.22}$$

written in the basis of the hyperfine states $\{|g_+g_+\rangle, |g_-g_+\rangle, |g_+g_-\rangle, |g_-g_-\rangle\}$. In the following we will discuss the various potentials separately.

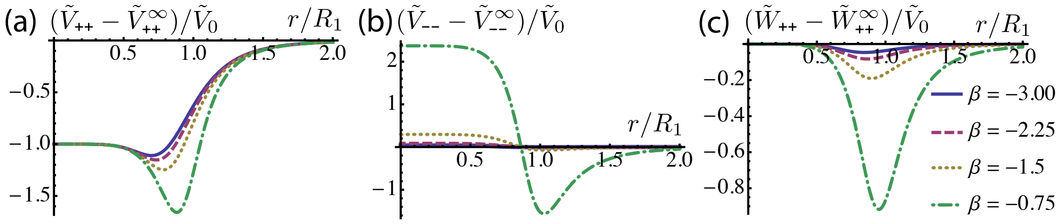

Figure 8.6. *Plot of the relative height given by Eqs.* (8.24) *for* $\alpha_1^2 = 1.41$ *(*$n = 60$*) and* $\sigma = -1$ *for various laser detuning fractions* β*.*

8.C.2 The potential $\tilde V_{++}$ and $\tilde V_{--}$

Adiabatic elimination up to fourth order in Ω/Δ of the Rydberg states yields

$$\tilde V_{++} = \frac{\Omega_-^2}{2\Delta_-} - \frac{\Omega_-^4}{4\Delta_-^3} + \frac{\Omega_-^4}{4\Delta_-^2}\frac{V_{++}-2\Delta_+}{W_{++}^2-(V_{++}-2\Delta_-)(V_{++}-2\Delta_+)},$$
$$\tilde V_{--} = \frac{\Omega_+^2}{2\Delta_+} - \frac{\Omega_+^4}{4\Delta_+^3} + \frac{\Omega_+^4}{4\Delta_+^2}\frac{V_{++}-2\Delta_-}{W_{++}^2-(V_{++}-2\Delta_-)(V_{++}-2\Delta_+)},$$

where asymptotically we just recover the single particle light shifts (up to fourth order)

$$\begin{aligned}\tilde V_{++}^\infty &\equiv \tilde V_{++}(r\to\infty) = \frac{\Omega_-^2}{2\Delta_-} - \frac{\Omega_-^4}{8\Delta_-^3},\\ \tilde V_{--}^\infty &\equiv \tilde V_{--}(r\to\infty) = \frac{\Omega_+^2}{2\Delta_+} - \frac{\Omega_+^4}{8\Delta_+^3}.\end{aligned} \tag{8.23}$$

The relative height of the potentials becomes

$$\begin{aligned}(\tilde V_{++}-\tilde V_{++}^\infty)/\tilde V_0 &= \frac{1-\alpha_1^2-\sigma\beta(r/R_1)^6}{\alpha_1^2-[1-\sigma(r/R_1)^6][1-\beta\sigma(r/R_1)^6]},\\ (\tilde V_{--}-\tilde V_{--}^\infty)/\tilde V_0 &= \left(\frac{\Omega_+}{\Omega_-}\right)^4\frac{1}{\beta^3}\frac{1-\alpha_1^2-\sigma(r/R_1)^6}{\alpha_1^2-[1-\sigma(r/R_1)^6][1-\beta\sigma(r/R_1)^6]},\end{aligned} \tag{8.24}$$

with $\alpha_1^2 = (w_{++}/c_{++})^2$ [shown in Fig. 8.2(b)], $\beta = \Delta_+/\Delta_-$, $\tilde V_0 = \Omega_-^4/(8\Delta_-^3)$, $\sigma = \mathrm{sign}(c_{++})\mathrm{sign}(\Delta_-)$ and $R_1^6 = |c_{++}|/(2|\Delta_-|)$. Due to the resolvent both potentials can be divergent for $W_{++}^2-(V_{++}-2\Delta_-)(V_{++}-2\Delta_+) = 0$, when two Born-Oppenheimer surfaces undergo an avoided crossing. This happens at

$$R_{\mathrm{div}}^6 = \frac{(\Delta_-+\Delta_+)\,c_{++}\pm\sqrt{(\Delta_--\Delta_+)^2\,c_{++}^2+4\Delta_-\Delta_+w_{++}^2}}{4\Delta_-\Delta_+} = \frac{1+\beta\pm\sqrt{(1-\beta)^2+4\beta\alpha_1^2}}{2\beta}\sigma R_1^6. \tag{8.25}$$

In order to avoid such divergences and to obtain step-like potentials we require $\mathrm{Im}(R_{\mathrm{div}}) \neq 0$. For $\alpha_1^2 > 1$ this is for example the case when $\beta < 1-2\alpha_1^2+2\alpha_1\sqrt{\alpha_1^2-1}$. Figure 8.6 shows a typical example of Eq. (8.24) for $n = 60$ where $\alpha_1^2 = 1.41$ and $\sigma = -1$. In this case the potential has no singularity (avoided crossing) for $\beta < -0.30$.

For $\alpha_1 = 0$ one obtains the well known result of a single dressed Rydberg level, i.e. $(\tilde V_{++} - \tilde V_{++}^\infty)/\tilde V_0 = -1/\left[1-\sigma(r/R_1)^6\right]$ [7].

8.C.3 Coupling element $\tilde{W}_{++}$

For the coupling matrix element $\tilde{W}_{++}$ adiabatic elimination up to fourth order in Ω/Δ yields

$$\tilde{W}_{++} = -e^{i\Delta\phi}\frac{\Omega_-^2\Omega_+^2}{4\Delta_-\Delta_+}\frac{W_{++}}{W_{++}^2 - (V_{++} - 2\Delta_-)(V_{++} - 2\Delta_+)} \tag{8.26}$$

where $\Delta\phi = (\mathbf{k}_1 - \mathbf{k}_2)(\mathbf{r}_1 + \mathbf{r}_2)$ is the phase difference between the two lasers at the center of mass position. Note that this phase can be gauged away using a local gauge transformation – a rotation around the z-axis in the spin-basis. Asymptotically and at the origin ($r = 0$) the coupling matrix element vanishes

$$\tilde{W}_{++}(r \to \infty) = 0, \qquad \text{and} \qquad \tilde{W}_{++}(r \to 0) = 0. \tag{8.27}$$

In dimensionless units $\tilde{W}_{++}$ reads

$$\tilde{W}_{++}/\tilde{V}_0 = -\frac{1}{2\beta}\left(\frac{\Omega_+}{\Omega_-}\right)^2 \frac{\alpha_1\sigma(r/R_1)^6}{\alpha_1^2 - [1 - \sigma(r/R_1)^6]\,[1 - \beta\sigma(r/R_1)^6]}. \tag{8.28}$$

Again, this matrix element is regular for $\alpha_1^2 > 1$ and $\beta < 1 - 2\alpha_1^2 + 2\alpha_1\sqrt{\alpha_1^2 - 1}$.

Figure 8.6(c) shows a typical example of Eq. (8.28) for $n = 60$ where $\alpha_1^2 = 1.41$ and $\sigma = -1$. In this case the potential has no singularity (avoided crossing) for $\beta < -0.30$. The coupling matrix element has a maximum at

$$\begin{aligned} R_{1,\max}^6 &= \sqrt{(1 - \alpha_1^2)/\beta R_1^6} \qquad \text{with} \\ \tilde{W}_{++}(R_{1,\max}) &= -e^{i\Delta\phi}\frac{\tilde{V}_0}{2\beta}\left(\frac{\Omega_+}{\Omega_-}\right)^2 \frac{\alpha_1}{1 + 2\sqrt{\beta\left(1 - \alpha_1^2\right)} + \beta}. \end{aligned} \tag{8.29}$$

8.C.4 Potential $\tilde{V}_{+-}$

For the potential $\tilde{V}_{+-}$ adiabatic elimination up to fourth order in Ω/Δ yields

$$\tilde{V}_{+-} = \frac{\Omega_-^2}{4\Delta_-} + \frac{\Omega_+^2}{4\Delta_+} - \frac{\Omega_-^4}{16\Delta_-^3} - \frac{\Omega_+^2\Omega_-^2}{16\Delta_-^2\Delta_+} - \frac{\Omega_+^2\Omega_-^2}{16\Delta_-\Delta_+^2} - \frac{\Omega_+^4}{16\Delta_+^3} + \frac{(\Delta_- + \Delta_+)^2\,\Omega_-^2\Omega_+^2\,(\Delta_- + \Delta_+ - V_{+-})}{16\Delta_-^2\Delta_+^2\left((\Delta_- + \Delta_+ - V_{+-})^2 - W_{+-}^2\right)} \tag{8.30}$$

where asymptotically we just recover the single particle light shifts (up to fourth order)

$$\tilde{V}_{+-}^{\infty} \equiv \tilde{V}_{++}(r \to \infty) = \frac{\Omega_-^2}{4\Delta_-} - \frac{\Omega_-^4}{16\Delta_-^3} + \frac{\Omega_+^2}{4\Delta_+} - \frac{\Omega_+^4}{16\Delta_+^3}. \tag{8.31}$$

The relative height of the potential becomes

$$(\tilde{V}_{+-} - \tilde{V}_{+-}^{\infty})/\tilde{V}_0 = \frac{(1 + \beta)}{2\beta^2}\left(\frac{\Omega_+^2}{\Omega_-}\right)^2 \frac{\frac{1}{2}(1 + \beta)\sigma'(r/R_2)^6 - 1 + \alpha_2^2}{\left[\frac{1}{2}(1 + \beta)\sigma'(r/R_2)^6 - 1\right]^2 - \alpha_2^2} \tag{8.32}$$

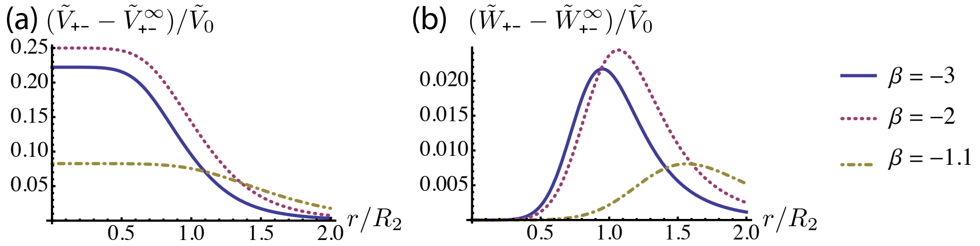

Figure 8.7. *We plot the relative height of* $\tilde{V}_{+-}$ *given by Eq.* (8.32) *(left panel) and of* $\tilde{W}_{+-}$ *given by Eq.* (8.36) *(right panel) for* $\alpha_2^2 = 0.46$ *(*$n = 60$*),* $\Omega_- = \Omega_+$ *and* $\sigma' = 1$ *for various laser detuning fractions* β*.*

with $\alpha_2^2 = (W_{+-}/c_{+-})^2$ [shown Fig. 8.2(b)], $\sigma' = \mathrm{sign}(c_{+-})\mathrm{sign}(\Delta_-)$ and $R_2^6 = |c_{+-}|/(2|\Delta_-|)$. Due to the resolvent the second term can be divergent for $(\Delta_- + \Delta_+ - V_{+-})^2 - W_{+-}^2 = 0$, when two potential surfaces undergo an avoided crossing. This happens at

$$R'^6_{\mathrm{div}} = \frac{c_{+-} \pm w_{+-}}{\Delta_- + \Delta_+} = \frac{1 \pm \alpha_2}{\frac{1}{2}(1+\beta)}\sigma' R_2. \tag{8.33}$$

In order to avoid such divergences and to obtain step-like potentials we require $R_{\mathrm{div}} \in \mathbb{C}$. This can only be fulfilled for $-1 < \alpha_2 < 1$ and $\beta < -1$. Figure 8.7 shows a typical example of Eq. (8.32) for $n = 60$ where $\alpha_2^2 = 0.46$ and $\sigma' = 1$. In this case the potential has no singularity (avoided crossing) for $\beta < -1$. We note that for $\beta = -1$ the potential vanishes.

8.C.5 Coupling element $\tilde{W}_{+-}$

For the coupling matrix element $\tilde{W}_{+-}$ adiabatic elimination up to fourth order in Ω/Δ yields

$$\tilde{W}_{+-} = e^{i\Delta\phi_{12}} \frac{\Omega_-^2\Omega_+^2}{16\Delta_-^2\Delta_+^2} \frac{(\Delta_- + \Delta_+)^2\, W_{+-}}{(\Delta_- + \Delta_+ - V_{+-})^2 - W_{+-}^2} \tag{8.34}$$

where $\Delta\phi_{12} = (\mathbf{k}_1 - \mathbf{k}_2)(\mathbf{r}_1 - \mathbf{r}_2)$ is the phase difference between the two lasers and relative position. Asymptotically and at the origin ($r = 0$) the coupling matrix element vanishes

$$\tilde{W}_{+-}(r \to \infty) = 0, \qquad \text{and} \qquad \tilde{W}_{+-}(r \to 0) = 0. \tag{8.35}$$

In dimensionless units $\tilde{W}_{+-}$ reads

$$\tilde{W}_{+-}/\tilde{V}_0 = \left(\frac{\Omega_+}{\Omega_-}\right)^2 \frac{1}{2\beta^2} \frac{\alpha_2 \frac{1}{2}(1+\beta)^2 \sigma'(r/R_2)^6}{\left[\frac{1}{2}(1+\beta)\sigma'(r/R_2)^6 - 1\right]^2 - \alpha_2^2}. \tag{8.36}$$

Again, this matrix element is regular for $-1 < \alpha_2 < 1$ and $\beta < -1$. Figure 8.7 (right panel) shows a typical example of Eq. (8.36) for $n = 60$ where $\alpha_1^2 = 1.41$ and $\sigma = -1$. We note that for $\beta = -1$ the coupling matrix element vanishes. The coupling matrix element has a maximum at

$$\begin{aligned} R^6_{2,\max} &= -\frac{2\sqrt{1-\alpha_2^2}}{1+\beta} R_2^6 \qquad \text{with} \\ \tilde{W}_{+-}(R_{2,\max}) &= -\frac{\tilde{V}_0}{4\beta^2}\left(\frac{\Omega_+}{\Omega_-}\right)^2 \left(\sqrt{1-\alpha_2^2} - 1\right)\frac{\beta+1}{\alpha_2}. \end{aligned} \tag{8.37}$$

Bibliography

[1] C. Lacroix, P. Mendels, and F. Mila, *Introduction to Frustrated Magnetism: Materials, Experiments, Theory*, Springer Series in Solid-State Sciences (Springer, 2011).

[2] M. Lewenstein, A. Sanpera, and V. Ahufinger, *Ultracold Atoms in Optical Lattices: Simulating quantum many-body systems* (OUP Oxford, 2012).

[3] S. Trotzky, P. Cheinet, S. Fölling, M. Feld, U. Schnorrberger, A. M. Rey, A. Polkovnikov, E. A. Demler, M. D. Lukin, and I. Bloch, Science **319**, 295 (2008); D. Greif, T. Uehlinger, G. Jotzu, L. Tarruell, and T. Esslinger, Science **340**, 1307 (2013); M. Anderlini, P. J. Lee, B. L. Brown, J. Sebby-Strabley, W. D. Phillips, and J. V. Porto, Nature **448**, 452 (2007).

[4] J. Simon, W. S. Bakr, R. Ma, M. E. Tai, P. M. Preiss, and M. Greiner, Nature **472**, 307 (2011); F. Meinert, M. J. Mark, E. Kirilov, K. Lauber, P. Weinmann, A. J. Daley, and H. C. Nägerl, Phys. Rev. Lett. **111**, 053003 (2013).

[5] T. F. Gallagher, *Rydberg Atoms*, Cambridge Monographs on Atomic, Molecular and Chemical Physics (Cambridge University Press, 2005); M. Saffman, T. G. Walker, and K. Mølmer, Rev. Mod. Phys. **82**, 2313 (2010); D. Comparat and P. Pillet, J. Opt. Soc. Am. **27**, A208 (2010); R. Löw, H. Weimer, J. Nipper, J. B. Balewski, B. Butscher, H. P. Büchler, and T. Pfau, J. Phys. B **45**, 113001 (2012).

[6] G. Günter, H. Schempp, M. Robert-de Saint-Vincent, V. Gavryusev, S. Helmrich, C. S. Hofmann, S. Whitlock, and M. Weidemüller, Science **342**, 954 (2013); T. E. Lee, S. Gopalakrishnan, and M. D. Lukin, Phys. Rev. Lett. **110**, 257204 (2013); M. Müller, L. Liang, I. Lesanovsky, and P. Zoller, New J. Phys. **10**, 093009 (2008).

[7] J. B. Balewski, A. T. Krupp, A. Gaj, S. Hofferberth, R. Löw, and T. Pfau, New J. Phys. **16**, 063012 (2014); C. S. Hofmann, G. Günter, H. Schempp, N. L. M. Müller, A. Faber, H. Busche, M. Robert-de Saint-Vincent, S. Whitlock, and M. Weidemüller, Front. Phys. **9**, 571 (2013); G. Pupillo, A. Micheli, M. Boninsegni, I. Lesanovsky, and P. Zoller, Phys. Rev. Lett. **104**, 223002 (2010); N. Henkel, R. Nath, and T. Pohl, Phys. Rev. Lett. **104**, 195302 (2010); J. Honer, H. Weimer, T. Pfau, and H. P. Büchler, Phys. Rev. Lett. **105**, 160404 (2010); A. Dauphin, M. Müller, and M. A. Martin-Delgado, Phys. Rev. A **86**, 053618 (2012); N. Malossi, M. M. Valado, S. Scotto, P. Huillery, P. Pillet, D. Ciampini, E. Arimondo, and O. Morsch, Phys. Rev. Lett. **113**, 023006 (2014); A. W. Glaetzle, M. Dalmonte, R. Nath, I. Rousochatzakis, R. Moessner, and P. Zoller, eprint arXiv:1404.5326 (2014).

[8] K. D. Nelson, X. Li, and D. S. Weiss, Nat. Phys. **3**, 556 (2007); P. Schauß, M. Cheneau, M. Endres, T. Fukuhara, S. Hild, A. Omran, T. Pohl, C. Gross, S. Kuhr, and I. Bloch, Nature **491**, 87 (2012); Y. O. Dudin and A. Kuzmich, Science **336**, 887 (2012); F. Nogrette, H. Labuhn, S. Ravets, D. Barredo, L. Béguin, A. Vernier, T. Lahaye, and A. Browaeys, Phys. Rev. X **4**, 021034 (2014); M. Schlosser, S. Tichelmann, J. Kruse, and G. Birkl, Quantum Inf Process **10**, 907 (2011).

[9] A. Abdelrahman, M. Vasiliev, K. Alameh, and P. Hannaford, Phys. Rev. A **82**, 012320 (2010); V. Y. F. Leung, D. R. M. Pijn, H. Schlatter, L. Torralbo-Campo, A. L. La Rooij, G. B. Mulder, J. Naber, M. L. Soudijn, A. Tauschinsky, C. Abarbanel, B. Hadad, E. Golan, R. Folman, and R. J. C. Spreeuw, Rev. Sci. Instrum. **85**, 053102 (2014).

[10] J. Carrasquilla, Z. Hao, and R. G. Melko, eprint arXiv:1407.0037 (2014).

[11] Y.-C. He, D. N. Sheng, and Y. Chen, Phys. Rev. Lett. **112**, 137202 (2014); S. Yan, D. A. Huse, and S. R. White, Science **332**, 1173 (2011).

[12] A. Micheli, G. K. Brennen, and P. Zoller, Nat. Phys. **2**, 341 (2006).

[13] A. Reinhard, T. Liebisch, B. Knuffman, and G. Raithel, Phys. Rev. A **75**, 032712 (2007).

[14] T. G. Walker and M. Saffman, Phys. Rev. A **77**, 032723 (2008).

[15] I. Beterov, I. Ryabtsev, D. Tretyakov, and V. Entin, Phys. Rev. A **79**, 052504 (2009).

[16] S. Trebst, U. Schollwöck, M. Troyer, and P. Zoller, Phys. Rev. Lett. **96**, 250402 (2006); A. Kantian, A. J. Daley, and P. Zoller, Phys. Rev. Lett. **104**, 240406 (2010); A. S. Sørensen, E. Altman, M. Gullans, J. V. Porto, M. D. Lukin, and E. Demler, Phys. Rev. A **81**, 061603 (2010).

[17] Y.-P. Huang, G. Chen, and M. Hermele, Phys. Rev. Lett. **112**, 167203 (2014).

[18] S.-S. Gong, W. Zhu, and D. N. Sheng, Sci. Rep. **4**, 6317 (2014).

[19] Z. Nussinov and J. van den Brink, eprint arXiv:1303.5922 (2013).

ACKNOWLEDGMENTS

This work would not have been possible without the support I received from many people!

I want to thank Prof. Peter Zoller for giving me the chance to work in his outstanding group and for supervising my PhD thesis. I have chosen his group not only because of his reputation as a brilliant physicist, but also because of the profound influence he had on me as a teacher. My interest in the research topics was augmented by the enthusiasm and atmosphere of discussion that prevails in his group, where everyone is motivated to strive for excellence. I am very grateful for the many inspiring discussions, his constant support and advice. Furthermore, I want to thank Prof. Zoller for giving me the opportunity to participate in summer schools and conferences around the world. I am forever in your debt for affording me the chance to visit world renowned research facilities such as Harvard, Stanford, Yale, and the Universities of California (Berkeley), Colorado (Boulder), Wisconsin (Madison), Heidelberg, Pisa, Bern, Dresden and Strasbourg. I will cherish these experiences forever.

Thank you to all people I have had the privilege of working with over the last four years. The stimulating discussions with experimentalists from Prof. Immanuel Bloch's group in Munich and from Prof. Ferdinand Schmidt-Kaler's group in Mainz are particularly memorable. A special thanks also goes to R. Nath, M. Dalmonte, W. Lechner, and G. Pupillo. In spite of their busy work schedules, their unwavering support and motivation always helped me through difficult moments. I have learnt a lot from you. The warm welcome offered to me by Steve Rolston and Trey Porto in Maryland and Misha Lukin at Harvard will stay with me forever.

Furthermore, I want to thank the current and former members of the group, the IQOQI and the Physics departments. The pleasant, supportive and open-minded working atmosphere they created provided the incentive for fascinating discussions on various physical problems. To my office mates Markus, Hannes and Marcello, I say thank you for the good times! The support of secretaries Doris, Elisabeth and Nicole and computer administrators David and Valentin is very much appreciated.

Moreover, I want to thank my enthusiastic high school physics teacher Michael Schwarzer for awakening my interest in this subject and for motivating me to study physics.

Additionally, I have to thank many people outside the University for making my time in Innsbruck so pleasant. Especially, these are Berni, Chalry, David, Elias, Florian, Lukas F., Lukas S., and Markus, who have accompanied me from high school on and through the physics studies.

Thanks is also due to many others who have helped me over the years, in particular my parents Rosmarie and Wolfgang and my brother Reinhard, who have given me all the love and support I needed. It would all have been impossible without them. This thesis is dedicated to them, for being the best family anyone could ever imagine!

Alexander Glätzle, Innsbruck, 2014

CURRICULUM VITAE

Alexander W. Glätzle

(as of September 2014)

Personal information

Full name:	Alexander Wolfgang Glätzle
Academic title:	Mag. rer. nat.
Address:	Hunoldstraße 16, 6020 Innsbruck, Austria
Date of birth:	September 26th, 1984
Place of birth:	Ehenbichl (Austria)
Citizenship:	Austrian
Parents:	Rosmarie and Dr. Wolfgang Glätzle
Sibling:	Mag. Reinhard Glätzle

Education

1991 – 1995	Elementary school, Reutte
1995 – 2003	Bundesrealgymnasium, Reutte
June 2003	Matura with highest distinction (high school diploma, general qualification for university entrance)
2004 – 2009	Studying Physics at the Leopold-Franzens-Universität Innsbruck
June 2009	Masters of Science (with first class honors), University of Innsbruck Thesis: *“A single trapped atom in front of an oscillating mirror”* under the supervision of Prof. Peter Zoller, University of Innsbruck
Since Jan. 2010	PhD studies in Theoretical Physics under the supervision of Prof. Peter Zoller at the Institute for Theoretical Physics, University of Innsbruck

Publications and Preprints

8. **Frustrated Quantum Magnetism with Laser-Dressed Rydberg Atoms**
A. W. Glaetzle, M. Dalmonte, R. Nath, Christian Gross, Immanuel Bloch, and P. Zoller
arXiv:1410.3388 (2014-10-05).

7. **Dynamical preparation of laser-excited anisotropic Rydberg crystals in 2D optical lattices**
B. Vermersch, M. Punk, A. Glätzle, C. Gross, P. Zoller
arXiv:1408.0662 (2014-08-04)

6. **Quantum Spin Ice and dimer models with Rydberg atoms**
A. Glätzle, M. Dalmonte, R. Nath, I. Rousochatzakis, R. Mössner, P. Zoller
Phys. Rev. X **4** 041037 (2014-11-25)

5. **Parallel execution of quantum gates in a long linear ion chain via Rydberg mode shaping**
W. Li, A. Glätzle, R. Nath, I. Lesanovsky
Phys. Rev. A **87** 052304 (2013-05-06)

4. **Driven-dissipative dynamics of a strongly interacting Rydberg gas**
A. Glätzle, R. Nath, B. Zhao, G. Pupillo, P. Zoller
Phys. Rev. A **86** 043403 (2012-10-02)

3. **Atomic Rydberg Reservoirs for Polar Molecules**
B. Zhao*, A. Glätzle*, G. Pupillo, P. Zoller
Phys. Rev. Lett. **108** 193007 (2012-05-11)
* both authors contributed equally to this work

2. **QED with a spherical mirror**
G. Hetet, L. Slodicka, A. Glätzle, M. Hennrich, R. Blatt
Phys. Rev. A **82** 063812 (2010-12-09)

1. **A single trapped atom in front of an oscillating mirror**
A. Glätzle, K. Hammerer, A. J. Daley, R. Blatt, P. Zoller
Opt. Com. **283** 758 (2010-03-15)

Seminar and Conference Talks

18. **Frustrated magnetism with Rydberg atoms and ions**
group seminar of Prof. H. Haeffner, UC Berkeley
2014-08-15, Berkeley, CA, USA

17. **Exotic forms of magnetism with Rydberg dressed atoms**
group seminar of Prof. M. Lukin, Harvard University
2014-07-25, Cambridge, MA, USA

16. **Quantum spin ice with Rydberg dressed atoms**
group seminar of Prof. Pupillo, Laboratoire de Physique Quantique, ISIS
2014-07-02, Strasbourg, France

15. **Applications of Rubidium Rydberg atoms excited to p-states**
    Rydberg meeting with the group of C. Gross
    2014-01-21, Innsbruck, Austria

14. **Quantum spin ice with Rydberg dressed atoms**
    group seminar of Prof. J. Ye and A. M. Rey, Joint Institute for Laboratory Astrophysics, (JILA)
    2013-12-11, Boulder, CO, USA

13. **Quantum spin ice with Rydberg dressed atoms**
    group seminar of Prof. M. Saffman, University of Wisconsin
    2013-12-03, Madison, WI, USA

12. **Exploring anisotropic Rydberg interactions with application to frustrated magnetism**
    Rydberg meeting with group of Prof. Weidemüller, University of Heidelberg
    2013-11-14, Heidelberg, Germany

11. **Quantum spin ice with Rydberg dressed atoms**
    Chist–era R-ION meeting
    2013-11-12, Mainz, Germany

10. **Applications of Rubidium Rydberg atoms in p-states**
    Rydberg meeting, MPQ Garching
    2013-10-30, Garching, Germany

9. **Frustrated Magnetism in Rydberg atoms and Ions**
    SFB meeting, University of Innsbruck
    2013-10-24, Innsbruck, Austria

8. **Non-equilibrium dynamics with Rydberg atoms and polar molecules**
    Invited talk at the ESF Conference on Cold and Ultracold Molecules
    2012-11-18, Obergurgl, Austria

7. **Non-equilibrium dynamics of Rydberg atoms and polar molecules**
    group seminar of Prof. E. Arimondo, University of Pisa
    2012-06-13, Pisa, Italy

6. **Non-equilibrium dynamics of Rydberg atoms and polar molecules**
    group seminar of Prof. S. Rolston and Prof. T. Porto JQI, University of Maryland
    2012-04-11, College Park, MD, USA

5. **Rydberg Reservoirs for Polar Molecules**
    group seminar Prof. D. DeMille, Yale University
    2012-03-29, New Haven, CT, USA

4. **Non-equilibrium dynamics with Rydberg atoms and polar molecules**
    Conference on Cold and Ultracold Molecules
    2012-11-20, Obergurgl, Austria

3. **Non-equilibrium dynamics with Rydberg atoms and polar molecules**
    Chist-era R-Ion meeting
    2012-03-05, Mainz, Germany

2. **Sympathetic cooling of polar molecules with Rydberg atoms**
   SFB meeting, University of Innsbruck
   2011-02-23, Innsbruck, Austria

1. **Sympathetic cooling of molecules with dressed Rydberg atoms**
   Rydberg meeting between Prof. Arimondo's (Pisa, Italy) and Prof. Zoller's group
   2010-12-15, Innsbruck, Austria

Poster presentations

14. **Quantum Ice and dimer models with ultra-cold Rydberg atoms and ions**
    A. Glätzle, R. Nath, M. Dalmonte, P. Zoller, R. Gerritsma, F. Schmidt-Kaler, I. Rousochatzakis, R. Moessner
    The 24th International Conference on Atomic Physics (ICAP)
    2014-08-03, Washington, D.C., USA

13. **Quantum Ice and dimer models with ultra-cold Rydberg atoms and ions**
    A. Glätzle, R. Nath, M. Dalmonte, P. Zoller, R. Gerritsma, F. Schmidt-Kaler, I. Rousochatzakis, R. Moessner
    Gordon conference on Quantum Science
    2014-07-27, Easton, MA, USA

12. **Aspects of Quantumness in Rydberg Crystal Formation**
    A. Carmele, A. Glätzle, W. Lechner, P. Zoller
    UQUAM Workshop Venice 2014
    2014-04-28, Venice, Italy

11. **Quantum Ice and dimer models with ultra-cold Rydberg atoms and ions**
    A. Glätzle, R. Nath, M. Dalmonte, P. Zoller, R. Gerritsma, F. Schmidt-Kaler, I. Rousochatzakis, R. Moessner
    UQUAM Workshop Venice 2014
    2014-04-28, Venice, Italy

10. **Van der Waals mixing of Rydberg Zeeman levels – new types of interactions potentials and sources of entanglement**
    B. Vermersch, A. Glätzle, P. Zoller
    UQUAM Workshop Venice 2014
    2014-04-28, Venice, Italy

9. **Frustrated Magnetism in Rydberg atoms and ions**
   A. Glätzle, R. Nath, M. Dalmonte, P. Zoller, R. Gerritsma, F. Schmidt-Kaler, I. Rousochatzakis, R. Moessner
   International Conference on Quantum Optics 2014
   2014-02-23, Obergurgl, Austria

8. **Frustrated Magnetism in Rydberg atoms and Ions**
   A. Glätzle, R. Nath, M. Dalmonte, P. Zoller, R. Gerritsma, F. Schmidt-Kaler, I. Rousochatzakis,

R. Moessner
IQsim13, Quantum Simulations with Trapped Ions
2013-12-16, Brighton, UK

7. **Frustrated Magnetism in Rydberg atoms and ions**
A. Glätzle, R. Nath, M. Dalmonte, P. Zoller, R. Gerritsma, F. Schmidt-Kaler, I. Rousochatzakis, R. Moessner
SFB meeting
2013-10-24, Innsbruck, Austria

6. **Frustrated Magnetism in Rydberg atoms and ions**
R. Nath, A. Glätzle, M. Dalmonte, P. Zoller, R. Gerritsma, F. Schmidt-Kaler, I. Rousochatzakis, R. Moessner
School on "Ultracold Rydberg Physics"
2013-07-01, Dresden, Germany

5. **Atomic Rydberg Reservoirs for Polar Molecules**
A. Glätzle, B. Zhao, G. Pupillo, P. Zoller
Winter School on Rydberg Physics and Quantum Information
2013-02-12, Obergurgl, Austria

4. **Rydberg Reservoirs for Polar Molecules**
A. Glätzle, B. Zhao, G. Pupillo, P. Zoller
Coherence Summer School
2012-09-16, Pisa, Italy

3. **Atomic Rydberg Reservoirs for Polar Molecules**
A. Glätzle, B. Zhao, G. Pupillo, P. Zoller
International Conference on Quantum Optics
2012-02-12, Obergurgl, Austria

2. **A single trapped atom in front of an oscillating mirror**
A. Glätzle, K. Hammerer, A. J. Daley, R. Blatt, P. Zoller
Summer School on Scalable Quantum Computing with Light and Atoms
2009-08-17, Cargese (Corse), France

1. **A single trapped atom in front of an oscillating mirror**
A. Glätzle, K. Hammerer, A. J. Daley, R. Blatt, P. Zoller
PreDoc Summer School on Laser cooling and Bose-Einstein condensation
2008-10-05, Les Houches, France

Conferences, summer schools and research visits

2014

- University of California, Berkeley, CA, USA, visit P. Schindler, 15.-22.8.2014
- Stanford University, visit Prof. B. Lev, Palo Alto, CA, USA, 10.-15.8.2014

- The 24th International Conference on Atomic Physics (ICAP), Washington, D.C., USA, 4.-8.8.2014
- Gordon conference on Quantum Science, Easton, MA, USA, 28.7.-1.10.2014
- Harvard University, visit Prof. M. Lukin, Cambridge, MA, USA, 21.-27.7.2014
- Institut de Science et d'Ingenierie Supramoleculaires, visit Prof. G. Pupillo, Strasbourg, France, 1.-6.7.2014
- UQUAM workshop, Venice, Italy, 28.4..-2.5.2014
- Max-Planck-Institut für Quantenoptik, visit C. Gross, Garching, Germany, 19.-20.5.2014
- International Conference on Quantum Optics 2014, 23.2.-01.3., 2014, Obergurgl, Austria
- Rydberg meeting with the group of Prof. I. Bloch, Innsbruck, Austria, 20.-22.1.2014

2013

- 1st Quantum Simulations with Trapped Ions workshop 2013 (IQsim13), Brighton, UK, 16.-20.12.2013
- University of Wisconsin, visit Prof. M. Saffman, Madison, WI, USA, 2.-8.12.2013
- University of Colorado, visit Prof. J. Ye and Prof. A. M. Rey, Boulder, CO, USA, 9.-15.12.2013
- University of Heidelberg, visit Prof. M. Weidemueller, Heidelberg, Germany 14.-15.12.2013
- RION meeting, Mainz, Germany, 11.-13.12.2013
- Max-Planck-Institut für Quantenoptik, visit Prof. I. Bloch, Garching, Germany, 30.10.2013
- ERC Kick off meeting, Garching, Germany, 18.9.2013
- RION meeting, Nottingham, UK, 22.-25.4.2013
- Winter School on Rydberg physics and Quantum Information 2013, Obergurgl, Austria, 10.-15.2.2013

2012

- Quantum Optics Conference, Obergurgl, Austria, 13.-18.02.2012
- Chist–era Ryd-Ion Meeting, Mainz, Germany, 04.-07.03.2012
- Harvard University, Group of Prof. Lukin, MA, USA, 20.-31.3.2012
- Yale University, visit Prof. D. DeMille, New Haven, USA, 29.3.2012
- Joint Quantum Institute, visit S. Rolston and T. Porto, MD, USA, 1.-16.4.2012
- University of Pisa, visit Prof. E. Arimondo, Pisa, Italy, 12.-14.6.2012
- Max-Planck-Institute for Quantum Optics, visit Prof. I. Bloch, Garching, Germany, 21.-22.6.2012
- Albert Einstein Center for Fundamental Physics, visit Prof. U.-J. Wiese, Bern, Switzerland, 23.- 29.7.2012
- Coherence Summer School, Pisa, Italy, 17.-23.9.2012
- Chist–era Rydberg meeting, Innsbruck, Austria, 18.-19.10.2012
- Conference on Cold and Ultracold Molecules, Obergurgl, Austria 19.-25.11.2012
- Max-Planck-Institute for the Physics of Complex Systems, visit Prof. R. Moessmer, Dresden, Germany, 26.-28.11.2012

2011

- SFB Meeting, Wien, Austria, 19.-20.5.2011
- OePG Meeting, Lausanne, Switzerland, 14.-17.6.2011
- Workshop on Coherence and Decoherence at Ultracold Temperatures, Munich, Germany, 6.-9.9.2011
- Chistera Ryd-Ion Meeting Kick off meeting, Überlingen, Germany, 23.-25.08.2011

2010

- Capri Spring School on Transport in Nanostructures 2010, Capri, Italy, 11.-18.04.2010

2009

- SCALA Summer School on Scalable Quantum Computing with Light and Atoms in Cargese (Corse), France, 17.-29.08.2009
- 5th SFB-Meeting, Vienna, Austria, 10.-11.12.2009

2008

- SFB Summer School, Innsbruck, Austria, 9.-12.7.2008
- Condensed Matter Physics with cold atoms and molecules, Oxford, UK, 22.- 26.9. 2008
- Laser Cooling and Bose-Einstein Condensation, Les Houches, France, 28.9.-10.10. 2008

2006

- ICAP Summer School, Innsbruck, 9.-14.7.2006

Awards and Prizes

2003	Bronze medal at the “22nd österreichischen Physikolympiade”, Fürstenfeld, Austria
2004, 2008 and 2009	Academic merit scholarship of the University of Innsbruck

Teaching

Exercise Classes
Mar 2011 – Jul 2011: Mathematical Methods 1
Oct 2011 – Feb 2012: Theoretical Physics 1 (Classical Mechanics)
Mar 2012 – Jul 2012: Mathematical Methods 1
Oct 2012 – Feb 2013: Theoretical Physics 1 (Classical Mechanics)

Tutor, Institute for Theoretical Physics, University of Innsbruck:
Mar 2006 – Jul 2006: "Theoretische Physik 1 – Electrodynamics" (H. J. Briegel)
Oct 2006 – Feb 2007: "Theoretische Physik 2 – Quantum Theory" (P. Zoller)
Mar 2007 – Jul 2007: "Theoretische Physik 1 – Electrodynamics" (H. J. Briegel)
Oct 2007 – Feb 2008: "Theoretische Physik 2 – Quantum Theory" (P. Zoller)
Mar 2008 – Jul 2008: "Theoretische Physik 3 – Statistical Physics" (P. Zoller)
Oct 2008 – Feb 2009: "Theoretische Physik 2 – Quantum Theory" (H. Ritsch)
Mar 2009 – Jul 2009: "Theoretische Physik 2 – Quantum Theory" (H. J. Briegel)

Physics-related employment

2010 (Jan 1 – Apr 30)	*Wissenschaftlicher Mitarbeiter*, Inst. for Theoretical Physics, Univ. of Innsbruck
2010 (May 1) – 2012 (Apr 30)	*Forschungsassistent*, Inst. for Theoretical Physics, Univ. of Innsbruck
2012 (May 1) – 2013 (Dec 31)	*Research Assistant*, IQOQI, Innsbruck, Austrian Academy of Science
2014 (Jan 1) – 2014 (Jul 31)	*Forschungsassistent*, Inst. for Theoretical Physics, Univ. of Innsbruck
2014 (Aug 1) —	*Research Assistant*, IQOQI, Innsbruck, Austrian Academy of Science

Other Interests

- playing the guitar and piano
- International Yacht Master License for sailing and motor boats: The holder is entitled to command a sailing or motor yacht of maximum length 80 ft in navigation area 3 (offshore - 200 nautical miles from coast). Issued: Federal Ministry of Transport, Austrian Sailing Federation, Vienna 27.10.2010 (S-006629)
- Short Range Certificate: international certificate that authorizes the holder to operate VHF radiotelephone ship stations and VHF radio equipment for the Global Maritime Distress and Safety System (GMDSS). Issued: Bundesministerium für Verkehr, Bau und Stadtentwicklung, Federal Republic of Germany, Nürnberg, 03.03.2012 (Nr. 074126-F)
- Judo black belt (shodon), issued by the Austria Judo Federation (2001)
  1993 – 2003: Member of the Judo club Reutte
  1999 – 2003 Assistant Trainer of the Judo Club Reutte

A. W. Glätzle, Innsbruck, September 2014